

Dissertation zur Erlangung des Doktorgrades
der Fakultät für Chemie und Pharmazie
der Ludwig-Maximilians-Universität München

**Designing Semiconductors and Catalysts
for Photoelectrochemical Hydrogen Production**

von

Jonathan Kampmann

aus

München, Deutschland

2020

Erklärung

Diese Dissertation wurde im Sinne von § 7 der Promotionsordnung vom 28. November 2011 von Herrn Prof. Dr. Thomas Bein betreut.

Eidesstattliche Versicherung

Diese Dissertation wurde eigenständig und ohne unerlaubte Hilfe bearbeitet.

München, den 3. März 2020

Jonathan Kampmann

Dissertation eingereicht am: 4. Dezember 2019

1. Gutachter: Prof. Dr. Thomas Bein

2. Gutachterin: Prof. Dr. Dina Fattakhova-Rohlfing

Mündliche Prüfung am: 17. Februar 2020

Abstract

This thesis presents the results of a number of projects dealing with the challenge of hydrogen production from sunlight, promoting a medium to store and transport renewable energy. Different nanostructured organic and inorganic semiconductors as well as metallic co-catalysts were synthesized and combined to thin film devices, which can be envisioned to work like artificial leaves. These devices were extensively studied by various physical methods like X-ray diffraction, electron microscopy, X-ray photoelectron spectroscopy, spectrophotometry, nuclear magnetic resonance spectroscopy and density functional theory calculations. Finally, their abilities regarding the harvesting of sunlight and their catalytic properties for hydrogen evolution were investigated by photoelectrochemical methods.

The first chapter describes the influence of tin doping on the performance of hematite photoanodes using model photoabsorber layers with different tin doping concentrations and concentration gradients prepared via atomic layer deposition. This study aims for the basic understanding of effects of dopants on fundamental rate-determining kinetic and recombination steps of metal oxide photoelectrodes.

The second chapter elucidates the phenomenon of photocorrosion with the example of lithium doped copper oxide photocathodes. While this material appears to be an efficient material at first glance, it corrodes by copper reduction from its own photogenerated electrons in contact with water. This observation was studied in depth to reveal the underlying mechanism of photocorrosion. Additionally, a suitable protection approach for this material is discussed and the hydrogen evolution of those final devices is quantified.

The third chapter presents the first study of covalent organic frameworks serving as photoelectrodes. By self-organization, this organic material grows conjugated two-dimensional sheets that stack in the third dimension, forming crystalline and porous polymers. The synthesized material called *BDT-ETTA* was grown as flat films with its one-dimensional pores oriented perpendicular to the surface of the underlying conductive substrate. Those devices were shown to exhibit a suitable band gap alignment

for hydrogen evolution and were applied to reduce water by the use of sunlight. Finally, the combination with a platinum cocatalyst revealed the catalytic activity of the photoactive material itself as bottleneck for the targeted application, whereas the diversity of possible optical and electronic properties can be tuned by the selection of appropriate building blocks, offering an auspicious material system for the evolution of hydrogen from sunlight.

The fourth chapter explores electrophoretic deposition as a well-working technique for the film deposition of covalent organic frameworks, also in combination with metallic platinum nanoparticles. With the example of the previously introduced *BDT-ETTA*, the influence of morphology and added cocatalyst on the photoelectrochemical performance is discussed. Devices exhibiting textural porosity, in addition to the intrinsic porosity of the covalent organic framework itself, showed an increased photoactivity compared to flat electrodes. Their combination with a nanosized platinum cocatalyst leads to strongly enhanced photocurrents, alleviating the catalytic bottleneck of the discussed material.

Finally, the perspectives for the continuation of the above projects are discussed in the last chapter.

Contents

Erklärung

Eidesstattliche Versicherung

Erklärung.....iii

Eidesstattliche Versicherung.....iii

Acknowledgements Fehler! Textmarke nicht definiert.

Abstracti

Contents..... 1

1 Introduction 7

1.1 The role of hydrogen in a sustainable society 7

1.2 Synthesis approaches for hydrogen gas from renewable energy..... 9

1.3 Theory of photoelectrochemical water splitting..... 10

1.3.1 The ideal photoelectrode..... 10

1.3.2 Different architectures of photoelectrochemical cells..... 12

1.3.3 The mechanisms of light-driven reactions at semiconductor-liquid interfaces 15

1.3.4 Common challenges of photoelectrolysis 18

1.4 State-of-the-art semiconductors for PEC water splitting..... 18

1.4.1 Metal oxides 18

1.4.2 Solid-state photovoltaic cells 23

1.4.3	Crystalline organic frameworks.....	24
1.5	Synthesis methods	28
1.5.1	Sol-gel reactions	28
1.5.2	Synthesis of covalent organic frameworks.....	29
1.6	Scope of this thesis	32
1.7	References	33
2	Characterization techniques	43
2.1	X-ray Diffraction.....	43
2.1.1	Theory.....	43
2.1.2	Geometries.....	45
2.2	Electron Microscopy.....	46
2.2.1	Scanning Electron Microscopy	46
2.2.2	Focused Ion Beam Technology.....	47
2.2.3	Transmission Electron Microscopy	49
2.2.4	Spectroscopic methods.....	52
2.3	X-ray Photoelectron Spectroscopy	54
2.4	Spectrophotometry.....	55
2.5	Nuclear magnetic resonance spectroscopy	57
2.6	Photoelectrochemical Analysis.....	62
2.6.1	Cyclovoltammetry and Chronoamperometry	63
2.6.2	Incident Photon to Current Efficiency.....	64
2.6.3	Hydrogen detection.....	65
2.7	References	66
3	Sn-doped hematite for photoelectrochemical water splitting: the effect of Sn concentration	69

Abstract..... 70

3.1 Introduction..... 70

3.2 Experimental..... 71

 3.2.1 Preparation of photoanodes..... 71

 3.2.2 Microstructural Characterization..... 72

 3.2.3 Optical Characterization 73

 3.2.4 Photoelectrochemistry 73

 3.2.5 Computational details 74

3.3 Results and Discussion..... 74

 3.3.1 Atomic Layer Deposition of Sn-doped Hematite..... 74

 3.3.2 Crystallinity of ALD Sn-doped hematite 80

 3.3.3 Photoelectrochemical Water Splitting 82

3.4 Conclusions 83

3.5 References 84

4 How photocorrosion can trick you: A detailed study on low-bandgap Li doped CuO photocathodes for solar hydrogen production.....87

Abstract..... 88

4.1 Introduction..... 88

4.2 Results and Discussion..... 90

4.3 Conclusions100

4.4 Supporting Information.....101

 4.4.1 Experimental details.....101

 4.4.2 Additional figures.....107

4.5 References120

5 Oriented Films of Conjugated 2D Covalent Organic Frameworks as Photocathodes for Water Splitting.....	127
Abstract.....	128
5.1 Introduction.....	128
5.2 Results and discussion.....	129
5.2.1 Synthesis of COF systems.....	129
5.2.2 Photoelectrochemical properties of COF films.....	133
5.3 Conclusion.....	137
5.4 Experimental Section.....	138
5.4.1 General procedure for BDT-ETTA COF films:.....	138
5.4.2 Structural characterization.....	138
5.5 Associated Content.....	139
5.6 Author Information.....	139
5.7 Acknowledgments.....	140
5.8 References.....	140
5.9 Supporting Information.....	143
5.9.1 Materials and Methods.....	143
5.9.2 Synthetic procedures.....	145
5.9.3 Electrochemical measurements.....	147
5.9.4 SEM.....	155
5.9.5 X-Ray Diffraction Analysis.....	156
5.9.6 Sorption.....	157
5.9.7 Structural simulations of BDT-ETTA COF.....	158
5.9.8 IR Spectroscopy.....	161
5.9.9 Thermogravimetric Analysis.....	162

5.9.10	Elemental Analysis	162
5.9.11	NMR Spectra.....	163
5.9.12	References.....	167
6	Covalent Organic Framework Films by Electrophoretic Deposition - Creating efficient Morphologies for Catalysis	168
	Abstract.....	169
6.1	Introduction.....	169
6.2	Experimental Section	171
6.3	Results and Discussion.....	174
6.4	Conclusion	184
6.5	Associated Content.....	185
6.6	Author Information.....	185
6.7	Acknowledgment.....	185
6.8	Abbreviations	185
6.9	References	186
6.10	Supporting Information	190
6.10.1	Deposition of BDT-ETTA on FTO, ITO and titanium foil.....	190
6.10.2	Deposition of BDT-ETTA in anisole, ethyl acetate and toluene	191
6.10.3	DLS Data for ultrasound treated BDT-ETTA COF	192
6.10.4	Transmission electron micrographs.....	193
6.10.5	COF EPD film physisorption	196
6.10.6	Fourier-transformed infrared spectroscopy	197
6.10.7	BDT-ETTA COF time-dependent thickness plot.....	198
6.10.8	Voltage dependent deposition of BDT-ETTA.....	199
6.10.9	Mass-dependent deposition of COF-300	200

6.10.10	Large area deposition of BDT-ETTA COF	201
6.10.11	SEM Micrographs of BDT-ETTA COF deposited on a porous mesh.....	202
6.10.12	Thickness dependent PEC Current measurements and Chronoamperometry	203
6.10.13	Stability of BDT-ETTA COF after PEC catalysis.....	203
6.10.14	TEM of Pt nanoparticles	204
6.10.15	References.....	205
7	Conclusions and Outlook.....	207
8	Publications and Conference Contributions.....	211
8.1	Publications.....	211
8.2	Contribution to Conferences.....	212
8.2.1	Oral Presentations	212
8.2.2	Poster Presentations.....	212

1 Introduction

1.1 The role of hydrogen in a sustainable society

Our modern society is based on industrial investment and economic growth. As the needed energy is mainly covered by burning fossil sources like oil, coal or natural gas, mankind has released both heat and greenhouse gases like carbon dioxide and nitrogen oxides into our atmosphere which were stored in the earth during the course of several hundred million years. Consequently, it is easy to imagine that this fact can cause significant changes of the earth's climate such as more frequently occurring extreme weather conditions and a warming of the earth's surface. Additionally, the search for new deposits of fossil fuels gets more and more expensive and our reserves are getting lean.

For these reasons, we need to change our energy supply towards the use of sustainable sources. Germany, one of the forerunner countries regarding the integration of renewable energies, generated 84% of its electricity from fossil fuels in 2014, even though Germany had, at that time, an installed wind power capacity of 35.92 GW as well as an installed solar power capacity of 37.34 GW, which would be more than enough to cover the average aggregate gross power consumption of 57.55 GW.¹ The key to remove this discrepancy is an efficient way of storage, distribution and supply of this energy.

Even better than numerous pumped-storage power plants or giant battery stacks, energy storage in the form of chemical bonds is able to cover these demands. Among different chemical components, hydrogen can provide a comparably high theoretical energy density per mol due to its low molecular weight. If hydrogen is used in a fuel cell to generate electricity, the single emission product from its reaction with oxygen is water (Eq. 1.1). Therefore, hydrogen can be used as climate-neutral fuel to power mobility, as it is currently demonstrated in trains, cars, ships and even airplanes.

The role of hydrogen in a sustainable society



Furthermore, hydrogen is also needed to synthesize ammonia via the Haber-Bosch process (Eq. 1.2) in a quantity of over 140 million tons per year. While ammonia can also be used as energy carrier, most of those large quantities are used to provide fertilizers like ammonium nitrate or urea for agriculture.²⁻³ Therefore, the Haber-Bosch process was awarded with the Nobel prize in chemistry in 1918.



Unfortunately, nearly all of the used hydrogen is currently produced from steam reforming of natural gas (Eq. 1.3).⁴ This source needs to be changed to a sustainable alternative in the near future to become independent from fossil resources.



All in all, our modern world and its economic growth is based on non-ending energy supply. With the prospect of dwindling resources, increasing emissions and climate change, one must urgently look for alternatives to oil, gas and coal. Hydrogen, or its derivatives, are well-suited chemical energy carriers to supersede the established energy economy based on fossil fuels.

1.2 Synthesis approaches for hydrogen gas from renewable energy

Hydrogen gas can be produced in various ways from renewable energy. A versatile technology is electrolysis using a so-called proton exchange membrane (PEM), which enables generation of hydrogen with high pressure at room temperature. It is powered with electricity that can be produced by any technique, preferably a renewable one like solar cells or wind power. A hydrogen evolution reaction (HER) catalyst like platinum is applied on one side of the polymer membrane, while an oxygen evolution reaction (OER) catalyst such as iridium dioxide covers the other side. With the addition of an electrical potential, both gases are evolved from an aqueous electrolyte and can be collected separately.

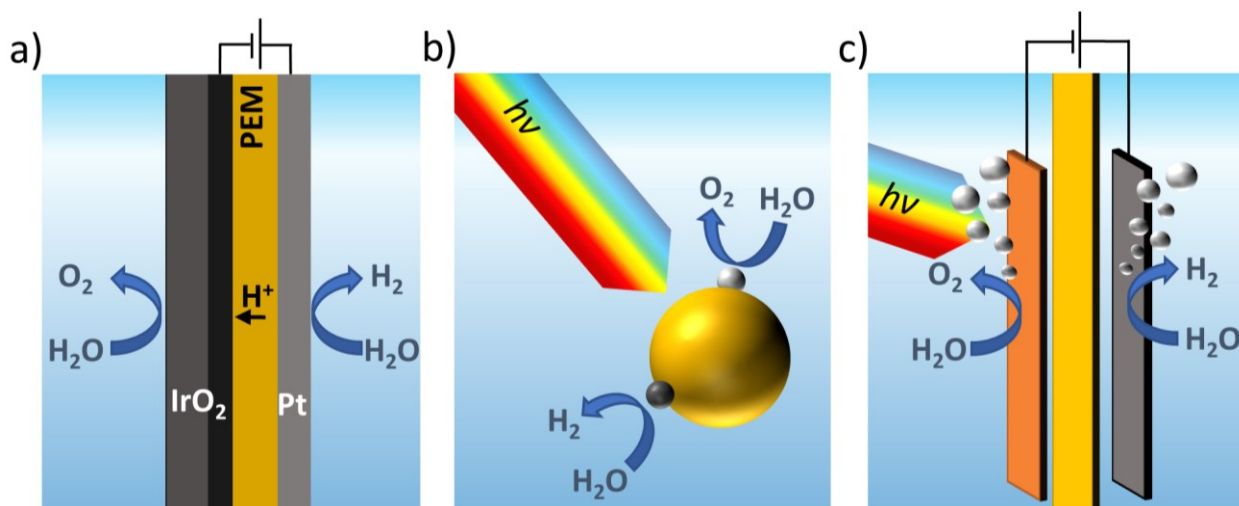


Figure 1.1. Possible approaches for sustainable hydrogen production: a) dark electrolysis, b) photocatalysis or c) photoelectrochemistry.

Beside this, other technologies explore the direct conversion of sunlight to hydrogen with the goal of minimizing electric losses and therefore maximizing the so called solar-to-hydrogen efficiency. To this end, suitable semiconductors are directly immersed into an aqueous electrolyte and evolve both oxygen and hydrogen gas under illumination. In photocatalysis, semiconductor particles are dispersed in the electrolyte. These particles need to have a suitable band alignment and band gap to cover the redox potential of both half reactions as well as catalytic surfaces or cocatalysts for both oxygen and hydrogen evolution. While this process could be easily scalable to industrial dimensions, the product is an explosive oxyhydrogen gas mixture, which would require great efforts to be separated afterwards. To prevent this complication, research in this field is mostly performed using

Theory of photoelectrochemical water splitting

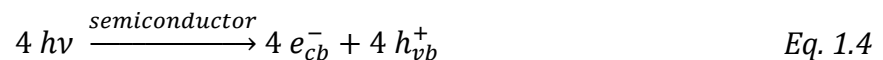
sacrificial agents. These additives in the electrolyte are used to scavenge electron holes, therefore facilitating the redox reaction and suppressing the oxygen evolution reaction. This approach would be viable for large scale industrial application if the hydrogen production could be combined with a product-oriented oxidation, e.g., the production of chlorine gas. Otherwise, the large required quantities of those additives that get oxidized and continually consumed during the reaction would likely exceed the value of the produced hydrogen.

The photoelectrochemical approach combines the principles of electrolysis and photocatalysis. The HER and OER processes take place on different electrodes as in electrolysis, but using sunlight as the source of energy as in photocatalysis. Under incident sunlight, hydrogen and oxygen are produced on the semiconductor surfaces in both half cells and the products are directly separated for further storage. This system is expected to reduce product cross-contamination and minimize energy losses and fabrication cost as compared to the other approaches mentioned above.⁵⁻⁶ Currently rather low yields (below 5% solar-to-hydrogen efficiency) hamper commercialization of photoelectrolysis for a large scale hydrogen production, therefore further research is needed, both on materials and mechanistic understanding, to make this technology economically feasible. In the end, each technology needs to be studied and optimized separately to satisfy the needs of specific applications.

1.3 Theory of photoelectrochemical water splitting

1.3.1 The ideal photoelectrode

In recent years, the research on new materials for artificial photosynthesis has increased substantially. These compounds need to exhibit semiconducting properties to be able to convert light into electricity or directly into chemical energy. Semiconductors can absorb photons with higher or equal energy than their band gap. This results in the excitation of electrons to the conduction band, leaving behind so-called 'electron holes' in the valence band (Eq. 1.4). Electron holes are no actual particles; they are rather described as a positively charged void in the valence band.

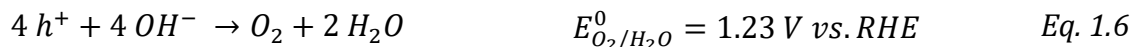


$h\nu$: Energy of one photon

e_{cb}^- : Electron in the conduction band

h_{vb}^+ : Electron hole in the valence band

The ideal semiconductor for this application is able to absorb as much of the incident light as possible, as, in the ideal case, two absorbed photons correlate directly to one evolved hydrogen molecule. A high absorption coefficient is often the result of a direct optical band gap. In this case, only a thin layer of semiconducting material is needed to absorb a sufficient amount of light. Nevertheless, many of the investigated semiconductors have indirect band gaps. But this is only one important property, as the electron-hole pairs created by absorption of photons need also to be separated efficiently. Materials with good charge separation properties are indicated by a low relative permittivity. The lower the Coulomb force between the electron and the electron hole, the easier they can be split up and convert water to hydrogen and oxygen gas. If the photoabsorber is a p-type semiconductor, the electrons move to the solid-electrolyte interface and reduce water to hydrogen (Eq. 1.5). The holes are conducted to a counter electrode, where they oxidize water to form oxygen gas (Eq. 1.6). Under standard conditions, the required free energy for the water splitting reaction is $\Delta G = 237 \text{ kJ mol}^{-1}$. A minimum bandgap of 1.23 eV is required to provide this energy, corresponding to an absorption threshold of around 1000 nm.⁷



e^{-} : Electron h^{+} : Electron hole E^0 : Standard electrode potential RHE: Reversible hydrogen electrode

The efficiency of a photovoltaic device is commonly determined by the open circuit potential, the short circuit current, the fill factor and the incident light intensity. In case of a photoelectrochemical device, the open circuit voltage corresponds to the chemical potential of the water splitting reaction of 1.23V and can therefore be considered constant. Additional, kinetic overpotentials and energy losses at the semiconductor-liquid interface require an additional potential to be covered, which results in a total required energy of 1.6 – 2.4 eV per generated electron-hole pair.⁸ In a standardized experiment, also the incident light intensity is held constant to the equivalent of one sun (100 mW cm^{-2} , AM1.5G, see chapter 2.4). Therefore, the single variable for calculating the photoelectrochemical efficiency is the rate of hydrogen (or oxygen) production at the chemical potential of hydrogen

Theory of photoelectrochemical water splitting

evolution of 1.23 V vs. RHE (see Eq. 1.5 and 1.6) without additional overpotentials. The rate of hydrogen evolution directly correlates to the photocurrent if all possible side reactions, e.g. corrosion of the photoabsorber or reduction of oxygen gas, can be excluded. The efficiency of a photoelectrochemical device is therefore directly proportional to the obtained photocurrent and can be calculated according to Eq. 1.7.⁹

$$\frac{\text{chemical potential} \times \text{rate}}{\text{light intensity}} = \frac{1.23 \text{ V} \times \text{current} (\text{mA cm}^{-2})}{100 \text{ mW cm}^{-2}} \quad \text{Eq. 1.7}$$

Ideally, the semiconductors' surfaces should exhibit some specific catalytic activity themselves, which otherwise needs to be provided by cocatalysts. If the kinetic overpotentials for electron transfer processes at the solid-electrolyte interface are considered, an optimal bandgap of 1.5 – 2.4 eV can be postulated. Experimental and theoretical studies showed an expected maximum photocurrent density of 12.6 mA cm⁻² for a single optimal absorber (with an optical band gap of 2.23 eV and 1.0 V of assumed losses per photon), based on Shockley-Queisser limit, and a maximum conversion efficiency of incident photons to hydrogen of 15%.^{6,10-11} Solar-to-hydrogen efficiencies of tandem cells (concept see next chapter) containing a photoanode and a photocathode are calculated to have their maximum at 29.7% (for optical band gaps of 1.6 and 0.95 eV for top and bottom cell electrode, respectively).¹² If such efficiency can be obtained and combined with long-term stability using low-cost materials, the concept of PEC water splitting would become eligible for an industrial application.

1.3.2 Different architectures of photoelectrochemical cells

A photoelectrochemical cell is usually either built with one semiconductor as single photoabsorber or with two semiconductors combined to a tandem cell. In a full device, anode and cathode are electrically connected and immersed in an aqueous electrolyte. Both electrolyte compartments are connected with an ion-selective membrane while the produced hydrogen and oxygen gases are collected separately. This prevents the accumulation of an explosive gas mixture and avoids complex gas separation procedures.

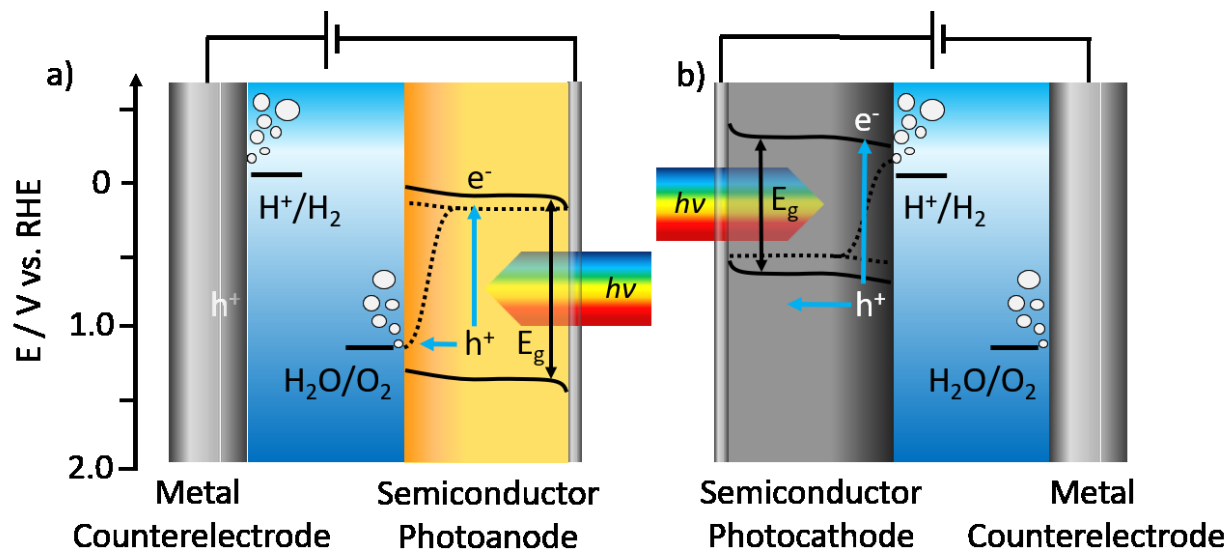


Figure 1.2. Schematic drawing of photoelectrochemical setups using a single absorber on a transparent conductive substrate connected to a metal counter electrode. For this approach, either an n-type semiconductor can be used as photoanode (a) or a p-type semiconductor as photocathode (b). The ion-selective separator membrane is not shown for clarity.

To study only one half-reaction of the water splitting reaction, the single absorber approach is the most commonly used. To this end, the photoelectrode needs to be connected to a counter electrode (Figure 1.2). The counter electrode is usually made of platinum, as it exhibits distinct electrochemical stability in a broad potential range and does not polarize during the measurement, while the electrode provides fast electron transfer to the electrolyte. A single absorber material should have a bandgap of at least 1.7 eV to generate sufficient photovoltage for the water splitting reaction and all additional kinetic overpotentials.⁹ In order to provide the electrochemical driving force, the valence band energy E_{VB} of a photoanode needs to be significantly more positive than the oxygen evolution potential. Consequently, also the conduction band energy E_{CB} of a photocathode needs to be lower than the hydrogen evolution potential. For small bandgap semiconductors, an additional bias can be applied to compensate the occurring potential difference.¹³ Only a small number of metal oxides like TiO_2 or SrTiO_3 ¹⁴ exhibit E_{VB} and E_{CB} edges suitable for both hydrogen and oxygen evolution, and SrTiO_3 was used for so-called unassisted water splitting.¹⁵

Theory of photoelectrochemical water splitting

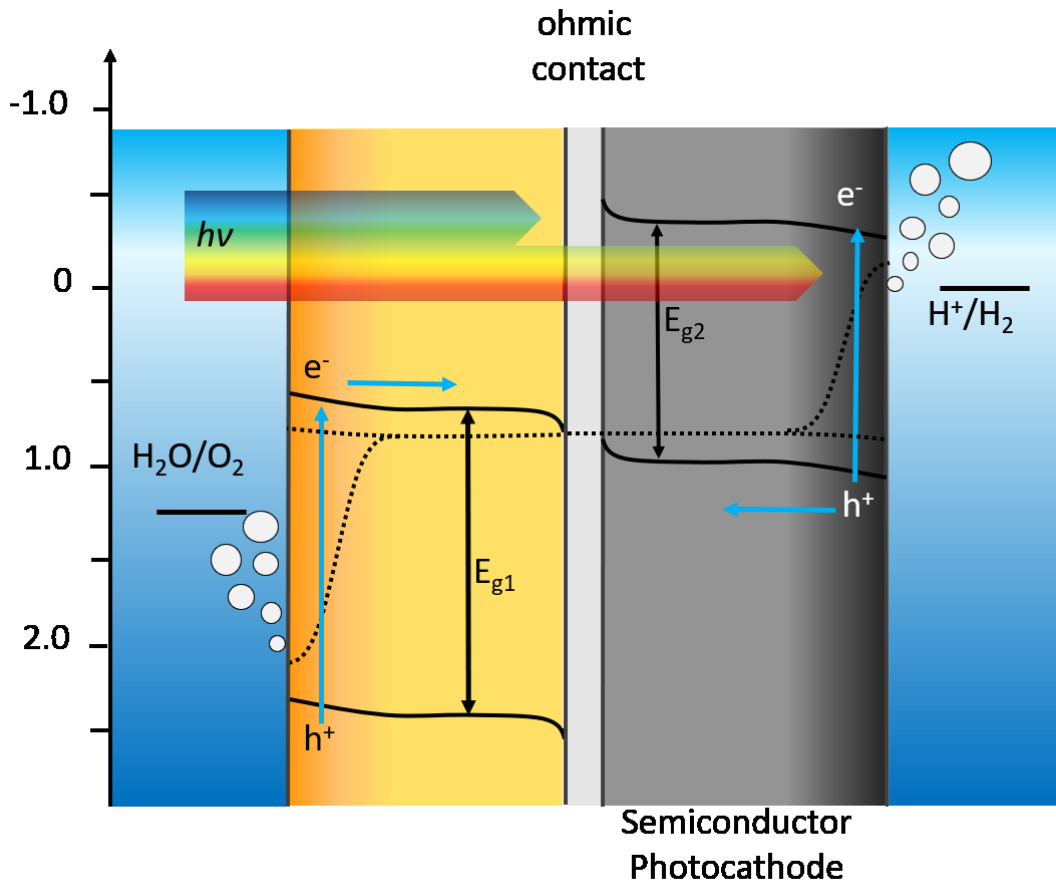


Figure 1.3. Schematic drawing of a photoelectrochemical tandem cell composed of a photoanode connected to a photocathode. By the use of semiconductors with different suitable bandgaps, their combination allows for the absorption of a significant range of the sunlight spectrum.

Another possible device architecture is the combination of an n-type and a p-type semiconductor to a tandem cell (Figure 1.3). The used semiconductors can have more narrow bandgaps compared to a single-absorber photoelectrode, which has to provide all the energy of the water splitting reaction by itself. The combination of one photoabsorber with a wider band gap, commonly the photoanode, in front of another electrode, commonly a photocathode, with a lower band gap, allows for a significantly increased absorption of visible light, especially in the red and near IR region. Therefore, tandem cells can more easily provide enough energy to drive the water splitting reaction.^{7, 16} Ideally, both semiconductors absorb an equal number of incident photons and provide therefore a comparable photocurrent to maximize the device efficiency.

1.3.3 The mechanisms of light-driven reactions at semiconductor-liquid interfaces

The defining characteristic of photoelectrochemical water splitting is the direct interface between the photoelectrode and the electrolyte. If a semiconducting electrode, in this example a p-type photocathode, and a metal counter electrode are immersed in an aqueous electrolyte, the corresponding work function ϕ_{SC} , the electron affinity A_e , the valence band (VB), the conduction band (CV) and the Fermi level ($E_{F,SC}$) of the photocathode as well as the Fermi level of the metal counter electrode ($E_{F,M}$) and its work function ϕ_M and the redox potentials of water can be described relative to the vacuum level and the standard hydrogen electrode (SHE) potential according to Figure 1.4a.

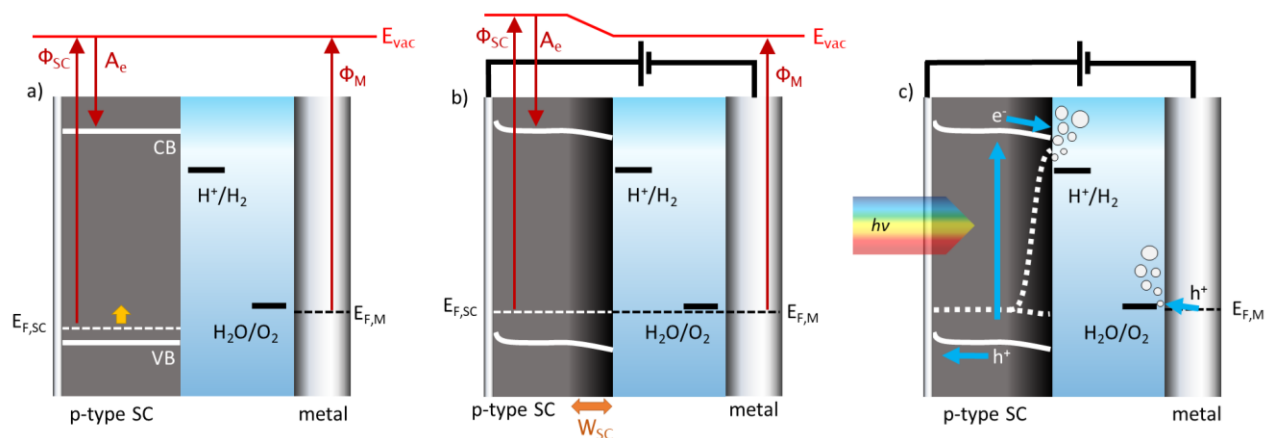


Figure 1.4: a) A p-type semiconductor photocathode and a metal counter electrode are immersed in an aqueous electrolyte. The corresponding work functions ϕ , the electron affinity A_e , valence band (VB), conduction band (CV) and the Fermi level ($E_{F,SC}$) of the photocathode as well as the Fermi level of the counter electrode ($E_{F,M}$) and the redox potentials of water are included with respect to the vacuum level E_{vac} . b) If both electrodes are connected, the Fermi levels will match. The lift of $E_{F,SC}$ is indicated with a yellow arrow in (a). The application of a reductive potential on the cathode leads to the formation of a space charge layer W_{SC} and bending of both CB and VB. The electrochemical driving force of the HER is marked with $\Delta\phi$. c) Illuminating the semiconductor leads to the excitation of electrons from the VB to the CB. The Fermi level splits up in the space charge layer region, which additionally facilitates charge separation. Electrons move to the SC surface and electron holes to the metal counter electrode, leading to the evolution of hydrogen and oxygen gas, respectively.

The interface between the semiconductor and the aqueous electrolyte, also called semiconductor-liquid junction, can be described as a Schottky-type contact. If the photocathode is electrically connected to the counter electrode, both Fermi levels will match. In this configuration, a high enough external potential would already lead to electrolysis of the aqueous electrolyte. For a

Theory of photoelectrochemical water splitting

photoelectrochemical application, the external potential is kept small as the energy needed to drive the water splitting reaction is intended to be solely covered by the excitation of the semiconductor upon illumination, but this already causes a slight band bending. Ionized donor species are left behind and the region is depleted of free charge carriers, creating the space charge layer W_{sc} (Figure 1.4b). Illumination of the photocathode results in the splitting of its Fermi level into two quasi-Fermi levels, excitation of charge carriers and photoelectrolysis of the electrolyte (Figure 1.4c). For a p-type semiconductor, this results in an excess of holes at the semiconductor-liquid junction while for an n-type semiconductor, electrons are concentrated there. The resulting electric field amplifies the bending of the semiconductor's energy bands in the region of the space charge layer. Minority carriers are driven to the surface, which reduces electron – hole recombination in the bulk material.¹⁷ This band bending can be neglected for nanostructured and mesoporous materials. Their small domain sizes allow only for a small band bending, which is lower than the thermal energy at room temperature. For this reason, minority carrier movement can solely be described by diffusion. Additional bias can be applied to withdraw majority carriers from the semiconductor-electrolyte junction to further reduce recombination losses.

Several experimental techniques were developed to characterize the mechanisms and kinetics of reactions at the interface between a semiconductor and an electrolyte upon illumination. Incident photon to current conversion efficiency (IPCE) measurements are able to quantify the ratio of the obtained photocurrent density j_{photo} to the incident photon flux I_0 multiplied with the electrical charge q (Eq. 1.8).¹⁷ Furthermore, the IPCE can be described as the product of the light harvesting efficiency η_{LH} , the charge transfer efficiency η_{trans} and the electron hole separation efficiency η_{sep} .¹⁸

$$IPCE = \frac{j_{photo}}{I_0 \cdot q} = \eta_{LH} \cdot \eta_{trans} \cdot \eta_{sep} \quad Eq. 1.8$$

As discussed earlier, the electron hole separation efficiency is a very important characteristic of suitable semiconductors and can be determined by measuring the *IPCE* as well as calculating η_{LH} and η_{trans} . The light harvesting efficiency can be calculated from the wavelength depending absorption coefficient $\alpha(\lambda)$ and the film thickness d (Eq. 1.9). This assumption can only be made if light scattering and internal reflection are neglected.

$$\eta_{LH} = 1 - e^{-\alpha(\lambda)d} \quad \text{Eq. 1.9}$$

The charge transfer efficiency can be experimentally determined by transient current measurements. Most nanostructured photoelectrodes show a characteristic current response to chopped light (Figure 1.5). The ratio of steady state current density j_{ss} and instantaneous current density j_0 results in the charge transfer efficiency of minority carriers moving to the electrolyte (Eq. 1.10).¹⁸

$$\eta_{trans} = \frac{j_{ss}}{j_0} \quad \text{Eq. 1.10}$$

The electronic potential of PEC measurements is conventionally described in Volts versus the reference hydrogen electrode (RHE). The space charge layer and consequently also the charge transfer efficiency strongly depend on the potential at the semiconductor-liquid junction. Therefore, the electrochemical potential needs to be monitored with care. At pH 0, electrons with potential of 0.0 V vs. RHE exhibit an energy of -4.5 eV relative to the vacuum level.¹⁹

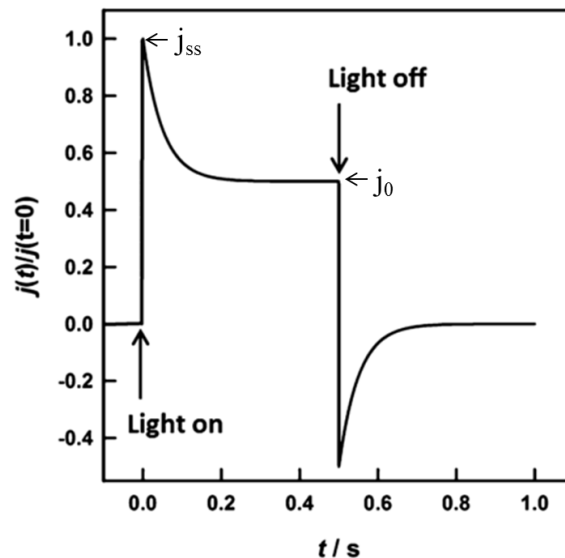


Figure 1.5: Calculated transient current response for an n-type semiconductor with 50 % transfer efficiency.¹⁸

State-of-the-art semiconductors for PEC water splitting

1.3.4 Common challenges of photoelectrolysis

Beside the conversion of sunlight energy into hydrogen and oxygen gas, several other undesired processes can occur in the course of the photoelectrochemical reaction, minimizing its total efficiency. Stability under operating conditions is one of the key requirements of the investigated materials for being integrated in a possible device application. The electrodes should exhibit intrinsic (electro-) chemical stability under illumination, in the intended potential range and in the used electrolyte. For the latter, the pH value of aqueous electrolytes is often crucial and possible instabilities of well-studied materials can be initially assessed in Pourbaix diagrams.²⁰ While it is possible to protect a photoelectrode against the direct contact with the electrolyte, protection layers often do not show sufficient catalytic activity regarding hydrogen or oxygen evolution. As the other key feature of a photoelectrode is certainly its performance, cocatalysts are often used to accelerate the kinetics of surface charge transfer reactions and therefore boost the efficiency of hydrogen or oxygen evolution. Measurement artifacts that can be easily misinterpreted are currents originating from the reduction of oxygen dissolved in the electrolyte. This can be excluded by using a special, closed cell that can be purged with an inert gas like nitrogen or argon to remove any oxygen. However, the oxygen reduction currents are usually in the range of around 10 – 100 $\mu\text{A cm}^{-2}$ and are therefore more likely relevant for low-performing photocathodes.

1.4 State-of-the-art semiconductors for PEC water splitting

1.4.1 Metal oxides

The discovery of photoelectrochemical water splitting started in the late 1970's with the description of oxygen evolution on TiO_2 by P. J. Boddy.²¹ His work was soon followed by A. Fujishima and K. Honda, who built a PEC cell by combining the TiO_2 photoelectrode with a Pt counter electrode that evolved hydrogen and oxygen under UV-light illumination.²² This cell design formed the basis for today's research on photoactive materials. Another prominent example for binary transition metal oxide semiconductors is WO_3 , which was first described in 1976 by Butler *et al.* to be applicable for the photoelectrolysis of water.²³ While both materials exhibit good stability under operating conditions, their large band gaps of 3.0 – 3.2 eV (TiO_2) and 2.7 eV (WO_3) only allow the absorption of UV light.²⁴⁻²⁵ In order to harvest a larger portion of the visible spectrum, lower band gap materials needed to be explored. While the investigation of SnO_2 and SrTiO_3 did not result in any significant improvement of those disadvantages,²⁶ the discovery of $\alpha\text{-Fe}_2\text{O}_3$ (hematite) by K. L. Hardee in 1976²⁷ opened a new

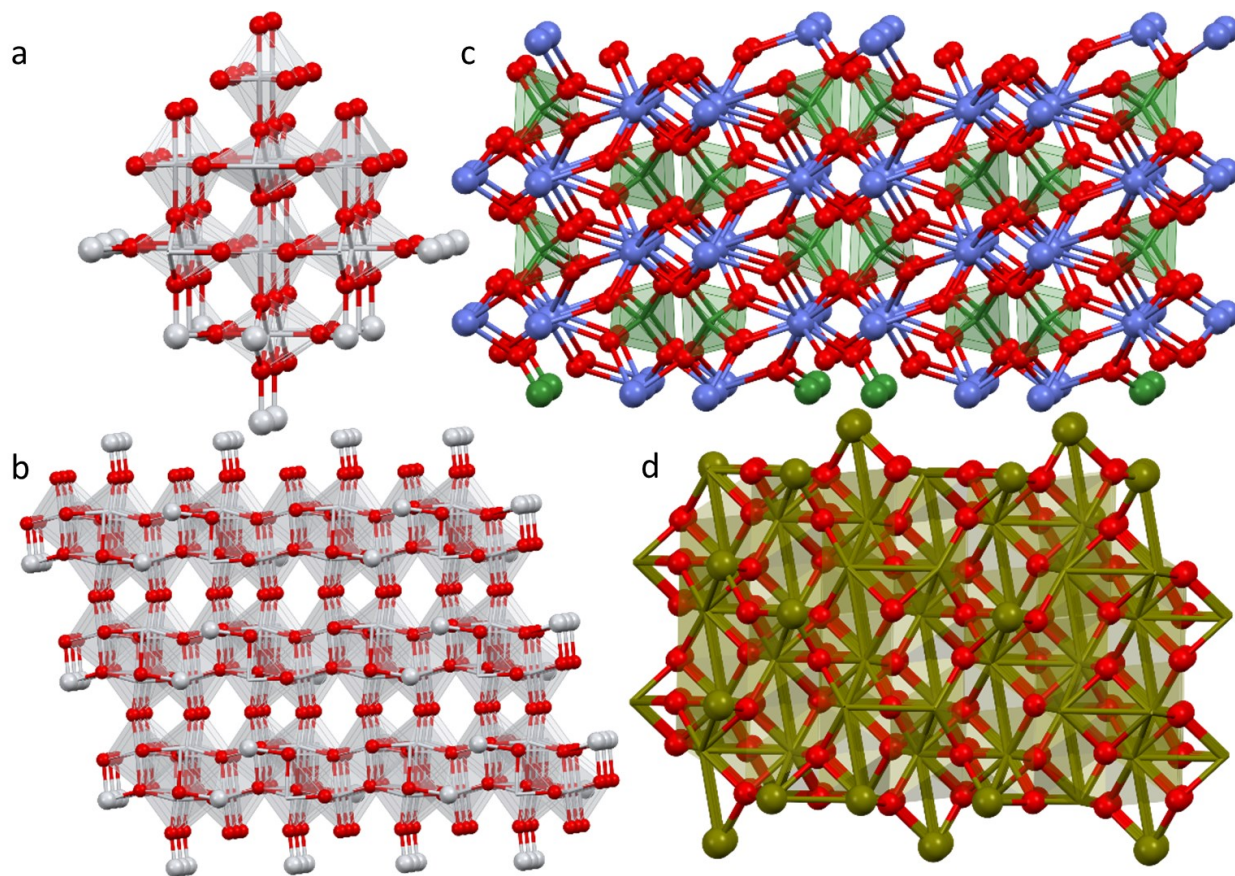


Figure 1.6: Crystal structures of rutile-TiO₂²⁸ (a), anatase-TiO₂²⁹ (b), BiVO₄³⁰ (c) and α-Fe₂O₃³¹ (d). Color code: oxygen (red), titanium (light grey), bismuth (blue), vanadium (dark green) and iron (khaki-green).

chapter in the field of artificial photosynthesis. With its comparably low band of 2.0 - 2.2 eV, hematite films can absorb a significant fraction of the incident sunlight.³² It can be synthesized from abundant, cheap and non-toxic elements and it additionally proved to be extremely stable under operating conditions.³³ For those reasons, hematite was intensively studied, also within our group. L. Peter explored α-Fe₂O₃ as a model system to study fundamental processes occurring during light-driven water splitting, like describing energetics and kinetics under chopped or modulated light intensity. The subsequent application of photoelectrochemical impedance spectroscopy, photocurrent transient analysis and intensity-modulated photocurrent spectroscopy allowed researchers to study the influence of dopants like Sn⁴⁺ ^{18, 34-35}, Tl⁴⁺ ³⁶⁻³⁷ or Si⁴⁺ ^{32, 38} on the electrochemical performance. Furthermore, I. Kondofersky et al. combined hematite with macroporous host systems made of

State-of-the-art semiconductors for PEC water splitting

$\text{SnO}_2\text{:Sb}^{39}$ or WO_3^{39} to increase the light absorption. But even though disadvantages of hematite like its short minority carrier diffusion length can be overcome by nanostructuring the material³², its surface still exhibits insufficient OER kinetics. Therefore, various cocatalysts based on $\text{Co}_3\text{O}_4^{40-41}$, the cobalt phosphate “Co-Pi”⁴², $\text{Ni}(\text{OH})_2^{43}$ or MnO_x^{44} were successfully applied to increase the PEC performance of hematite-based photoanodes up to 4.32 mA cm^{-2} at $1.23 \text{ V vs. RHE}^{45}$. Although this value is impressive and based on years of intensive research, it is still far away from the theoretical maximum of 12 mA cm^{-2} . Therefore, the search for new suitable semiconductors was extended to ternary oxides, as it was expected that the positions of valence and conduction bands could be tuned by increased hybridization of different s and p orbitals. This led to the development of new materials candidates like CuWO_4^{46} , $\text{ZnFe}_2\text{O}_4^{47}$ and BiVO_4^{48} . Especially BiVO_4 , with a suitable, indirect bandgap of $2.4 - 2.5 \text{ eV}$ originating from its high valence band energy maximum composed from O $2p$ and Bi $6s$ states⁴⁹, received a lot of interest in the past years. Substituting small amounts of V^{5+} with Mo^{6+} or W^{6+} resulted in a significantly increased electrical conductivity⁵⁰⁻⁵¹ and interfacial SnO_2 layers acted as ‘hole mirrors’, therefore reduced recombination and improved the charge carrier collection efficiency⁵¹. Also in the case of BiVO_4 , the combination of the photoabsorber with a suitable cocatalyst like Co-Pi⁵⁰, FeOOH or NiOOH⁵² resulted in very efficient photoanode systems with low photocurrent onset potentials and current densities of up to 6.72 mA cm^{-2} in a core-shell nanorod structure with WO_3 .⁵³ While this comes close to the maximal theoretical photocurrent of BiVO_4 of 7.5 mA cm^{-2} , new n-type semiconductors need to be explored to reach the targeted solar-to-hydrogen efficiency of 10% needed for the construction of a bigger test device.¹⁹ Unfortunately, BiVO_4 shows signs of instability under PEC conditions, suffering from corrosion and vanadium leaching in aqueous electrolytes, which is accelerated under illumination.⁵⁴⁻⁵⁶

Another possibility to increase the hydrogen production of photoelectrochemical devices is the focus on suitable photocathodes with a lower bandgap to combine them to a tandem cell together with a photoanode (see chapter 1.3.2). Besides $\text{CaFe}_2\text{O}_4^{57}$, which is basically the p-type analogue of ZnFe_2O_4 , the majority of known photocathode materials include copper. This originates from a strong contribution of Cu-3d states to the bandgap structure (Figure 1.7), which keeps the resulting bandgap comparably low. The most intensively studied semiconductors of this class are CuO and Cu_2O . They exhibit bandgaps of $1.35 \text{ eV} - 1.7 \text{ eV}$ and $2.0 - 2.2 \text{ eV}$ for CuO and Cu_2O respectively, are non-toxic and can be synthesized from widely available copper precursors⁵⁸⁻⁶² The conduction band edges of both

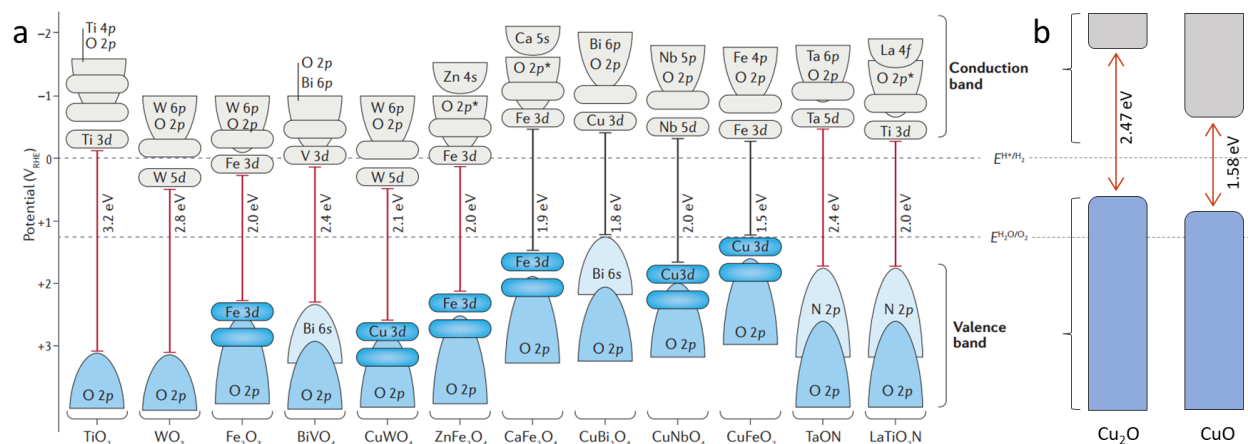


Figure 1.7: a) Bandgap structures of various n-type (black) and p-type (red) metal oxide and oxynitride semiconductors used for PEC water splitting. Their valence and conduction band energy levels are given with respect to the reverse hydrogen electrode (RHE) potential (left) and the redox potentials of water (right).¹⁹ b) Additional band gap positions for Cu₂O and CuO adapted from Yang et al.⁶³

intrinsic p-type semiconductors⁵⁹⁻⁶⁰ fit both the reduction potentials of water^{61, 64} and CO₂⁶⁵, which qualifies them for photoelectrochemical applications. On the other hand, especially Cu₂O is known for its instability under operating conditions.⁶⁶ Protection layers of various metal oxides and the combination with suitable cocatalysts allowed for the fabrication of very active devices based on Cu₂O, with current densities of up to 8 mA cm⁻² at 0 V vs. RHE.^{64, 67-70} Whereas CuO is very interesting as tandem cell bottom electrode due to its comparably low bandgap, its intrinsic instability has not been viewed as detrimental as in the case of Cu₂O. It exhibits p-type conductivity caused by copper vacancies⁷¹, but the charge carriers are strongly localized. Fortunately, the tenorite crystal structure⁷² allows the incorporation of various dopants like Li, Ni, Zn, Co, Mg, Ag, Cr, Fe and Mg, which can strongly influence the electrical conductivity.^{58, 73-77} The properties of Li-doped CuO, its photocorrosion and a suitable protection approach are an essential part of this thesis and discussed later on. To overcome these stability issues and optimize the bandgap position, copper-based p-type semiconductors were also extended to ternary oxides. The most typical elements mixed with copper oxide are bismuth, iron and niobium. For instance, CuBi₂O₄ was discovered in a combinatorial screening⁷⁸ and aroused interest due to its suitable bandgap of 1.6 – 1.8 eV and a high photocurrent onset potential of over 1 V vs. RHE.

State-of-the-art semiconductors for PEC water splitting

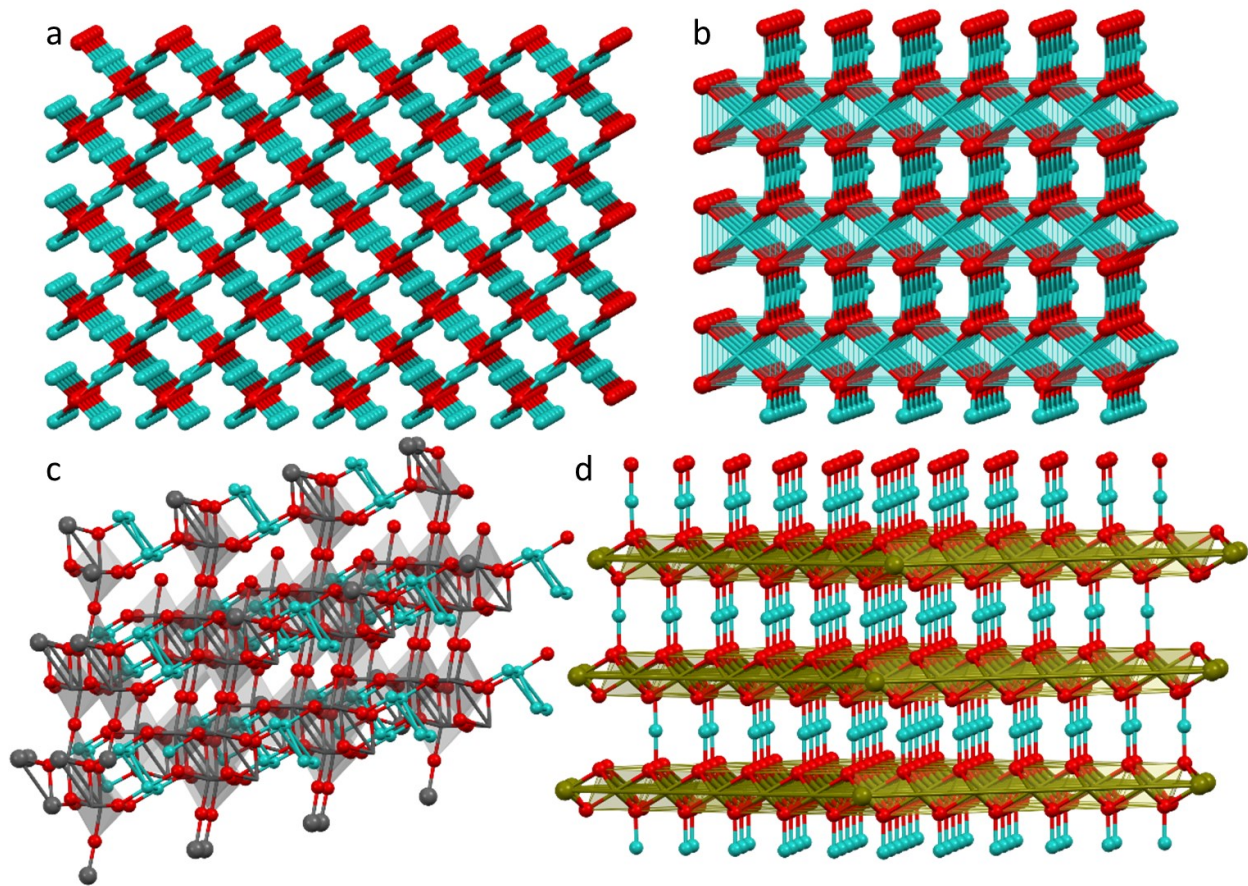


Figure 1.8: Crystal structures of cuprite/ Cu_2O ⁷⁹ (a), tenorite/ CuO ⁸⁰ (b), CuNbO_3 ⁸¹ (c) and CuFeO_2 ⁸² (d). Color code: oxygen (red), copper (blue), niobium (dark grey) and iron (khaki-green).

Unfortunately, it shows low conversion efficiencies which results in photocurrents of only 25-35 $\mu\text{A cm}^{-2}$, and even the combination with a Pt cocatalyst resulted in rather small photocurrents of less than 100 $\mu\text{A cm}^{-2}$.⁸³⁻⁸⁴ Furthermore, it proved to be relatively stable in basic electrolytes but also suffers from photocorrosion in neutral pH^{83, 85}, just like CuO and Cu_2O . Besides this, the copper niobium oxides CuNbO_3 and CuNb_3O_8 were applied as photocathode materials. CuNbO_3 was shown to be an interesting candidate, with a slightly wider bandgap of 2.0 eV resulting from a $\text{Cu } 3d^{10} - \text{Nb } 5d^2$ transition,⁸⁶ and good stability against photocorrosion. Photocurrent densities of 0.4 mA cm^{-2} and IPCE values of 5% at 350 nm are a good starting point for further optimization⁸⁷, but even the variation of the copper – niobium ratio to CuNb_3O_8 brought no significant improvement of PEC performance⁸⁸. Another well-studied ternary metal oxide is CuFeO_2 , which exhibits *p*-type conductivity like most compounds forming the delafossite crystal structure.⁸⁹ With an indirect

bandgap of 1.5 eV, CuFeO_2 would be highly qualified as tandem cell bottom electrode. Unfortunately, its surface is rather inactive for the evolution of hydrogen, which leads to charge accumulation at the semiconductor – liquid junction. This, and the instability at lower potentials at neutral pH, requires the use of protection layers and cocatalysts to reach hydrogen evolution photocurrent densities of 0.4 mA cm^{-2} .⁹⁰ On the other hand, CuFeO_2 is remarkably stable in basic pH⁹¹ and catalytically active for CO_2 reduction⁹²⁻⁹³, which makes the material very interesting for further research if the charge separation at its surface can be improved.

1.4.2 Solid-state photovoltaic cells

In principle, an attractive approach towards assembling a photoelectrochemical cell is the use of a well-studied photovoltaic cell as light absorber. Nevertheless, all the relevant materials require additional protection layers and cocatalysts to achieve the required efficiency and stability. At an early stage, PEC cells based on materials like *p*-type silicon, functionalized with a platinum cocatalyst and embedded in a polymeric protection layer, were reported.⁹⁴ The effort was soon extended to multijunction electrodes of amorphous silicon to provide sufficient photovoltage to drive the water splitting reaction while harvesting a larger fraction of the solar spectrum. In combination with NiFe_yO_x or $\text{Co}_x\text{Mo}^{\text{VI}}_{(1-x)}\text{Mo}^{\text{V}}_x\text{O}_3$ (“CoMo”) as cocatalysts, those devices reached solar-to-hydrogen (STH) efficiencies of 7.8% in outdoor tests for 300 days.⁹⁵⁻⁹⁶ In the meanwhile, other photovoltaic cells were also applied to produce hydrogen from water. For example, a tandem n/pn/p GaInP/GaAs junction used as photoabsorber, protected by a thin steel layer from the electrolyte and combined with two Pt electrodes, reached solar-to-hydrogen efficiencies of over 16%.⁹⁷ However, the used compounds are mostly rare, expensive, toxic and/or intrinsically unstable in water, which hinders their device application. This impediment led the focus back to silicon based photoelectrodes, while shifting the research towards low-cost, earth abundant catalysts like molybdenum sulfide clusters.⁹⁸⁻⁹⁹ Current densities of 12 mA cm^{-2} at 0.0 V vs. RHE were achieved with a Ti/TiO_x protected n+p-Si solar cell in combination with a molybdenum sulfide catalyst¹⁰⁰, which can compete with Pt-containing devices. However, all the above approaches are basically similar to a conventional photovoltaic cell connected to an electrolyzer, with the added challenge of long-term stability upon immersing the photoelectrode into an aqueous electrolyte. Therefore, researchers focused more and more on metal oxides and organic materials.

1.4.3 Crystalline organic frameworks

Stability under operating conditions has emerged as an intrinsic problem of most metal oxides and photovoltaic cells. To overcome this drawback, crystalline organic frameworks may be considered to be an attractive alternative. In the past few years, they have emerged as a completely new class of photocatalytically active materials. They form micro- and/or mesoporous structures, originally inspired by intensive research on zeolites, and often offer high surface areas. Therefore, these substances can potentially evince rapid charge or mass transport and a high density of active sites within the material, making this structural motif highly interesting for catalytic applications.¹⁰¹ In terms of hydrogen evolution applications, they have been applied as sensitizers for photocatalytic water splitting devices¹⁰², while even purely carbon-based materials were already shown to exhibit catalytically active surfaces for hydrogen evolution.¹⁰³ Crystalline organic frameworks can be divided in two classes: metal organic frameworks (MOFs) and covalent organic frameworks (COFs), which both are discussed in this chapter.

MOFs are a class of materials made up of coordinating organic ligands that assemble around a metal ion or a metal cluster, forming highly crystalline and porous network structures.¹⁰¹ The functionality of these coordination polymers originates from the interaction of organic chelate linkers and inorganic metal ion or cluster sites. While the metal ion or metal cluster often works as the active center, employing tailored organic ligand molecules introduces new functionalities that can enable novel catalytic processes like photocatalytic hydrogen evolution.^{101, 104-105} The organic linker can be seen as a functional building block that allows for modification of the structural and chemical properties of the network. However, the stability of MOFs strongly depends on the strength of the coordination bonds, which in some cases might hinder the application of an interesting system due to a lack of thermal and chemical stability.¹⁰¹

Another emerging class of crystalline organic polymers are covalent organic frameworks (COFs). Organic linker molecules form covalent bonds via condensation reactions to give crystalline, porous networks.¹⁰⁶ Several possible applications in catalysis, gas storage, chemical sensing, optoelectronics and drug delivery have been discovered for this new material class.¹⁰⁷⁻¹⁰⁹ The chemical linkage bonds of COFs are variable and can be adapted according to the properties of the type of covalent bond needed for the respective application.

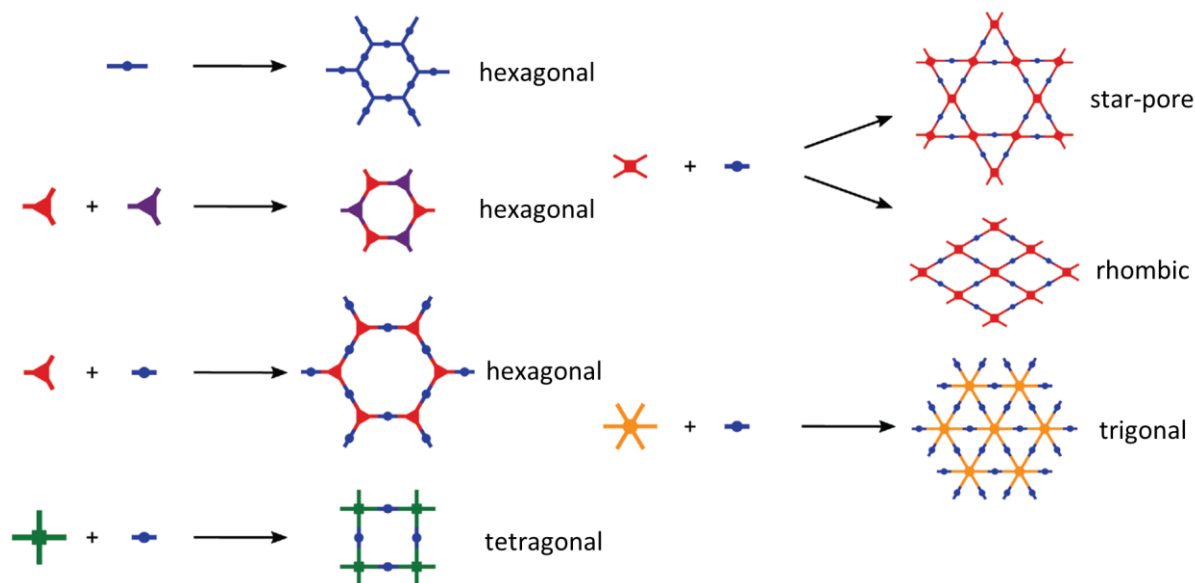


Figure 1.9: Illustration of structural diversity for two-dimensional COFs dependent on the choice of linker and its inherent symmetry.¹⁰⁷

The most common linkage bonds are boronate esters, imines, hydrazones, azines, β -ketoenamines, boroxines and imides, which were recently complemented by sp^2 – carbon/carbon bridged COFs¹¹⁰⁻¹¹¹ (Figure 1.10). It is crucial that all these bond formation mechanisms are (slightly) reversible, allowing the network structure to anneal and error-correct during the synthesis. The formation of a crystalline structure only occurs if the linkers are paired in the correct ratios with respect to each other. The pore shapes and sizes of the network can be directly controlled by the choice of the linkers (Figure 1.9).¹⁰⁷ Most linker condensations so far result in conjugated two dimensional sheets with defined lattice symmetry. Stacking of these sheets in the third dimension, most commonly in an AA stacking mode, creates the 3D morphology of the network.¹¹² An emerging alternative structure motive are 3D-COFs, with covalent bonds directed into all three dimensions directly originating from the linker condensation.¹¹³ The choice of linkers gives direct control over the symmetry of the network, influencing properties like pore shape and size, and allowing for an even more rational design of COFs.

State-of-the-art semiconductors for PEC water splitting

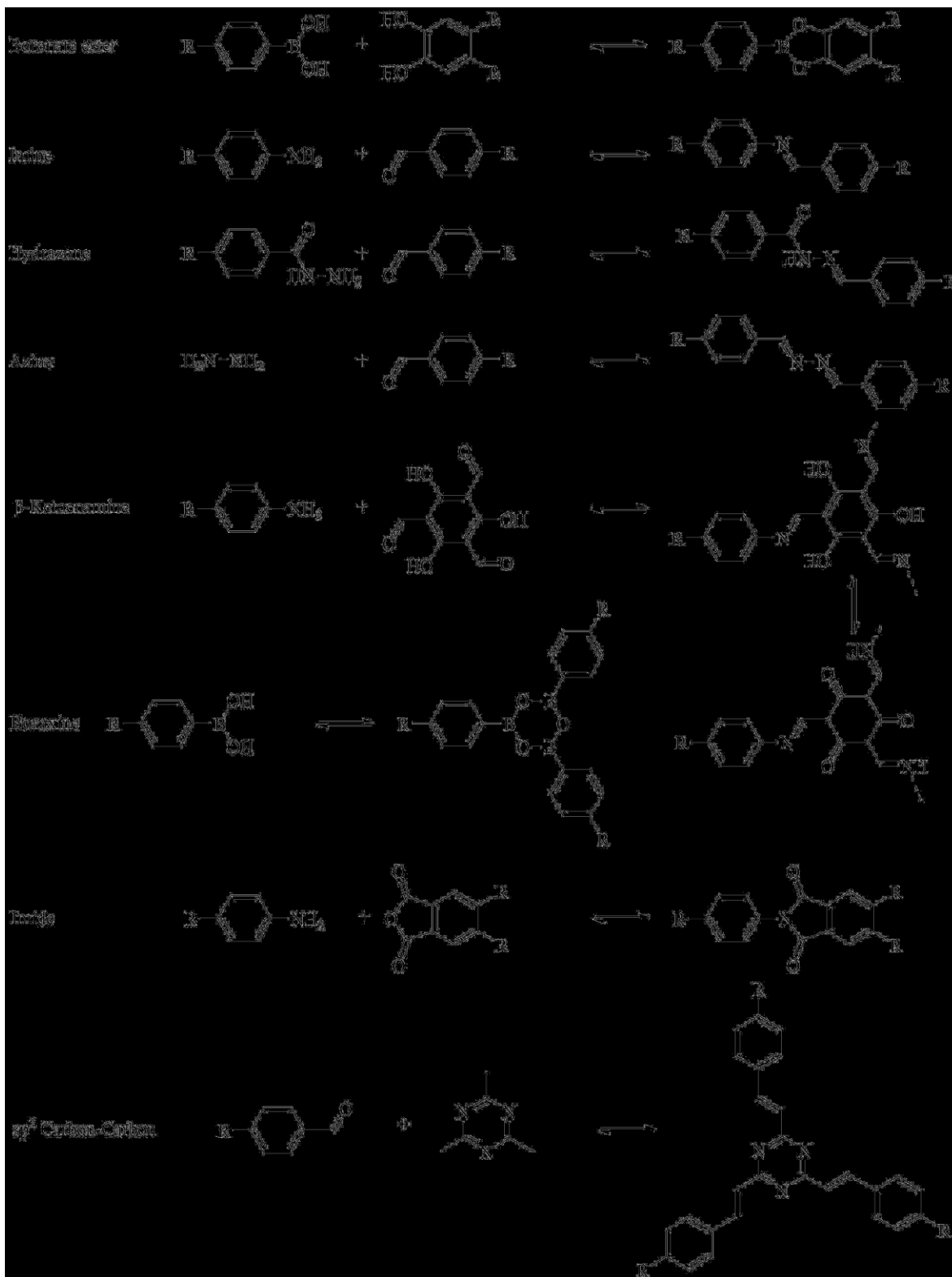


Figure 1.10: Different linkage motifs of covalent organic frameworks.^{107, 110-111}

Besides the ability to control the structure of COFs by the selection of linkers, it is also possible to functionalize them. Extended conjugated π -systems form as 2D COF sheets by co-condensation of the linker pairs. These large delocalized electronic systems have a significantly different energetic structure compared to the individual linker components. This often results in a change of the physiochemical properties; the COF becomes catalytically active, possesses novel chemical reactivity and is able to absorb more light. Depending on the intended catalytic mechanism, functional groups can be pre-synthetically and post-synthetically introduced into the COF if the linker contains eligible anchoring groups.¹¹⁴ Choosing linker materials inherently expressing properties that may be interesting for a catalytic process, COFs can be designed that combine these functionalities and promote their catalytic behavior by implementing them in a crystalline porous network.¹¹⁵

Using their good (and tunable) absorption of visible light, COFs were investigated as photosensitizers for photocatalytic hydrogen evolution. The first studies in this field were based on triazine COFs.¹¹⁶ Their performance was strongly depending on the nitrogen content, which seemed to be an important factor for the hydrogen evolution rate.¹¹⁷ While COFs without nitrogen in the central aryl ring were basically inactive, an increase in nitrogen atoms substituting C-H groups resulted in an increased average hydrogen production rate of up to $1703 \mu\text{mol h}^{-1} \text{g}^{-1}$, which is competitive with most carbon nitride photocatalysts.¹¹⁸⁻¹¹⁹ In addition, the sulfur content of COFs was also reported to have a strong impact on the photocatalytic activity.¹²⁰ Still, all of those systems require cocatalysts like platinum or cobaloxim complexes for the hydrogen evolution reaction, as well as special sacrificial electron donors like triethanolamine or ascorbic acid to match the semiconductor's valence band energy level.¹²¹⁻¹²²

As part of this thesis project, COFs were firstly applied as cathodes for photoelectrochemical water splitting (see chapter 5). A BDT-ETTA COF was synthesized that was shown to be able to use photogenerated electrons driving the hydrogen evolution reaction of the water splitting process without the use of additional cocatalysts.¹²³ The high level of possible control over the molecular structure allows for a rational design of catalytic sites, which was shown very recently with the example of conjugated acetylenic polymers (CAPs) on copper support. A 400 nm thick film of poly(2,5-diethynylthieno[3,2-b]thiophene) (p-DET) showed a remarkably higher HER activity compared to similar structures with lower sulfur content, namely three other CAPs (poly(1,4-diethynylbenzene) (pDEB), poly(2,6-diethynyl-naphthalene) (pDEN) and poly(2,5-diethynylthiophene) (pDTT)).¹²⁴ Another important example for tunable catalytic properties of

Synthesis methods

organic materials was presented on three-dimensional carbon fiber cloths (CFCs). While they are commonly used as catalyst support, an amide group functionalized CFC (A-CFC) was described to be a highly active HER catalyst in both alkaline and acidic media with an extremely small overpotential of 71 mV at $j_{10 \text{ mA/cm}^2}$, which is smaller than that of 20 wt% Pt/C (79 mV), combined with long-term stability of up to 18000 cycles. This finding was based on extensive density functional theory (DFT) calculations, modelling the active sites for hydrogen evolution and transferring this knowledge to the actual synthesis of the A-CFC.¹¹⁵ Transferring these concepts to covalent organic frameworks, they will most likely represent a new class of photoactive materials, able to directly catalyze the conversion from solar energy to chemical energy. With the prospect of obtaining porous, thermally and chemically stable, catalytically active photoelectrodes for electrochemical water splitting, COFs seem to present a highly interesting class of materials.

1.5 Synthesis methods

1.5.1 Sol-gel reactions

Sol-gel reactions are widely applied for the preparation of metal oxide nanoparticles and thin films. The development of this technique dates back to 1846 when SiO_2 was synthesized for the first time by hydrolysis of tetraethylorthosilicate under acidic conditions.¹²⁵ In the late 1980s, this procedure was developed further to allow its application for the preparation of a wide variety of metal oxides such as TiO_2 , MgO , Al_2O_3 , ZrO_2 , $\alpha\text{-Fe}_2\text{O}_3$, Fe_3O_4 , SrTiO_3 , BaTiO_3 or CeO_2 .¹²⁶ Additionally, successful doping of SiO_2 , TiO_2 and ZrO_2 was shown to be possible by sol-gel processing.¹²⁶⁻¹²⁷ The sol-gel reaction can be divided into several distinct steps and used to create several different morphologies (Figure 1.11). Suitable metal oxide precursors are dissolved in water or organic solvents. Subsequently, hydrolysis and condensation reactions form a stable solution, the sol. This liquid can be further processed in different ways: It can be deposited on a solid substrate by methods including spin coating, dip coating or drop casting. Removal of the solvent leads to a xerogel film that can be subsequently transformed into a dense thin film by calcination at increased temperatures. Aging of the sol leads to an increased viscosity due to ongoing polycondensation reactions until the solvent has completely vanished. The resulting xerogel can also be transformed into a dense ceramic or glass by heating. Supercritical drying of the wet gel maintains the porosity by forming an aerogel. In addition, powders of uniformly sized and shaped particles can be prepared by precipitation from the sol. The sol-gel process offers a few advantages compared to conventional solid-state reactions.

Besides powders, it offers an efficient technique for the preparation of more complex structures and morphologies. Many parameters such as pH value, metal salt concentration, aging time and temperature have an influence on the reaction. If so desired, the formation of micelles during the preparation of the sol results in particles with a diameter in the nanometer range and allows for a homogenous distribution of introduced dopants.¹⁸ Furthermore, the calcination temperature needed for the formation of highly crystalline metal oxide nanoparticles can be much lower than in solid-state reactions.¹²⁶

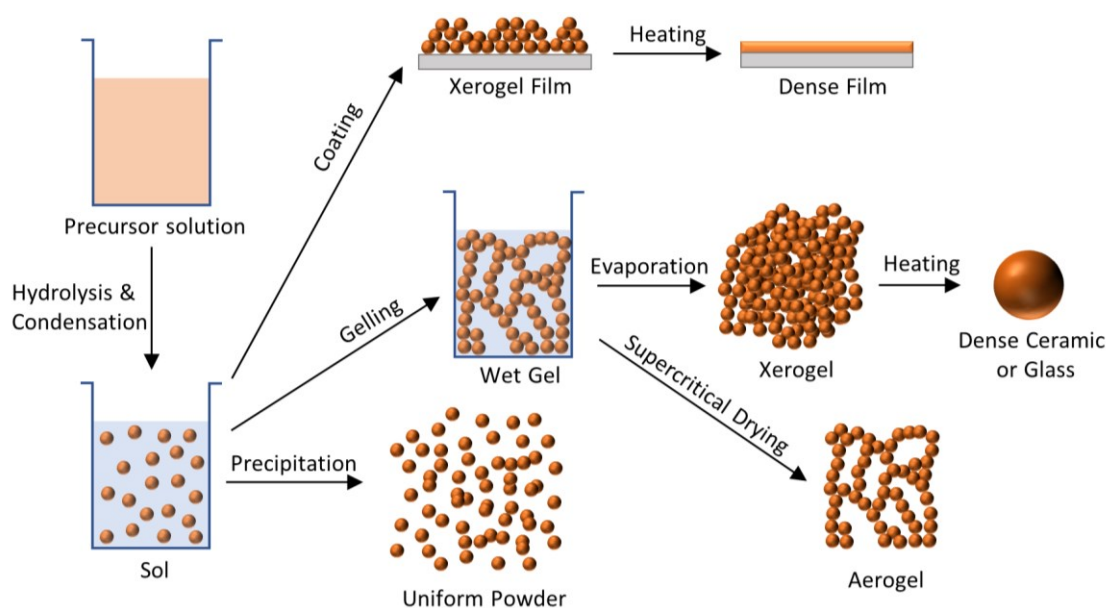


Figure 1.11: The sol-gel synthesis approach for various morphologies of metal oxides. Graphic reproduced from Niederberger and Pinna.¹²⁸

1.5.2 Synthesis of covalent organic frameworks

The successful synthesis of covalent organic frameworks is a challenging task. Generally, the achieved degree of crystallinity is a key aspect, which can be influenced by the applied synthetic conditions. Highly crystalline samples indicate the formation of a porous network and exhibit the correct functionality of a COF. In 2D COFs, it is crucial that linker molecules connect as "pairs", so that symmetric two-dimensional polymer sheets can form, which then are able to stack in an orderly fashion. To achieve correct linkage between the organic building blocks, reversible bond formation is

Synthesis methods

a key requirement; crystalline samples can only form if the reaction mechanism allows for annealing of incorrectly connected linkers. Once a crystalline sample is obtained, it usually exhibits good stability upon air exposure and over time. However, postsynthetic modifications or purification can compromise crystallinity if the covalent bonds react with the solvent, or the solvent molecules deposit between the stacked sheets, destroying the porous structure of the COF. While there is an ever-increasing amount of possible synthetic approaches for obtaining a COF, each system has its individual reaction conditions under which it reaches the best stability and crystallinity. Therefore, obtaining crystalline samples represents one of the biggest challenges when it comes to the synthesis of covalent organic frameworks.¹⁰⁷

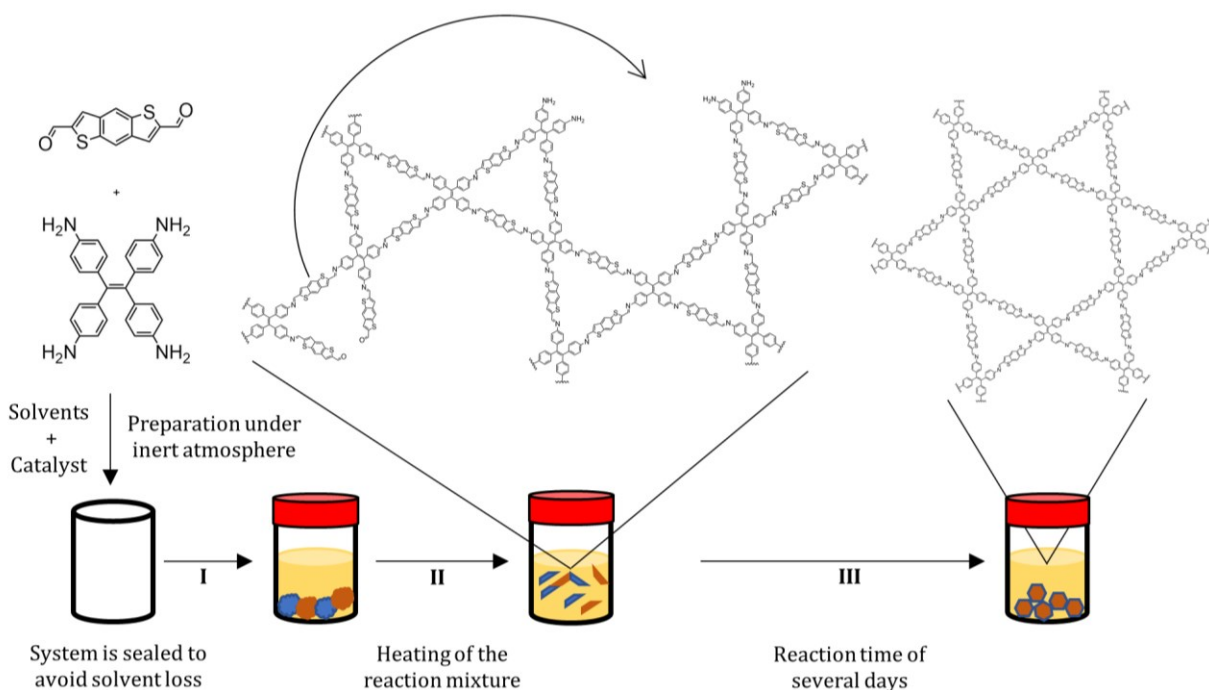


Figure 1.12: Illustration of the formation of a BDT-ETTA COF during the solvothermal synthesis. Step I: Linkers have been deposited into the reaction vial and are not significantly soluble in the solvent mixture. No reaction takes place. Step II: Heating of the reaction mixture causes solvation of the linkers and their co-condensation reaction. Reversible bond formation allows for annealing. Step III (may occur in parallel to step II): 2D COF sheets are formed and stack onto each other to give a 3D COF network. Those COF particles cannot be held in solution and precipitate as bulk powders, which can subsequently be removed from the solution.

The easiest and most common approach for synthesizing COFs is the solvothermal synthesis. Linkers, solvents and, if needed, a catalyst for bond formation are mixed and sealed in a closed system, e.g. a PTFE screw cap-sealed autoclave, under inert atmosphere conditions. The reaction mixture is heated up to temperatures above the solvents' boiling points for several days. After sufficient time to complete the COF formation has elapsed, the precipitate can be removed from the reaction solution. In some cases, washing the COF with anhydrous solvents improves crystallinity by removing solvent residues and oligomers from the network's pores. The solvent mixtures and reaction conditions, such as temperature and time of the heating process, need to be optimized for every COF system individually. Ideally, the linkers are partially soluble in the used solvent mixture already at room temperature. Once the reaction mixture is heated, their solubility increases and the linkers can react in co-condensation reactions, causing the formation of the supramolecular COF structure which then precipitates (Figure 1.12).

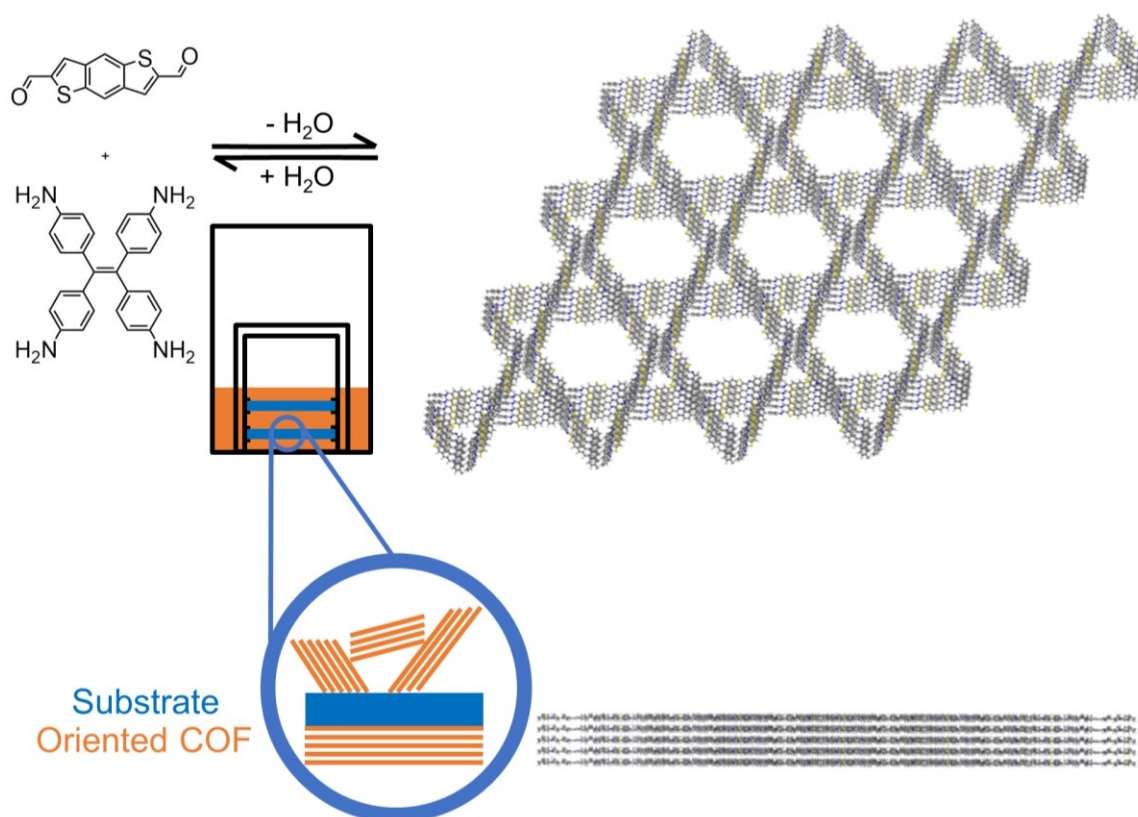


Figure 1.13: Scheme of a solvothermal thin film synthesis. The COF forms oriented crystalline films on the downward facing side of the substrate.

Scope of this thesis

While solvothermal reactions usually yield good results for various systems, inhomogeneous linker concentrations in the solution, the reaction time and the difficulty of potential industrial upscaling may pose disadvantages that need to be overcome for large scale application of COF systems in the future. A broad range of alternative and promising synthetic approaches keep emerging, like microwave reactors for shorter reaction times or continuous flow set ups allowing for more precise control of linker concentrations and reaction conditions.¹²⁹⁻¹³⁰ Oriented and crystalline COF thin films can be prepared analogously to the solvothermal synthesis of COF bulk samples. The reaction procedure takes place as depicted in Figure 1.13, with the difference that a film substrate is submerged within the reaction solution. During co-condensation of the linkers, the COF starts to grow directly on the substrate. The COF layers will gradually stack upon each other, creating an oriented crystalline film on the bottom side of the substrate while non-oriented COF precipitates on its top. For this purpose, reaction conditions like solvent volume, amount of catalyst and concentration of linkers need to be adapted compared to the corresponding bulk synthesis to result in homogenous, oriented COF films of the desired thickness.

1.6 Scope of this thesis

This thesis aims for the exploration of semiconducting materials and nanosized catalysts suitable for solar hydrogen production. Two examples of the well-established metal oxide materials classes are discussed, followed by fundamental work on covalent organic frameworks. The latter are introduced as a new class of semiconductors usable for applications in photoelectrochemical cells.

The activity of metal oxide photoelectrode materials like α -Fe₂O₃ or CuO can be greatly improved by the incorporation of suitable dopants, which improves charge carrier transport, increases the optical absorption and changes catalytic properties. Additionally, their limitations in photoelectrochemical performance and stability are examined. While the ideal tin doping concentration profile of hematite photoanodes is discussed, the phenomenon of light triggered corrosion is studied in depth on Li doped CuO photocathodes.

To potentially overcome the intrinsic limitations of metal oxide photoelectrodes, covalent organic frameworks are presented as a previously unknown class of materials suitable for photoelectrochemical water splitting. While the discussed example BDT-ETTA shows good light absorption and suitable bandgap positions, it lacks the sufficient catalytic activity for hydrogen evolution. The latter however can be improved by application of a platinum nanoparticle cocatalyst.

Furthermore, electrophoretic deposition is shown to result in active electrodes exhibiting high structural and textural surface areas and the possibility of a co-deposition with platinum nanoparticles. These results serve as basis for the development of new covalent organic frameworks specifically designed for their application in photoelectrochemical water splitting devices.

1.7 References

- (1) Sinn, H.-W., Buffering Volatility: A Study on the Limits of Germany's Energy Revolution. *CESifo Working Paper Series No. 5950* **2016**.
- (2) Apodaca, L. E., Mineral Commodity Summaries. Survey, U. S. G., Ed. 2019; pp 116-117.
- (3) Verfahren zur synthetischen Darstellung von Ammoniak aus den Elementen. Patent DE235421, 13.10.1908.
- (4) Georg Schiller, G. W. Production of hydrogen. Patent US2083795, 15.6.1937.
- (5) Turner, J. A., A Realizable Renewable Energy Future. *Science* **1999**, *285* (5428), 687-689.
- (6) Walter, M. G.; Warren, E. L.; McKone, J. R.; Boettcher, S. W.; Mi, Q.; Santori, E. A.; Lewis, N. S., Solar water splitting cells. *Chem Rev* **2010**, *110* (11), 6446-73.
- (7) Hisatomi, T.; Kubota, J.; Domen, K., Recent advances in semiconductors for photocatalytic and photoelectrochemical water splitting. *Chemical Society Reviews* **2014**, *43* (22), 7520-7535.
- (8) Walter, M. G.; Warren, E. L.; McKone, J. R.; Boettcher, S. W.; Mi, Q.; Santori, E. A.; Lewis, N. S., Solar Water Splitting Cells. *Chemical Reviews* **2010**, *110* (11), 6446-6473.
- (9) Peter, L., *Photoelectrochemical Water Splitting*. The Royal Society of Chemistry: Cambridge, 2013; Vol. 9.
- (10) Lubitz, W.; Reijerse, E. J.; Messinger, J., Solar water-splitting into H₂ and O₂: design principles of photosystem II and hydrogenases. *Energy & Environmental Science* **2008**, *1* (1), 15-31.
- (11) Prévot, M. S.; Sivula, K., Photoelectrochemical Tandem Cells for Solar Water Splitting. *The Journal of Physical Chemistry C* **2013**, *117* (35), 17879-17893.
- (12) Hu, S.; Xiang, C.; Haussener, S.; Berger, A. D.; Lewis, N. S., An analysis of the optimal band gaps of light absorbers in integrated tandem photoelectrochemical water-splitting systems. *Energy & Environmental Science* **2013**, *6* (10), 2984-2993.

References

- (13) Tachibana, Y.; Vayssieres, L.; Durrant, J. R., Artificial photosynthesis for solar water-splitting. *Nat Photon* **2012**, *6* (8), 511-518.
- (14) van de Krol, R.; Liang, Y.; Schoonman, J., Solar hydrogen production with nanostructured metal oxides. *Journal of Materials Chemistry* **2008**, *18* (20), 2311.
- (15) Mavroides, J. G.; Kafalas, J. A.; Kolesar, D. F., Photoelectrolysis of water in cells with SrTiO₃ anodes. *Applied Physics Letters* **1976**, *28* (5), 241-243.
- (16) Fornarini, L.; Nozik, A. J.; Parkinson, B. A., The energetics of p/n photoelectrolysis cells. *The Journal of Physical Chemistry* **1984**, *88* (15), 3238-3243.
- (17) Lewerenz, H.-J.; Peter, L., *Photoelectrochemical Water Splitting: Materials, Processes and Architectures*. Royal Society of Chemistry: 2013.
- (18) Dunn, H. K.; Feckl, J. M.; Müller, A.; Fattakhova-Rohlfing, D.; Morehead, S. G.; Roos, J.; Peter, L. M.; Scheu, C.; Bein, T., Tin doping speeds up hole transfer during light-driven water oxidation at hematite photoanodes. *Phys Chem Chem Phys* **2014**, *16* (44), 24610-20.
- (19) Sivula, K.; van de Krol, R., Semiconducting materials for photoelectrochemical energy conversion. *Nature Reviews Materials* **2016**, *1*, 15010.
- (20) Beverskog, B.; Puigdomenech, I., Revised Pourbaix diagrams for copper at 25 to 300 C. *Journal of The Electrochemical Society* **1997**, *144* (10), 3476-3483.
- (21) Boddy, P. J., Oxygen Evolution on Semiconducting TiO₂. *Journal of The Electrochemical Society* **1968**, *115* (2).
- (22) Fujishima, A.; Honda, K., Electrochemical Photolysis of Water at a Semiconductor Electrode. *Nature* **1972**, *238* (5358), 37-38.
- (23) Butler, M. A.; Nasby, R. D.; Quinn, R. K., Tungsten trioxide as an electrode for photoelectrolysis of water. *Solid State Communications* **1976**, *19* (10), 1011-1014.
- (24) Janáky, C.; Rajeshwar, K.; de Tacconi, N. R.; Chanmanee, W.; Huda, M. N., Tungsten-based oxide semiconductors for solar hydrogen generation. *Catalysis Today* **2013**, *199*, 53-64.
- (25) Kapilashrami, M.; Zhang, Y.; Liu, Y.-S.; Hagfeldt, A.; Guo, J., Probing the Optical Property and Electronic Structure of TiO₂ Nanomaterials for Renewable Energy Applications. *Chemical Reviews* **2014**, *114* (19), 9662-9707.
- (26) Bolts, J. M.; Wrighton, M. S., Correlation of photocurrent-voltage curves with flat-band potential for stable photoelectrodes for the photoelectrolysis of water. *The Journal of Physical Chemistry* **1976**, *80* (24), 2641-2645.
- (27) Hardee, K. L., Semiconductor Electrodes. *Journal of The Electrochemical Society* **1976**, *123* (7).
- (28) Persson, K. Materials Data on TiO₂ (SG:136) by Materials Project. United States, **2014**.
- (29) Persson, K. Materials Data on TiO₂ (SG:12) by Materials Project. United States, **2014**.

- (30) Persson, K. Materials Data on VBiO_4 (SG:60) by Materials Project. United States, **2014**.
- (31) Persson, K. Materials Data on Fe_2O_3 (SG:167) by Materials Project. United States, **2014**.
- (32) Cesar, I.; Sivula, K.; Kay, A.; Zboril, R.; Grätzel, M., Influence of Feature Size, Film Thickness, and Silicon Doping on the Performance of Nanostructured Hematite Photoanodes for Solar Water Splitting. *The Journal of Physical Chemistry C* **2008**, *113* (2), 772-782.
- (33) Peter, L. M., Energetics and kinetics of light-driven oxygen evolution at semiconductor electrodes: the example of hematite. *J Solid State Electrochem* **2012**, *17* (2), 315-326.
- (34) Frydrych, J.; Machala, L.; Tucek, J.; Siskova, K.; Filip, J.; Pechousek, J.; Safarova, K.; Vondracek, M.; Seo, J. H.; Schneeweiss, O.; Grätzel, M.; Sivula, K.; Zboril, R., Facile fabrication of tin-doped hematite photoelectrodes – effect of doping on magnetic properties and performance for light-induced water splitting. *Journal of Materials Chemistry* **2012**, *22* (43).
- (35) Hufnagel, A. G.; Hajiyani, H.; Zhang, S.; Li, T.; Kasian, O.; Gault, B.; Breitbach, B.; Bein, T.; Fattakhova-Rohlfing, D.; Scheu, C.; Pentcheva, R., Why Tin-Doping Enhances the Efficiency of Hematite Photoanodes for Water Splitting-The Full Picture. *Advanced Functional Materials* **2018**, *28* (52).
- (36) Pu, A.; Deng, J.; Li, M.; Gao, J.; Zhang, H.; Hao, Y.; Zhong, J.; Sun, X., Coupling Ti-doping and oxygen vacancies in hematite nanostructures for solar water oxidation with high efficiency. *Journal of Materials Chemistry A* **2014**, *2* (8).
- (37) Rioult, M.; Magnan, H.; Stanescu, D.; Barbier, A., Single Crystalline Hematite Films for Solar Water Splitting: Ti-Doping and Thickness Effects. *The Journal of Physical Chemistry C* **2014**, *118* (6), 3007-3014.
- (38) Chemelewski, W. D.; Hahn, N. T.; Mullins, C. B., Effect of Si Doping and Porosity on Hematite's ($\alpha\text{-Fe}_2\text{O}_3$) Photoelectrochemical Water Oxidation Performance. *The Journal of Physical Chemistry C* **2012**, *116* (8), 5255-5261.
- (39) Kondofersky, I.; Dunn, H. K.; Müller, A.; Mandlmeier, B.; Feckl, J. M.; Fattakhova-Rohlfing, D.; Scheu, C.; Peter, L. M.; Bein, T., Electron Collection in Host-Guest Nanostructured Hematite Photoanodes for Water Splitting: The Influence of Scaffold Doping Density. *ACS Applied Materials & Interfaces* **2015**, *7* (8), 4623-4630.
- (40) Feckl, J. M.; Dunn, H. K.; Zehetmaier, P. M.; Müller, A.; Pendlebury, S. R.; Zeller, P.; Fominykh, K.; Kondofersky, I.; Döblinger, M.; Durrant, J. R.; Scheu, C.; Peter, L.; Fattakhova-Rohlfing, D.; Bein, T., Ultrasmall Co_3O_4 Nanocrystals Strongly Enhance Solar Water Splitting on Mesoporous Hematite. *Advanced Materials Interfaces* **2015**, *2* (18).
- (41) Riha, S. C.; Klahr, B. M.; Tyo, E. C.; Seifert, S.; Vajda, S.; Pellin, M. J.; Hamann, T. W.; Martinson, A. B., Atomic layer deposition of a submonolayer catalyst for the enhanced photoelectrochemical performance of water oxidation with hematite. *ACS Nano* **2013**, *7* (3), 2396-405.

References

- (42) Klahr, B.; Gimenez, S.; Fabregat-Santiago, F.; Bisquert, J.; Hamann, T. W., Photoelectrochemical and impedance spectroscopic investigation of water oxidation with "Co-Pi"-coated hematite electrodes. *J Am Chem Soc* **2012**, *134* (40), 16693-700.
- (43) Wang, G.; Ling, Y.; Lu, X.; Zhai, T.; Qian, F.; Tong, Y.; Li, Y., A mechanistic study into the catalytic effect of Ni(OH)₂ on hematite for photoelectrochemical water oxidation. *Nanoscale* **2013**, *5* (10), 4129-33.
- (44) Yang, X.; Du, C.; Liu, R.; Xie, J.; Wang, D., Balancing photovoltage generation and charge-transfer enhancement for catalyst-decorated photoelectrochemical water splitting: A case study of the hematite/MnO_x combination. *Journal of Catalysis* **2013**, *304*, 86-91.
- (45) Kim, J. Y.; Magesh, G.; Youn, D. H.; Jang, J.-W.; Kubota, J.; Domen, K.; Lee, J. S., Single-crystalline, wormlike hematite photoanodes for efficient solar water splitting. *Scientific Reports* **2013**, *3*, 2681.
- (46) Yourey, J. E.; Pyper, K. J.; Kurtz, J. B.; Bartlett, B. M., Chemical Stability of CuWO₄ for Photoelectrochemical Water Oxidation. *The Journal of Physical Chemistry C* **2013**, *117* (17), 8708-8718.
- (47) Yao, J.; Li, X.; Li, Y.; Le, S., Density Functional Theory Investigations on the Structure and Electronic Properties of Normal Spinel ZnFe₂O₄. *Integrated Ferroelectrics* **2013**, *145* (1), 17-23.
- (48) Walsh, A.; Yan, Y.; Huda, M. N.; Al-Jassim, M. M.; Wei, S.-H., Band Edge Electronic Structure of BiVO₄: Elucidating the Role of the Bi s and V d Orbitals. *Chemistry of Materials* **2009**, *21* (3), 547-551.
- (49) Cooper, J. K.; Gul, S.; Toma, F. M.; Chen, L.; Liu, Y.-S.; Guo, J.; Ager, J. W.; Yano, J.; Sharp, I. D., Indirect Bandgap and Optical Properties of Monoclinic Bismuth Vanadate. *The Journal of Physical Chemistry C* **2015**, *119* (6), 2969-2974.
- (50) Pilli, S. K.; Furtak, T. E.; Brown, L. D.; Deutsch, T. G.; Turner, J. A.; Herring, A. M., Cobalt-phosphate (Co-Pi) catalyst modified Mo-doped BiVO₄ photoelectrodes for solar water oxidation. *Energy & Environmental Science* **2011**, *4* (12), 5028-5034.
- (51) Liang, Y.; Tsubota, T.; Mooij, L. P. A.; van de Krol, R., Highly Improved Quantum Efficiencies for Thin Film BiVO₄ Photoanodes. *The Journal of Physical Chemistry C* **2011**, *115* (35), 17594-17598.
- (52) Kim, T. W.; Choi, K.-S., Nanoporous BiVO₄ Photoanodes with Dual-Layer Oxygen Evolution Catalysts for Solar Water Splitting. *Science* **2014**, *343* (6174), 990.
- (53) Pihosh, Y.; Turkevych, I.; Mawatari, K.; Uemura, J.; Kazoe, Y.; Kosar, S.; Makita, K.; Sugaya, T.; Matsui, T.; Fujita, D.; Tosa, M.; Kondo, M.; Kitamori, T., Photocatalytic generation of hydrogen by core-shell WO₃/BiVO₄ nanorods with ultimate water splitting efficiency. *Scientific Reports* **2015**, *5*, 11141.
- (54) Toma, F. M.; Cooper, J. K.; Kunzelmann, V.; McDowell, M. T.; Yu, J.; Larson, D. M.; Borys, N. J.; Abelyan, C.; Beeman, J. W.; Yu, K. M.; Yang, J.; Chen, L.; Shaner, M. R.; Spurgeon, J.; Houle, F. A.; Persson, K. A.; Sharp, I. D., Mechanistic insights into chemical and photochemical

transformations of bismuth vanadate photoanodes. *Nature Communications* **2016**, 7 (1), 12012.

(55) Lee, D. K.; Choi, K.-S., Enhancing long-term photostability of BiVO₄ photoanodes for solar water splitting by tuning electrolyte composition. *Nature Energy* **2018**, 3 (1), 53-60.

(56) Zhang, S.; Rohloff, M.; Kasian, O.; Mingers, A. M.; Mayrhofer, K. J. J.; Fischer, A.; Scheu, C.; Cherevko, S., Dissolution of BiVO₄ Photoanodes Revealed by Time-Resolved Measurements under Photoelectrochemical Conditions. *The Journal of Physical Chemistry C* **2019**, 123 (38), 23410-23418.

(57) Matsumoto, Y.; Omae, M.; Sugiyama, K.; Sato, E., New photocathode materials for hydrogen evolution: calcium iron oxide (CaFe₂O₄) and strontium iron oxide (Sr₇Fe₁₀O₂₂). *The Journal of Physical Chemistry* **1987**, 91 (3), 577-581.

(58) Koffyberg, F. P.; Benko, F. A., A photoelectrochemical determination of the position of the conduction and valence band edges of p-type CuO. *Journal of Applied Physics* **1982**, 53 (2), 1173-1177.

(59) Meyer, B. K.; Polity, A.; Reppin, D.; Becker, M.; Hering, P.; Klar, P. J.; Sander, T.; Reindl, C.; Benz, J.; Eickhoff, M.; Heiliger, C.; Heinemann, M.; Bläsing, J.; Krost, A.; Shokovets, S.; Müller, C.; Ronning, C., Binary copper oxide semiconductors: From materials towards devices. *physica status solidi (b)* **2012**, 249 (8), 1487-1509.

(60) Heinemann, M.; Eifert, B.; Heiliger, C., Band structure and phase stability of the copper oxides Cu₂O, CuO, and Cu₄O₃. *Physical Review B* **2013**, 87 (11), 115111.

(61) Chauhan, D.; Satsangi, V.; Dass, S.; Shrivastav, R., Preparation and characterization of nanostructured CuO thin films for photoelectrochemical splitting of water. *Bulletin of Materials Science* **2006**, 29, 709.

(62) Olsen, L. C.; Bohara, R. C.; Urie, M. W., Explanation for low-efficiency Cu₂O Schottky-barrier solar cells. *Applied Physics Letters* **1979**, 34 (1), 47-49.

(63) Yang, Y.; Xu, D.; Wu, Q.; Diao, P., Cu₂O/CuO Bilayered Composite as a High-Efficiency Photocathode for Photoelectrochemical Hydrogen Evolution Reaction. *Scientific Reports* **2016**, 6, 35158.

(64) Paracchino, A.; Laporte, V.; Sivula, K.; Grätzel, M.; Thimsen, E., Highly active oxide photocathode for photoelectrochemical water reduction. *Nat Mater* **2011**, 10 (6), 456-461.

(65) Ba, X.; Yan, L.-L.; Huang, S.; Yu, J.; Xia, X.-J.; Yu, Y., New Way for CO₂ Reduction under Visible Light by a Combination of a Cu Electrode and Semiconductor Thin Film: Cu₂O Conduction Type and Morphology Effect. *The Journal of Physical Chemistry C* **2014**, 118 (42), 24467-24478.

(66) Kakuta, S.; Abe, T., Structural characterization of Cu₂O after the evolution of H₂ under visible light irradiation. *Electrochemical and Solid-State Letters* **2009**, 12 (3), P1-P3.

References

- (67) Paracchino, A.; Mathews, N.; Hisatomi, T.; Stefik, M.; Tilley, S. D.; Gratzel, M., Ultrathin films on copper(i) oxide water splitting photocathodes: a study on performance and stability. *Energy & Environmental Science* **2012**, *5* (9), 8673-8681.
- (68) Zhang, Z.; Wang, P., Highly stable copper oxide composite as an effective photocathode for water splitting via a facile electrochemical synthesis strategy. *Journal of Materials Chemistry* **2012**, *22* (6), 2456-2464.
- (69) Azevedo, J.; Tilley, S. D.; Schreier, M.; Stefik, M.; Sousa, C.; Araújo, J. P.; Mendes, A.; Grätzel, M.; Mayer, M. T., Tin oxide as stable protective layer for composite cuprous oxide water-splitting photocathodes. *Nano Energy* **2016**, *24*, 10-16.
- (70) Luo, J.; Steier, L.; Son, M.-K.; Schreier, M.; Mayer, M. T.; Grätzel, M., Cu₂O Nanowire Photocathodes for Efficient and Durable Solar Water Splitting. *Nano Letters* **2016**, *16* (3), 1848-1857.
- (71) Jeong, Y. K.; Choi, G. M., Nonstoichiometry and electrical conduction of CuO. *Journal of Physics and Chemistry of Solids* **1996**, *57* (1), 81-84.
- (72) Tunell, G.; Posnjak, E.; Ksanda, C., Geometrical and optical properties, and crystal structure of tenorite. *Zeitschrift für Kristallographie-Crystalline Materials* **1935**, *90* (1), 120-142.
- (73) Iijima, T.; Toyoguchi, Y.; Nishimura, J.; Ogawa, H., Button-type lithium battery using copper oxide as a cathode. *Journal of Power Sources* **1980**, *5* (1), 99-109.
- (74) Kuksenko, S. P., On the Possibility of Using Lithium-doped Copper Oxide in Lithium Cells. *Russian Journal of Applied Chemistry* **2004**, *77* (6), 1019-1021.
- (75) Chiang, C.-Y.; Shin, Y.; Ehrman, S., Li Doped CuO Film Electrodes for Photoelectrochemical Cells. *Journal of The Electrochemical Society* **2011**, *159* (2), B227-B231.
- (76) Chand, P.; Gaur, A.; Kumar, A.; Kumar Gaur, U., Structural and optical study of Li doped CuO thin films on Si (1 0 0) substrate deposited by pulsed laser deposition. *Applied Surface Science* **2014**, *307*, 280-286.
- (77) Chiang, C.-Y.; Shin, Y.; Ehrman, S., Dopant Effects on Copper Oxide Photoelectrochemical Cell Water Splitting. *Energy Procedia* **2014**, *61*, 1799-1802.
- (78) Arai, T.; Konishi, Y.; Iwasaki, Y.; Sugihara, H.; Sayama, K., High-Throughput Screening Using Porous Photoelectrode for the Development of Visible-Light-Responsive Semiconductors. *Journal of Combinatorial Chemistry* **2007**, *9* (4), 574-581.
- (79) Persson, K. Materials Data on Cu₂O (SG:224) by Materials Project. United States, **2014**.
- (80) Persson, K. Materials Data on CuO (SG:131) by Materials Project. United States, **2014**.
- (81) Persson, K. Materials Data on NbCuO₃ (SG:12) by Materials Project. United States, **2016**.
- (82) Persson, K. Materials Data on FeCuO₂ (SG:166) by Materials Project. United States, **2014**.

- (83) Hahn, N. T.; Holmberg, V. C.; Korgel, B. A.; Mullins, C. B., Electrochemical Synthesis and Characterization of p-CuBi₂O₄ Thin Film Photocathodes. *The Journal of Physical Chemistry C* **2012**, *116* (10), 6459-6466.
- (84) Park, H. S.; Lee, C.-Y.; Reisner, E., Photoelectrochemical reduction of aqueous protons with a CuO|CuBi₂O₄ heterojunction under visible light irradiation. *Physical Chemistry Chemical Physics* **2014**, *16* (41), 22462-22465.
- (85) Berglund, S. P.; Abdi, F. F.; Bogdanoff, P.; Chemseddine, A.; Friedrich, D.; van de Krol, R., Comprehensive Evaluation of CuBi₂O₄ as a Photocathode Material for Photoelectrochemical Water Splitting. *Chemistry of Materials* **2016**, *28* (12), 4231-4242.
- (86) Harb, M.; Masih, D.; Takanabe, K., Screened coulomb hybrid DFT investigation of band gap and optical absorption predictions of CuVO₃, CuNbO₃ and Cu₅Ta₁₁O₃₀ materials. *Physical Chemistry Chemical Physics* **2014**, *16* (34), 18198-18204.
- (87) Joshi, U. A.; Palasyuk, A. M.; Maggard, P. A., Photoelectrochemical Investigation and Electronic Structure of a p-type CuNbO₃ Photocathode. *The Journal of Physical Chemistry C* **2011**, *115* (27), 13534-13539.
- (88) Joshi, U. A.; Maggard, P. A., CuNb₃O₈: A p-Type Semiconducting Metal Oxide Photoelectrode. *The Journal of Physical Chemistry Letters* **2012**, *3* (11), 1577-1581.
- (89) Nagarajan, R.; Duan, N.; Jayaraj, M. K.; Li, J.; Vanaja, K. A.; Yokochi, A.; Draeseke, A.; Tate, J.; Sleight, A. W., p-Type conductivity in the delafossite structure. *International Journal of Inorganic Materials* **2001**, *3* (3), 265-270.
- (90) Prévot, M. S.; Guijarro, N.; Sivula, K., Enhancing the Performance of a Robust Sol-Gel-Processed p-Type Delafossite CuFeO₂ Photocathode for Solar Water Reduction. *ChemSusChem* **2015**, *8* (8), 1359-1367.
- (91) Prevot, M. S.; Li, Y.; Guijarro, N.; Sivula, K., Improving charge collection with delafossite photocathodes: a host-guest CuAlO₂/CuFeO₂ approach. *Journal of Materials Chemistry A* **2016**, *4* (8), 3018-3026.
- (92) Kang, U.; Choi, S. K.; Ham, D. J.; Ji, S. M.; Choi, W.; Han, D. S.; Abdel-Wahab, A.; Park, H., Photosynthesis of formate from CO₂ and water at 1% energy efficiency via copper iron oxide catalysis. *Energy & Environmental Science* **2015**, *8* (9), 2638-2643.
- (93) Gu, J.; Wuttig, A.; Krizan, J. W.; Hu, Y.; Detweiler, Z. M.; Cava, R. J.; Bocarsly, A. B., Mg-Doped CuFeO₂ Photocathodes for Photoelectrochemical Reduction of Carbon Dioxide. *The Journal of Physical Chemistry C* **2013**, *117* (24), 12415-12422.
- (94) Dominey, R. N.; Lewis, N. S.; Bruce, J. A.; Bookbinder, D. C.; Wrighton, M. S., Improvement of photoelectrochemical hydrogen generation by surface modification of p-type silicon semiconductor photocathodes. *Journal of the American Chemical Society* **1982**, *104* (2), 467-482.
- (95) Rocheleau, R. E.; Miller, E. L.; Misra, A., High-efficiency photoelectrochemical hydrogen production using multijunction amorphous silicon photoelectrodes. *Energy & Fuels* **1998**, *12* (1), 3-10.

References

- (96) Monk, P. M. S.; Ali, T.; Partridge, R. D., The effect of doping electrochromic molybdenum oxide with other metal oxides: Correlation of optical and kinetic properties. *Solid State Ionics* **1995**, *80* (1), 75-85.
- (97) Khaselev, O.; Bansal, A.; Turner, J. A., High-efficiency integrated multijunction photovoltaic/electrolysis systems for hydrogen production. *International Journal of Hydrogen Energy* **2001**, *26* (2), 127-132.
- (98) Hou, Y.; Abrams, B. L.; Vesborg, P. C. K.; Björketun, M. E.; Herbst, K.; Bech, L.; Setti, A. M.; Damsgaard, C. D.; Pedersen, T.; Hansen, O.; Rossmesl, J.; Dahl, S.; Nørskov, J. K.; Chorkendorff, I., Bioinspired molecular co-catalysts bonded to a silicon photocathode for solar hydrogen evolution. *Nature Materials* **2011**, *10*, 434.
- (99) Benck, J. D.; Lee, S. C.; Fong, K. D.; Kibsgaard, J.; Sinclair, R.; Jaramillo, T. F., Designing Active and Stable Silicon Photocathodes for Solar Hydrogen Production Using Molybdenum Sulfide Nanomaterials. *Advanced Energy Materials* **2014**, *4* (18).
- (100) Seger, B.; Laursen, A. B.; Vesborg, P. C.; Pedersen, T.; Hansen, O.; Dahl, S.; Chorkendorff, I., Hydrogen production using a molybdenum sulfide catalyst on a titanium-protected n(+)p-silicon photocathode. *Angew Chem Int Ed Engl* **2012**, *51* (36), 9128-31.
- (101) Kitagawa, S.; Kitaura, R.; Noro, S.-i., Functional Porous Coordination Polymers. *Angewandte Chemie International Edition* **2004**, *43* (18), 2334-2375.
- (102) Zhang, L.; Cui, P.; Yang, H.; Chen, J.; Xiao, F.; Guo, Y.; Liu, Y.; Zhang, W.; Huo, F.; Liu, B., Metal–Organic Frameworks as Promising Photosensitizers for Photoelectrochemical Water Splitting. *Advanced Science* **2016**, *3* (1), 1500243.
- (103) Sim, U.; Yang, T.-Y.; Moon, J.; An, J.; Hwang, J.; Seo, J.-H.; Lee, J.; Kim, K. Y.; Lee, J.; Han, S.; Hong, B. H.; Nam, K. T., N-doped monolayer graphene catalyst on silicon photocathode for hydrogen production. *Energy & Environmental Science* **2013**, *6* (12), 3658-3664.
- (104) Wu, H. B.; Xia, B. Y.; Yu, L.; Yu, X.-Y.; Lou, X. W., Porous molybdenum carbide nano-octahedrons synthesized via confined carburization in metal-organic frameworks for efficient hydrogen production. *Nature Communications* **2015**, *6*, 6512.
- (105) Jiao, Z.; Zheng, J.; Feng, C.; Wang, Z.; Wang, X.; Lu, G.; Bi, Y., Fe/W Co-Doped BiVO₄ Photoanodes with a Metal–Organic Framework Cocatalyst for Improved Photoelectrochemical Stability and Activity. *ChemSusChem* **2016**, *9* (19), 2824-2831.
- (106) Côté, A. P.; Benin, A. I.; Ockwig, N. W.; O’Keeffe, M.; Matzger, A. J.; Yaghi, O. M., Porous, crystalline, covalent organic frameworks. *Science* **2005**, *310* (5751), 1166-70.
- (107) Lohse, M. S.; Bein, T., Covalent Organic Frameworks: Structures, Synthesis, and Applications. *Advanced Functional Materials* **2018**, *28* (33), 1705553.
- (108) Bai, L.; Phua, S. Z. F.; Lim, W. Q.; Jana, A.; Luo, Z.; Tham, H. P.; Zhao, L.; Gao, Q.; Zhao, Y., Nanoscale covalent organic frameworks as smart carriers for drug delivery. *Chemical Communications* **2016**, *52* (22), 4128-4131.

- (109) Shi, X.; Yao, Y.; Xu, Y.; Liu, K.; Zhu, G.; Chi, L.; Lu, G., Imparting Catalytic Activity to a Covalent Organic Framework Material by Nanoparticle Encapsulation. *ACS Applied Materials & Interfaces* **2017**, *9* (8), 7481-7488.
- (110) Zhao, Y.; Liu, H.; Wu, C.; Zhang, Z.; Pan, Q.; Hu, F.; Wang, R.; Li, P.; Huang, X.; Li, Z., Fully Conjugated Two-Dimensional sp²-Carbon Covalent Organic Frameworks as Artificial Photosystem I with High Efficiency. *Angew Chem Int Ed Engl* **2019**, *58* (16), 5376-5381.
- (111) Chen, R.; Shi, J. L.; Ma, Y.; Lin, G.; Lang, X.; Wang, C., Designed Synthesis of a 2D Porphyrin-Based sp² Carbon-Conjugated Covalent Organic Framework for Heterogeneous Photocatalysis. *Angew Chem Int Ed Engl* **2019**, *58* (19), 6430-6434.
- (112) Cai, S.-L.; Zhang, K.; Tan, J.-B.; Wang, S.; Zheng, S.-R.; Fan, J.; Yu, Y.; Zhang, W.-G.; Liu, Y., Rationally Designed 2D Covalent Organic Framework with a Brick-Wall Topology. *ACS Macro Letters* **2016**, *5* (12), 1348-1352.
- (113) Lin, G.; Ding, H.; Yuan, D.; Wang, B.; Wang, C., A Pyrene-Based, Fluorescent Three-Dimensional Covalent Organic Framework. *Journal of the American Chemical Society* **2016**, *138* (10), 3302-3305.
- (114) Huang, N.; Krishna, R.; Jiang, D., Tailor-Made Pore Surface Engineering in Covalent Organic Frameworks: Systematic Functionalization for Performance Screening. *Journal of the American Chemical Society* **2015**, *137* (22), 7079-7082.
- (115) Xue, Y.; Hui, L.; Yu, H.; Liu, Y.; Fang, Y.; Huang, B.; Zhao, Y.; Li, Z.; Li, Y., Rationally engineered active sites for efficient and durable hydrogen generation. *Nat Commun* **2019**, *10* (1), 2281.
- (116) Stegbauer, L.; Schwinghammer, K.; Lotsch, B. V., A hydrazone-based covalent organic framework for photocatalytic hydrogen production. *Chemical Science* **2014**, *5* (7), 2789-2793.
- (117) Vyas, V. S.; Haase, F.; Stegbauer, L.; Savasci, G.; Podjaski, F.; Ochsenfeld, C.; Lotsch, B. V., A tunable azine covalent organic framework platform for visible light-induced hydrogen generation. *Nature Communications* **2015**, *6*, 8508.
- (118) Wang, Y.; Zhao, S.; Zhang, Y.; Fang, J.; Chen, W.; Yuan, S.; Zhou, Y., Facile Synthesis of Self-Assembled g-C₃N₄ with Abundant Nitrogen Defects for Photocatalytic Hydrogen Evolution. *ACS Sustainable Chemistry & Engineering* **2018**, *6* (8), 10200-10210.
- (119) Wang, Y.; Zhao, S.; Zhang, Y.; Chen, W.; Yuan, S.; Zhou, Y.; Huang, Z., Synthesis of graphitic carbon nitride with large specific surface area via copolymerizing with nucleobases for photocatalytic hydrogen generation. *Applied Surface Science* **2019**, *463*, 1-8.
- (120) Wang, X.; Chen, L.; Chong, S. Y.; Little, M. A.; Wu, Y.; Zhu, W. H.; Clowes, R.; Yan, Y.; Zwijnenburg, M. A.; Sprick, R. S.; Cooper, A. I., Sulfone-containing covalent organic frameworks for photocatalytic hydrogen evolution from water. *Nat Chem* **2018**, *10* (12), 1180-1189.
- (121) Banerjee, T.; Haase, F.; Savasci, G.; Gottschling, K.; Ochsenfeld, C.; Lotsch, B. V., Single-Site Photocatalytic H₂ Evolution from Covalent Organic Frameworks with Molecular

References

- Cobaloxime Co-Catalysts. *Journal of the American Chemical Society* **2017**, *139* (45), 16228-16234.
- (122) Banerjee, T.; Gottschling, K.; Savasci, G.; Ochsenfeld, C.; Lotsch, B. V., H₂ Evolution with Covalent Organic Framework Photocatalysts. *ACS Energy Letters* **2018**.
- (123) Sick, T.; Hufnagel, A. G.; Kampmann, J.; Kondofersky, I.; Calik, M.; Rotter, J. M.; Evans, A.; Döblinger, M.; Herbert, S.; Peters, K.; Böhm, D.; Knochel, P.; Medina, D. D.; Fattakhova-Rohlfing, D.; Bein, T., Oriented Films of Conjugated 2D Covalent Organic Frameworks as Photocathodes for Water Splitting. *Journal of the American Chemical Society* **2018**, *140* (6), 2085-2092.
- (124) Sun, H.; Oner, I. H.; Wang, T.; Zhang, T.; Selyshchev, O.; Neumann, C.; Fu, Y.; Liao, Z.; Xu, S.; Hou, Y.; Turchanin, A.; Zahn, D. R. T.; Zschech, E.; Weidinger, I. M.; Zhang, J.; Feng, X., Molecular Engineering of Conjugated Acetylenic Polymers for Efficient Cocatalyst-free Photoelectrochemical Water Reduction. *Angew Chem Int Ed Engl* **2019**, *58* (30), 10368-10374.
- (125) Ebelmen, M., Recherches sur les combinaisons des acides borique et silicique avec les éthers. *Ann. Chim. Phys.* **1846**, (16), 129.
- (126) Hench, L. L.; West, J. K., The sol-gel process. *Chemical Reviews* **1990**, *90* (1), 33-72.
- (127) Matijević, E.; Budnik, M.; Meites, L., Preparation and mechanism of formation of titanium dioxide hydrosols of narrow size distribution. *Journal of Colloid and Interface Science* **1977**, *61* (2), 302-311.
- (128) Niederberger, M.; Pinna, N., *Metal oxide nanoparticles in organic solvents: synthesis, formation, assembly and application*. Springer Science & Business Media: 2009.
- (129) Lee, G.-Y.; Lee, J.; Vo, H. T.; Kim, S.; Lee, H.; Park, T., Amine-Functionalized Covalent Organic Framework for Efficient SO₂ Capture with High Reversibility. *Scientific Reports* **2017**, *7* (1), 557.
- (130) Peng, Y.; Wong, W. K.; Hu, Z.; Cheng, Y.; Yuan, D.; Khan, S. A.; Zhao, D., Room Temperature Batch and Continuous Flow Synthesis of Water-Stable Covalent Organic Frameworks (COFs). *Chemistry of Materials* **2016**, *28* (14), 5095-5101.

2 Characterization techniques

2.1 X-ray Diffraction

X-ray diffraction has become the most common analytical technique for structure determination of crystalline substances. It can be used to investigate a broad range of materials: starting from classical solid inorganic matter like metals, metal oxides and different minerals over organic-inorganic hybrid materials like lead-halide perovskites or metal-organic frameworks, or completely organic crystals like covalent organic frameworks including their complex nanostructures, up to crystalline biological compounds like proteins or DNA. However, this method allows for several variations to tailor it for the respective experiment. The theoretical basics and different instrument geometries are discussed in the following subchapter.

2.1.1 Theory

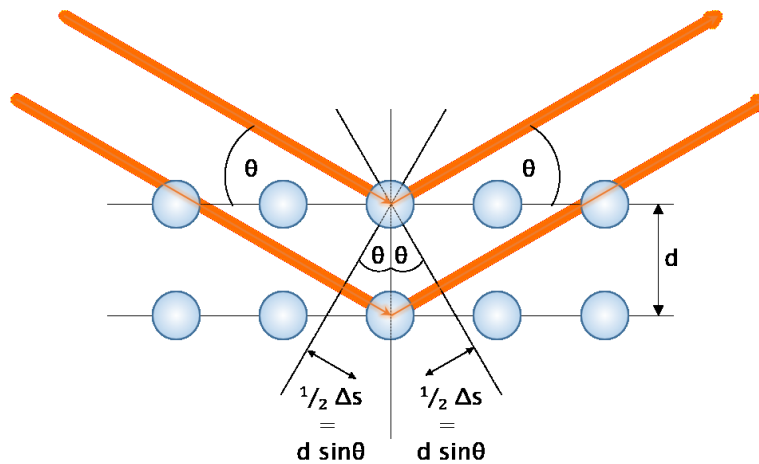


Figure 2.1. Schematic illustration of Bragg's law.

The interatomic distances of crystalline materials are of similar dimension as the wavelength of typical X-ray radiation, wherefore the radiation should be diffracted by those materials. In 1912, Max

X-ray Diffraction

v. Laue described this phenomenon and was therefore awarded with the Nobel prize in physics in 1914.¹ Based on his work, W. H. Bragg and W. L. Bragg described the diffraction of X-ray radiation on crystalline materials and interpreted the resulting intensity distribution as an interference pattern of equally spaced atomic crystal lattice planes (Figure 2.1)²⁻³, paving the way for structure determination of crystalline matter which was also rewarded with the Nobel prize in physics in 1915.¹ The Bragg equation (Eq. 2.1) describes the condition for constructive interference by bringing the wavelength of the used X-rays λ in relation to their angle of incidence θ and the lattice spacing d , while n is an integer number ($n = 1, 2, 3, \dots$) describing the order of interference.⁴

$$n \lambda = 2 d \sin\theta \quad \text{Eq. 2.1}$$

This non-destructive method was originally developed to determine the structure of single crystals, but it can also be applied to analyze polycrystalline powders or thin film samples. X-rays are typically generated by a tubular cathodic filament at high voltages. They emit a continuum of bremsstrahlung which is filtered to select a specific wavelength for diffraction experiments. Typically, the K_{α} transitions are selected due to their high intensity. Depending on the investigated material, different X-ray wavelengths can be chosen to match the structural questions at hand and to control other aspects such as absorption or fluorescence by the material, e.g. Cu- $K_{\alpha 1}$ ($\lambda = 1.54433 \text{ \AA}$) or Mo- $K_{\alpha 1}$ ($\lambda = 0.713543 \text{ \AA}$).⁵ The resulting diffraction pattern can contain various crystal phases where the comparison with a crystal structure database (e.g. the ICSD by FIZ Karlsruhe⁶) may lead to their identification. Furthermore, the width of the reflexes depends on the size of the crystallites/domains. This phenomenon is described by the Scherrer equation (Eq. 2.2), where the size of an isotropic crystal p can be determined from the full width at half-maximum broadening ($FWHM$) of a reflection and the Scherrer constant K (0.9 for most cases).⁷

$$d = \frac{K \lambda}{FWHM \cos\theta} \quad \text{Eq. 2.2}$$

2.1.2 Geometries

An X-ray diffraction (XRD) experiment can be conducted either in transmission (Debye-Scherrer)⁸ or in reflection (Bragg-Brentano)⁹ geometry (Figure 2.2). In transmission mode, the powder sample is placed in an X-ray transparent sample holder (e.g. glass tube or polymer foil) and can be rotated during the measurement. The X-ray beam is focused on the sample while the detector moves in a circle around the sample position detecting reflections in the 2θ range. Additionally, the angle of the sample holder can be varied to allow scanning 2θ values above 90° .

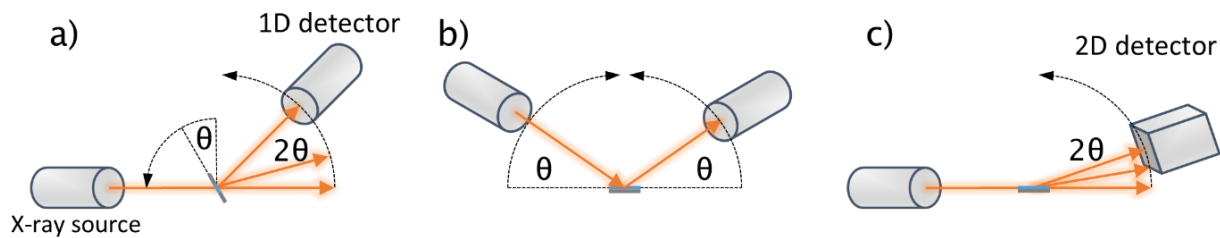


Figure 2.2. Different geometries for XRD measurements, namely Debye-Scherrer (a), Bragg-Brentano (b) and grazing incidence diffraction (c).

For the characterization of thin films, a measurement in reflection mode can be useful to avoid absorption of X-ray intensity or the appearance of additional reflexes by the substrate. Such an examination can be conducted in two different ways. In the θ - θ mode, both X-ray source and detector are moved in similar steps scanning all angles θ between them and the sample surface. Only reflexes caused by crystallographic planes oriented parallel to the substrate will be detected. In the 2θ mode, the position of the X-ray source stays constant while only the detector is moved by 2θ . In this case, highly oriented films fulfill the Bragg condition only for its specific diffraction angle. Especially if a very low angle of incidence of the X-rays is chosen (grazing incidence XRD), the radiation interacts with a significantly higher volume of film material resulting in a stronger signal.¹⁰ Additionally, the degree of orientation of crystallites with respect to the surface can be determined using a two-dimensional detector.¹¹

Electron Microscopy

2.2 Electron Microscopy

In the field of nanoscience, the materials' structure and morphology soon becomes too small to be imaged with conventional light microscopy. According to *Abbe's law*, domains need to have a minimal size of roughly 150 – 200 nm to be detected in a conventional light microscope. Ruska and Knoll constructed the first electron microscope back in 1932.¹² The electrons used here have a wavelength in the picometer range, which nowadays allows for a spatial resolution of less than 0.5 Å and enables imaging of complex nanostructures.¹³

2.2.1 Scanning Electron Microscopy

Scanning electron microscopy is commonly used to image micro- and nanostructured sample topographies. An electron beam with an energy of about 1 to 40 keV is focused by an arrangement of condenser lenses and apertures and used to scan over the sample's surface (Figure 2.3a). The incident electron beam can interact with the sample in various ways, which is illustrated in Figure 2.3b. The different kinds of interactions of the incident electron beam with the sample can be used for further investigation of the material.¹⁴

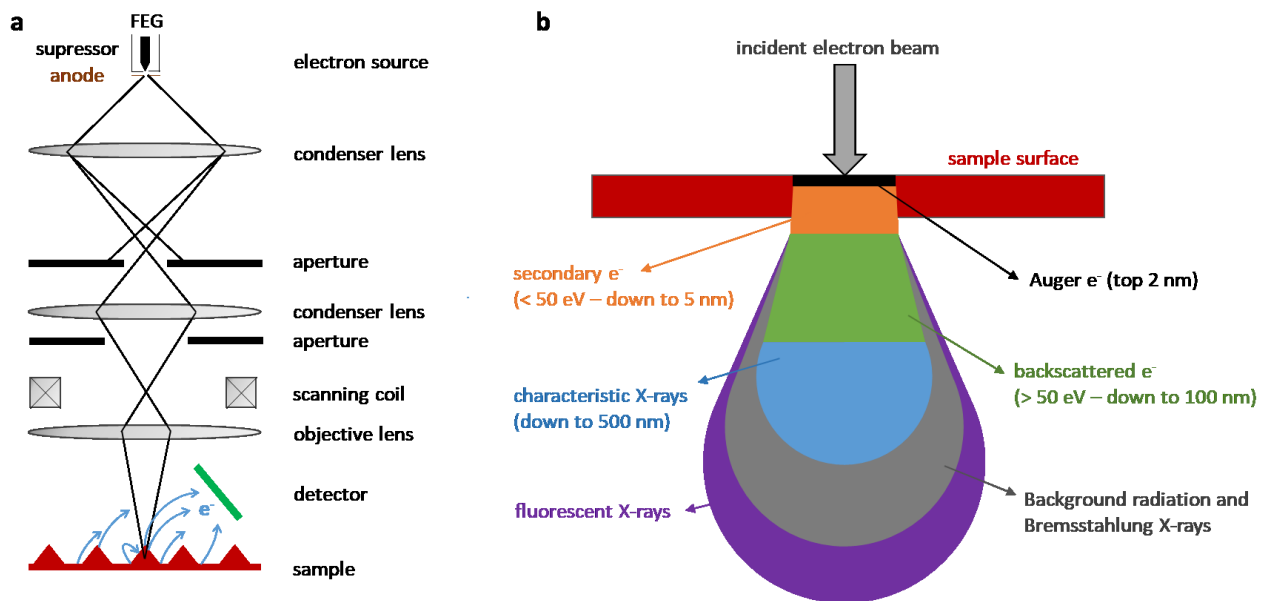


Figure 2.3. a) Schematic illustration of a scanning electron microscope and the image generation of a structured sample topography. b) Possible ways of electron – matter interaction and the emitted radiation with corresponding interaction volume.

The electrons interact either quasi-elastically or inelastically with the sample, which results in the emission of Auger electrons from the upper 2 nm of the surface, secondary electrons ($E < 50$ eV) from down to 5 nm and backscattered electrons ($E > 50$ eV) from down to 100 nm escape depth. Their escape depth is limited by their comparable low energy. Additionally, characteristic X-rays, originating from electron beam interaction with the upper 500 nm of the sample surface, can be collected by a special detector and used to analyze the sample composition (see section 2.2.4.1). Also, the contrast is dominated on steep surfaces and sharp edges of the material (edge effect). For these reasons, secondary electrons detection creates edge and shadowing effects and is commonly used to image the sample's topography with a high signal-to-noise ratio. Backscattered electrons are released from deeper sample levels in a quasi-elastic scattering process. For this reason, their yield depends on the scattering power of the investigated material (Z-contrast) and can be used to create an image possessing material contrast. In this case, heavier elements appear brighter in the obtained image than lighter elements.¹⁵⁻¹⁶ Furthermore, electron beam interaction with deep regions of the sample matter releases background radiation as well as Bremsstrahlung and fluorescent X-rays.

2.2.2 Focused Ion Beam Technology

The focused ion beam (FIB) technology is closely related to SEM, and both are nowadays often combined in the same workstation. In contrast to the electron beam of an SEM, the FIB uses a beam of ions like Ga^+ at a comparably low current. While the ion beam can also be used for imaging, FIB is mostly used to either deposit material locally on the sample surface or to mill down parts of the sample. This is possible due to the significantly higher kinetic energy of accelerated ions compared to electrons and can be used to prepare very thin lamellae for the investigation with a transmission electron microscope (TEM) (Figure 2.4). Such a TEM cross section is commonly prepared according to the following procedure: After the deposition of a platinum protection layer on the *to be investigated* sample area (step 1), the surrounding area is milled down little by little to create a nearly freestanding part of the sample (step 2). This part is then attached to a conventional TEM grid (step 3) and further thinned until it reaches a thickness of around 100 nm, which makes it transparent for electrons in the TEM (step 4).⁴

Electron Microscopy

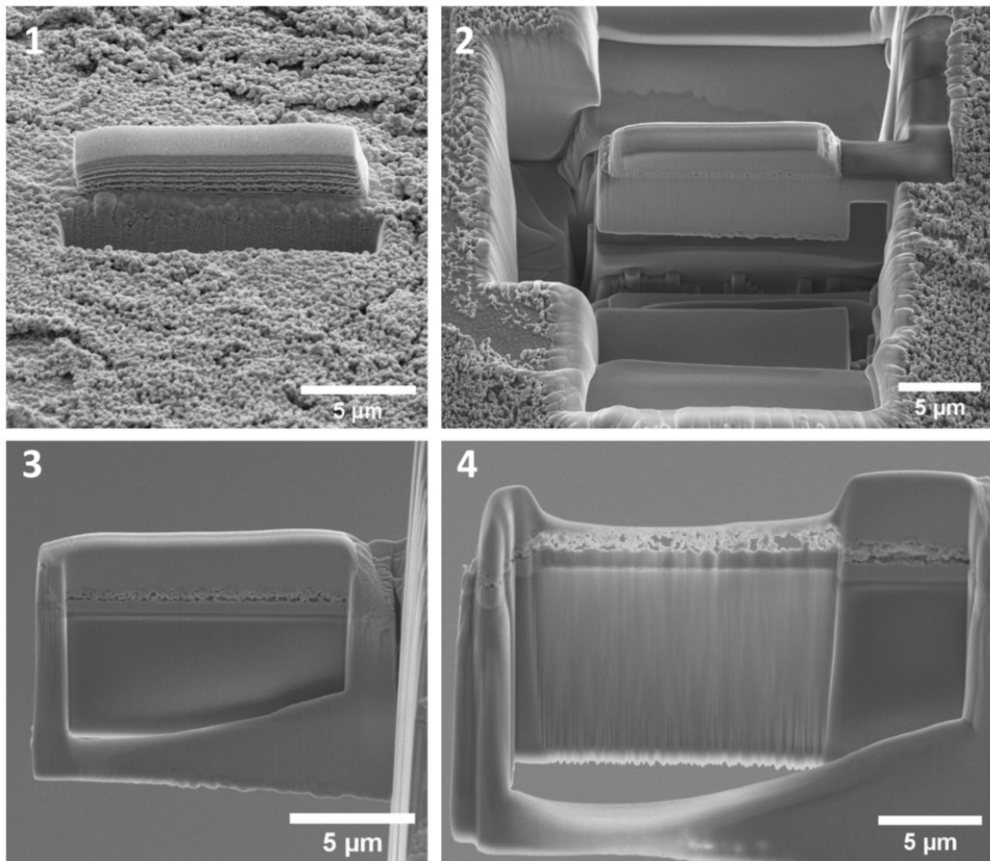


Figure 2.4. SEM images during the preparation of a thin lamella from a nanostructured Li_xCuO film in consecutive order (images by Dr. Tristan Harzer).

2.2.3 Transmission Electron Microscopy

2.2.3.1 *Diffraction, Bright and Dark Field imaging*

In a transmission electron microscope (TEM), an electron beam is focused on the sample in a high vacuum system and the transmitted electrons are used for imaging. Therefore, the specimen needs to be thinner than about 100 nm to be transparent enough for penetration by the beam. The electrons are either generated by thermal emission from a cathodic filament like tungsten or lanthanum hexaboride at a temperature of up to 1800 °C or by a field emission gun using a very strong electric field (10^9 Vm^{-1}). Afterwards, the electrons are accelerated towards the anode with a selectable voltage between 60 and 300 kV. The electron beam is then focused on the specimen by a complex system of condenser lenses. The transmitted electrons are again focused with another system of objective, intermediate and projector lenses on a fluorescent screen or a charge-coupled device camera (Figure 2.5). Different operation modes can be selected to image the back focal plane (diffraction mode) or the image plane (imaging mode). While the latter is commonly used to take a picture of the investigated area, a diffraction pattern can be obtained by projecting the back focal plane on the screen. In bright field (BF) mode, an aperture is placed in the back focal plane. Therefore, the diffracted beams are blocked selectively which results in an increased contrast in the obtained image. If the aperture is placed around distinct diffraction spots, only the phases of the specimen causing the spots appear bright in the resulting, so called dark field (DF), image.⁴

Electron Microscopy

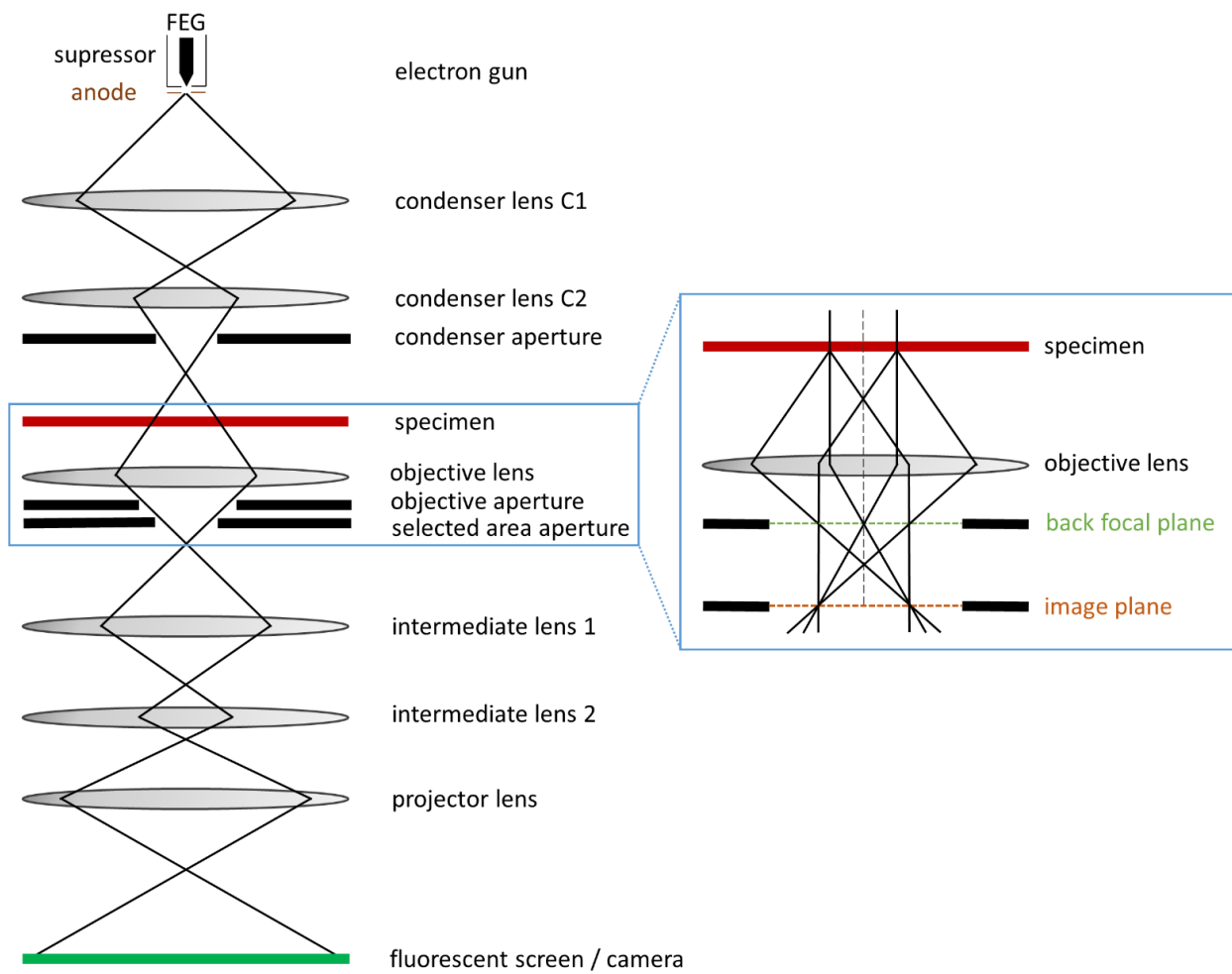


Figure 2.5. Schematic setup of a transmission electron microscope. The inset illustrates the use of different apertures for the focus on image or back focal plane.

2.2.3.2 Scanning Transmission Electron Microscopy

The electron beam in a TEM can be used to scan over the specimen in a manner comparable to SEM, whereas still transmitted electrons are used for imaging. Various scanning transmission electron microscopy (STEM) detectors are placed below the sample, which are assembled as multiple ring detectors to distinguish between signals of different scattering angles (Figure 2.6). While the BF detector is in the middle, the first ring is an annular dark field (ADF) detector followed by a high angle annular dark field (HAADF) detector. This arrangement counts the intensity of electrons having a different scattering angle. Due to the dependence of the scattering angle on the atomic number Z (*Rutherford* scattering probability), an HAADF-STEM image contains a certain material contrast depending on the atomic weight of the sample materials. The detector geometry makes STEM particularly suitable for analytical techniques such as energy dispersive X-ray (EDX) and electron energy loss spectroscopy (EELS).⁴

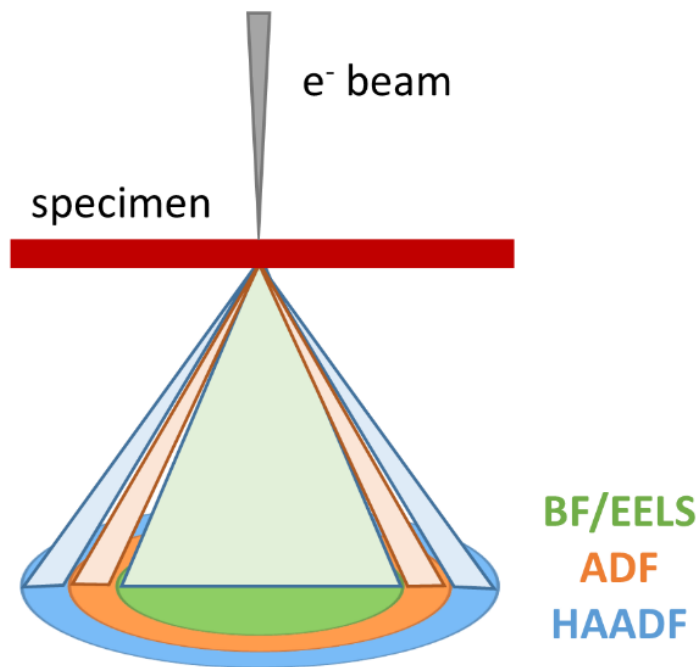


Figure 2.6.: Schematic illustration of a STEM detector setup to distinguish between electrons with different scattering angles.

Electron Microscopy

2.2.4 Spectroscopic methods

The various possible interactions of the electron beam with the sample can be used for a detailed analysis of its composition. In combination with STEM, both the elemental composition and the atoms' oxidation state can be probed spatially-resolved and used to create a map of a defined sample area.

2.2.4.1 Energy Dispersive X-ray Spectroscopy

Energy dispersive X-ray (EDX) spectroscopy is a widely used technique to analyze the sample's composition in an electron microscope. Under the incident electron beam, inner shell electrons of the investigated matter are ejected from the atoms. The remaining hole is filled by an electron from an outer shell and consequently, the corresponding energy is released as X-rays and Bremsstrahlung (Figure 2.7). The possible electron transfers are described by distinct labels (e.g. K_1 , K_2 , L_1) and their energy differences are specific for each atom.¹⁷ Therefore, the elemental composition of a spot or an area can be determined from the obtained X-ray spectrum. The yield of emitted X-rays depends on the atomic number of each atom (being more efficient for heavier elements), which limits the detection of lighter elements like hydrogen, helium or lithium.

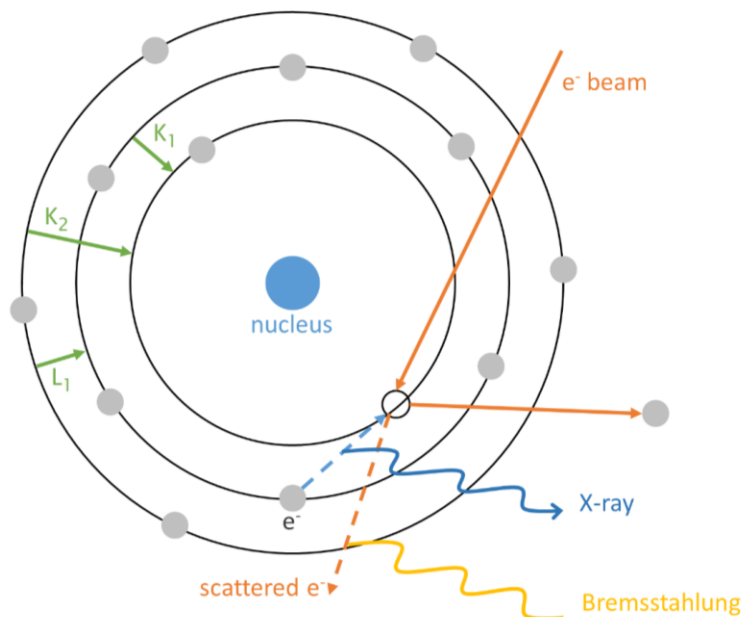


Figure 2.7. Schematic formation of element-characteristic X-rays and Bremsstrahlung from the interaction of the electron beam with the sample.

2.2.4.2 Electron Energy Loss Spectroscopy

In contrast to EDX, electron energy loss spectroscopy (EELS) uses electrons that were inelastically scattered by the sample. The occurring energy loss ΔE with respect to the incident electron beam energy E_0 is detected by a special EELS spectrometer, where the electrons are separated according to their energy by a magnetic prism (Figure 2.8a). While the resulting EELS spectrum can be used to distinguish between different elemental compositions, its resolution strongly depends on the monochromaticity of the incident electrons. Therefore, a monochromator is typically needed to investigate the near edge fine structure in the core loss region of the EELS spectrum, which is characteristic for the ionization state of the single atomic species. This information can even be used to distinguish between different oxidation states of the same element (Figure 2.8b).⁴

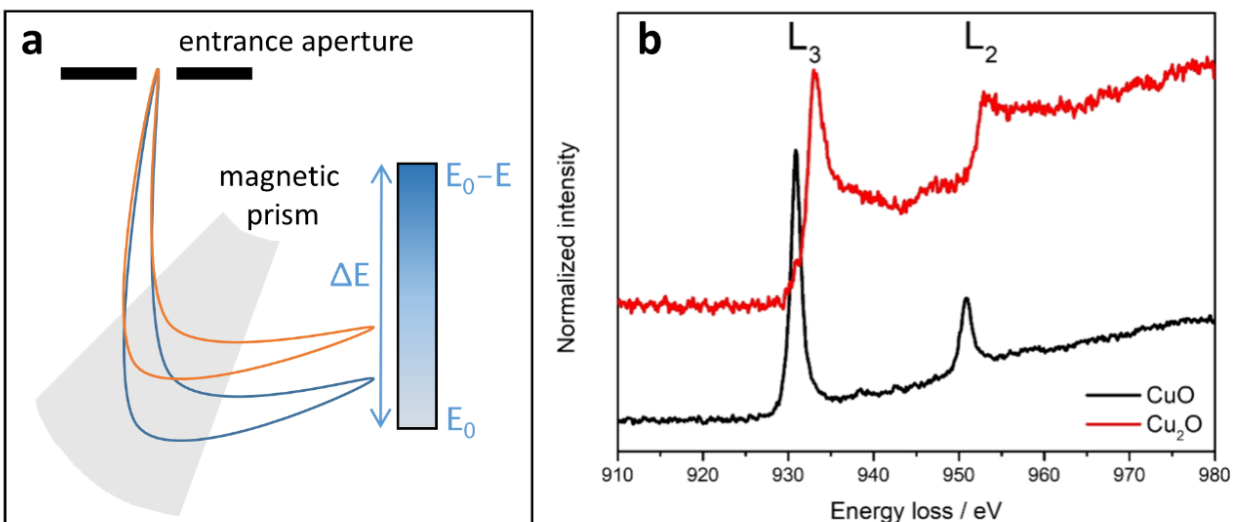


Figure 2.8. Schematic illustration of the separation of electrons with different energy losses by a magnetic prism (a) and an exemplary EELS core-loss spectrum of two copper oxides. The shift of the L₂ and the L₃ edge can be used to distinguish between Cu¹⁺ and Cu²⁺.

X-ray Photoelectron Spectroscopy

2.3 X-ray Photoelectron Spectroscopy

Detailed information about a sample's surface composition can be obtained from X-ray photoelectron spectroscopy (XPS). Here, the sample is placed in an ultrahigh vacuum (UHV) chamber and irradiated with X-rays. If a sample atom absorbs an X-ray photon, an inner shell electron can be removed from the atom. Subsequently, its energy is determined by a hemisphere-shaped electron analyzer and a detector (Figure 2.9).⁴

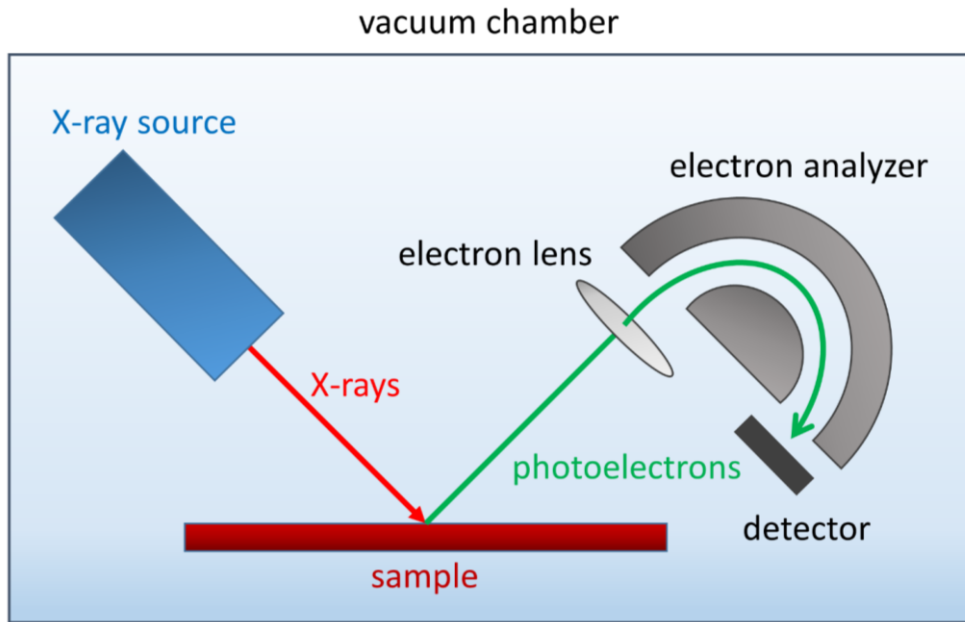


Figure 2.9. Schematic illustration of an XPS spectroscopy setup.

The electron binding energy E_b is specific for each element and can be calculated from the X-ray photon energy $h\nu$, the detected kinetic electron energy E_{kin} and the detector work function ϕ (Eq. 2.4).

$$E_b = h\nu - E_{kin} - \phi \quad \text{Eq. 2.3}$$

The detected electron energy is usually in the range of a few hundred eV. Therefore, their mean free path in solid matter is quite short. This limits the probing depth to around 1.5 nm, which makes XPS a highly surface sensitive technique.¹⁷⁻¹⁸ Additional to the elemental composition, XPS can also probe the oxidation state of the respective elements as the binding energy of inner shell electrons is stronger for more highly oxidized atoms. This slight increase can only be detected with an XPS spectrometer

with sufficiently high resolution, which also allows for the detection of Auger electrons. Auger electron spectroscopy is only sensitive to the upper few atomic layers of the sample and can be used to gain even more surface sensitive information. Auger electron spectroscopy is especially used in case of lighter elements.¹⁹

2.4 Spectrophotometry

Spectrophotometry is a widely applied technique to quantify the absorption properties of photoactive materials. As the ideal band gap of semiconductors used in photoelectrochemical devices is around 1.5 – 3.0 eV, they absorb light in the ultra violet, the visible and the near infrared range of the visible spectrum (Figure 2.10).²⁰

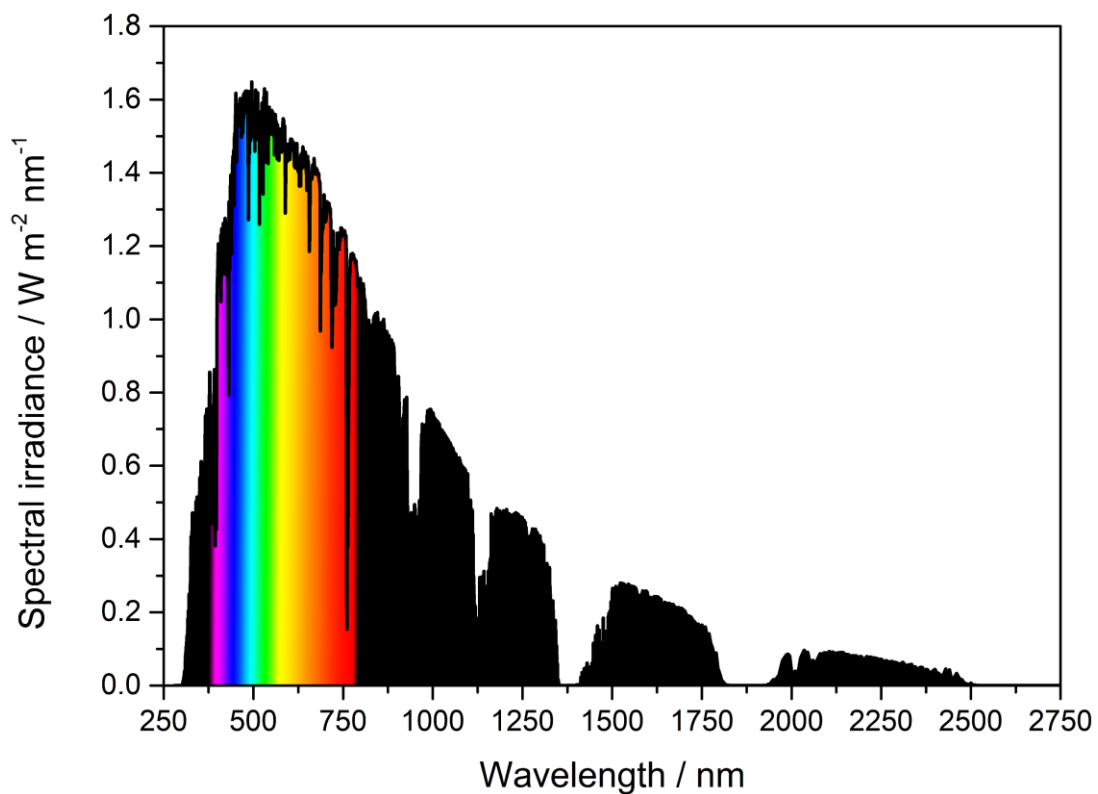


Figure 2.10. Standard ASTM G173-03 air mass 1.5 global (AM1.5G) solar spectrum²¹ with illustrated visible part.

Spectrophotometry

A commonly used UV-Vis spectrometer contains a deuterium lamp as UV light source and a tungsten lamp for light in the visible range. The wavelength of the incident photons with intensity I_0 is selected in variable step size by a monochromator while the spot size can be adjusted and focused with an iris system. An integrating sphere (used to also measure reflection/scattering from the sample) and a photomultiplier tube (PMT) and InGaAs detectors quantify the fraction of transmitted light intensity I_T . The *Lambert-Beer* law can be used to calculate the wavelength-dependent absorbance $A(\lambda)$ of the sample (Eq. 2.4).

$$A(\lambda) = -\log_{10} \frac{I_T(\lambda)}{I_0(\lambda)} \quad \text{Eq. 2.4}$$

For the characterization of thin films on (transparent conductive oxide coated) glass substrates, intensity losses by reflection and scattering as well as the absorption of the substrate itself need to be considered. At first glance it may appear that these contributions could simply be subtracted from the absorption of the whole device. But as these effects do not only occur at the first surface hit by the incident photons, Klahr et al. described a convenient procedure to quantify the corrected absorbance of a thin film material $A_{corr}(\lambda)$ which takes account of these phenomena (Eq. 2.5).²²

$$A_{corr}(\lambda) = -\log_{10} \left(\frac{\frac{T_{sample}(\lambda)}{T_{substrate}(\lambda)}}{1 - \frac{R_{sample}(\lambda) - R_{substrate}(\lambda)}{T_{substrate}(\lambda)}} \right) \quad \text{Eq. 2.5}$$

Transmission data of the sample $T_{sample}(\lambda)$, the substrate $T_{substrate}(\lambda)$ as well as the respective reflectance data of the sample $R_{sample}(\lambda)$ and the substrate $R_{substrate}(\lambda)$ are determined in separate measurements and afterwards used to calculate $A_{corr}(\lambda)$. The spectral data can further be used to calculate the optical band gap of the investigated material by the *Tauc plot* method.²³ If $(\alpha h\nu)^x$ is plotted vs. $h\nu$ (with ν as photon frequency) the optical absorption appears as linear increase, which can be calculated for different transitions ($x = 2$ for direct and $x = 0.5$ for indirect transitions). The band gap energy E_g can be obtained from a linear extrapolation to $(\alpha h\nu)^x = 0$.

2.5 Nuclear magnetic resonance spectroscopy

Identification and characterization of COF linker molecules and intermediates can be performed via nuclear magnetic resonance spectroscopy. The method is based on the excitation of nuclear magnetic spin momenta. NMR active nuclei possess an uneven number of protons or neutrons causing an overall nuclear spin unequal to zero. A simplified explanation of a particle's spin is the rotation around its own axis. According to the *Maxwell equations*, this implies the formation of a magnetic field by rotating the permanent charge of its proton building blocks for a nucleus with a spin other than zero. This field is characteristic for each nucleus depending on its proton/ neutron composition. If nuclei with a permanent spin momentum are exposed to an external, homogeneous magnetic field, the previously degenerated energy levels for the different possible spin states of the nucleus split up into different energy levels (Figure 2.11).²⁴⁻²⁵

Based on the excitation of spin states between these different energy levels, an NMR spectrum can be recorded. This can be described by the following equation:

$$\Delta E = \gamma \hbar B_0 \quad \text{Eq. 2.6}$$

ΔE stands for the needed excitation energy, γ for the gyromagnetic constant which is specific for every NMR active nucleus and needs to be determined experimentally, \hbar is the reduced *Planck constant* and B_0 the value of the applied magnetic field in [T]. During an NMR experiment, the sample is put into a permanent, homogeneous magnetic field and exposed to short pulses of electromagnetic radiation. These pulses possess a broad spectrum of frequencies which interact all at once with the nucleus. Once excited, the nucleus releases the absorbed energy in the form of spin-lattice and spin-spin relaxation, creating a time dependent energy signal. This signal can be transformed to an energy dependent intensity spectrum by Fourier transformation, which is often depicted as the intensity plotted against $\Delta\delta$ [ppm] scale. The ppm scale normalizes the energy dependence towards a known standard, allowing for the comparison of spectra recorded with different magnetic fields (Eq. 2.7). The scale is usually normalized on the signal of tetramethylsilane, which is set to 0 ppm.²⁴

Nuclear magnetic resonance spectroscopy

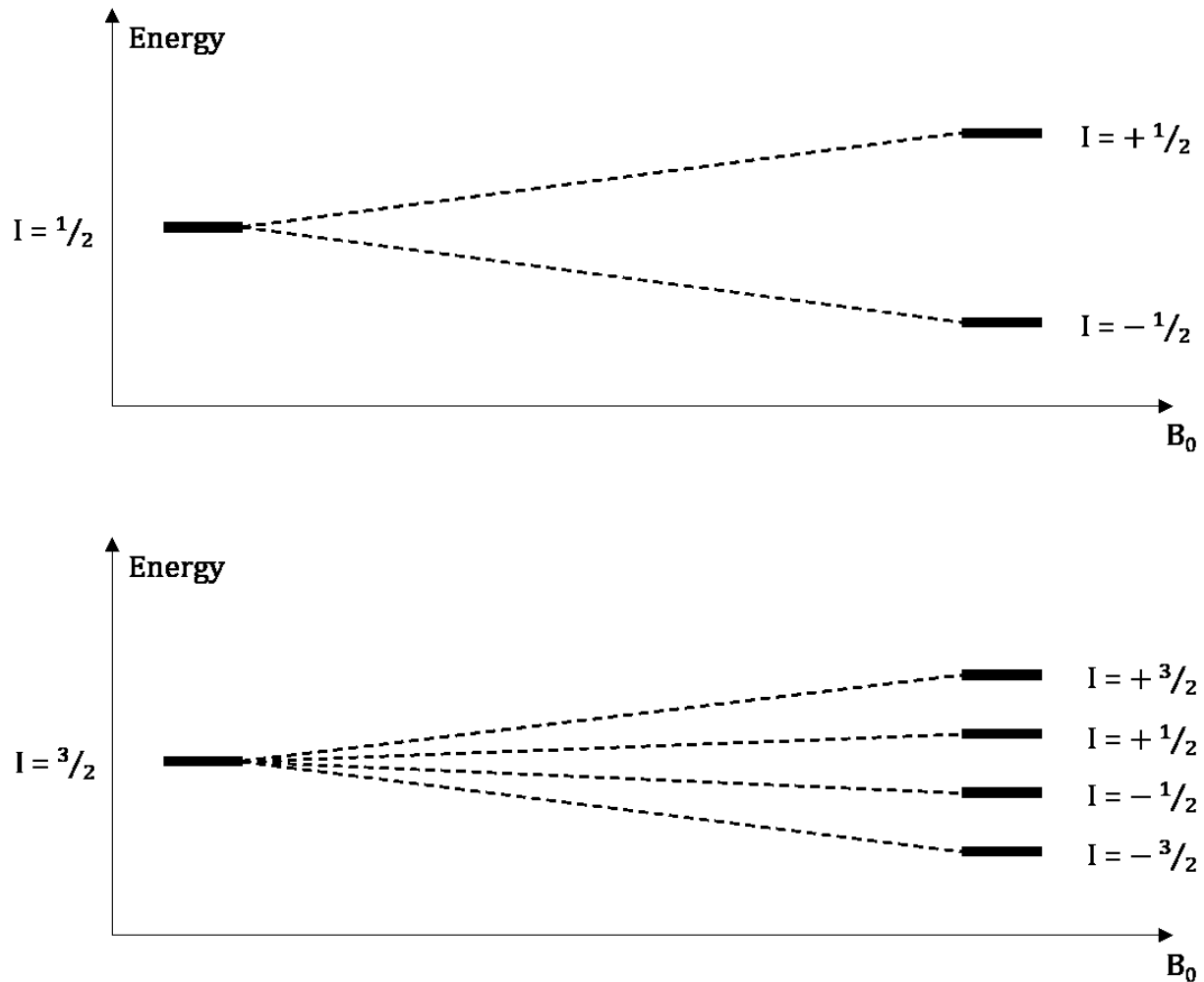


Figure 2.11: Energy level distribution of nuclear spin states in a homogeneous magnetic field with the nuclear spin (I) and the externally applied magnetic field (B_0).

$$\Delta\delta[\text{ppm}] = \frac{\nu_{\text{sample}} - \nu_{\text{reference}}}{\nu_{\text{reference}}} \quad \text{Eq. 2.7}$$

The position of the excitation signal depends on the chemical environment of the nucleus. The electron shell of each atom creates an individual magnetic field due to movement of electrons in the applied homogeneous magnetic field. This induced magnetic field is inversely oriented to the applied external magnetic field, shielding the nucleus from excitation. If this nucleus is surrounded by atoms with high electronegativity, a strong pull on the shielding electrons is exerted. This exposes the nucleus to the magnetic field, decreasing the needed energy for excitation and moving the signal to

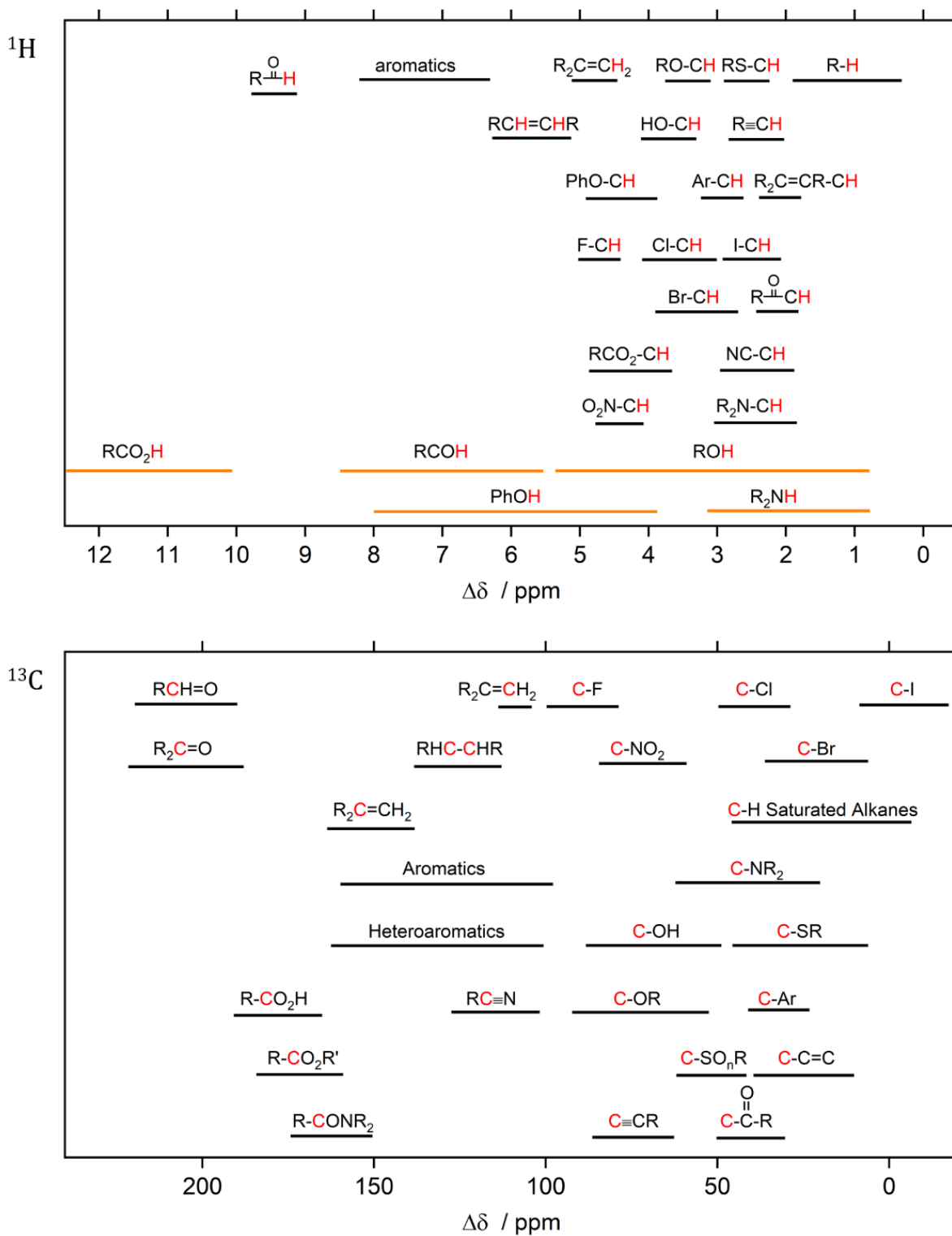


Figure 2.12: Generalized chemical shifts for ^1H and ^{13}C nuclei depending on their chemical environment²⁵⁻²⁶

Nuclear magnetic resonance spectroscopy

higher ppm values. Analogously, for nuclei surrounded by an electron donating chemical environment the shielding effect causes the need for higher resonance frequencies, moving the signal to lower ppm values. Signals for ^1H nuclei usually appear in a range from 0 ppm to 14 ppm and signals of ^{13}C nuclei from 0 ppm to 200 ppm (Figure 2.12).²⁶ Additionally, adjacent nuclei can couple with the nucleus' chemical environment. This causes further splitting of the energy levels, leading to the formation of multiplet signals (Figure 2.13).

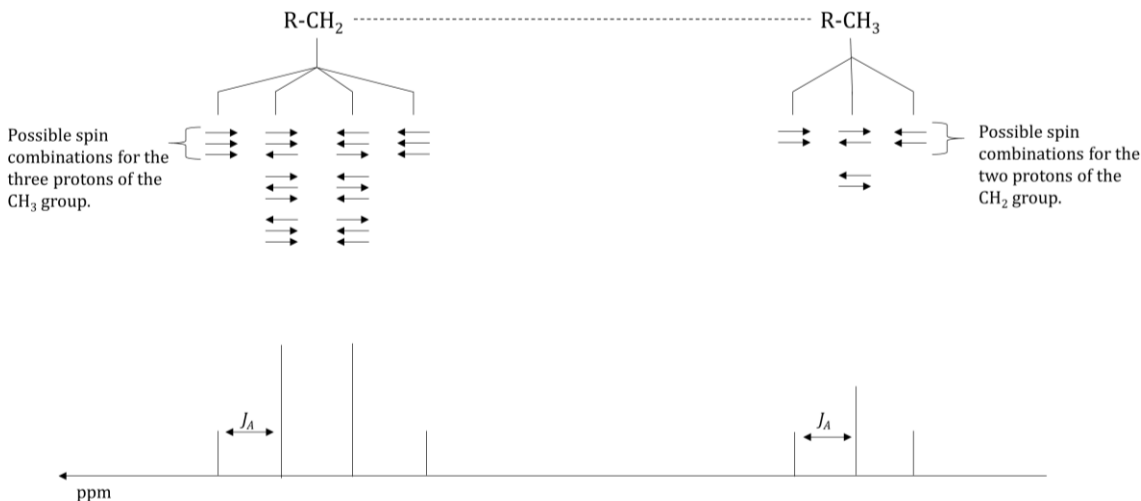


Figure 2.13: Schematic J -coupling between adjacent CH_2 and CH_3 group protons. Each proton possesses its own spin configuration with $I = \pm 1/2$. As indicated by arrows, the protons of each chemical group form different spin state combinations. Depending on the number of protons, and other atoms bound to the same carbon atom, characteristic magnetic fields result. These magnetic fields are being communicated through the binding electrons between the respective chemical groups (e.g. CH_2 and CH_3), further splitting up the energy levels of the adjacent proton nuclei, which causes the formation of multiplets. J_A represents the coupling constant, which is the energy difference $\Delta\nu$ [Hz] of the resulting energy levels for the possible spin state combinations caused by the interaction with the coupling partner.

Characterization techniques

NMR spectra were recorded on a Bruker Avance III HD 400 MHz and 800 MHz spectrometer equipped with a CryoProbeT M, Bruker AXR300, Varian VXR400 S and Bruker AMX600 spectrometers operating at 400 MHz, 800 MHz, 300 MHz, 400 MHz and 600 MHz for proton nuclei and 100 MHz, 75 MHz, 100 MHz, 150 MHz for carbon nuclei, respectively. Proton chemical shifts are expressed in parts per million (ppm, δ scale) and are referenced to residual protium in the NMR solvent (CDCl₃: 7.26, methanol-d₃: 4.78, acetone-d₅: 2.05, CDHCl₂: 5.32). Carbon chemical shifts are expressed in parts per million (δ scale, assigned carbon atom) and are referenced to the carbon resonance of the NMR solvent (CDCl₃: 77.16, CD₃OD: 49.00, acetone-d₆: 29.84, CD₂Cl₂: 54.00). ¹H NMR spectroscopic data are reported as follows: Chemical shift in ppm (multiplicity, coupling constants *J* (Hz), integration intensity, assigned proton). The multiplicities are abbreviated with s (singlet), br s (broad singlet), d (doublet), t (triplet), q (quartet) and m (multiplet). In case of combined multiplicities, the multiplicity with the larger coupling constant is stated first. Except for multiplets, the chemical shift of all signals, as well as for centrosymmetric multiplets, is reported as the center of the resonance range. Coupling constants *J* are reported in Hz. All raw fid files were processed and the spectra analyzed using the program MestReNOVA 12.0 from Mestrelab Research S. L.

Photoelectrochemical Analysis

2.6 Photoelectrochemical Analysis

The efficiency of new materials to evolve hydrogen and oxygen from water under illumination can be quantified in a photoelectrochemical measurement. In the ideal case, the current under illumination is directly proportional to the photoelectrolysis reaction. However, additional signals can occur from competing reactions like the corrosion of the electrode material or the reduction of oxygen dissolved in the electrolyte.

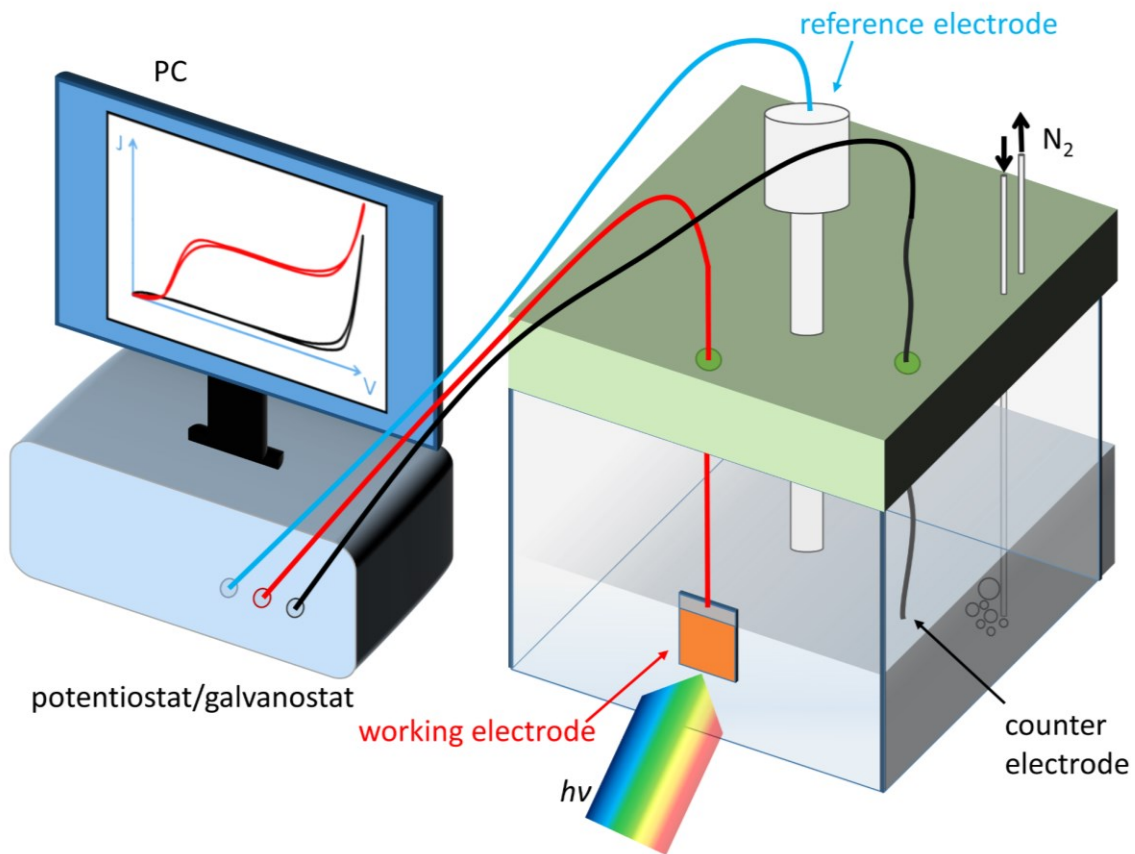


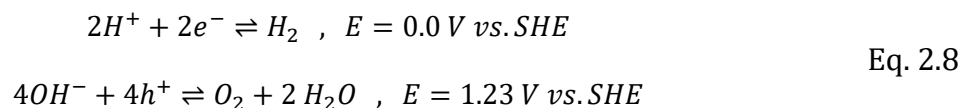
Figure 2.14. Experimental setup used for cyclic voltammetry and chronoamperometry measurements of photocathodes. To exclude additional signals resulting from the reduction of dissolved oxygen in the aqueous electrolyte, the electrochemical chamber is closed and constantly purged with nitrogen or argon.

To avoid any additional current signals resulting from the reduction of dissolved oxygen, a custom built photoelectrochemical cell (Figure 2.14) was used for the characterization of photocathode materials. This cell is closed and purged with nitrogen or argon 30 minutes prior to each measurement. During measurements, the purging is continued at a moderate rate. The sample inside

the PEC cell can be illuminated through an inset quartz glass window (*Präzisions Glas & Optik GmbH*, UV-quality, thickness 2 mm) with an incident photon flux equivalent to the intensity of sunlight (10^{17} cm⁻² s⁻¹ for a 455 nm LED (*Thorlabs*) or 100 mW cm⁻² in case of an ASTM G173-03 air mass 1.5 global (AM1.5G, see Figure 2.10) solar simulator (*Solar Light Model 16S*) based on a 300 W Xe arc lamp and a suitable set of optical filters), which is calibrated at the sample's position using a certified *Fraunhofer* ISE silicon reference cell with a KG5 IR-cutoff filter prior to each measurement. If all undesirable side reactions are excluded, the sample can be investigated with a wide range of experimental procedures that are described in the following.

2.6.1 Cyclovoltammetry and Chronoamperometry

Cyclovoltammetry is a widely applied technique to investigate electrochemical reactions. The to-be-investigated material, which is used as working electrode, is connected to a potentiostat/galvanostat (*Metrohm μAutolab III* or *PGStat302N*) in a three-electrode setup, together with a reference electrode and a counter electrode (Figure 2.14). This way, a changing potential within a defined range versus the reference electrode can be applied. While the potential is varied with a set scan speed, the resulting current is recorded and evaluated with a PC running the corresponding software program *Nova 1.11*. From the resulting *I-V* curve, the electrochemical potential of a reduction or oxidation reaction and its specific activity can be determined. In order to characterize the activity of photoelectrodes, a sufficient potential range around the theoretical potential of the expected reaction is chosen (Eq. 2.8).



The cyclovoltammetry measurement is then performed in the dark and under illumination. The resulting photocurrent can be calculated by subtracting the dark current from the current under illumination at the same potential. The photocurrent is a benchmark for the activity of a sample under incident light as it is directly proportional to the amount of evolved product. In a chronoamperometry measurement, a constant potential is applied on the working electrode and the current is recorded for a certain timescale with defined increment. This type of measurement is typically used to investigate the stability of photoelectrodes, but it is as well used to drive the to-be-investigated reaction in case of incident-photon-to-current efficiency (IPCE) or hydrogen evolution measurements.

Photoelectrochemical Analysis

2.6.2 Incident Photon to Current Efficiency

The incident-photon-to-current efficiency (IPCE), the ratio of generated photocurrent density J_{WE} and the incident photon flux Φ (Eq. 2.9), is an important parameter for the characterization of photoelectrodes.

$$IPCE(\lambda) = \frac{J_{WE}(\lambda)}{q\phi(\lambda)} \quad \text{Eq. 2.9}$$

During an IPCE measurement, a chronoamperometric measurement is performed at a static potential in the previously described three-electrode setup. For the determination of realistic IPCE values, two distinct light sources are needed. The photoelectrode is constantly illuminated by a white light source (AM1.5G solar simulator) combined with an OD 3.0 filter to reduce the intensity to 0.1 mW cm^{-2} at the photoelectrode's surface.

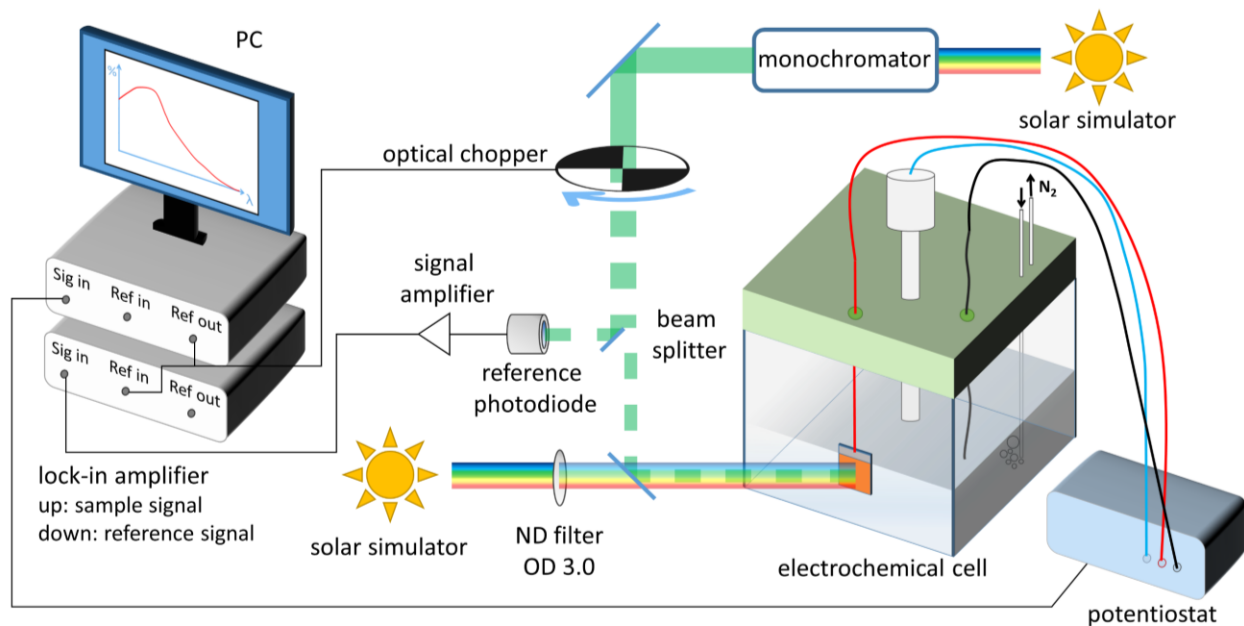


Figure 2.15. Experimental setup for an incident-photon-to-current efficiency measurement, which allows a wavelength-dependent quantification of photocurrent with respect to the incident photon flux.

The sample is simultaneously illuminated by monochromatic light, which is obtained from a 150 W Xe short arc lamp (*LOT Oriel*) combined with a monochromator (*Horiba microHR*). Its wavelength can be varied in a defined step size to determine the IPCE over the whole visible spectrum. If no additional

white light is used, the recorded IPCE values might be lower than they actually are, as semiconductors behave very differently in the dark and under illumination. The monochromatic light is chopped at a certain frequency (typically 1 Hz for PEC applications) and induces an additional current response J_{WE} in the chronoamperometric measurement, which can be very little compared to the absolute photocurrent. The setup used for all IPCE measurements of this work was built up by Florian Auras as part of his PhD thesis.²⁷ A schematic illustration of this setup is shown in Figure 2.15, where a combination of two lock-in amplifiers is used. One half of the monochromatic light intensity is selected by a beam splitter, detected by a reference diode analyzed by the first lock-in amplifier by taking the frequency input from the optical chopper into account. A second lock-in amplifier uses this signal to extract the time-depending current signal from the potentiostat. The resulting signal is then evaluated by a LabView program running on a connected PC. This program calculates the $IPCE$ from the photocurrent J_{ref} , which is produced by a photodiode with known $IPCE_{ref}$ (Eq. 2.10).

$$IPCE(\lambda) = \frac{J_{WE}(\lambda)}{J_{ref}(\lambda)} IPCE_{ref}(\lambda) \quad \text{Eq. 2.10}$$

2.6.3 Hydrogen detection

The hydrogen produced by photocathode materials can be detected with the described setup (Figure 2.16) to verify that the observed photocurrent results from the reduction of water. Here, a micro sensor (*Unisense A/S H₂-NPLR*) with a hydrogen-selective silicone membrane was combined with a three-electrode setup. The micro sensor was calibrated in a two-point measurement using the corresponding program (*Unisense A/S SensorTrace 1.4*). The data point for $c(\text{H}_2) = 0$ mM was acquired in nitrogen-purged electrolyte (typically aqueous 0.1 M Na₂SO₄ solution at pH 7), while the second measuring point of $c(\text{H}_2) = 40.7$ mM was recorded in the same electrolyte purged with forming gas (5 vol% H₂ in Ar, *AirLiquide ARCAL15*) for 20 minutes, taking in account the saturation concentration of pure H₂ gas in water of 813 μM atm⁻¹²⁸ and the partial pressure of hydrogen in the forming gas. To minimize the electrolyte volume and therefore maximize the detectable hydrogen concentration, a 2 mL polymethylmethacrylate (PMMA) cuvette was used as PEC cell. The working electrode was glued on a drilled-in hole (Ø 7 mm) and connected to the potentiostat together with a platinum wire counter electrode and a Hg/Hg₂SO₄/K₂SO₄ (sat.) reference electrode. The hydrogen micro sensor was placed in the cuvette, which was subsequently sealed using modelling clay. As the polarization of the

References

micro sensor is very sensitive and critical for a correct measurement, no magnetic stirring is possible in order to avoid any interfering signals.

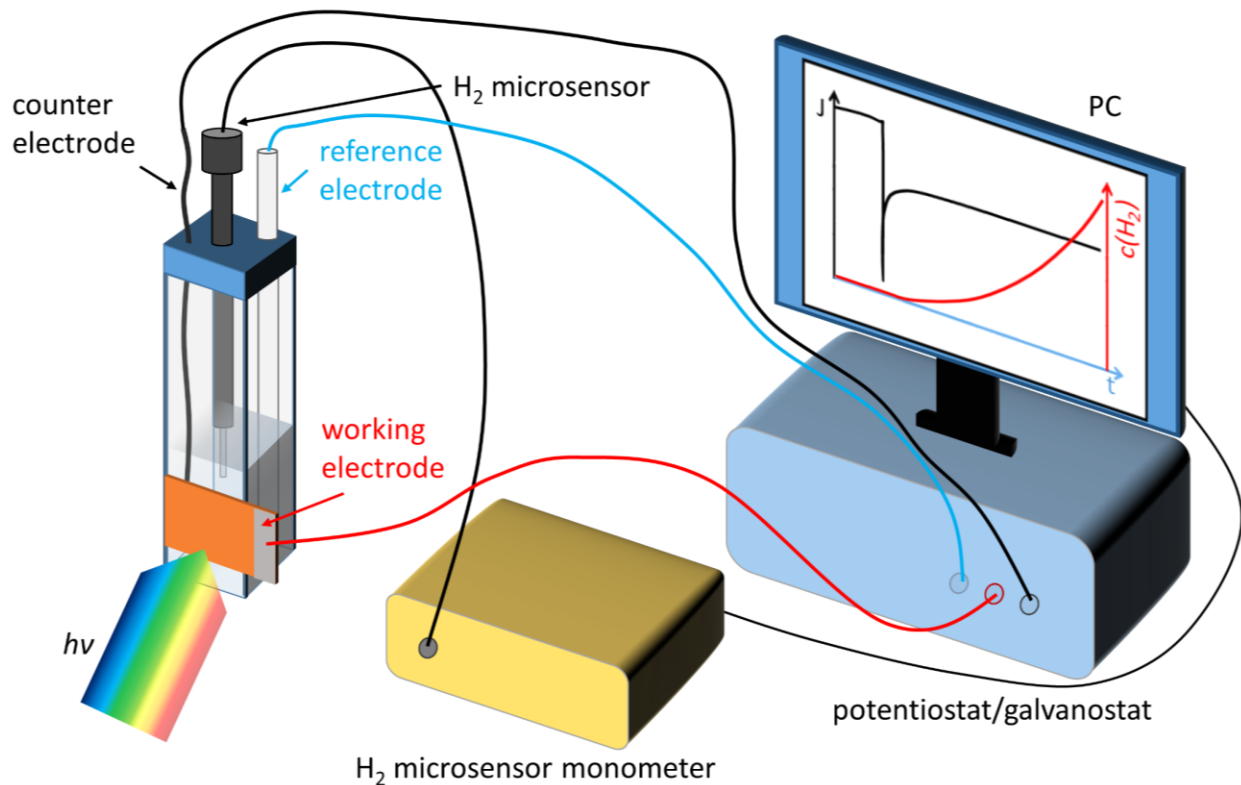


Figure 2.16. The concentration of hydrogen dissolved in the electrolyte, which is produced under illumination during a chronoamperometry measurement, can be quantified with a needle sensor equipped with a hydrogen selective silicon membrane.

2.7 References

- (1) Prandl, W., Walter Borchardt-Ott: Kristallographie: Eine Einführung für Naturwissenschaftler. 3. überarbeitete und erweiterte Auflage, Springer-Verlag, Berlin, Heidelberg 1990, ISBN 3-540-52931-4, 265 Seiten, brosch., Preis: DM 34. *Berichte der Bunsengesellschaft für physikalische Chemie* **1992**, 96 (3), 521-522.
- (2) Bragg, W. H., X-rays and Crystals. *Nature* **1912**, 90 (2243), 219-219.
- (3) Bragg, W. L., The Analysis of Crystals by the X-ray Spectrometer. *Proceedings of the Royal Society of London. Series A, Containing Papers of a Mathematical and Physical Character* **1914**, 89 (613), 468-489.
- (4) David Brandon, W. D. K., *Microstructural Characterization of Materials, 2nd Edition*. John Wiley and Sons, Ltd: 2008.

- (5) Schwarzenbach, D., *Crystallography*. Wiley: Chichester, 1996.
- (6) Inorganic Crystal Structure Database. <https://icsd.fiz-karlsruhe.de/> (accessed 13.09.2019).
- (7) Patterson, A. L., The Scherrer Formula for X-Ray Particle Size Determination. *Physical Review* **1939**, *56* (10), 978-982.
- (8) Peter Debye, P. S., Interferenzen an regellos orientierten Teilchen im Röntgenlicht. *Nachrichten von der Gesellschaft der Wissenschaften zu Göttingen, Mathematisch-Physikalische Klasse* **1916**, 1-15.
- (9) Brentano, J., Focussing method of crystal powder analysis by X-rays. *Proceedings of the Physical Society of London* **1924**, *37* (1), 184-193.
- (10) Jens Als-Nielsen, D. M., *Elements of Modern X-ray Physics*. Wiley: Chichester, 2011.
- (11) Metzger, T. H.; Mintova, S.; Bein, T., Nanoscale crystal orientation in silicalite-1 films studied by grazing incidence X-ray diffraction. *Microporous and Mesoporous Materials* **2001**, *43* (2), 191-200.
- (12) Knoll, M.; Ruska, E., Das Elektronenmikroskop. *Zeitschrift für Physik* **1932**, *78* (5), 318-339.
- (13) Kisielowski, C.; Freitag, B.; Bischoff, M.; van Lin, H.; Lazar, S.; Knippels, G.; Tiemeijer, P.; van der Stam, M.; von Harrach, S.; Stekelenburg, M.; Haider, M.; Uhlemann, S.; Müller, H.; Hartel, P.; Kabius, B.; Miller, D.; Petrov, I.; Olson, E. A.; Donchev, T.; Kenik, E. A.; Lupini, A. R.; Bentley, J.; Pennycook, S. J.; Anderson, I. M.; Minor, A. M.; Schmid, A. K.; Duden, T.; Radmilovic, V.; Ramasse, Q. M.; Watanabe, M.; Erni, R.; Stach, E. A.; Denes, P.; Dahmen, U., Detection of Single Atoms and Buried Defects in Three Dimensions by Aberration-Corrected Electron Microscope with 0.5-Å Information Limit. *Microscopy and Microanalysis* **2008**, *14* (5), 469-477.
- (14) McMullan, D., Scanning electron microscopy 1928–1965. *Scanning* **1995**, *17* (3), 175-185.
- (15) Goldstein, J.; Newbury, D. E.; Joy, D. C.; Lyman, C. E.; Echlin, P.; Lifshin, E.; Sawyer, L.; Michael, J. R., *Scanning Electron Microscopy and X-Ray Microanalysis, Third Edition*. Springer US: 2003.
- (16) Cao, G., *Nanostructures & Nanomaterials - Synthesis, Properties & Applications*. 2004.
- (17) Gao, G., *Nanostructures & Nanomaterials*. Imperial College Press: London, 2004.
- (18) Seah, M. P.; Dench, W. A., Quantitative electron spectroscopy of surfaces: A standard data base for electron inelastic mean free paths in solids. *Surface and Interface Analysis* **1979**, *1* (1), 2-11.
- (19) Levsen, K., Physikalische Methoden in der Chemie: ESCA. *Chemie in unserer Zeit* **1976**, *10* (2), 48-53.

References

- (20) Prévot, M. S.; Sivula, K., Photoelectrochemical Tandem Cells for Solar Water Splitting. *The Journal of Physical Chemistry C* **2013**, *117* (35), 17879-17893.
- (21) Janáky, C.; Rajeshwar, K.; de Tacconi, N. R.; Chanmanee, W.; Huda, M. N., Tungsten-based oxide semiconductors for solar hydrogen generation. *Catalysis Today* **2013**, *199*, 53-64.
- (22) Klahr, B. M.; Martinson, A. B.; Hamann, T. W., Photoelectrochemical investigation of ultrathin film iron oxide solar cells prepared by atomic layer deposition. *Langmuir* **2011**, *27* (1), 461-8.
- (23) Tauc, J., Optical properties and electronic structure of amorphous Ge and Si. *Materials Research Bulletin* **1968**, *3* (1), 37-46.
- (24) Hesse, M.; Meier, H.; Zeeh, B., *Spektroskopische Methoden in der organischen Chemie*. Georg Thieme Verlag: 2005.
- (25) Nelson, J. H., *Nuclear Magnetic Resonance Spectroscopy*. Prentice Hall: 2003.
- (26) Michigan State University: Proton and Carbon Chemical Shift Ranges. <https://www2.chemistry.msu.edu/faculty/reusch/orgpage/nmr.htm> (accessed 06.09.2019).
- (27) Auras, F. Solar Light Harvesting with Nanostructured Organic and Hybrid Photovoltaic Devices. Dissertation, Ludwig-Maximilians-Universität München, **2013**.
- (28) Wiesenburg, D. A.; Guinasso, N. L., Equilibrium solubilities of methane, carbon monoxide, and hydrogen in water and sea water. *Journal of Chemical & Engineering Data* **1979**, *24* (4), 356-360.

3 Sn-doped hematite for photoelectrochemical water splitting: the effect of Sn concentration

This chapter is based on the following publication:

Siyuan Zhang,[‡] Hamidreza Hajiyani,[‡] Alexander G. Hufnagel,[‡] **Jonathan Kampmann**, Benjamin Breitbach, Thomas Bein, Dina Fattakhova-Rohlfing, Rossitza Pentcheva and Christina Scheu, *Zeitschrift für Physikalische Chemie*, **2019**.

[‡] These authors contributed equally to this work.

Link to the published article: <https://doi.org/10.1515/zpch-2019-1482>

©2020 Christina Scheu et al., published by De Gruyter, Berlin/Boston. This work is licensed under the Creative Commons Attribution 4.0 Public License.

Jonathan Kampmann evaluated the optical absorbance data as well as the aqueous photoelectrochemistry experiments and wrote the corresponding parts of the manuscript.

Abstract

Abstract

Hematite-based photoanodes have been intensively studied for photoelectrochemical water oxidation. The *n*-type dopant Sn has been shown to benefit the activity of hematite anodes. We demonstrate in this study that Sn-doped hematite thin films grown by atomic layer deposition can achieve uniform doping across the film thickness up to at least 32 mol%, far exceeding the equilibrium solubility limit of less than 1 mol%. On the other hand, with the introduction of Sn doping, the hematite crystallite size decreases and many twin boundaries form in the film, which may contribute to the low photocurrent observed in these films. Density functional theory calculations with a Hubbard *U* term show that Sn doping has multiple effects on the hematite properties. With increasing Sn⁴⁺ content, the Fe²⁺ concentration increases, leading to a reduction of the band gap and finally to a metallic state. This goes hand in hand with an increase of the lattice constant.

3.1 Introduction

Hematite ($\alpha\text{-Fe}_2\text{O}_3$) has long been studied for photoelectrochemical (PEC) water oxidation¹⁻¹⁶. It has a suitable band gap of ~ 2.1 eV for solar light absorption, a high absorption coefficient and an adequate band alignment to drive the demanding water oxidation reaction². The fundamental limit of hematite, like many other transition metal oxides, is its poor conductivity. Both types of charge carriers, electrons and holes, are highly localized in space, and transport occurs by a phonon-assisted polaron mechanism. For *n*-type hematite photoanodes, the minority carrier hole has a diffusion length of only 2-4 nm³ and is hence very prone to recombination. Therefore, only the photogenerated holes originating in the top few nanometers of a hematite layer can reach the interface for the water oxidation reaction.

Nanostructuring hematite photoanodes^{2,4-7} is a common strategy to remedy the limited hole diffusion length by providing a shorter transport path for the photogenerated holes to reach the interface. Nevertheless, it is difficult to design nanostructures with a critical dimension matching the hole diffusion length. In addition, the conductivity may be further compromised by the surface and by crystallographic defects in the bulk⁶, and quantum confinement may alter the band structure and alignment⁷.

Another possibility is to improve the transport properties of hematite by substituting other elements⁸, such as Al, Si, Ti, Cr, Ni, Cu, Zn, Zr, Nb, Mo, Sn, Pt, as has been summarized in a previous report⁹. In a recent study, Sn doping was demonstrated to have the highest photocurrent and the lowest

photovoltage onset among other commonly studied *n*-type dopants¹⁰. Improving the *n*-type conductivity in a photoanode not only improves the current collection through the FTO substrate, but also reduces the probability of recombination with holes. It is noteworthy that Sn has either been doped into hematite by the addition of a chemical precursor⁹⁻¹², or through diffusion from the fluorine doped tin oxide (FTO) substrate via annealing at high annealing temperatures¹³⁻¹⁵. In our recent study¹⁶, we have identified two beneficial effects of Sn in the hematite lattice. Sn-doped hematite with < 20 nm thickness has been fabricated by atomic layer deposition (ALD), which is ultrathin and yet capable of absorbing 44% of the incident solar photons with an energy above the band gap. By introducing Sn doping at different locations of the films, it has been established that Sn doping on the surface and in the ~5 nm subsurface volume has a beneficial effect on the transport properties. In combination with first principles electronic structure calculations, Sn doping on the surface was shown to improve the interface activity by passivating surface trap states, while the subsurface doping was responsible for an improved charge separation by inducing a band edge gradient. In contrast, doping Sn throughout the thickness of the film does not translate to improved efficiency.

For screening the effect of doping elements, the doping concentration rarely exceeds 1 – 5 mol%. One practical constraint is the solubility of foreign atoms in the hematite structure⁸. For example, SnO₂ has a very limited solubility in hematite, less than 1 mol% below 800 °C¹⁷. A higher solubility of 6 mol%¹⁸ and 20 mol%¹⁷ of SnO₂ has been demonstrated in hematite nanoparticles, which found applications in the gas sensor industry¹⁷. ALD is a powerful technique to deposit films that are far from their thermal equilibrium. In this study, we demonstrate that Sn can be incorporated into the hematite crystal structure at a concentration as high as 32 mol%. Hematite thin films with 6, 14, and 32 mol% Sn concentrations were studied by X-ray diffraction (XRD), scanning transmission electron microscopy (STEM) and spectroscopy, and their structural and electronic characteristics were correlated to density functional theory (DFT) calculations. The photocurrents derived from hematite photoanodes peak at low Sn concentration, and vanish as the Sn concentration exceeds 32 mol%.

3.2 Experimental

3.2.1 Preparation of photoanodes

The oxide films were deposited on FTO-coated glass substrates (Pilkington, 7 Ω per square), prepared by successive sonication in Extran (Merck) solution, ultrapure water (MilliQ, 18.2 MΩ cm), and 2-propanol for 15 min and drying in a stream of nitrogen. Single side polished Si(100) wafers (Siltronic

Experimental

AG) were used as substrates for microstructural characterization (section 3.2.2). Ferrocene (Aldrich, 98%) was purified by sublimation prior to use.

A Picosun R-200 Advanced ALD system was used for all depositions. The chamber temperature was 250 °C at a pressure of approximately 10 hPa. Nitrogen (Air Liquide, 99.999 %) was used at a constant flow rate of 100 sccm per precursor feed line and 150 sccm for the reactor chamber as a carrier and purge gas. Hematite was deposited by alternating between exposures to ferrocene, kept in a stainless steel cylinder at 90 °C, and ozone, produced by an INUSA AC2025 ozone generator fed with 1 vol% N₂ in O₂ (Air Liquide, 99.9995%). One full cycle consisted of a 1 s ferrocene pulse, 6 s purge, 6 s ozone pulse and a final 8 s purge. Tin oxide was deposited from SnCl₄ (SAFC electronic grade) and MilliQ water, both kept in stainless steel cylinders at 18 °C. One deposition cycle consisted of a 0.1 s SnCl₄ pulse, 6 s purge, 15 s water pulse and final 8 s purge. Mixed oxide films were prepared interspersing one cycle of tin oxide after every N cycles of hematite, resulting in films with an ALD cycle ratio of the two oxides of 1 : N , which is used to identify samples throughout this study. This was done by alternating between N hematite deposition cycles and one tin oxide cycle until 1000 hematite cycles were reached, then capping with another N hematite cycles. A thicker pure hematite film was grown for structural characterization using 1600 cycles, consisting of a 1.5 s ferrocene pulse, 7 s static exposure and 8 s purge, followed by a 6 s ozone pulse, 7 s static exposure and 8 s purge. After deposition, the films were annealed in air at 600 °C for 30 min with a heating rate of 3.2 °C/min, and then cooled naturally to room temperature.

Higher Sn concentration is achieved by higher ALD cycle ratios 1 : N , i.e., lower number of hematite cycles, N , in between the tin oxide cycles. The ALD growth rate of hematite using the chemistry above are approximately 0.025 nm/cycle. However, the growth rate of doped films can deviate significantly, as hematite and tin oxide undergo heterogeneous nucleation on each other, which may be subject to delaying or promoting effects of the substrate.

3.2.2 Microstructural Characterization

XRD was performed using a Rigaku SmartLab 9 kW X-ray diffractometer with a Cu-K α (1.54056 Å) radiation source produced at 45 kV and 200 mA, a parallel beam optic and an energy-dispersive line detector. The in-plane 2θ scan was configured using the 5-circle goniometer with a scan speed of 2°/min and 0.12° per 2θ step. For the in-plane diffraction, both the incident and diffracted beams are nearly parallel to the sample surface, so that the penetration depth of the beam is within 100 nm of

the surface. The technique measures lattice planes that are nearly perpendicular to the sample surface. Simulation of the X-ray pattern was performed using the Bruker TOPAS software for the fundamental parameter fit (Pawley method). Pole figures of hematite thin films were recorded on a Seifert Theta/Theta diffractometer with a Co-K α (1.78897 Å) radiation source produced at 40 kV and 30 mA, a parallel beam optic and an energy-dispersive point detector.

Further microstructure characterization was conducted in a Titan Themis microscope operated at 300 kV. Aberration correction of the probe-forming lenses enables a probe size of < 1 Å and a convergence semi-angle of 23.8 mrad. High angle annular dark field (HAADF) and annular bright field (ABF) micrographs were collected using annular detectors with collection semi-angles in the range of 73-200 mrad and 8-16 mrad, respectively. Energy dispersive spectroscopy (EDS) was done using a SuperX Si drift detector. Elemental quantification was performed using the Bruker Espirit software by the standardless Cliff-Lorimer method. Electron energy loss spectroscopy (EELS) was conducted using a Gatan Quantum ERS spectrometer operated in the image-coupled mode with a collection semi-angle up to 35 mrad.

3.2.3 Optical Characterization

UV-Vis absorption data of hematite film electrodes were obtained on a Perkin Elmer Lambda 1050 UV/Visible/NIR spectrophotometer combined with an integrating sphere. The intrinsic absorbance of the films was calculated by applying an expression derived by Klahr et al.¹⁹, which corrects for substrate absorption as well as substrate and film reflectance.

3.2.4 Photoelectrochemistry

PEC measurements were performed in a 20 cm³ optical glass three-electrode cell with 0.1 M NaOH as the electrolyte. The oxide film was masked with poly-tetrafluoroethene adhesive tape to limit the exposed area to 0.159 cm², contacted with silver paste and used as the working electrode. For cyclic voltammetry (CV) measurements, the film was connected as working electrode to a Metrohm PGStat302N potentiostat. Additionally, a Pt wire counter electrode and a saturated Ag/AgCl reference electrode (Sigma Aldrich, 0.197 V vs. standard hydrogen electrode) were used to apply defined potential sweeps and to record the resulting current in a three electrode setup. CV measurements were performed at a scan rate of 20 mV s⁻¹. The potential vs. reversible hydrogen electrode (RHE) in V was calculated from the measured potential vs. Ag/AgCl at pH = 13 according to the equation:

Results and Discussion

$$\left(\frac{V_{RHE} - V_{Ag/AgCl}}{V}\right) = 0.197 + 0.059 pH$$

The film was illuminated from the front side by a blue light emitting diode (Thorlabs, 455 nm). The flux incident on the electrode was set to be 10^{17} cm⁻² s⁻¹ at the sample position prior to each measurement using a certified Fraunhofer ISE silicon reference cell with a KG5 IR-cutoff filter.

3.2.5 Computational details

DFT calculations were carried out with the VASP code, which uses the projected augmented wave (PAW) method, and pseudopotentials²⁰⁻²³. We also adopted the generalized-gradient approximation (GGA-PBE96)²⁴ for the exchange correlation functional and an effective Hubbard value $U - J = 4.3$ eV to describe static electronic correlations of the *3d* states of Fe using Dudarev's approach²⁵. For converged results, we used a plane-wave cut-off of 500 eV and a Monkhorst-Pack *k*-point mesh of $7 \times 7 \times 4$ ²⁶. A full relaxation of the unit cell and the ionic positions was performed until the residual forces were less than 0.01 eV Å⁻¹.

3.3 Results and Discussion

3.3.1 Atomic Layer Deposition of Sn-doped Hematite

3.3.1.1 Phase

Hematite has a trigonal structure (space group R-3c, number 167), an isostructure to corundum (α -Al₂O₃). The hexagonal unit cell is conventionally used, so are the hexagonal Miller-Bravais indices (*h, k, i, l*) to label the diffraction. We use the full 4 indices in this manuscript, whereas most studies omit the dummy index $i = -h - k$. Note however, the rhombohedral index also uses 3 indices, but they are defined using the rhombohedral unit cell. The conversion between the 2 systems of the low-index lattice planes is listed in Table 3.1.

XRD characterization was conducted on the ultrathin hematite films grown on flat Si(100) substrates. A fiber texture has been demonstrated for undoped hematite¹⁶ with the plane normal of Fe₂O₃ (0,0,0,6) (*c*-plane) parallel to the growth direction. In order to maximize the signal from the ultrathin films, we applied the in-plane diffraction geometry with grazing incidence, while collecting diffractions only from planes 90° to the growth direction due to the fiber texture. As shown in Table 3.1 and Figure 3.1a, the peaks observed in this geometry are all in-plane reflections, including (1,1,-2,0), (3,0,-3,0), and (2,2,-4,0).

Sn-doped hematite for photoelectrochemical water splitting: the effect of Sn concentration

Table 3.1: Conversion between the hexagonal Miller-Bravais index and the rhombohedral index of the low-index hematite planes, and their inclination angles to the *c*-plane normal (growth direction of the fiber textured film). The in-plane reflections are highlighted in bold.

2θ (°)	Plane spacing (Å)	Hexagonal index	Rhombohedral index	Inclination to the growth direction (°)
24.0	3.70	(0,1,-1,2)	(1,1,0)	58
33.0	2.71	(1,0,-1,4)	(2,1,1)	38
35.4	2.53	(1,1,-2,0)	(1,0,-1)	90
39.0	2.30	(0,0,0,6)	(2,2,2)	0
40.6	2.22	(1,1,-2,3)	(2,1,0)	61
43.3	2.09	(2,0,-2,2)	(2,0,0)	72
49.2	1.85	(0,2,-2,4)	(2,2,0)	58
53.7	1.70	(1,1,-2,6)	(3,2,1)	42
57.1	1.61	(1,2,-3,2)	(2,1,-1)	77
57.2	1.61	(0,1,-1,8)	(3,3,2)	22
62.1	1.49	(2,1,-3,4)	(3,1,0)	64
63.6	1.46	(3,0,-3,0)	(2,-1,-1)	90
69.1	1.36	(2,0,-2,8)	(4,2,2)	38
71.5	1.32	(1,0,-1,10)	(4,3,3)	18
71.8	1.31	(1,1,-2,9)	(4,3,2)	31
75.0	1.27	(2,2,-4,0)	(2,0,-2)	90

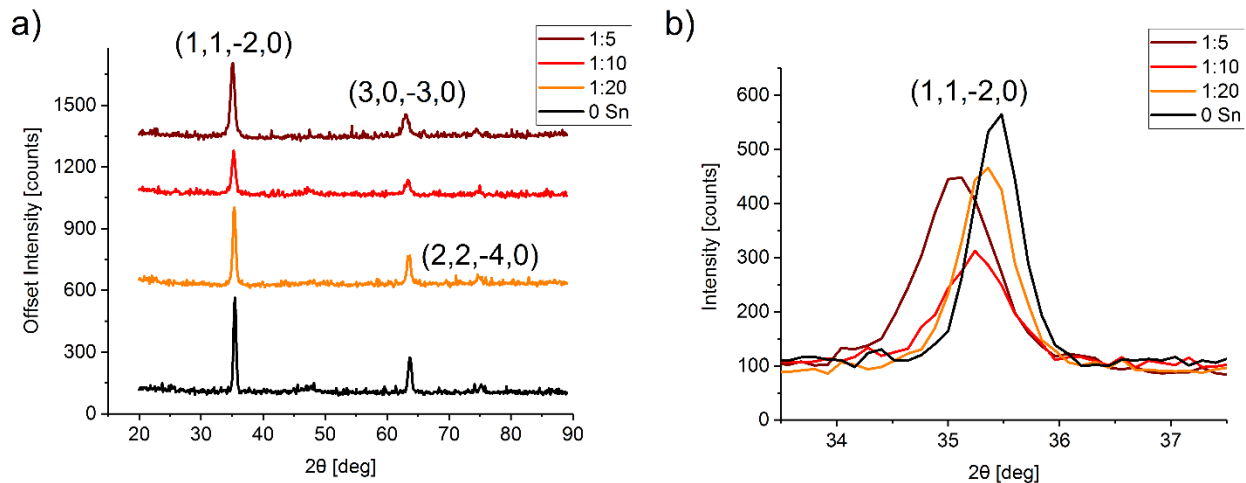


Figure 3.1:(a) In-plane XRD of Sn-doped hematite with various ALD cycle ratios and (b) the enlarged view on the (1,1,-2,0) reflection.

Results and Discussion

As the concentration of Sn increases, no new reflections have been identified. This may suggest the absence of crystalline phases other than hematite, but cannot exclude the formation of crystalline phases with a different texture and hence not contributing to in-plane diffraction. The (1,1,-2,0) reflection shifts monotonically to the left as the Sn concentration increases, indicating an expansion of the lattice parameter a , which is summarized in Table 3.2.

3.3.1.2 Chemical composition

The chemical composition of the thin films and their homogeneity were studied by EDS and EELS in STEM. It has been noted in our earlier study 28 that due to the fluorescence artefact of Sn from the FTO substrate, EDS is inappropriate to quantify small amounts of Sn in the hematite thin film. In this study, we quantify Sn in the hematite films grown on the Si(100) substrate so that the fluorescence artefact is no longer a concern. As shown in Table 3.2, the Sn concentration increases as the ALD cycle ratio of 1 cycle of SnO₂ per N cycles of Fe₂O₃ (abbreviated 1: N) increases, i.e., tin oxide layers are separated by fewer layers of iron oxide. A high Sn concentration of 32 mol% is reached at the ratio of 1:5, approximating to the chemical formula SnFe₂O_x. Even at this composition, a homogeneous distribution of Fe and Sn throughout the film thickness is evidenced in Figure 2.2b, and there is no indication of a second phase. Homogeneous doping of Sn is further evidenced by the monotonous expansion of the in-plane lattice parameter a . With the Sn concentrations evaluated by EDS, a linear expansion of a is evaluated as 0.03% per mol% of Sn. This is comparable to the evaluation from Sn-doped hematite nanoparticles¹⁷ where both lattice parameters a and c expand by 0.02% per mol% of Sn.

Table 3.2: Summary of Sn-doped hematite thin films with various ALD cycle ratios: Chemical composition (EDS), lattice parameters (XRD), chemical shift of Fe-L₃ edge (EELS) and the deduced Fe²⁺ concentration.

ALD cycle ratio	Sn (mol%) **	a (Å)	Fe-L ₃ edge (eV) *	Fe ²⁺ (mol%) **
0	0	5.0629 ± 0.0006	710.22 ± 1.37	0
1:20	6	5.0766 ± 0.0007	710.12 ± 1.47	6
1:10	14	5.0893 ± 0.0013	710.08 ± 1.74	8
1:5	32	5.1129 ± 0.0010	710.02 ± 1.57	12

* The notation ± in this column does not refer to uncertainty, rather the width (1 standard deviation) of the peak from a Gaussian profile fitting. ** A relative error of ±5% can be considered as a systematic error from Cliff-Lorimer quantification of Sn. An absolute error of ±1 mol% can be taken for the quantification of Fe²⁺, considering a pixel-precision, 0.05 eV, of the Fe-L₃ edge.

Sn-doped hematite for photoelectrochemical water splitting: the effect of Sn concentration

The incorporation of Sn is further evidenced by the EELS Sn-M_{4,5} edge (Figure 3.2c) and the effect of Sn on the oxidation state of Fe. As discussed in a previous work, a shift of the EELS Fe-L₃ edge (Figure 3.2d) towards lower energy loss corresponds to the reduction of Fe³⁺. Integrating the EELS spectra from within Sn-doped hematite, a monotonic shift of the Fe-L₃ position is observed towards lower energy loss. This is in agreement with theoretical studies^{9, 16} that suggest that Fe atoms adjacent to substitutional Sn⁴⁺ atoms can be reduced to a Fe²⁺ state. In Sn-doped hematite, the Fe L₃ edge is a superposition of the Fe³⁺ and Fe²⁺ spectra. Hence, a shift of the peak centroid towards lower energy loss is expected together with a broadening of the profile, as shown in Figure 3.2c and Table 3.2. Fe³⁺ and Fe²⁺ minerals were characterized to have a 1.7 eV difference in the Fe-L₃ position²⁹. The fraction of Fe²⁺ ions was then obtained by linearly interpolating their peak chemical shift. As shown in Table 3.2, the Fe²⁺ concentration increases more moderately as the Sn concentration in hematite increases.

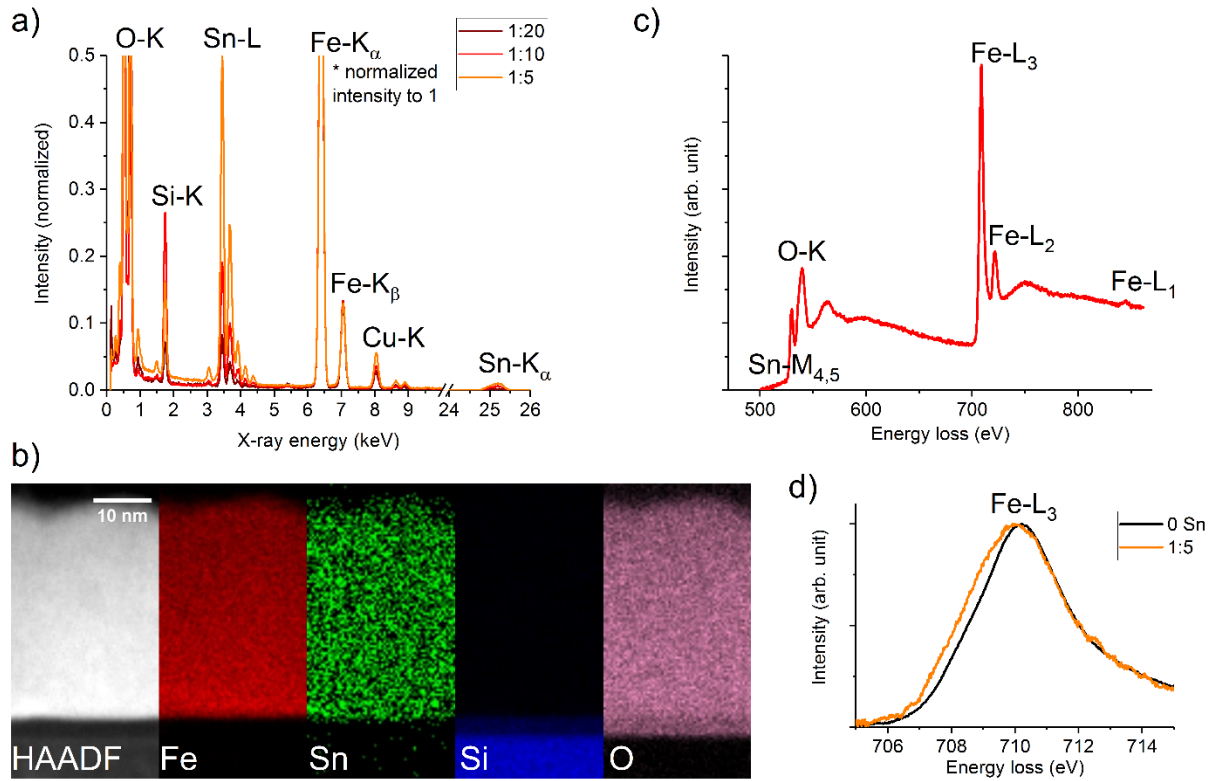


Figure 3.2: (a) EDS spectra of Sn-doped hematite thin films with various ALD cycle ratios and (b) EDS elemental maps of the film with an ALD cycle ratio 1:5. (c) EELS spectrum of the film with an ALD cycle ratio 1:20 after background subtraction and (d) the chemical shift of the Fe-L₃ edge between undoped hematite and Sn-doped hematite with an ALD cycle ratio 1:5.

Results and Discussion

3.3.1.3 Theoretical understanding from DFT+U calculations

To gain insight into the effect of higher Sn concentrations on the properties of hematite we have performed density functional theory calculations with a Hubbard U parameter. Three different Sn concentrations were selected: 8.33, 16.67 and 33.33 mol%. Different distributions were studied in the 30-atom unit cell for 16.67 and 33.33 mol%. Their respective lowest energy configurations are displayed in Figure 3.3, with their corresponding electronic properties including oxidation states of iron and the evolution of lattice parameters with Sn-concentration. In our previous work ¹⁶, we have shown that doping with a single Sn⁴⁺ ion in the 30-atom α -Fe₂O₃ unit cell (8 mol% doping, which is close to the experimental value of 6 mol% in Table 3.2) turns Fe³⁺ in the neighbouring cation layer to Fe²⁺. A similar effect was also previously observed for Ti-doped hematite ²⁷. The additional 3d-electron forms a localized band just below the Fermi-level (cf. density of states in Figure 3.3a). Analysis of oxidation states and electronic properties in Figure 3.3b-c shows that further increase of the Sn amount leads to a corresponding enhancement of the Fe²⁺ concentration (in line with the experimental measurement in Table 3.2) and reduction of the band gap. At 17 mol% Sn in Figure 3.3b, the localized band of one of the Fe²⁺ ions is close to the conduction band minimum. At 33 mol%, the Fermi level crosses the conduction band minimum and leads to n -type conductivity. The DFT+ U calculations render a monotonic increase of the lattice parameters and the volume (cf. Figure 3.3d). Overall the DFT+ U values are higher than in the experiments, likely due to the overestimation of lattice parameters typical for the GGA-PBE96 exchange correlation functional together with a Hubbard U correction. Moreover, while we have considered here substitutional doping of Sn, cation vacancies may also form to compensate the charge mismatch between Fe³⁺ and Sn⁴⁺ as an alternative to Fe³⁺ reduction.

Sn-doped hematite for photoelectrochemical water splitting: the effect of Sn concentration

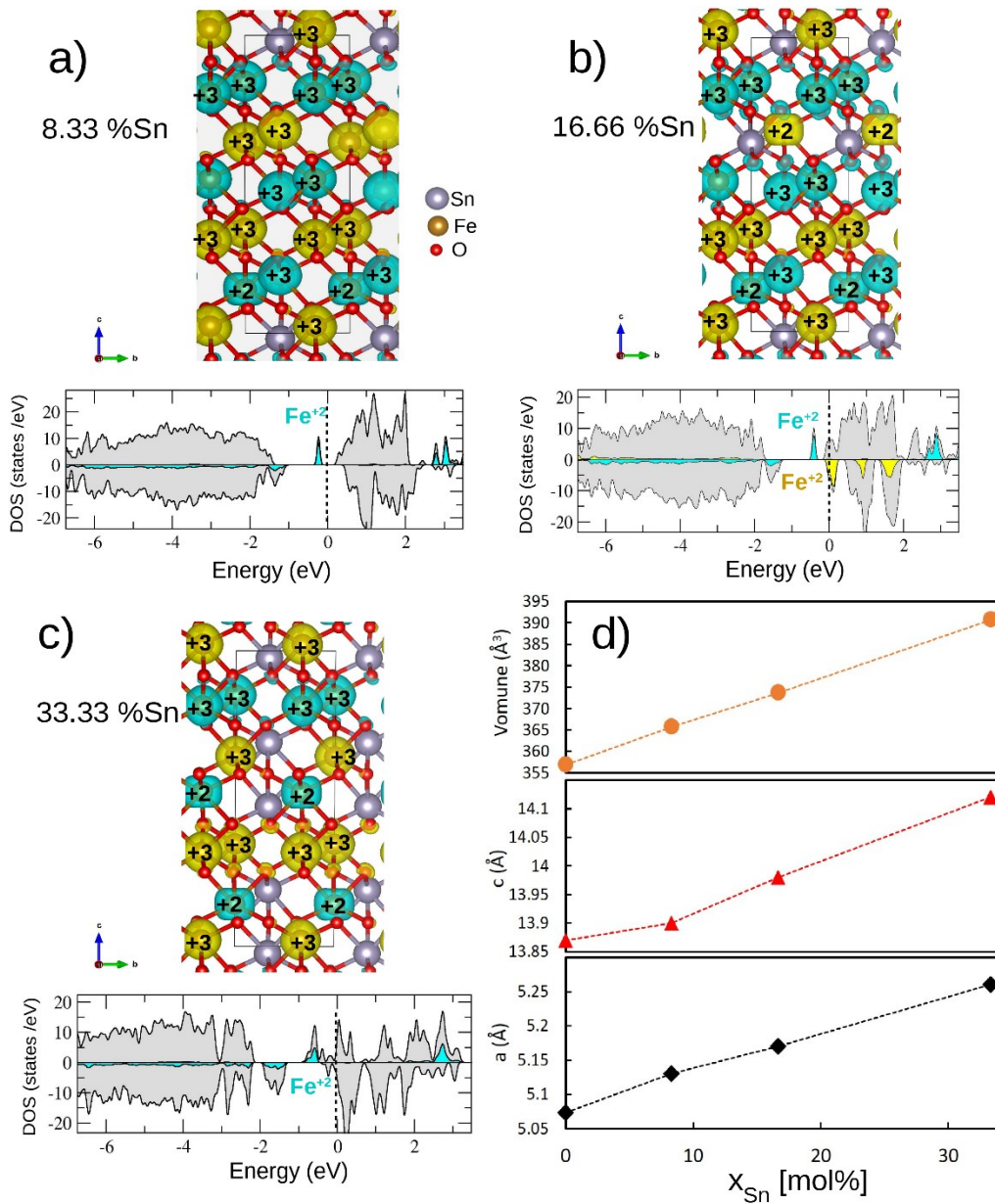


Figure 3.3: Side view and spin density of Sn-doped hematite with Sn concentration of a) 8.33, b) 16.67, and c) 33.33 mol%. Fe³⁺ (d5) and Fe²⁺ (d6) sites possess nearly spherical and flattened spin density, respectively. Fe, Sn, and O atoms are respectively marked by orange, grey, and red spheres. Majority and minority spin density is marked in yellow and cyan, respectively. The corresponding density of states shows a reduction of the band gap due to localized states in the gap related to the sixth electron at Fe²⁺. The partial density of states of Fe²⁺ is highlighted in yellow and cyan depending on the sign of the magnetic moment. d) Volume and lattice parameters of hematite as a function of Sn concentration.

Results and Discussion

3.3.2 Crystallinity of ALD Sn-doped hematite

In addition to the phase determination, we have applied XRD to study the crystallinity of the hematite thin films. It is noteworthy that in-plane diffraction is not suitable to quantify crystallinity as the grazing incidence geometry makes the measurement very sensitive to the surface alignment and its area. In our previous study¹⁶, we have relied on the Bragg-Brentano geometry (θ - 2θ scans) as well as out-of-plane pole figure measurements to evaluate the crystallinity. As shown in the (1,0,-1,4) pole figures (Figure 3.4), an apparent fiber texture is only observed in the hematite films without and with 6 mol% Sn. For the higher Sn concentrations, the pole figures become noisier, suggesting a decrease in the crystallinity.

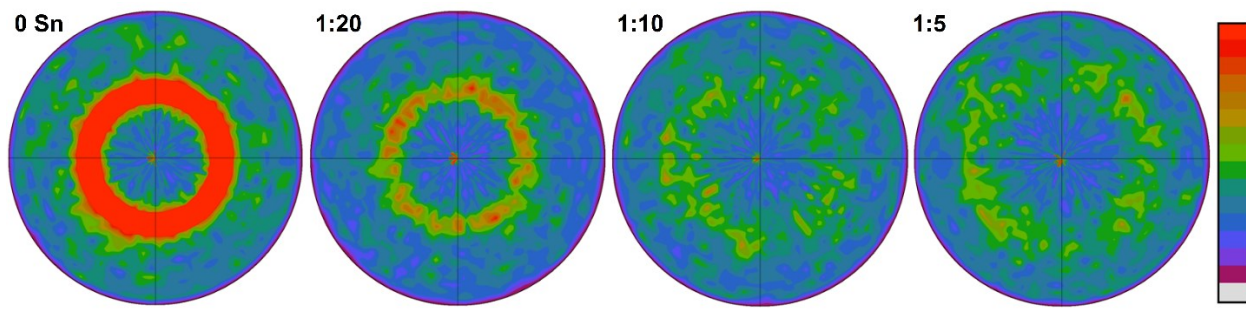


Figure 3.4: XRD (1,0,-1,4) pole figures of Sn-doped hematite thin films with various ALD cycle ratios.

In real space, the decrease in crystallinity is manifested by the decrease in grain sizes. As shown in the STEM micrograph (Figure 3.5a), the hematite thin films have columnar grains, and each grain has a vertical size equal to the film thickness. The surface termination is a (0,0,0,6) plane as evident in Figure 3.5b,c, which is in agreement with the XRD texture measurement. For the Sn-doped sample, however, many grains no longer span from the substrate to the surface, as shown by the highlighted grains in Figure 3.5d,g. Moreover, it is observed that many hematite grains have a twin relationship. As an example, Figure 3.5e shows the left and right grains in a twin relationship, whereas the middle part of the micrograph captures an overlapped area with both orientations. It is clear from the fast Fourier transform (FFT) pattern in Figure 3.5f that the twins have the mirror symmetry on the (0,0,0,6) as well as the (3,0,-3,0) planes. Finally, for the high Sn concentration at 32 mol%, even smaller hematite grains are observed. As the grain size is much below the thickness of the specimen, it is difficult to observe these grains in atomic resolution. Nevertheless, twins are evidenced by the

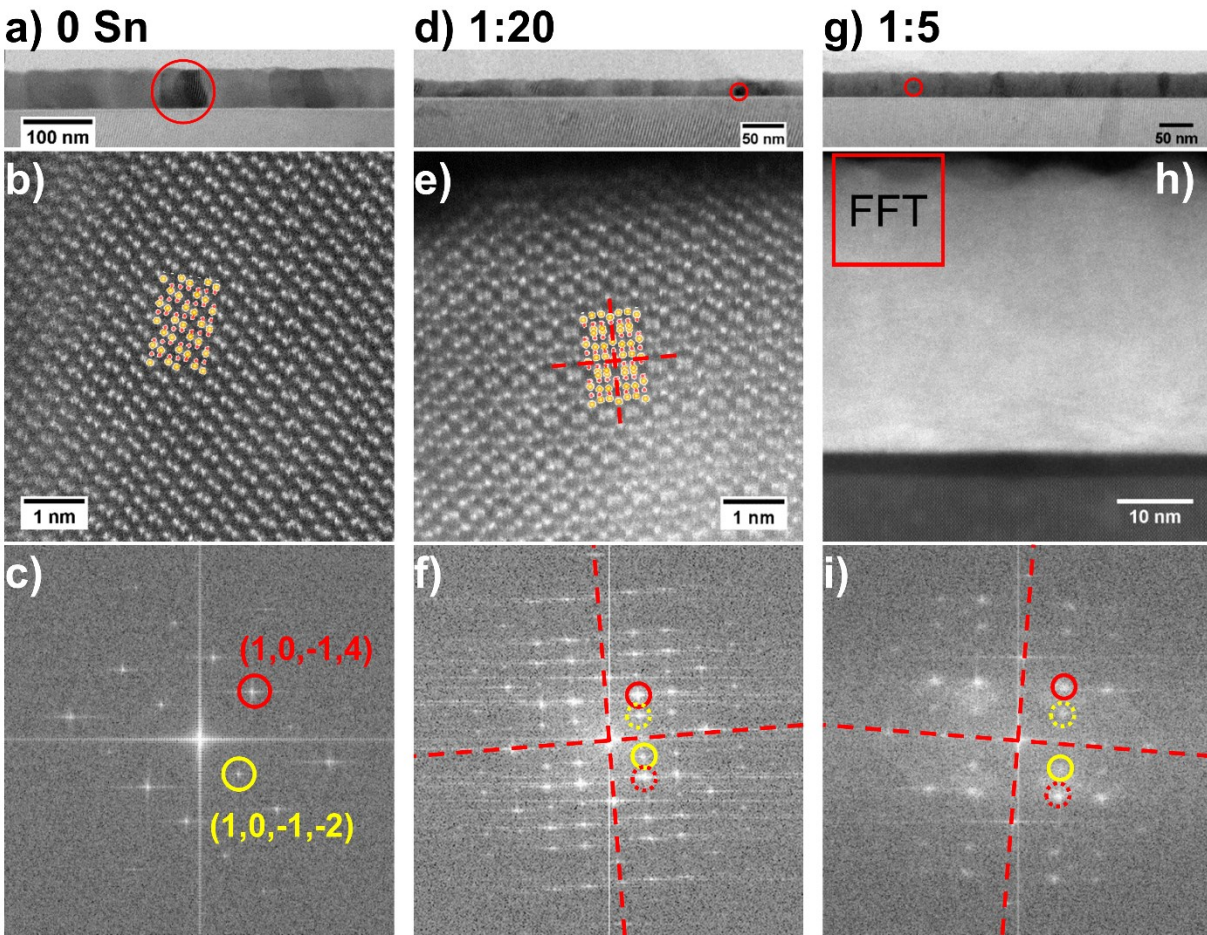


Figure 3.5: STEM images of hematite films (a,b,c) without Sn doping, (d,e,f) with 6 mol% Sn (ALD cycle ratio 1:20), and (g,h,i) with 32 mol% Sn (ALD cycle ratio 1:5). The first row shows ABF-STEM images to identify some individual grains as highlighted by the red circles. The second row shows atomic resolution HAADF-STEM images along the 1,-2,1,0 zone axis of hematite grains and twin boundaries. The atomic structure of hematite (Fe atoms in orange, O in red) and an overlaid twin are superimposed. The third row shows the FFT of their corresponding HAADF-STEM images with (1,0,-1,4) and (1,0,-1,-2) reflections marked by circles in red and yellow, and their twin variants marked by broken circles in their respective colors. The broken lines in (e,f,i) highlight the mirror symmetry of the twin.

FFT pattern in Figure 3.5i. As a common defect in hematite, twins are formed by dehydration of α -FeOOH³⁰, having a coherent boundary and a common oxygen sublattice.

Despite their chemical homogeneity, it is clear that the grains are smaller in the hematite films with higher Sn concentrations. This may be understood by the ALD process where the hematite layer deposition is more frequently interrupted by the SnO₂ deposition to realize higher Sn concentration. Nevertheless, the observed grain size is much bigger than the thickness of hematite deposition

Results and Discussion

between the SnO₂ deposition (< 1 nm). The calcination procedure is a determining factor to the crystallinity. A mild calcination temperature of 600 °C for 30 min was chosen for this set of samples, which has been demonstrated to promote short-range (~1 nm) diffusion to homogenize the Sn doping as well as to inhibit longer range diffusion¹⁶. While suitable for designing localized Sn doping profiles, such calcination does not result in highly crystallized films at higher Sn concentrations. Hematite has a melting point of 1565 °C. The temperatures during the ALD and the calcination processes do not exceed a homologous temperature of 0.5, which kinetically hinders the phase separation of oversaturated Sn.

Higher calcination temperatures of up to 800 °C¹³⁻¹⁵ have been reported to produce hematite thin film photoanodes on FTO substrates. Under these circumstances, however, Sn was found to diffuse into the hematite even from the FTO substrate^{13,15}. Long range diffusion may also cause unwanted Sn segregation as Sn has a low solubility in Fe₂O₃¹⁷. In a recent study on hematite sintered at 1300 °C³¹, Sn was demonstrated to segregate at the grain boundaries between the sintered particles. We have previously demonstrated that a pure hematite underlayer can promote the crystalline growth of Sn-doped hematite on top¹⁶. Overall, we have observed that the crystallinity of the hematite phase decreases as the Sn concentration increases. This compares well with the behaviour of ultrathin hematite films grown on FTO substrates¹⁶.

3.3.3 Photoelectrochemical Water Splitting

Cyclovoltammetry (CV) measurements were carried out on hematite thin film electrodes with various Sn concentrations in the dark and under illumination (Figure 3.6a, see Sec. 3.2.4 for further information). The photocurrent density at 1.23 V vs. RHE, calculated as the difference between the current density under illumination and the corresponding dark current density, peaks at ~0.4 mA cm⁻² for the film with an ALD cycle ratio of 1:100 (Figure 3.6b). Films with low ALD cycle ratios (1:40, 1:80, 1:100, 1:120, 1:150) overperform undoped hematite, which can be attributed to improved electrical conductivity and charge separation properties.^{9, 12, 16} On the other hand, films with higher Sn concentrations (ALD cycle ratios of 1:20, 1:10, 1:5) yield lower photocurrent density than undoped hematite.

As discussed in Sec. 3.3.2, the grain size of hematite decreases as the Sn concentration increases from 6 to 32 mol%. Crystallographic defects, including grain boundaries, are known to form trap states for charge carriers. Especially for hematite, a material known for slow hole transport, grain boundaries

Sn-doped hematite for photoelectrochemical water splitting: the effect of Sn concentration

have been demonstrated to cause carrier recombination ⁶. Additionally, films with high ALD cycle ratios of 1:10 and 1:5 show a significantly decreased optical absorbance in the visible range (Figure 3.6c). Therefore, we attribute the diminished PEC performance to both inferior crystallinity and a reduced absorbance with rising Sn concentration. As an outlook, it is also of interest to study the effect of dopants on the stability of hematite photoelectrodes by means of dissolution measurements ^{32, 33}.

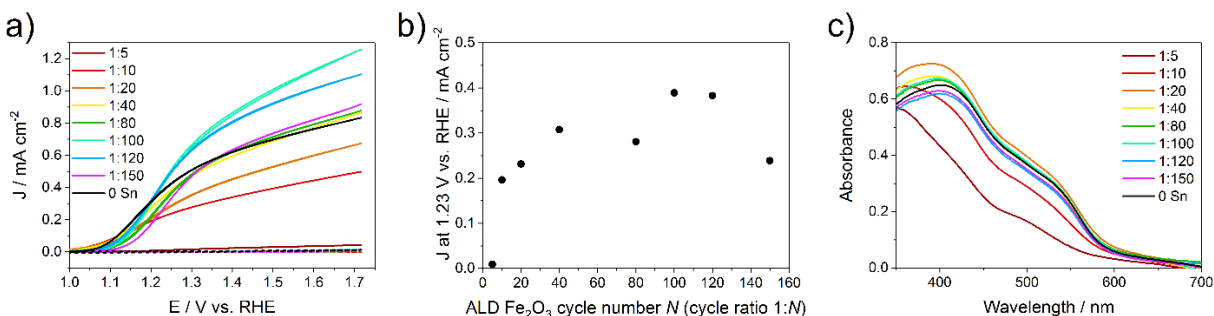


Figure 3.6: (a) CV curves of Sn-doped hematite (colored) and undoped hematite (black) photoanodes measured under illumination (solid lines) and in the dark (respective dashed lines). (b) The calculated photocurrent density at 1.23 V vs. RHE. (c) Optical absorbance of hematite films on FTO with different Sn concentrations used in PEC experiments.

3.4 Conclusions

We present a study on the effect of Sn concentration on the microstructure and PEC water oxidation activity of hematite photoanodes. It is demonstrated that by ALD, up to 32 mol% Sn can be homogeneously incorporated into the hematite phase, which also leads to reduction of a fraction of Fe^{3+} to Fe^{2+} . The photocurrent peaks at an ALD cycle ratio of 1:100, whereas the photocurrent vanishes for a ratio of 1:5, which corresponds to 32 mol% Sn in hematite. The DFT+ U results show that an increase of Sn content leads to an increase of Fe^{2+} concentration, which reduces the bandgap down to an n -type metallic state at 33 mol%. The theoretical results also confirm the increase of the lattice constants with Sn concentration found by in-plane XRD measurements. In addition, with the help of XRD pole figures, we found that the crystallinity of the hematite thin film decreases with increasing Sn concentration, which is correlated to the observation of twin boundaries from STEM micrographs. The increase of grain boundary density and decrease in optical absorption may explain the reduction in PEC activity at Sn concentrations above 6 mol%. Nevertheless, these metastable films with high and homogeneous Sn incorporation may find applications making use of the lattice expansion and other solid solution effects. ALD is a promising way to synthesize similar oversaturated

References

solid solution oxides, which can be explored as potential electrodes for photoelectrochemical water splitting.

Acknowledgment

We thank Dr Ramona Hoffmann and Dr Tristan Harzer for TEM sample preparation, and Merlin Junk for his contributions. We gratefully acknowledge the financial support by the Deutsche Forschungsgemeinschaft (DFG) within the Priority Program SPP 1613 (SolarH2) project and SFB/TRR247 (B4 and C4). AGH gratefully acknowledges funding by the Fonds der chemischen Industrie. We also acknowledge the grants for computational time at the Leibniz Rechenzentrum (grant pr87ro) and at magnitUDE of the Center of Computational Science and Simulation (DFG grant INST 20876/209-1 FUGG).

3.5 References

- (1) K.L. Hardee and A.J. Bard, *J. Electrochem. Soc.*, **1976**, 123, 1024.
- (2) K. Sivula, F. Le Formal and M. Grätzel, *ChemSusChem*, **2011**, 4, 432.
- (3) J.H. Kennedy and K.W. Frese Jr., *J. Electrochem. Soc.*, **1978**, 125, 709.
- (4) R. van de Krol, Y. Liang and J. Schoonman, *J. Mater. Chem.*, **2008**, 18, 2311.
- (5) A. Kay, I. Cesar and M. Grätzel, *J. Am. Chem. Soc.*, **2006**, 128, 15714.
- (6) U. Björkstén, J. Moser and M. Grätzel, *Chem. Mater.*, **1994**, 6, 858.
- (7) L. Vayssieres, C. Sathe, S.M. Butorin, D.K. Shuh, J. Nordgren and J. Guo, *Adv. Mater.*, **2005**, 17, 2320.
- (8) R. Shinar and J.H. Kennedy, *Solar Energy Mater.*, **1982**, 6, 323.
- (9) A. Mettenböcker, Y. Gönüllü, T. Fischer, T. Heisig, A. Sasinska, C. Maccato, G. Carraro, C. Sada, D. Barreca, L. Mayrhofer, M. Moseler, A. Held and S. Mathur, *Nano Energy*, **2016**, 19, 415.
- (10) K. D. Malviya, H. Dotan, D. Shlenkevich, A. Tsyganok, H. Mor and A. Rothschild, *J. Mater. Chem. A*, **2016**, 4, 3091.
- (11) N.T. Hahn and C.B. Mullins, *Chem. Mater.*, **2010**, 22, 6474.
- (12) H.K. Dunn, J.M. Feckl, A. Müller, D. Fattakhova-Rohlfing, S.G. Morehead, J. Roos, L.M. Peter, C. Scheu and T. Bein, *Phys. Chem. Chem. Phys.*, **2014**, 16, 24610.
- (13) Y. Ling, G. Wang, D.A. Wheeler, J.Z. Zhang and Y. Li, *Nano Lett.*, **2011**, 11, 2119.
- (14) C.D. Bohn, A.K. Agrawal, E.C. Walter, M.D. Vaudin, A.A. Herzing, P.M. Haney, A.A. Talin, V.A. Szalai, *J. Phys. Chem. C*, **2012**, 116, 15290.
- (15) B. Wickman, A. Bastos Fanta, A. Burrows, A. Hellman, J.B. Wagner and B. Iandolo, *Sci. Rep.* **2017**, 7, 40500.

**Sn-doped hematite for photoelectrochemical water
splitting: the effect of Sn concentration**

- (16) A.G. Hufnagel, H. Hajiyani, S. Zhang, T. Li, O. Kasian, B. Gault, B. Breitbach, T. Bein, D. Fattakhova-Rohlfing, C. Scheu and R. Pentcheva, *Adv. Funct. Mater.*, **2018**, 28, 1804472.
- (17) M. Takano, Y. Bando, N. Nakanishi, M. Sakai and H. Okinaka, *J. Solid State Chem.*, **1987**, 68, 153.
- (18) J.Z. Jiang, R. Lin, S. Morup, K.Nielsen, F.W. Poulsen, F.J. Berry, R. Clasen, *Phys. Rev. B*, **1997**, 55, 11.
- (19) B. M. Klahr, A. B. Martinson and T. W. Hamann, *Langmuir*, **2011**, 27, 461.
- (20) G. Kresse and J. Hafner, *Phys. Rev. B*, **1994**, 49, 14251.
- (21) G. Kresse and J. Furthmüller, *Comput. Mater. Sci.*, **1996**, 6, 15.
- (22) G. Kresse and J. Furthmüller, *Phys. Rev. B*, **1996**, 54, 11169.
- (23) P. Blöchl, *Phys. Rev. B*, **1994**, 50, 17953.
- (24) J. P. Perdew, K. Burke and M. Ernzerhof, *Phys. Rev. Lett.*, **1996**, 77, 3865.
- (25) S. L. Dudarev, G. A. Botton, S. Y. Savrasov, C. J. Humphreys and A. P. Sutton, *Phys. Rev. B*, **1998**, 57, 1505.
- (26) H. J. Monkhorst and J. D. Pack, *Phys. Rev. B*, **1976**, 13, 5188.
- (27) R. Pentcheva and H. Sadat Nabi, *Phys. Rev. B*, **2008**, 77, 172405.
- (28) S. Zhang and C. Scheu, *Microscopy*, **2018**, 67, i133.
- (29) P.A. van Aken and B. Liebscher, *Phys. Chem. Miner.*, **2002**, 29, 188.
- (30) F. Watari, J. van Landuyt, P. Delavignette, S. Amelinckx and N. Igata, *Phys. Stat. Sol. A*, **1982**, 73, 215.
- (31) M.R.S. Soares, C.A.R. Costa, E.M. Lanzoni, J. Bettini, C.A.O. Ramirez, F.L. Souza, E. Longo and E.R. Leite, *Adv. Electr. Mater.*, **2019**, 1900065.
- (32) J. Knöppel, S. Zhang, F.D. Speck, K.J.J. Mayrhofer, C. Scheu and S. Cherevko, *Electrochem. Commun.* **2018**, 96, 53.
- (33) S. Zhang, M. Rohloff, O. Kasian, A.M. Mingers, K.J.J. Mayrhofer, A. Fischer, C. Scheu and S. Cherevko, *J. Phys. Chem. C*, **2019**, 123, 23410.

References

4 How photocorrosion can trick you: A detailed study on low-bandgap Li doped CuO photocathodes for solar hydrogen production

This chapter is based on the following publication:

Jonathan Kampmann, Sophia Betzler, Hamidreza Hajiyani, Sebastian Häring, Michael Beetz, Tristan Harzer, Jürgen Kraus, Bettina V. Lotsch, Christina Scheu, Rossitza Pentcheva, Dina Fattakhova-Rohlfing* and Thomas Bein*, *submitted*.

Jonathan Kampmann synthesized all discussed materials, performed optical, structural and conductivity measurements as well as the aqueous photoelectrochemistry and hydrogen detection experiments. He evaluated the corresponding data, managed the project and wrote the corresponding parts of the manuscript.

Abstract

Abstract

The efficiency of photoelectrochemical tandem cells is still limited by the availability of stable low band gap electrodes. In this work, we report a photocathode based on lithium doped copper (II) oxide, a black p-type semiconductor. Density functional theory calculations with a Hubbard U term show that low concentrations of Li ($\text{Li}_{0.03}\text{Cu}_{0.97}\text{O}$) lead to an upward shift of the valence band maximum that crosses the Fermi level and results in a p-type semiconductor. Therefore, Li doping emerged as a suitable approach to manipulate the electronic structure of copper oxide based photocathodes. As this material class suffers from instability in water under operating conditions, the recorded photocurrents are repeatedly misinterpreted as hydrogen evolution evidence. We investigated the photocorrosion behavior of $\text{Li}_x\text{Cu}_{1-x}\text{O}$ cathodes in detail and give the first mechanistic study of the fundamental physical process. The reduced copper oxide species were localized by electron energy loss spectroscopy mapping. Cu_2O grows as distinct crystallites on the surface of $\text{Li}_x\text{Cu}_{1-x}\text{O}$ instead of forming a dense layer. Additionally, there is no obvious Cu_2O gradient inside the films, as Cu_2O seems to form on all $\text{Li}_x\text{Cu}_{1-x}\text{O}$ nanocrystals exposed to water. The application of a thin $\text{Ti}_{0.8}\text{Nb}_{0.2}\text{O}_x$ coating by atomic layer deposition and the deposition of a platinum co-catalyst increased the stability of $\text{Li}_x\text{Cu}_{1-x}\text{O}$ against decomposition. These devices showed a stable hydrogen evolution for 15 minutes.

4.1 Introduction

Events like the Paris agreement in the year 2015 again demonstrate the desire of our modern society to reduce emissions caused by fossil fuels. Consequently, the focus on research for sustainable energy sources has been increasing in recent years. Compared to wind power, hydroelectric power and tidal power plants, sunlight is by far the most prominent energy source we can exploit to meet mankind's rising demands.¹ An additional challenge beside harvesting sunlight and converting it into electricity is large scale energy storage, which is essential for the replacement of fossil fuels. One approach to address this demanding task is the use of hydrogen gas for powering both fuel cells and fertilizer production, envisioning the establishment of a so called 'hydrogen society'. Inspired by photosynthesis, photoelectrochemical (PEC) water splitting is a promising process to generate hydrogen and oxygen gas.²⁻⁵ While there is lively discussion on the subject, potential advantages of a photoelectrochemical cell compared to the combination of an electrolyzer with a conventional solar cell can be the reduction of overpotentials as well as reduced fabrication cost and complexity of the final devices.⁵⁻⁶ In contrast to photocatalysis, oxygen and hydrogen are produced in spatially

How photocorrosion can trick you: A detailed study on low-bandgap Li doped CuO photocathodes for solar hydrogen production

separated compartments, hence avoiding subsequent separation, facilitating their storage and preventing the accumulation of an explosive gas mixture. Suitable semiconducting materials for PEC cathodes are based on silicon⁶⁻⁹, metal oxides^{3,5} or organic semiconductors.¹⁰⁻¹² Many earth abundant metal oxides are known to exhibit reasonable stability as well as photoactivity in water splitting applications.¹³⁻¹⁵ This led to the development of synthesis methods for novel binary¹⁶⁻¹⁹ and ternary²⁰⁻²¹ metal oxides as well as doping of well-known metal oxides.²²⁻²⁴ Besides the extensive work on materials with optical bandgaps in the range of 2.0 – 3.0 eV,^{14-15, 24-26} there is also need for low band gap photoabsorbers in order to build efficient PEC tandem cells. Such devices consist of an *n*-type photoanode connected to a *p*-type photocathode to harvest a substantial portion of the solar spectrum, reaching theoretical solar-to-hydrogen conversion efficiencies up to 21.6%.^{5, 25, 27} Copper oxide based photocathodes have aroused broad interest due to their low toxicity and the good availability of copper based compounds.^{22, 28-34} The reported band gaps of 1.35 eV– 1.7 eV and 2.0 – 2.2 eV for CuO and Cu₂O respectively, allow for significant light absorption in the visible range and provide enough energy for photoelectrochemical reactions.³⁵⁻³⁹ The conduction band edges of the intrinsic *p*-type semiconductors CuO and Cu₂O³⁶⁻³⁷ fit both the reduction potentials of water^{14, 38} and CO₂⁴⁰, which enables the reduction of these reagents by photo-generated electrons. Additionally, doping CuO with Li has already been proven to be a suitable way to lower the optical band gap and increase the electrical conductivity,^{22-23, 35, 41} which is key to enhance its performance for photoelectrochemical water splitting applications. Therefore, the photoelectrochemical study solely covers results on Li doped CuO and does not compare it with undoped CuO. Several groups have reported the discovery of highly efficient photocathodes based on CuO.^{22, 33, 42-45} However, it has been observed that photocurrents may be easily misinterpreted as evidence for hydrogen evolution which should be critically scrutinized.⁴²⁻⁴⁴ On the other hand, also justified doubts exist already about the stability of this metal oxide under reductive potentials.⁴⁶⁻⁴⁷ High cathodic dark currents and a significant decay in performance within the first minutes under operating conditions could point towards cathodic corrosion of this photoabsorber.^{35, 48-49} The reduction potential of CuO in aqueous electrolyte lies above the reduction potential of water.²⁹ This implies the possibility of a competitive reduction of water and the photoabsorber itself, leading to the formation of reduced copper species such as Cu₂O and metallic copper under operating conditions, and consequently to a significant change of the photocathode morphology due to photocorrosion.^{47, 50-51} Other copper containing photocathode materials like Cu₂O,^{14, 52} CuFeO₂¹⁷ and CuBi₂O₄¹⁹ are also affected by photocorrosion, which further motivated us to investigate this phenomenon in detail. Recently, more detailed

Results and Discussion

corrosion studies on CuO⁵³ and BiVO₄⁵⁴⁻⁵⁶ concentrated on the mechanisms behind the loss in activity and addressed this by the use of protective layers and suitable cocatalysts. Here, we report on the first extensive photocorrosion study revealing detailed insights into the transformations taking place in copper (II) oxide thin film electrodes under operating conditions with special attention to the role of photo-induced electrons, which we propose to be applicable to various copper containing cathode materials used in photoelectrochemical measurements. We further describe a suitable approach to increase the stability of this *p*-type low bandgap semiconductor against decomposition and to decorate it with a Pt cocatalyst. With these results, we wish to contribute to the ongoing discussion about the stability of metal oxide photocathodes and point to ways towards the development of stable photoabsorbers for the generation of environmentally friendly hydrogen gas. Furthermore, we want to present a convenient method to manipulate the electronic structure of copper oxide which can be used to improve CO₂ reduction efficiencies.

4.2 Results and Discussion

Li_xCu_{1-x}O photocathode layers were prepared by spin coating an ethanolic solution of Cu(NO₃)₂ • 3 H₂O and LiNO₃ onto an FTO substrate. Calcination of these coatings at 400°C resulted in homogeneous black films with a thickness of about 1 μm. The calcined films obtained from the precursor solution contain large amounts of non-reacted LiNO₃ and Li₂CO₃ (ESI Figure 4.1), which can be removed by rinsing with water. X-ray diffraction (XRD) analysis (Figure 4.1a) reveals that the films are structurally closely related to the CuO tenorite phase (space group: *C2/c*, *a* = 4.6803(8) Å; *b* = 3.4176(2) Å; *c* = 5.1278(8) Å; β = 99.442 (1)° (ESI Figure 4.2))⁵⁷⁻⁵⁸ but exhibit slightly larger unit cell parameters (*a* = 4.6975(8) Å, *b* = 3.4346(6) Å, *c* = 5.1400(3) Å and β = 99.499(6)°). The small increase of the unit cell volume from 82.02(1) Å³ for the pure CuO to 82.93(1) Å³ for the CuO synthesized in the presence of Li salts indicates the incorporation of a small amount of Li⁺ ions, with a somewhat bigger ionic radius of 0.90 Å (in CN = 6) compared to the ionic radius of Cu²⁺ ions of 0.87 Å (in CN = 6), into the crystal lattice.²³ Inductively coupled plasma atomic absorption spectroscopy (ICP-AAS) analysis confirms the presence of 4 at% Lithium in the sample, which is the maximum amount that can be incorporated in the tenorite crystal structure.⁵⁹

How photocorrosion can trick you: A detailed study on low-bandgap Li doped CuO photocathodes for solar hydrogen production

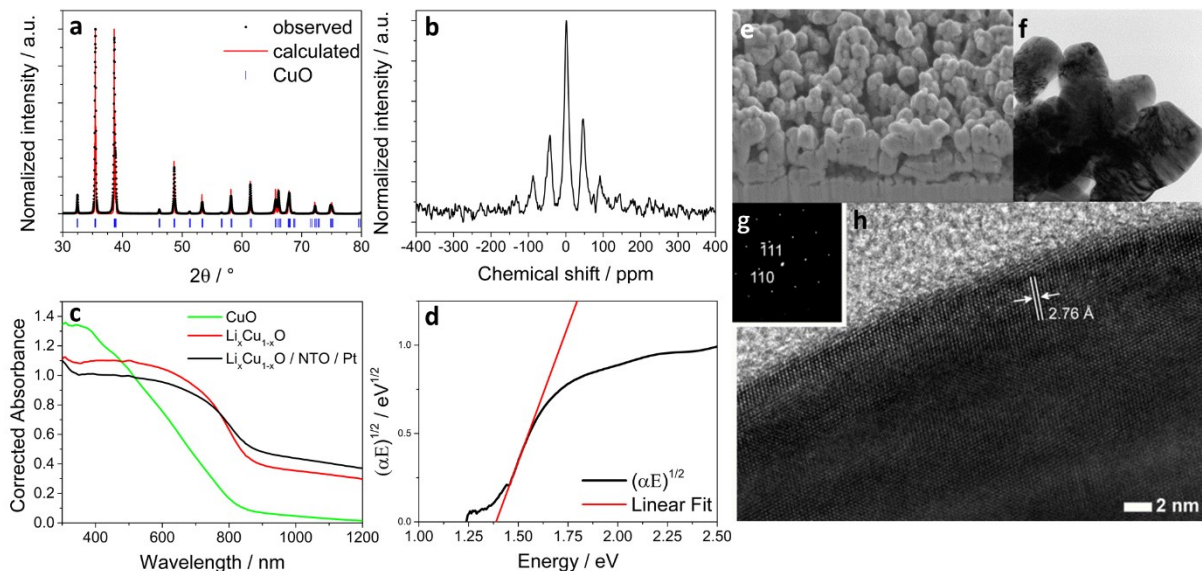


Figure 4.1. a) Rietveld refinement of $\text{Li}_x\text{Cu}_{1-x}\text{O}$ with observed data (\bullet) and calculated pattern (red line), blue vertical bars mark the positions of the diffraction lines of CuO (tenorite). b) ^7Li -NMR spectra of $\text{Li}_x\text{Cu}_{1-x}\text{O}$ showing a multiplet centered at 1.3 ppm. c) UV-Vis absorption spectrum of undoped CuO (green), $\text{Li}_x\text{Cu}_{1-x}\text{O}$ (red) and protected $\text{Li}_x\text{Cu}_{1-x}\text{O}/\text{NTO}/\text{Pt}$ films on FTO. d) Tauc plot of a $\text{Li}_x\text{Cu}_{1-x}\text{O}$ film on FTO showing an indirect bandgap of 1.39 eV. e) SEM cross section image of $\text{Li}_x\text{Cu}_{1-x}\text{O}$. f) TEM image of $\text{Li}_x\text{Cu}_{1-x}\text{O}$ particles. g, h) High-resolution TEM image of a highly crystalline $\text{Li}_x\text{Cu}_{1-x}\text{O}$ nanoparticle and its corresponding electron diffraction pattern.

Another evidence for the incorporation of Li in the structure is provided by solid state ^7Li nuclear magnetic resonance (NMR) analysis, which shows a multiplet (from spinning sidebands) centered at 1.3 ppm in the spectrum of a carefully washed $\text{Li}_x\text{Cu}_{1-x}\text{O}$ powder (Figure 4.1b). This signal is indicative for a non-metallic single phase, free of contaminations with diamagnetic compounds (i.e. Li_2O , LiCO_3 , LiNO_3). The electrical conductivity of Li-doped CuO was determined by Hall measurements (van der Pauw method) to be $6.0 \cdot 10^{-3} \text{ S cm}^{-1}$, which is an increase by a factor of 2.5 compared to undoped CuO ($2.4 \cdot 10^{-3} \text{ S cm}^{-1}$). While films of undoped CuO are of dark brown color, films of $\text{Li}_x\text{Cu}_{1-x}\text{O}$ are black. We attribute this observation to the formation of in-gap states, which can be caused by the introduction of point defects like cation doping or oxygen vacancies.⁶⁰ These optical properties were investigated by UV-Vis spectroscopy. $\text{Li}_x\text{Cu}_{1-x}\text{O}$ films demonstrate favorable light harvesting efficiencies across a broad wavelength range between 350 - 800 nm, covering part of the near infrared (IR) range, which exceeds that of our undoped CuO films (Figure 4.1c). Absorbance data of $\text{Li}_x\text{Cu}_{1-x}\text{O}$ films were used to calculate an indirect optical bandgap of 1.39 eV via Tauc plot analysis⁶¹ (Figure

Results and Discussion

4.1d), which is nearly the theoretical optimum for bottom materials used for high-efficiency PEC tandem cells.²⁷ The morphology of our $\text{Li}_x\text{Cu}_{1-x}\text{O}$ films was investigated by scanning electron microscopy (SEM, Figure 4.1e). The films are nanostructured and composed of interconnected nanoparticles forming disordered porous layers covering the whole FTO substrate. Transmission electron microscopy (TEM) images of $\text{Li}_x\text{Cu}_{1-x}\text{O}$ films reveal that they are composed of intergrown particles with a size of around 150 - 300 nm (Figure 4.1f). High-resolution TEM (HR-TEM) images (Figure 4.1h) and electron diffraction analysis (Figure 4.1g) reveal that these particles are single crystalline. The $d_{(110)}$ -spacing of monoclinic $\text{Li}_x\text{Cu}_{1-x}\text{O}$ was determined to be 2.76 Å, being in good agreement with the XRD patterns.

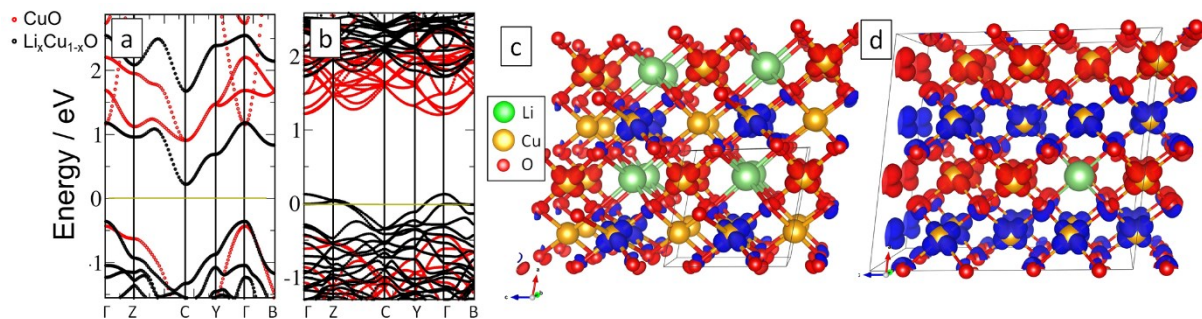


Figure 4.2. Electronic band structure of lithium doped CuO for two different Li concentrations of (a) $\text{Li}_{0.25}\text{Cu}_{0.75}\text{O}$ and (b) $\text{Li}_{0.032}\text{Cu}_{0.968}\text{O}$. The different numbers of bands are related to different cell sizes. The yellow line marks the Fermi level. In contrast to the insulating behaviour for $x_{\text{Li}}=25\%$ (note the reduced band gap w.r.t. to bulk CuO), the valence bands crossing the Fermi level for $x_{\text{Li}}=3.2\%$ indicate p-type conductivity. Spin density of lithium doped CuO in two different Li concentrations of (c) $\text{Li}_{0.25}\text{Cu}_{0.75}\text{O}$ and (d) $\text{Li}_{0.032}\text{Cu}_{0.968}\text{O}$ (Isosurface of $0.01 e/\text{\AA}^3$). Majority and minority spin densities are shown by blue and red, respectively. Note the significant contribution of oxygen for the low Li doping concentration of 3.2%.

To understand how the introduction of Li influences the electronic properties of CuO, we have performed density functional theory (DFT) calculations for Li-containing CuO including static electronic correlations within the GGA+U approach where the rotationally invariant formulation of Dudarev et al.⁶² was employed (see supporting information for further details). We have investigated the band gap as a function of the Hubbard U parameter and find that up to $U = 8$ eV the indirect band gap of CuO increases monotonically with the band gap reaching 1.46 eV. Beyond U of 8 eV it changes to a direct band gap of 2.1 eV (ESI Figure 4.3a). The band gap of 1.46 eV obtained for $U = 8$ eV is in good agreement with the band gap of 1.39 eV determined from the Tauc plot above and consistent with previous LDA+U studies with a somewhat lower value of $U = 6.5$ eV by Heinemann et al.³⁷ The

How photocorrosion can trick you: A detailed study on low-bandgap Li doped CuO photocathodes for solar hydrogen production

variation of lattice constants as a function of U is presented in ESI Figure 4.3b. The DFT predictions are in overall agreement with experimental lattice constants. The jump occurring between $U = 8$ eV and $U = 8.5$ eV is associated with the above mentioned transition from indirect to direct band gap. To determine the preferential position of Li atoms in the CuO structure we have calculated the solution energy of Li at different lattice positions. For substitutional doping of Cu and O sites the calculated values are -4.20 eV and 1.04 eV, respectively, while for the interstitial doping the solution energy was determined to be -0.025 eV. Therefore, we can conclude that thermodynamically the preferred configuration corresponds to the substitutional doping of Cu sites with Li atoms. Consequently, we postulate the delocalization of holes throughout the structure and a partial change of the copper oxidation state from Cu^{2+} to Cu^{3+} to maintain charge neutrality. The band structure of bulk $\text{Li}_x\text{Cu}_{1-x}\text{O}$ was calculated for a high lithium content of $x_{\text{Li}} = 25$ at% and a low content of $x_{\text{Li}} = 3.2$ at%, which is close to the experimentally determined Li level of ca. 4 at%. The band structure of $\text{Li}_x\text{Cu}_{1-x}\text{O}$ (Figure 4.2a and b) shows a very strong dependence of the amount of introduced Li. While for high concentration the band gap is strongly decreased to 0.64 eV, for low concentration the main effect is an upward shift of the valence band maximum that gets closer to the Fermi level and makes the system a p -type semiconductor. As shown in the spin density plots in Figure 4.2c and d, the underlying mechanisms are distinct: for $x_{\text{Li}} = 25$ at% substitution of Li^+ leads to a change in charge state of one copper to Cu^{1+} , while for $x_{\text{Li}} = 3.2$ at% the holes are delocalized at the oxygen sites leading to a p -type semiconductor. The solution energies of $\text{Li}_{0.032}\text{Cu}_{0.968}\text{O}$ and $\text{Li}_{0.25}\text{Cu}_{0.75}\text{O}$ are -4.2 eV and -3.1 eV respectively, indicating a reduction with increasing Li concentration due to Li-Li repulsion.

To sum up, Lithium doping causes an increased optical absorption of CuO in the infrared range and significantly increases the p -type conductivity, therefore we expect facilitated charge separation. As our morphology is beneficial for the strongly surface-depending water splitting reaction⁵, we determined the photoelectrochemical performance of $\text{Li}_x\text{Cu}_{1-x}\text{O}$ photocathodes by linear sweep voltammetry (LSV) in 0.1 M Na_2SO_4 aqueous solution (pH 7) starting at 0.7 V vs. RHE and scanning down towards -0.1 V vs. RHE under chopped AM 1.5 illumination. In the present case, the result of this procedure (Figure 4.3a) is very misleading, as the $\text{Li}_x\text{Cu}_{1-x}\text{O}$ film shows the typical behavior of a photocathode with instant photocurrent response upon illumination. This observation can easily be misinterpreted as a measure of hydrogen evolution efficiency, but indeed originates from both the reduction of water and the reduction of the transition metal oxide itself, which we elucidate in the present work. In addition, we performed cyclic voltammetry (CV) measurements in a potential range between 0.0 and 0.9 V vs. RHE (Figure 4.3b). The material shows a negligible dark current, indicating

Results and Discussion

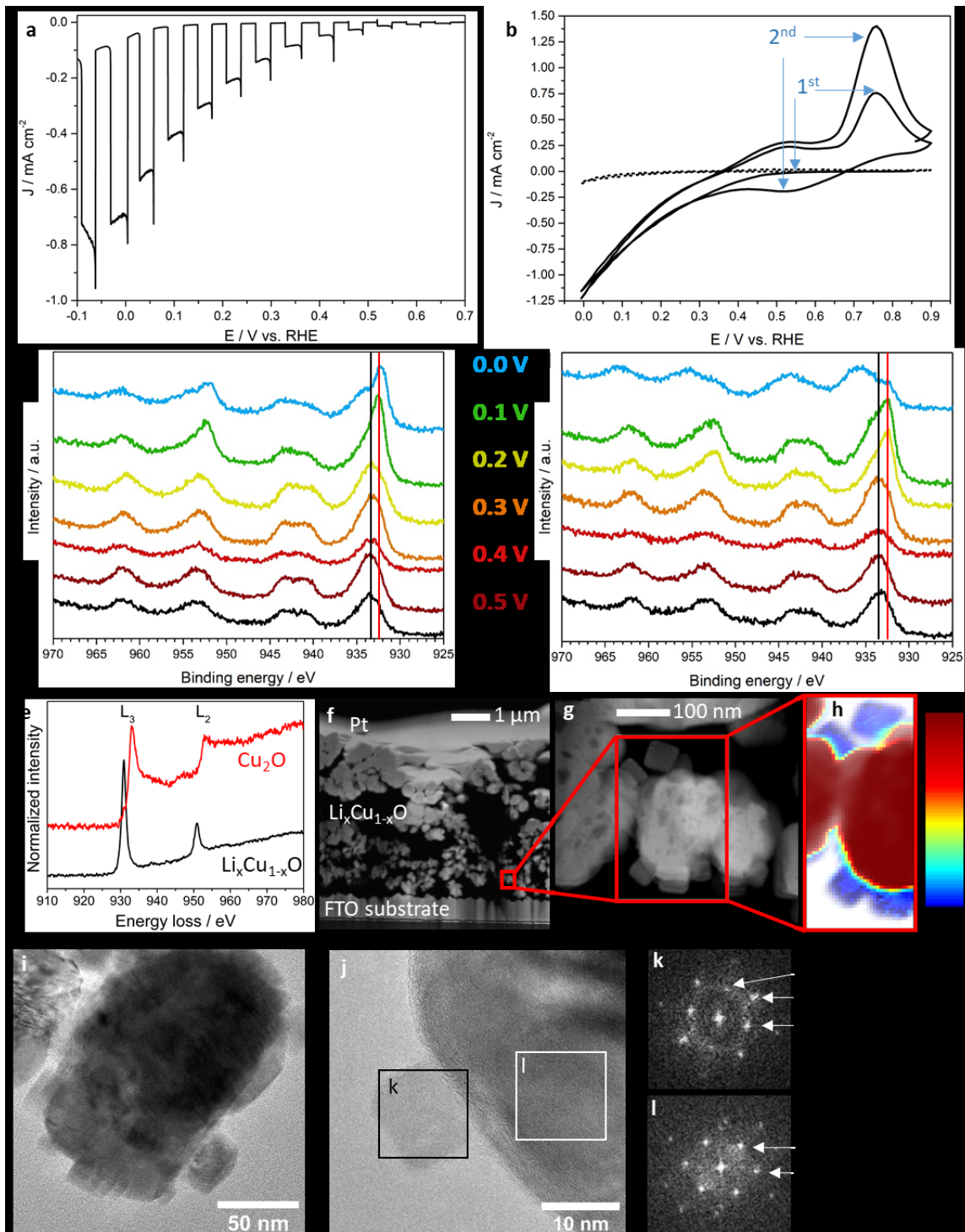


Figure 4.3. a) Linear sweep voltammogram of a bare $\text{Li}_x\text{Cu}_{1-x}\text{O}$ film under chopped AM 1.5 illumination, showing no signs of photocorrosion. The assumption of a working photocathode based on this experiment is very misleading, as the reductive currents originate from both water reduction and photocorrosion. b) Cyclic voltammety characterization of an unprotected

How photocorrosion can trick you: A detailed study on low-bandgap Li doped CuO photocathodes for solar hydrogen production

Li_xCu_{1-x}O photocathode in 0.1 M Na₂SO₄ at pH 7 in the dark (dashed line) and under AM 1.5 illumination through the substrate (solid line). c, d) Cu 2p XPS spectra measured of bare Li_xCu_{1-x}O films held at the respective potentials vs. RHE for 15 minutes each in the dark (c) and under AM1.5G illumination (d) (bars: black: Cu²⁺, red: Cu⁰ and Cu¹⁺). At a potential of 0.2 V vs. RHE, Li_xCu_{1-x}O is stable in the dark but corrodes to Cu₂O under illumination. e) Cu-L_{2,3} edges of CuO and Cu₂O distinguish between both copper oxidation states. The photocorrosion could be localized in a TEM cross section image (f, g) with corresponding EELS map (h), showing cubic Cu₂O crystals on the Li_xCu_{1-x}O surface. i) Overview image of one crystal scratched from a Li_xCu_{1-x}O film after an electrochemistry experiment performed for 15 min at 0.2 V under illumination, showing a roundish crystal overgrown by square crystals. (j) Average Background Subtraction Filtered (ABSF) high resolution TEM image showing one square crystal at the surface of a spherical one. The FFTs of the marked regions were indexed for Cu₂O (k) and CuO (l), respectively.

electrochemical stability in the scanned potential range. Under AM1.5G illumination (100 mW cm⁻²), a reductive current density can be observed below 0.5 V vs. RHE. However, significant oxidizing currents appear above 0.4 V vs. RHE in the back scan. To examine the electrochemical stability of our Li_xCu_{1-x}O photocathodes, we applied different constant potentials from 0.0 to 0.6 V vs. RHE for 15 minutes each, in the dark as well as under illumination (ESI Figure 4.7). X-ray photoelectron spectroscopy (XPS) measurements of these films after electrochemical reaction were used to get further insights into the stability of the electrode material. From the binding energy of the Cu 2p_{3/2}-peak (Figure 4.3c, d), the oxidation state of the copper at the electrode surface could be assigned to Cu(II) (933.6 eV) or Cu(I) (932.4 eV).⁶³ As can be seen in Figure 4.3c, copper (II) oxide remains stable without illumination down to 0.2 V vs. RHE. Below this potential a shift of the Cu 2p_{3/2}-peak to lower binding energies is observed, indicative for the reduction of copper (II) oxide to copper (I) oxide. Under AM1.5G illumination, we observed copper (I) oxide formation already at 0.2 V vs. RHE, indicating photocorrosion by light induced electrons at this potential. Deconvolution of the Cu 2p_{3/2}-peak as well as the corresponding Cu L₃VV Auger signals support this conclusion (ESI Figure 4.13). In agreement with the XPS data⁶³⁻⁶⁴, we attribute the reductive currents to a competitive reduction of both 2 H⁺ to H₂ and Cu²⁺ to Cu¹⁺, while the oxidizing currents occur from the oxidation of Cu¹⁺ to Cu²⁺.³⁵ Furthermore, we extended the potential range of several CV measurements stepwise on a new sample (ESI Figure 4.5). With scanning to lower potentials, more Cu²⁺ is photoreduced to Cu¹⁺, which gets reoxidized to Cu²⁺ at 0.75 V vs. RHE. This extremely sensitive method indicates a photocorrosion onset at approximately 0.45 V vs. RHE. Electron energy loss spectroscopy (EELS) allows one to directly monitor the oxidation states of elements on the nanometer scale using the near edge fine structure. The Cu-L_{2,3} edges of CuO and Cu₂O are characterized by a pair of white lines which result from the excitation of 2p_{3/2} (L₃) and 2p_{1/2} (L₂) electrons to unoccupied 3d states (Figure 4.3e). The

Results and Discussion

white lines of CuO are shifted to lower energy losses compared to Cu₂O.⁶⁵⁻⁶⁶ Thus, the energetic position of the two white lines was used in this study to identify the local distribution of the oxidation states in the thin films (ESI Figure 4.6). EELS requires electron transparent samples (thickness below 100 nm),⁶⁶ which in this study was achieved by preparing thin lamellae with a focused ion beam microscope. The resulting lamella represents a cross-section through the thin film (Figure 4.3f, g). A platinum protection layer was used to protect the sample from the gallium ions used for sample cutting and thinning. Oxidation state maps illustrate the local distribution of Cu₂O and CuO inside the thin film with the spatial resolution given by the pixel size of the map, which was commonly chosen between 2.5 and 5 nm using subpixel scanning to reduce beam damage. Both oxidation states are detected in the interfacial regions between the two phases. In the TEM images two different crystal morphologies are visible, large round crystals and smaller square crystals. The latter form preferably at the surface of the large crystals. EELS maps demonstrate that the two crystal morphologies correspond to the two oxidation states: the large crystals are pure CuO, while the smaller ones are Cu₂O (Figure 4.3h). This is confirmed by high resolution TEM imaging of the two crystal morphologies (Figure 4.3i, j) with their corresponding *fast Fourier transforms* (FFTs) indexed for CuO and Cu₂O (Figure 4.3k, l). Interestingly, Cu₂O grows as distinct crystallites on the surface of CuO instead of forming a dense layer on its surface. Additionally, there is no obvious Cu₂O gradient inside the films, as Cu₂O seems to form on all CuO nanocrystals exposed to water. We see a similar photocorrosion behavior on undoped CuO. After a potentiostatic measurement for 15 minutes at 0.2 V vs. RHE, also the surface of CuO is covered with cubic crystallites. Both the post-photoelectrochemical XRD pattern of CuO as well as FFTs and electron diffraction pattern of the regions covered with cubic crystals indicate the formation of the cuprite phase (Cu₂O) (ESI Figure 4.11). Therefore, we expect the same corrosion mechanism like on Li_xCu_{1-x}O photocathodes. To rule out artefacts introduced by the FIB sample preparation, FIB lamellae of reference samples that had not been used in photoelectrochemical experiments were investigated. The maps show a thin layer of reduced copper oxide at the surface of the CuO crystals (see ESI Figure 4.8), but no Cu₂O crystals. The reduction of the surface layer of CuO is most likely caused by a reaction of CuO with the Ga-ions used for the sample preparation.

How photocorrosion can trick you: A detailed study on low-bandgap Li doped CuO photocathodes for solar hydrogen production

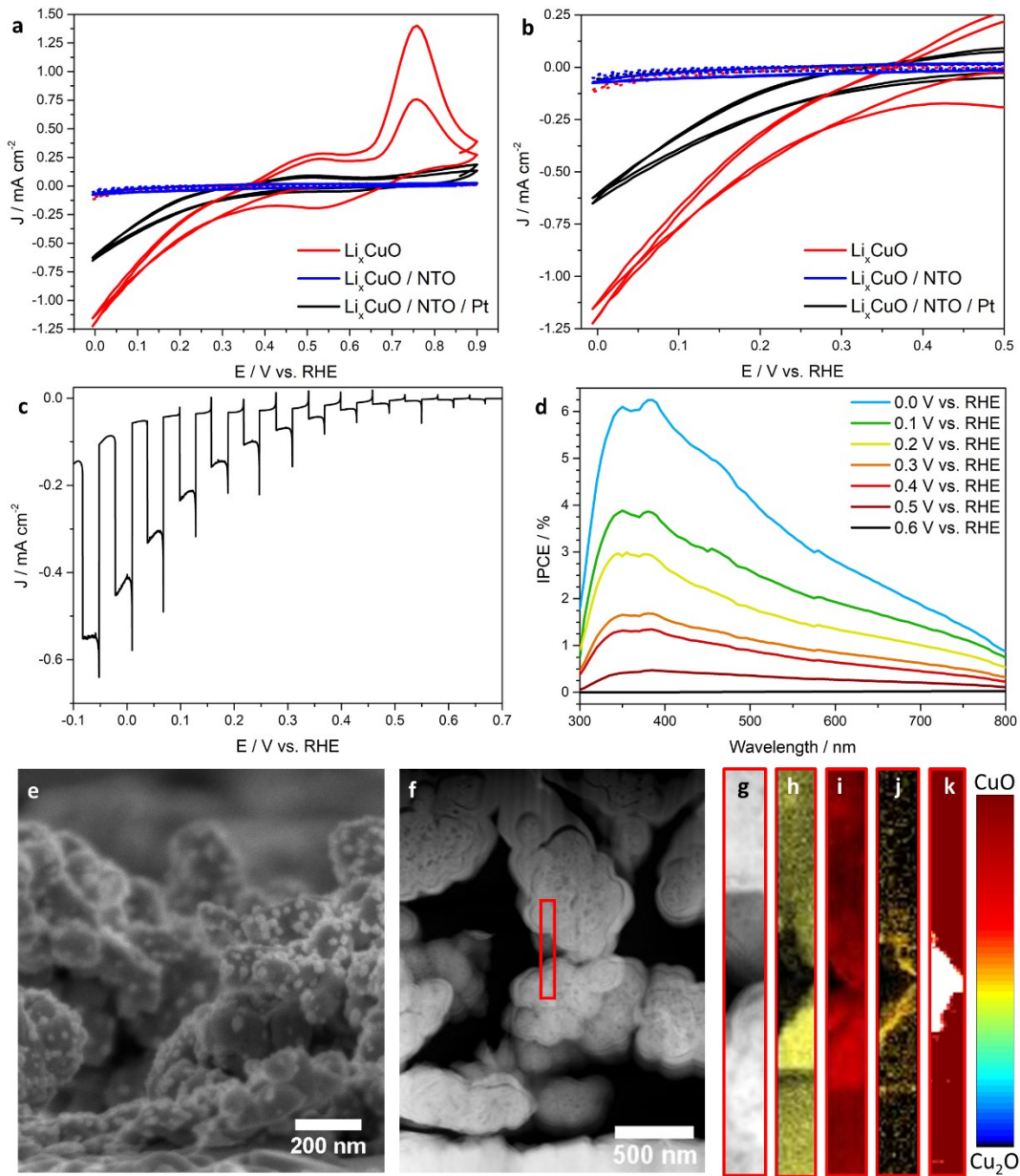


Figure 4.4. a) Cyclic voltammety measurements of $\text{Li}_x\text{Cu}_{1-x}\text{O}$ films protected with 2.5 nm thin $\text{Ti}_{0.8}\text{Nb}_{0.2}\text{O}_x$ (NTO) layer (blue) and additionally functionalized with Pt nanoparticles (black) compared to a bare $\text{Li}_x\text{Cu}_{1-x}\text{O}$ photocathode (red) in the dark (dashed) and under AM1.5 illumination (solid). b) Magnification of (a) in the lower potential range. c) Linear sweep voltammogram of a $\text{Li}_x\text{Cu}_{1-x}\text{O}/\text{NTO}/\text{Pt}$ film under chopped AM 1.5 illumination. d) Incident-photon-to-current-efficiency (IPCE) measurements at different potentials. e) SEM image of a $\text{Li}_x\text{Cu}_{1-x}\text{O}/\text{NTO}$ photocathode decorated with 20 nm sized Pt particles. f) STEM image of a cross section of a $\text{Li}_x\text{Cu}_{1-x}\text{O}/\text{NTO}/\text{Pt}$ device held for 15 min at 0.2 V vs. RHE under AM1.5 illumination. The marked area (red, g) was used for EDX mapping of Cu (h), O (i) and Ti (j). The corresponding EELS map (k) shows no sign of photocorrosion.

Results and Discussion

To stabilize our photoabsorber material, we coated our $\text{Li}_x\text{Cu}_{1-x}\text{O}$ films with a protective layer by atomic layer deposition (ALD), as this is a proven approach to protect copper oxides against photocorrosion.^{14, 32, 67} Among several tested coatings like TiO_2 , $\text{Ti}_{0.8}\text{Nb}_{0.2}\text{O}_x$ (NTO), SnO_x , Al:ZnO and Al_2O_3 , NTO exhibited the best results on our $\text{Li}_x\text{Cu}_{1-x}\text{O}$ morphology. After deposition, the applied $\text{Ti}_{0.8}\text{Nb}_{0.2}\text{O}_x$ layers are amorphous (ESI Figure 4.12),⁶⁸⁻⁶⁹ covering the complete surface of the nanostructured morphology of the $\text{Li}_x\text{Cu}_{1-x}\text{O}$ films without the formation of pinholes (ESI Figure 4.15), which has already been demonstrated to successfully protect Cu_2O .⁵² CV measurements of $\text{Li}_x\text{Cu}_{1-x}\text{O}/\text{NTO}$ films in aqueous 0.1 M Na_2SO_4 are free of oxidative current signals, indicating that the photoabsorber remains stable under illumination. In contrast to bare $\text{Li}_x\text{Cu}_{1-x}\text{O}$, NTO covered films showed no activity in terms of water reduction (Figure 4.4a and b, blue) due to the lack of a suitable cocatalyst.³ For this reason, we electrodeposited Pt nanoparticles on our $\text{Li}_x\text{Cu}_{1-x}\text{O}/\text{NTO}$ from a 1 mM methanolic H_2PtCl_6 solution (see experimental details for further information), as this is a proven way to improve HER kinetics on ALD protected copper oxide based photocathodes.¹⁴ 20 nm sized Pt particles are formed on the surface of the nanostructured $\text{Li}_x\text{Cu}_{1-x}\text{O}/\text{NTO}$ films (Figure 4.4e). A protection layer of 2.5 nm NTO showed the highest activity compared slightly thinner or thicker NTO layers, still allowing sufficient charge transport to the Pt cocatalyst (ESI Figure 4.14). We assume electron transport by tunneling through the protective layer due to its extremely small layer thickness. The described protection strategy causes no significant change in the light absorption properties of those devices compared to the pristine $\text{Li}_x\text{Cu}_{1-x}\text{O}$ films (Figure 4.1c). We see no signs of photocorrosion of $\text{Li}_x\text{Cu}_{1-x}\text{O}/\text{NTO}/\text{Pt}$ devices held for 15 min at 0.2 V vs. RHE under AM1.5G illumination. This is verified by EELS oxidation state mapping (Figure 4.4f, k and ESI Figure 4.16). Based on LSV measurements under chopped illumination, these devices show a distinct activity towards hydrogen evolution reaching up to $350 \mu\text{A cm}^{-2}$ at 0.0 V vs. RHE with a photocurrent onset at around 0.50 V vs. RHE (Figure 4.4c). Furthermore, we quantified the incident-photon-to-current-efficiency (IPCE) at different potentials from 0.6 to 0.0 V vs. RHE (Figure 4.4d). The photocathode is active over the whole visible spectrum, reaching parts of the IR range, with an IPCE maximum at an excitation wavelength of 380 nm. The IPCE increases with lower potentials, reaching up to 6.25% at 0.0 V vs. RHE.

How photocorrosion can trick you: A detailed study on low-bandgap Li doped CuO photocathodes for solar hydrogen production

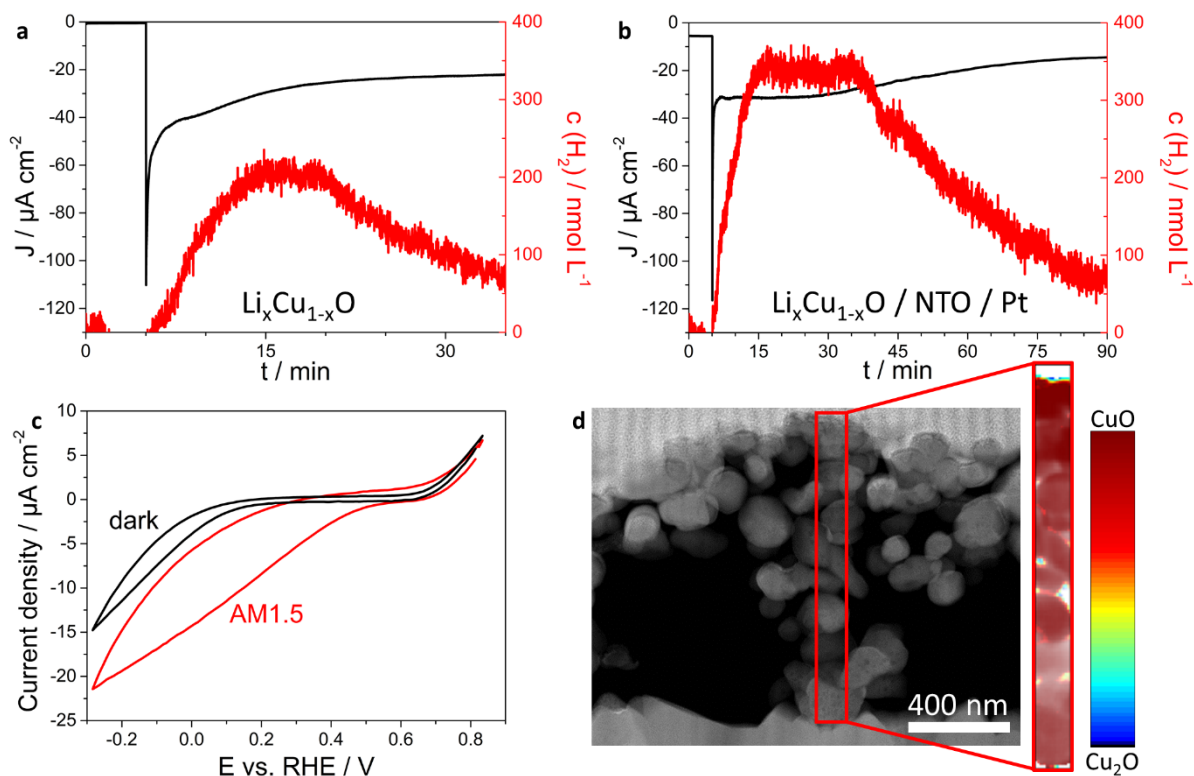


Figure 4.5. a, b) Chronoamperometric data (black) at 0.3 V vs. RHE with corresponding H_2 evolution (red), which is directly correlated to illumination starting after 5 minutes. While unprotected $\text{Li}_x\text{Cu}_{1-x}\text{O}$ films (a) start to degrade right after illumination, $\text{Li}_x\text{Cu}_{1-x}\text{O}/\text{NTO}/\text{Pt}$ photocathodes (b) show stable hydrogen evolution during the first 30 minutes. c, d) To probe the role of the water during the electrochemical reaction, a propylene carbonate electrolyte with an iodide triiodide redox couple was used as replacement. The CV measurement (c) as well as the TEM cross section with corresponding EELS map (d) of the film after a 15 minutes' stability test at 0.1 V vs. RHE show no sign of photocorrosion.

In addition, we performed stability tests of bare $\text{Li}_x\text{Cu}_{1-x}\text{O}$ and $\text{Li}_x\text{Cu}_{1-x}\text{O}/\text{NTO}/\text{Pt}$ films under illumination and quantified the evolved hydrogen. At a constant potential of 0.3 V vs. RHE, both photoelectrodes show a current response under illumination which is directly correlated to hydrogen evolution. The photocurrent of bare $\text{Li}_x\text{Cu}_{1-x}\text{O}$ decreases constantly and the hydrogen evolution stops after around 10 min of illumination due to photocorrosion of the material (ESI Figure 4.18), which results in a Faradaic efficiency of 61% after 10 minutes (Figure 4.5a). In contrast, the $\text{Li}_x\text{Cu}_{1-x}\text{O}/\text{NTO}/\text{Pt}$ device produces a stable photocurrent and evolves hydrogen with a Faradaic efficiency of 96% during the first 15 minutes after illumination (Figure 4.5b). Afterwards, both the hydrogen evolution and the current drop. We attribute the activity loss to the detachment of the Pt nanoparticles due to hydrogen bubble formation (see ESI Figure 4.17), whereas the decrease of

Conclusions

hydrogen concentration can be attributed to leakage from the photoelectrochemical cuvette-type cell used for hydrogen evolution experiments. We are currently working on the optimization of the cocatalyst deposition to increase both stability and activity of Li doped CuO photocathodes. Without direct contact to water, bare $\text{Li}_x\text{Cu}_{1-x}\text{O}$ is stable in a comparable potential range, as shown in a photoelectrochemical measurement in 1 mM iodide/triiodide ($\text{I}^- / \text{I}_3^-$) propylene carbonate electrolyte (Figure 4.5c) . No oxidative currents are detectable, which would indicate a $\text{Cu}^{1+} / \text{Cu}^{2+}$ reaction similar to the one shown in Figure 4.3b. Moreover, the $\text{Li}_x\text{Cu}_{1-x}\text{O}$ film was held under illumination at 0.1 V vs. RHE for 15 minutes. The corresponding EELS map of this sample shows no sign of photocorrosion. From this observation, we conclude that $\text{Li}_x\text{Cu}_{1-x}\text{O}$ could be used as stable photoabsorber as well as catalyst in a water-free electrolyte.

4.3 Conclusions

In this study, we have presented black Li-doped CuO thin films as cathodic light absorber for photoelectrochemical hydrogen evolution. The substitution of 4 at-% of Cu^{2+} with Li^+ ions has a substantial influence on the optical and electronic properties. The optical bandgap is reduced while both electrical conductivity and *p*-type character increase upon Li doping, which is beneficial for the application as photocathode material in a PEC tandem cell. DFT+U calculations confirm that the system becomes a *p*-type semiconductor for low Li concentrations due to the pronounced delocalization of holes. While $\text{Li}_x\text{Cu}_{1-x}\text{O}$ is stable in a non-aqueous electrolyte, it suffers from photocorrosion in contact with water. For the first time, the corrosion was studied in detail by cyclic voltammetry, X-ray photoelectron and electron energy loss spectroscopy. Therefore, we presented a detailed study on photocorrosion to provide a profound understanding of the underlying physical process which will be applicable to any copper based photocatalyst. Indeed, the performance of other reported photoelectrode systems should be critically revised. Under illumination and in direct contact with water, the reduced Cu_2O forms as distinct cubic crystals on the $\text{Li}_x\text{Cu}_{1-x}\text{O}$ surface. We demonstrate that $\text{Li}_x\text{Cu}_{1-x}\text{O}$ films can be stabilized to some degree against photocorrosion by using approaches common in photoelectrochemical research namely the application of a thin Nb:TiO₂ protection layer in combination with a Pt cocatalyst. Still, our described approach cannot solve the fundamental problem of intrinsic instability of metal oxide-based photocathodes in aqueous electrolytes. We suggest that similar fundamental problems of photocorrosion stability will be witnessed also in other copper containing photoabsorbers, therefore the photoelectrochemical performance and possible light-triggered material transformation should be revisited with special care. We doubt that the intrinsic

How photocorrosion can trick you: A detailed study on low-bandgap Li doped CuO photocathodes for solar hydrogen production

photocorrosion of copper oxide based photoelectrodes can be solved in any feasible way in aqueous electrolytes. However, the *in-situ* growth of Cu₂O due to photoreduction could be used for other types of electrochemical processes. As an example, the use as specific catalyst for CO₂ reduction in a water-free, methanolic electrolyte can be envisioned as both copper oxides were already described to be very active for this application.⁷⁰ By manipulating their electronic structure using various dopants like Li⁺, we expect to enhance both the efficiency of copper oxides and also fine tune the formation efficiencies for hydrocarbons like methane and ethylene.

Supporting Information

Supporting Information is available from the Wiley Online Library or from the author.

Acknowledgements

The presented work was supported by the German Research Foundation (DFG) via the SPP 1613, the Nanosystems Initiative Munich (NIM) and LMUexcellent funded by the DFG, the Bavarian research network 'Solar Technologies Go Hybrid', and the Center for Nanoscience (CeNS). Dr. Ilina Kondofersky, Dr. Markus Döblinger, Dr. Steffen Schmidt, Dr. Andreas Wisnet and Dr. Ramona Hoffmann are gratefully acknowledged for insightful discussions and help with the FIB and TEM measurements. We thank the students Leonard Moser and Jan Heinemann who participated in the research. We acknowledge computational time at SuperMUC of Leibniz Rechenzentrum, grant pr87ro.

Conflicts of interest

The authors declare no competing financial interest.

4.4 Supporting Information

4.4.1 Experimental details

4.4.1.1 Preparation of Li_xCu_{1-x}O films

Li_xCu_{1-x}O thin film photocathodes were prepared by spin coating (1000 rpm, 30 s, 100 μL) a precursor solution containing 1 M Cu(NO₃)₂ · 3 H₂O and 1 M LiNO₃ in ethanol. Undoped CuO films were prepared with the same method, but in absence of LiNO₃. Fluorine-doped tin oxide (FTO) coated glass (TEC 15 Glass, Dyesol) with a size of 1.5 cm x 2.0 cm was used as a substrate. The samples were subsequently calcined in air at 400 °C for 2 h (1.3 °C/min) and slowly cooled down to room temperature.

Supporting Information

4.4.1.2 Atomic Layer Deposition of Niobium doped Titanium oxide films

Atomic layer deposition of niobium doped titanium oxide thin films was carried out in a Picosun R-200 reactor at a temperature of 200 °C and a base pressure of 2 hPa. Nitrogen (Air Liquide, 99.999 %) was used as the purge and carrier gas. The carrier gas line flow during pulses was 40 sccm. Titanium isopropoxide (TIPO, Aldrich, 99.999 %) was supplied from a stainless steel vessel at 85 °C, niobium ethoxide (NEO, Strem, 99.9+ %) was evaporated from a glass vessel at 160 °C. Ultrapure water (MilliQ, 18.2 MΩ cm) was used as oxygen source and held in a stainless steel cylinder at room temperature. Each ALD cycle for TiO₂ includes two TIPO pulses (1.6 s pulse, 4.5 s static exposure, 6 s purge) and one water pulse (2 s pulse, 4.5 s static exposure, 7.5 s purge). The resulting growth rate was 0.038 nm cycle⁻¹ with a non-uniformity of 4 % across a 20 cm wafer. The ALD cycle for niobium oxide consisted of four NEO pulses (1.6 s pulse, 6.5 s static exposure, 6 s purge) and one water pulse as in the TiO₂ process. The resulting growth rate was 0.068 nm cycle⁻¹ with a non-uniformity of 4 % across a 20 cm wafer. Mixed oxide layers were grown by alternating 6 TiO₂ cycles with 1 NbO_x cycle resulting in an amorphous Ti_{0.80}Nb_{0.20}O_x dense film.

4.4.1.3 Pt deposition

For the deposition of Pt co-catalyst nanoparticles, an NTO-protected Li_xCu_{1-x}O film, a platinum mesh counter electrode and a Hg/Hg₂SO₄/K₂SO₄ (sat.) reference electrode were connected to a μ-Autolab III potentiostat and immersed in a methanolic 1 mM H₂PtCl₆ solution. Afterwards, a static potential of -0.557 V vs. Hg/Hg₂SO₄ was applied for 10 minutes without illumination.

4.4.1.4 Crystallographic Characterization

Powder X-ray diffraction (XRD) patterns were acquired on a STOE powder diffractometer (Cu-K_α, λ = 1.5406 Å) equipped with a position-sensitive Mythen-1K detector in transmission geometry. Lanthanum hexaboride (NIST LaB6 SRM 660b; space group: Pm $\bar{3}$ m; a = 4.15689(8) Å) was used as an internal standard for calibration of diffraction line positions. The XRD pattern of the sample and ~5% of lanthanum hexaboride were collected over a 2θ range of 10 to 81° with a step size of 0.015°. Li_xCu_{1-x}O unit cell parameters were obtained using the results from the Rietveld refinements⁷¹ of a powder diffraction pattern. The observed parameters are structurally closely related to those of tenorite (CuO, space group: C2/c; a = 4.6853(3) Å; b = 3.4257(1) Å; c = 5.1303(3) Å; β = 99.549(4)°; JCPDS-ICDD PDF card No. 45-937). XRD patterns of the thin film electrodes were acquired on a Bruker D8 Discover with Ni-filtered Cu K_α radiation and a LynxEye position-sensitive detector.

How photocorrosion can trick you: A detailed study on low-bandgap Li doped CuO photocathodes for solar hydrogen production

4.4.1.5 Electron microscopy

Scanning electron microscopy (SEM) measurements were performed on an FEI Helios NanoLab G3 UC scanning electron microscope using a 1 - 30 kV field emission gun and an Oxford instruments energy dispersive X-ray (EDX) spectroscopy detector.

A probe-corrected FEI Titan Themis transmission electron microscope (TEM) with a field emission gun (X-FEG) operated at 300 kV was applied to determine morphology, crystallography and elemental distribution. High-resolution TEM (HRTEM) and bright field (BF) images were received with a Ceta 16M camera while scanning TEM (STEM) measurements were performed with an annular dark field (ADF) detector. The thin film material was carefully scraped from the substrate with a razor blade and the powder was dispersed in ethanol. This liquid was deposited dropwise on a holey carbon grid to prepare the sample.

In addition, focused ion beam (FIB)-machined lamellae of film cross-sections were prepared in a FEI Helios 600i Dual Beam workstation. To locally probe the oxidation state of Cu, electron energy loss spectroscopy (EELS) in a transmission electron microscope (TEM) was used. Ion beam assisted Pt deposition with dimensions of $10 \times 2 \times 2 \mu\text{m}^3$ (length \times width \times height) was applied for sample surface protection during Ga^+ ion milling. $2 \mu\text{m}$ thick TEM lamellae were cut out of the films, transferred to a Mo TEM grid and initially thinned down to a thickness of around $0.7 \mu\text{m}$ using an acceleration voltage of 30 kV and beam currents of 430 pA and 230 pA. Final lamellae thinning was performed at 5 kV and 120 pA and subsequent polishing to minimize beam damage was carried out at 2 kV and 72 pA until a thickness of below 100 nm was reached.

Electron energy loss spectroscopy (EELS) data were acquired in scanning transmission mode at 300 kV using a probe-corrected FEI Titan Themis equipped with a monochromator and an Gatan Enfium ER spectrometer. An energy resolution of 0.2 eV was realized during the experiment, using a dispersion of 0.1 channels/pixel and a spectrometer entrance aperture of 5 mm. Subpixel scanning was used to reduce the electron beam damage during the spectrum acquisition on the sample yielding pixel sizes between 2 and 5 nm.

4.4.1.6 ^7Li NMR

Solid-State MAS NMR: Experiments were performed at 11.74 T on a Bruker DSX 500 spectrometer equipped with a commercial 4 mm triple-resonance MAS probe at ^7Li frequencies of 194.399 MHz. All experiments were performed in ZrO_2 rotors at room temperature. The one-dimensional ^7Li NMR

Supporting Information

spectrum was acquired with a 90° pulse length of 2.0 μ s, a recycle delay of 64 s and at a sample spinning frequency of 8 kHz.

4.4.1.7 Hall measurements

Hall measurements were performed using the *van der Pauw* technique in a four-point setup. For the characterization, pellets were pressed (80 kg/cm²) from powders (thickness 0.31 mm) and sintered at 400 °C for 24 h (2 °C/min) prior to the measurement.

4.4.1.8 Optical Characterization

UV-Vis spectra were obtained on a Perkin Elmer Lambda 1050 UV/Visible/NIR spectrophotometer with an integrating sphere. The absorbance of the films was calculated from both the transmittance and reflectance of the films correcting for the absorbance of the FTO substrate by applying an expression derived by Klahr *et al.*⁷² to the UV-Vis data.

4.4.1.9 Photoelectrochemical Characterization

Current-voltage (CV) and chrono-amperometry (CA) measurements were performed in a three electrode setup. A custom built closed one-compartment cell allowed a photoelectrochemical characterization in the absence of air. Therefore, argon or nitrogen purging of the aqueous 0.1 M Na₂SO₄ or 1mM iodide/triiodide (I⁻/I₃⁻) propylene carbonate electrolyte was started 30 minutes before the experiment and was continued during the measurement. The thin film photocathodes were masked with Teflon adhesive tape leaving free an area of 0.196 cm² for illumination. Argent conductive varnish was used to improve the electrical contact to the potentiostat. The photoelectrode, a Hg/Hg₂SO₄/K₂SO₄ (sat.) or RHE reference electrode and a platinum mesh counter electrode were connected to a μ -Autolab III potentiostat. Measurements were either performed in the dark or under simulated sunlight illumination. For the latter, the thin film electrodes were illuminated through the substrate side by an AM1.5G solar simulator (Solar Light Model 16S) at 100 mW cm⁻². CV measurements were performed either in the dark or under illumination by starting at 0.85 V vs. RHE, scanning at a sweep rate of 20 mV/s from positive to negative potentials down to 0.0 V vs. RHE and back to 0.9 V vs. RHE. In total, two cycles were performed for each measurement. Linear sweep voltammograms were performed at a scan rate of 2 mV/s, starting at 0.7 V vs. RHE and scanning down to -0.1 V vs. RHE. The light source was chopped manually. In the case of CA measurements, a steady potential was applied for a defined time and the resulting current was recorded in a time interval of 1 s.

4.4.1.10 Hydrogen detection

In order to verify that the observed photocurrent results from the reduction of water, a micro sensor (*Unisense A/S H₂-NPLR*) with a hydrogen selective silicone membrane was combined with a three electrode PEC setup. The micro sensor was calibrated in a two-point measurement using the corresponding program (*Unisense A/S SensorTrace 1.4*). The data point for $c = 0$ mM was acquired in Nitrogen-purged electrolyte (aqueous 0.1 M Na₂SO₄ solution at pH 7), while the second measuring point of $c = 40.7$ mM was recorded in the same electrolyte purged with forming gas (5 vol% H₂ in Ar, *AirLiquide ARCAL15*) for 20 minutes, taking in account the saturation concentration of pure H₂ gas in water of 813 $\mu\text{M atm}^{-1}$.⁷³ To minimize the electrolyte volume and therefore maximize the detectable hydrogen concentration, a 2 mL poly(methyl methacrylate) (PMMA) cuvette was used as PEC cell. The working electrode was glued on a drilled-in hole (\varnothing 7 mm) and connected to the potentiostat together with a Platinum wire counter electrode and a Hg/Hg₂SO₄/K₂SO₄ (sat.) reference electrode and filled with 1.7 mL electrolyte. The hydrogen micro sensor was placed in the cuvette, which was subsequently sealed using modelling clay. The hydrogen concentration was recorded with an interval time of 10 seconds. As the polarization of the micro sensor is very sensitive and critical for a correct measurement, magnetic stirring was not possible in order to avoid any interfering signals.

4.4.1.11 Computational details

Density-functional theory (DFT) calculations were performed using the VASP⁷⁴⁻⁷⁵ code with projector-augmented wave (PAW) pseudopotentials⁷⁶. The generalized-gradient approximation (GGA)⁷⁷ was used for the exchange-correlation functional, including an on-site Hubbard U term. The rotationally invariant approach of Dudarev et al.⁶² was adopted for the GGA+ U calculations. A Hubbard- U value for Cu of 8.0 eV gives an indirect gap of 1.46 eV for CuO, in close agreement with the 1.39 eV determined from the Tauc plot. This is consistent with previous LDA+ U results.⁷⁸ We note that previous experimental values range between 1.35-1.7eV.⁸⁻¹¹ To model different doping concentrations two different cell sizes with 8 and 64 atoms were adopted, corresponding to the bulk CuO and a 2x2x2 supercell, respectively. A plane-wave cut-off of 500 eV and a Monkhorst-Pack k-point mesh of 8x8x8 and 4x4x4 were used for the two unit cells, respectively. The Li solution energy (SE) indicates the preferred lattice positions of Li incorporation in the CuO structure and is defined as follows:

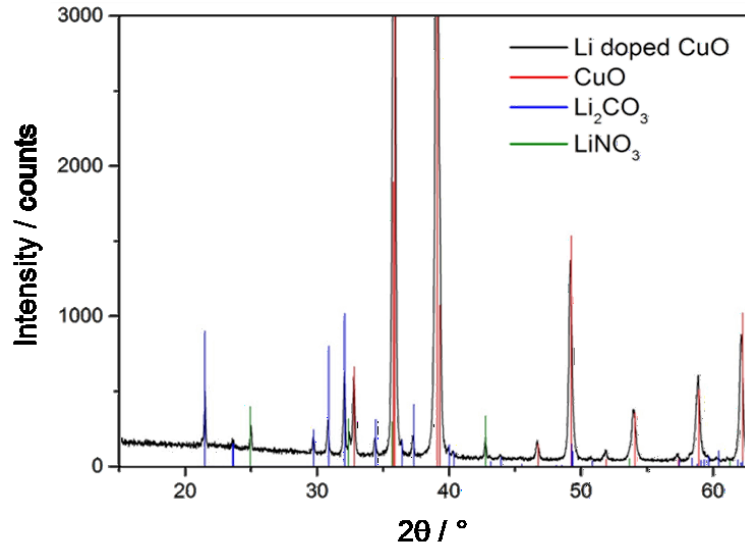
$$SE_{Li} = E_{Li_xCu_{1-x}O} - E_{CuO} - NE_{Li} + ME_{O/Cu} \quad \text{Eq. 1}$$

Supporting Information

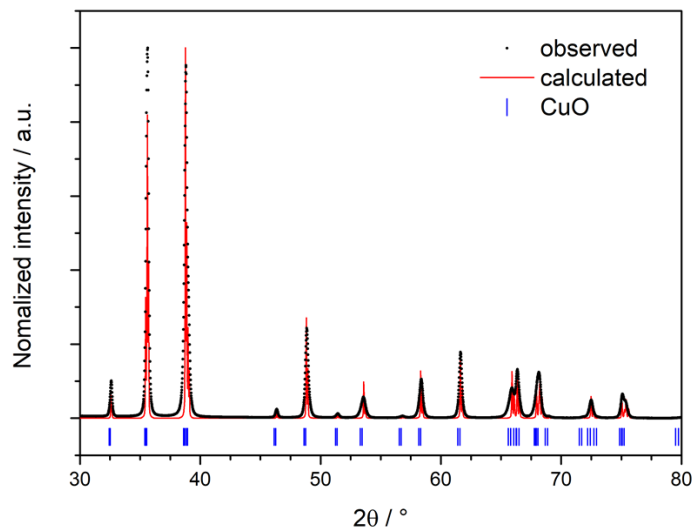
E_{Li_xCuO} and E_{CuO} represent the total energy of the doped and undoped structure, respectively. E_{Li} and $E_{O/Cu}$ is the energy of the elemental ground state of lithium, oxygen and copper. N is the number of lithium atoms substituted by M oxygen or copper. To calculate the solution energy a Cu or O was substituted by a Li atom and the structure fully relaxed.

How photocorrosion can trick you: A detailed study on low-bandgap Li doped CuO photocathodes for solar hydrogen production

4.4.2 Additional figures

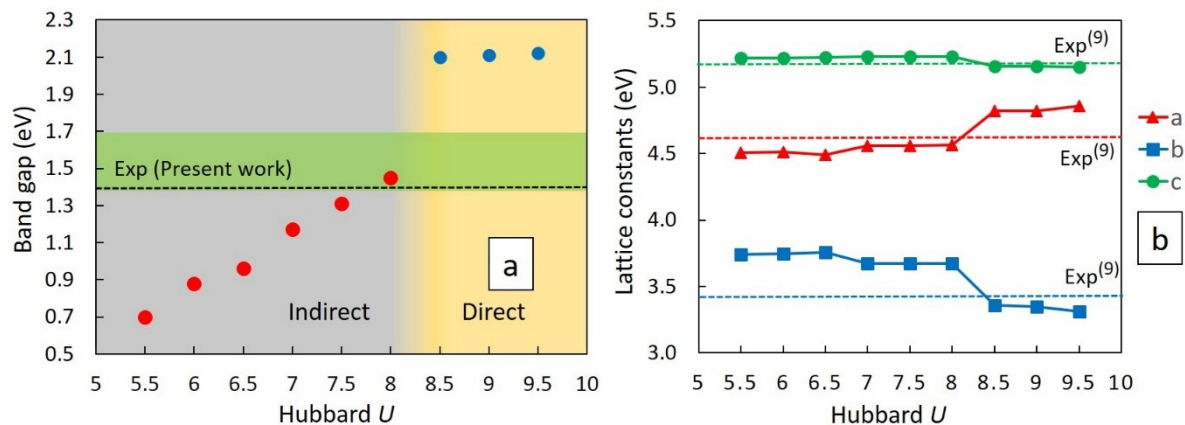


ESI Figure 4.1. XRD pattern of the film obtained directly after calcination. The film is a mixture of Li doped CuO, Li_2CO_3 and LiNO_3 . To obtain the single Li doped CuO phase the film is immersed in water for 2 hours to remove Li_2CO_3 and LiNO_3 .

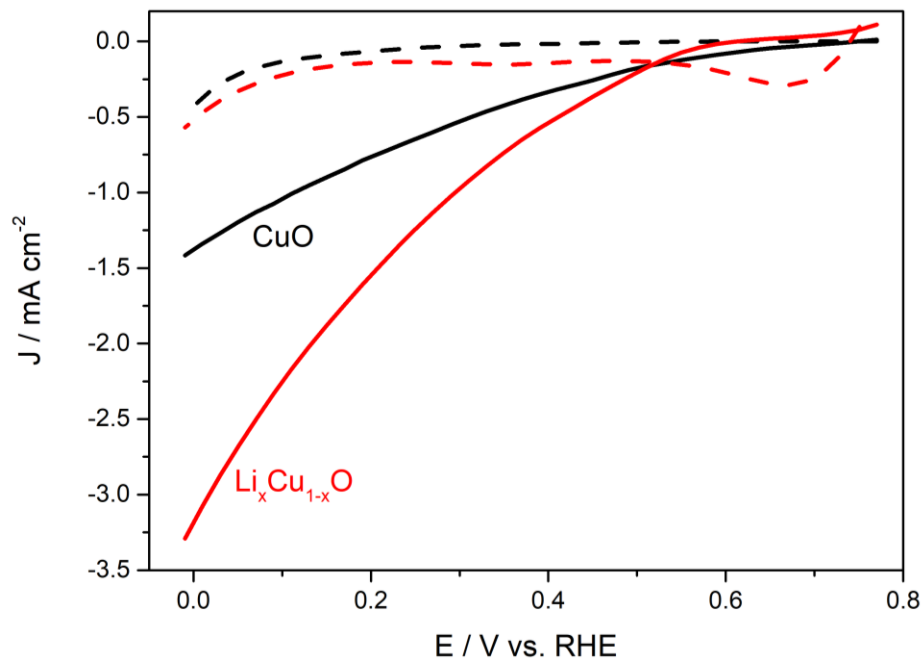


ESI Figure 4.2. Rietveld refinement of undoped CuO with observed data (·) and calculated pattern (red line), blue vertical bars mark the positions of the diffraction lines of CuO (tenorite).

Supporting Information

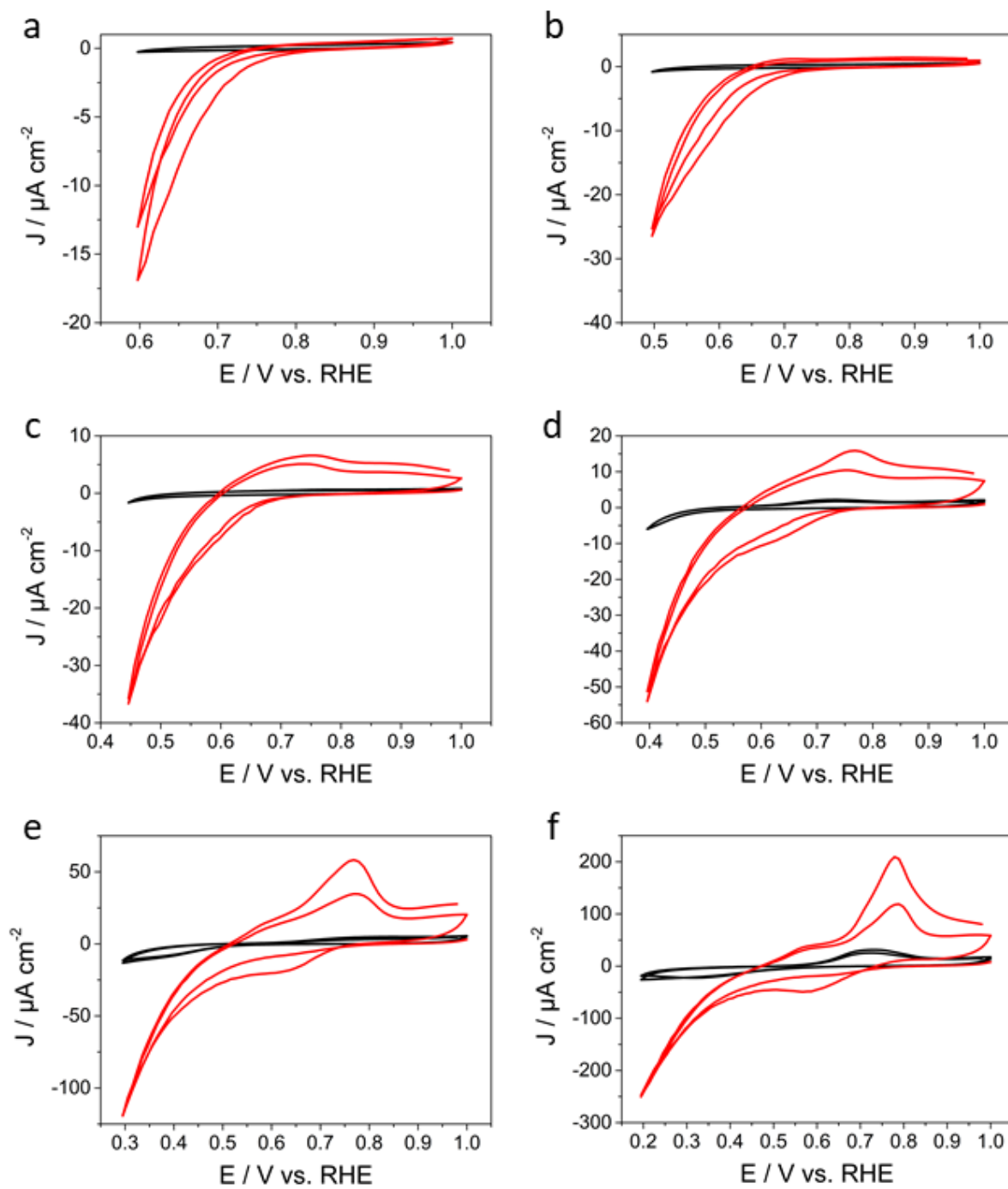


ESI Figure 4.3. a) Band gap and b) lattice constants of CuO as a function of Hubbard U . Experimental band gaps range between 1.35-1.7 eV, highlighted in green.^{36, 79-81} The band gap of 1.39 eV determined from the Tauc plot in this work is marked by a dashed line in a). The experimental lattice parameters denoted by dashed lines in b) are from Åsbrink et al..⁸²



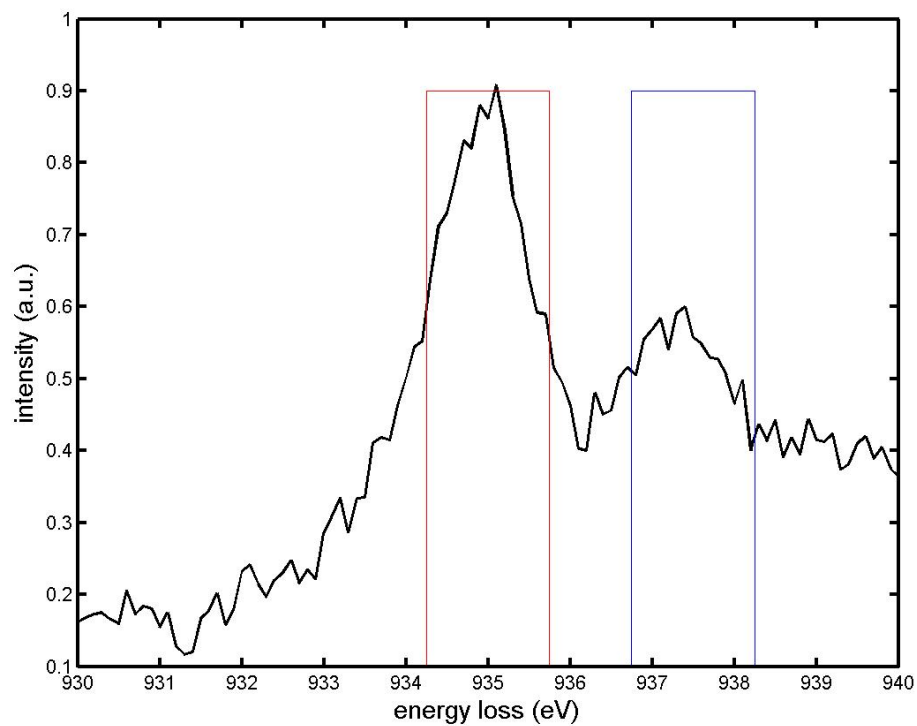
ESI Figure 4.4. Linear sweep voltammetry measurements of bare copper oxide photocathodes in the dark (dashed lines) and under AM1.5 illumination (solid lines). $\text{Li}_x\text{Cu}_{1-x}\text{O}$ films (red) exhibit significantly higher photocurrents compared to undoped CuO films.

How photocorrosion can trick you: A detailed study on low-bandgap Li doped CuO photocathodes for solar hydrogen production



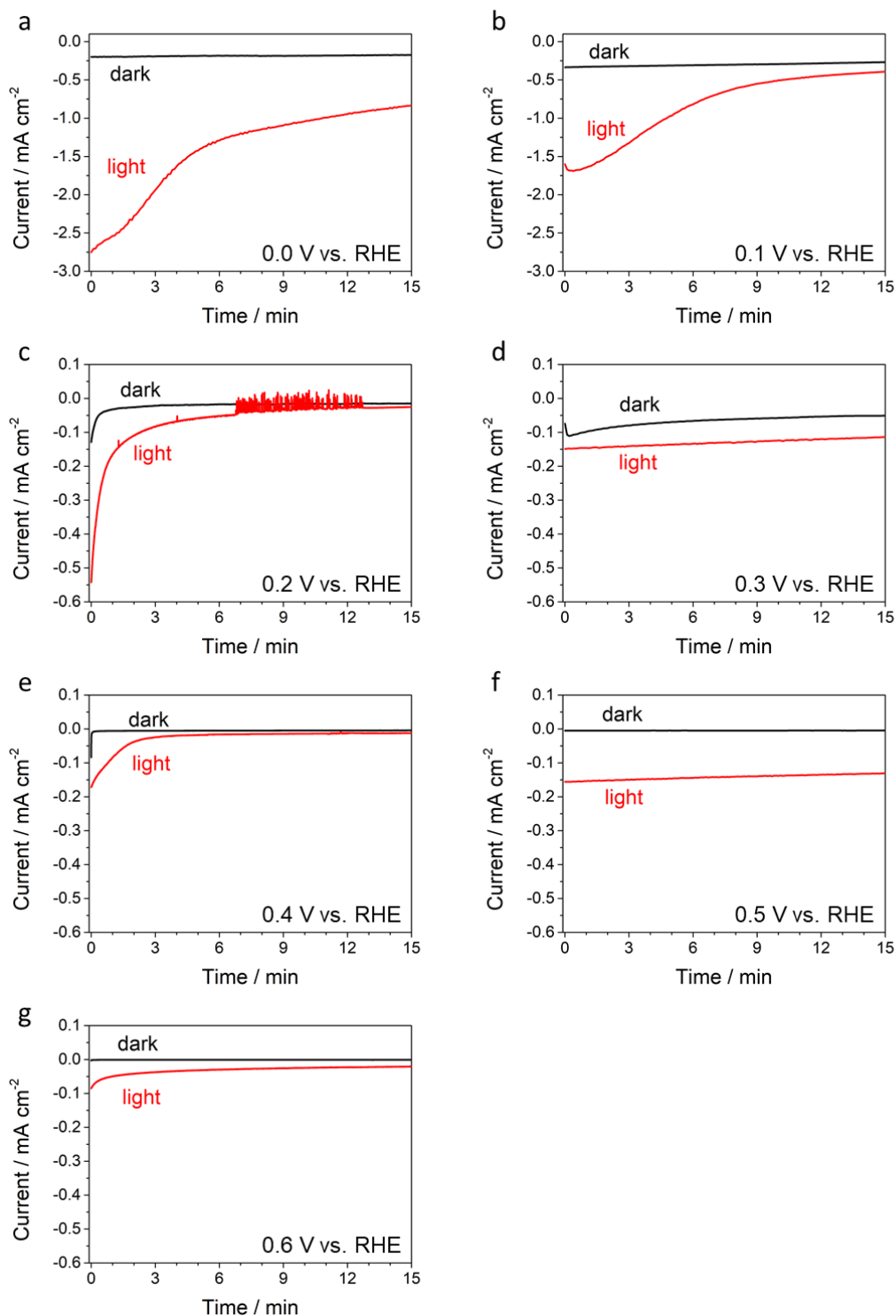
ESI Figure 4.5. Cyclic voltammety measurements of a bare $\text{Li}_x\text{Cu}_{1-x}\text{O}$ electrode in successive order from a – f. The potential range was extended stepwise to lower potentials, and consequently the photocorrosion gets more and more pronounced.

Supporting Information



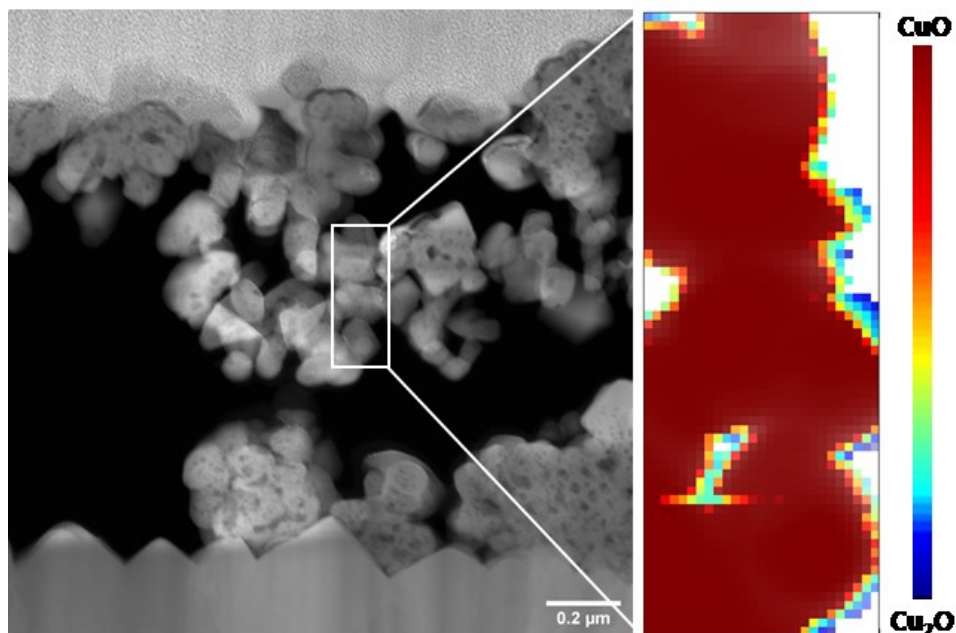
ESI Figure 4.6. To generate the EELS map tracking the oxidation state of Copper, the spectra were first aligned. After subtraction of the background via a power-law fit the intensity ratio of the Cu-L₃ edge of CuO (red) and Cu₂O (blue) were integrated in defined energy windows. The distribution of the two oxidation states is estimated by this intensity ratio.

How photocorrosion can trick you: A detailed study on low-bandgap Li doped CuO photocathodes for solar hydrogen production

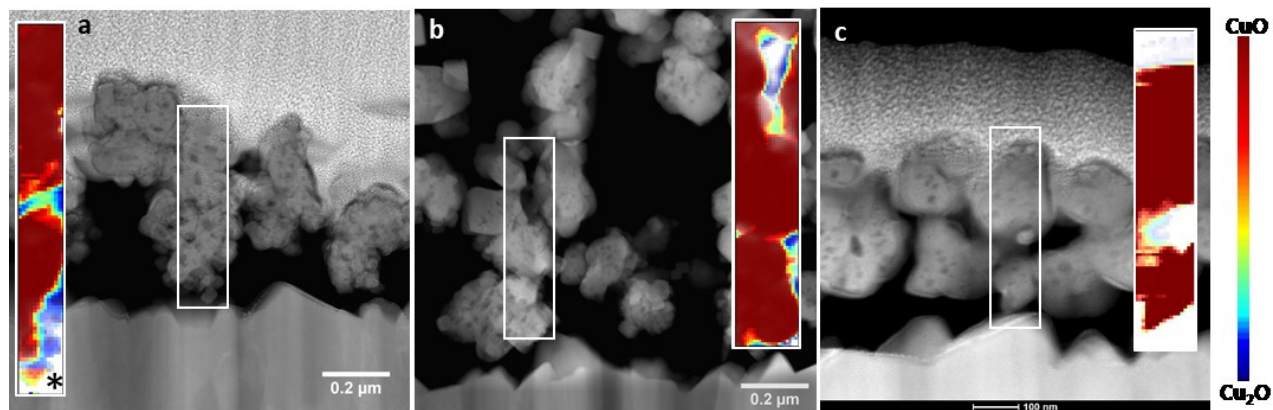


ESI Figure 4.7. Chronoamperometric data of unprotected $\text{Li}_x\text{Cu}_{1-x}\text{O}$ photocathodes at various potentials from 0.0 to 0.6 V vs. RHE in the dark (black) and under AM1.5 illumination (red). Afterwards, the respective samples were characterized by XPS (see Figure 3c,d). The spikes in (c) were caused by an increased flow of nitrogen purging.

Supporting Information

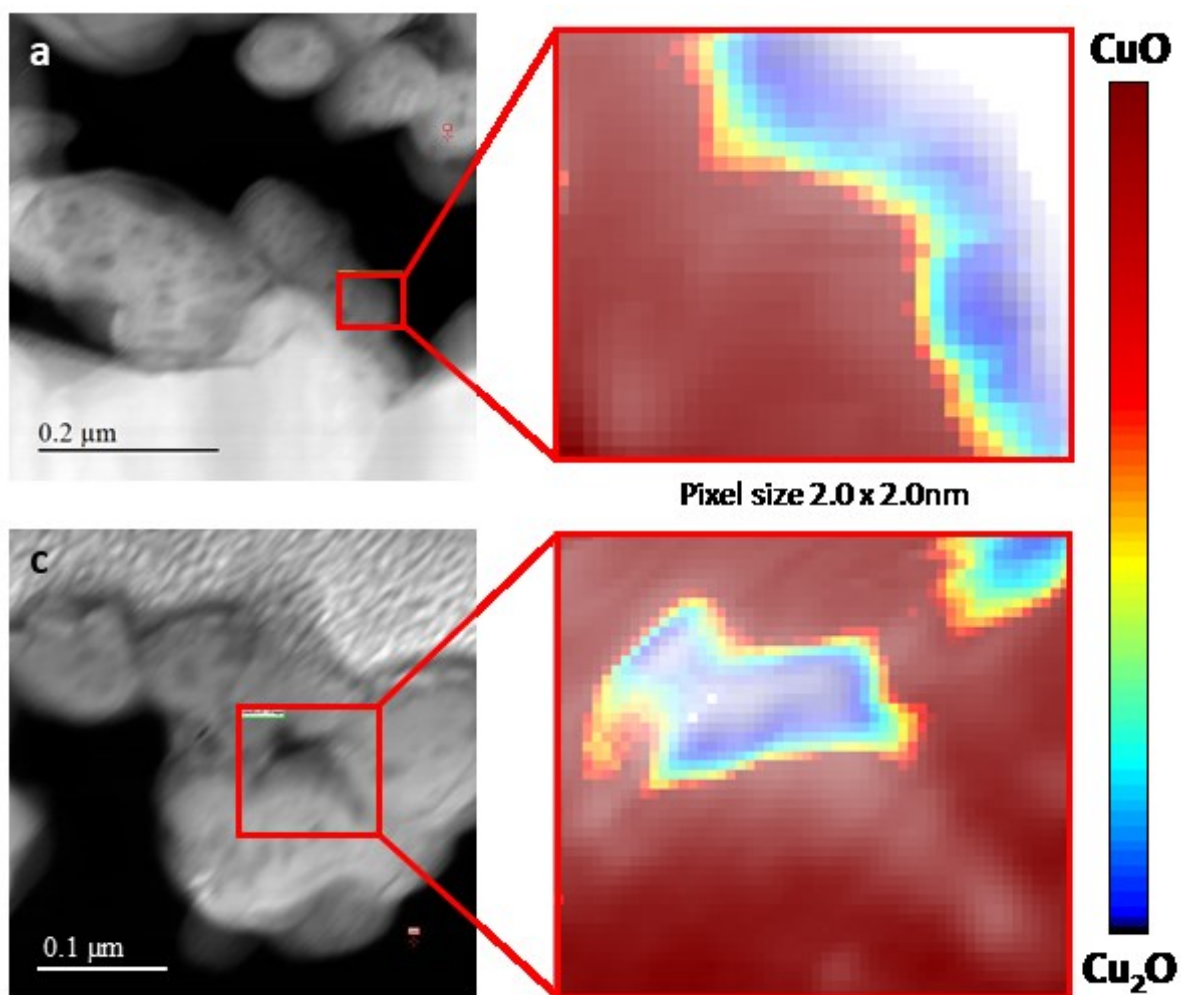


ESI Figure 4.8. An as-synthesized sample, which was never used in an electrochemical measurement, was used to investigate the effect of the FIB sample preparation. While the sample preparation causes a slight reduction of some regions of the $\text{Li}_x\text{Cu}_{1-x}\text{O}$ surface, no cubic Cu_2O crystals are formed by this procedure. Therefore, the FIB preparation method is supposed to have no effect on the photocorrosion study of $\text{Li}_x\text{Cu}_{1-x}\text{O}$ photocathodes.



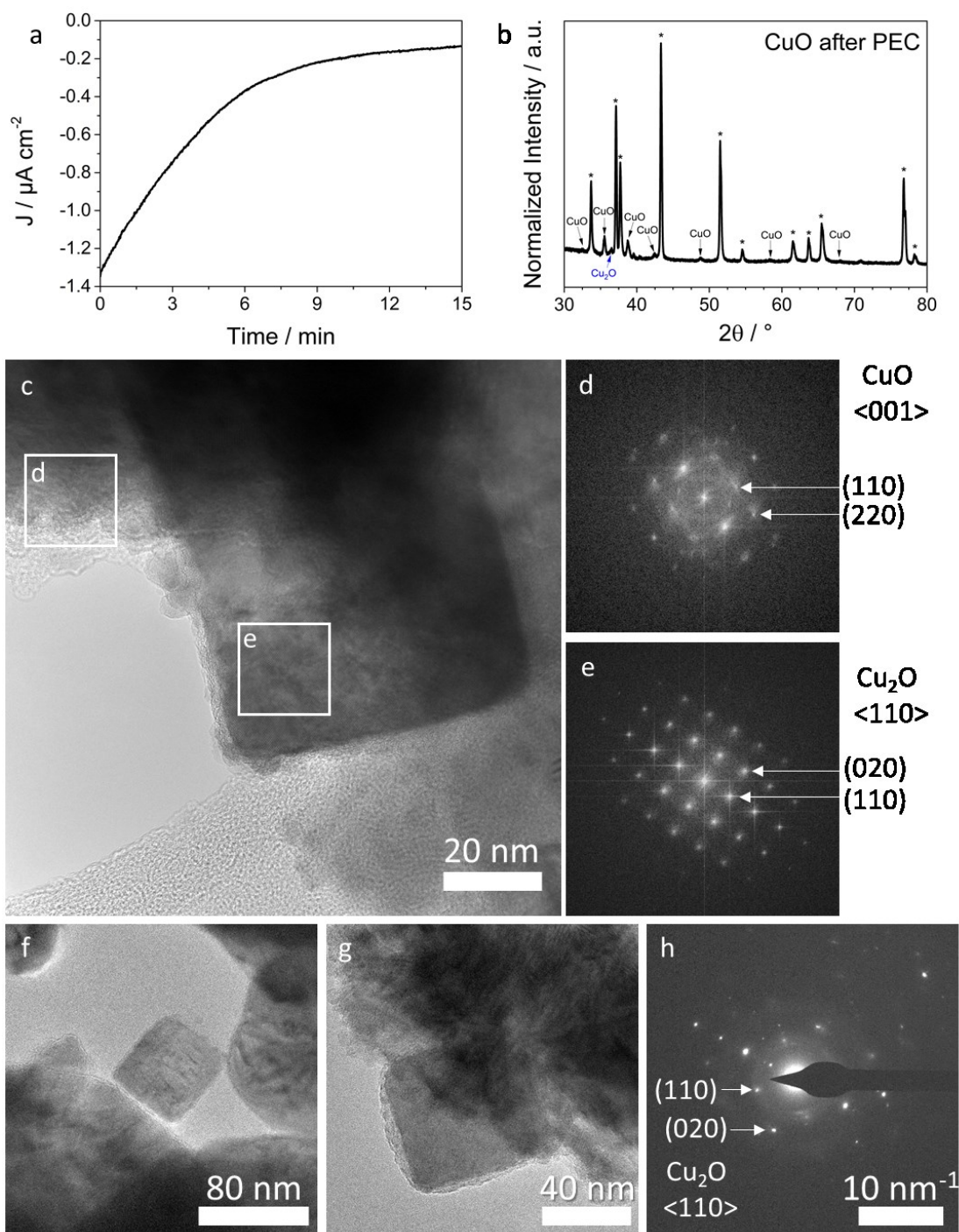
ESI Figure 4.9. $\text{CuO}/\text{Cu}_2\text{O}$ ratio maps based on EELS data of samples used for PEC water splitting at different potentials. (a) 0.1 V for 15 min, (b) 0.2 V for 15 min and (c) 0.3 V for 15 min. *Artifact of the spectrum alignment, should be Cu_2O .

How photocorrosion can trick you: A detailed study on low-bandgap Li doped CuO photocathodes for solar hydrogen production

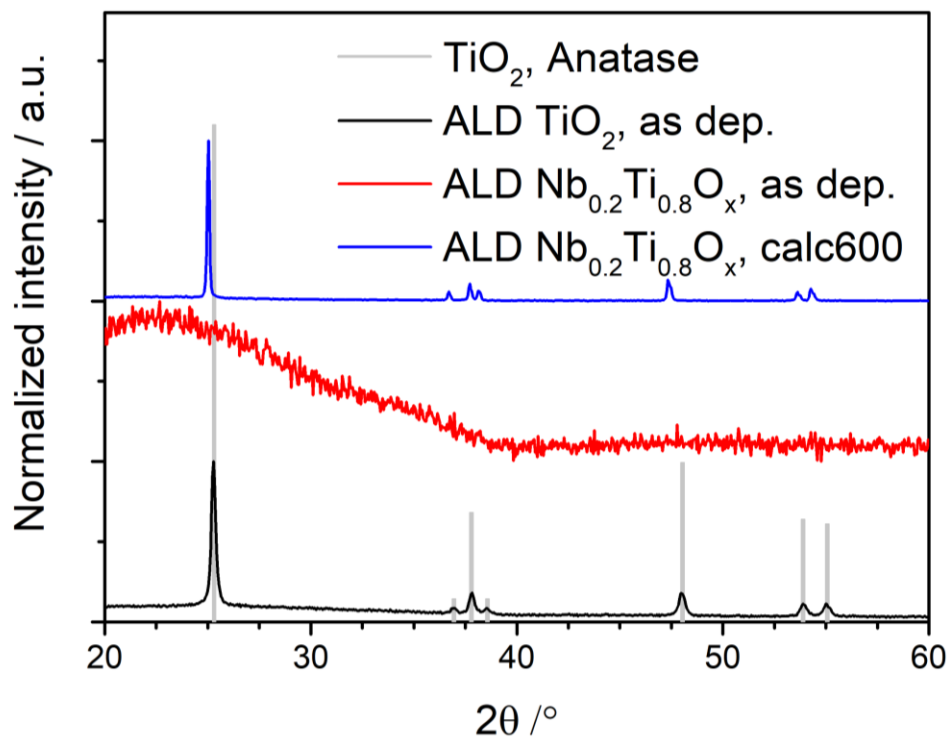


ESI Figure 4.10. TEM cross section images of $\text{Li}_x\text{Cu}_{1-x}\text{O}$ films after an electrochemistry experiment performed for 15 min at 0.3 V vs. RHE under illumination (a, c) with corresponding EELS maps (b, d, pixel size 4 nm^2).

Supporting Information

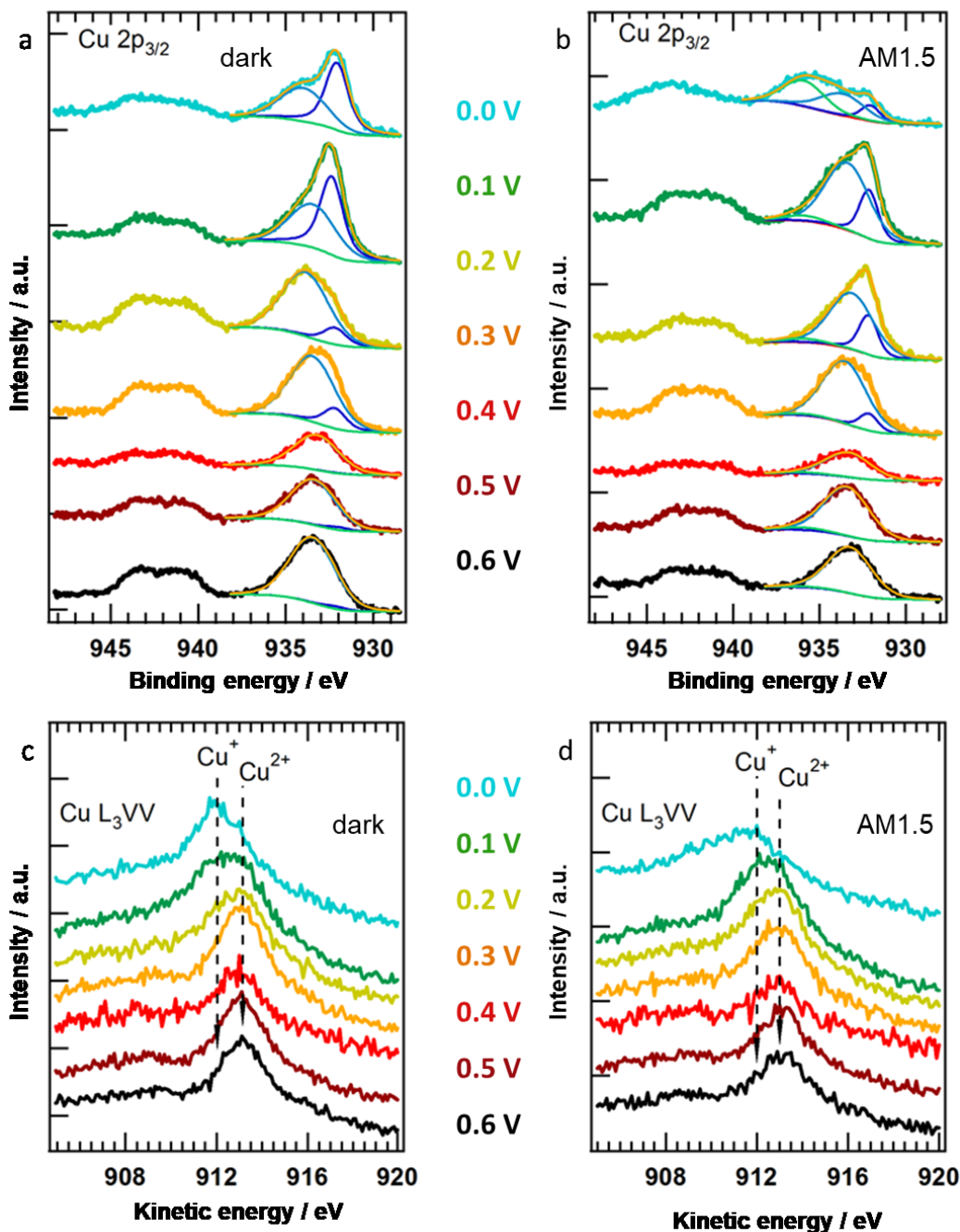


ESI Figure 4.11. a) Potentiostatic measurement of a bare, undoped CuO electrode at 0.2 V vs. RHE under AM 1.5 illumination. b) XRD pattern of the CuO film after the 15-minute stability test shown in (a), indicating the formation of Cu₂O (blue). c) High resolution TEM image showing one square crystal grown on the surface of the CuO structure. The FFTs of the marked regions were indexed for CuO (d) and Cu₂O (e). f, g) Further TEM images of Cu₂O grown on different spots of the CuO surface. h) Electron diffraction pattern of the cubic crystal depicted in (g) with the reflections indexed for Cu₂O.



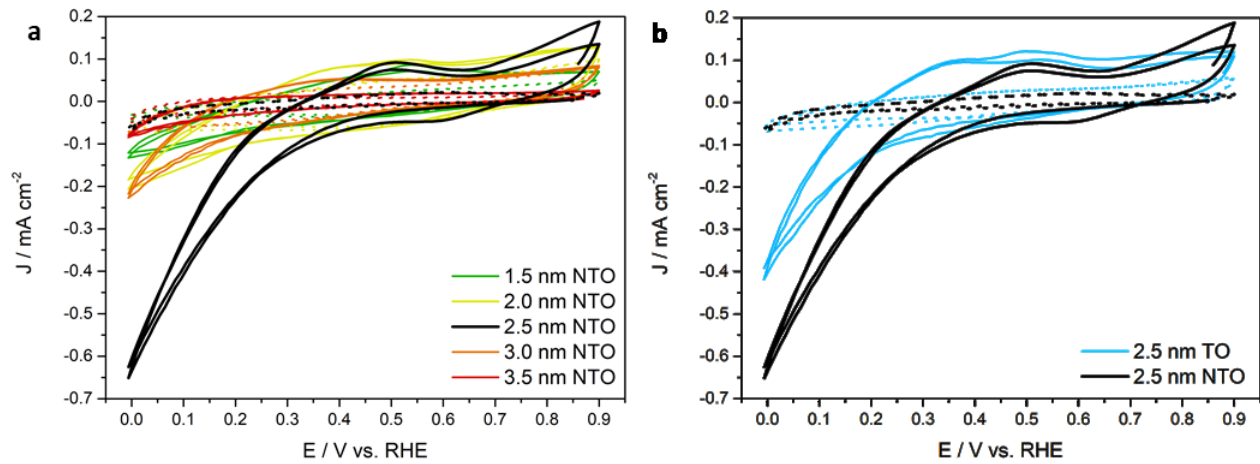
ESI Figure 4.12. XRD pattern of $Ti_{0.8}Nb_{0.2}O_x$ ALD films as deposited (black). These layers are amorphous, in contrast to pure TiO_2 layers (black). After calcination in 5% H_2/N_2 atmosphere at 600°C (blue), crystalline $Ti_{0.8}Nb_{0.2}O_x$ ALD layers are obtained.

Supporting Information

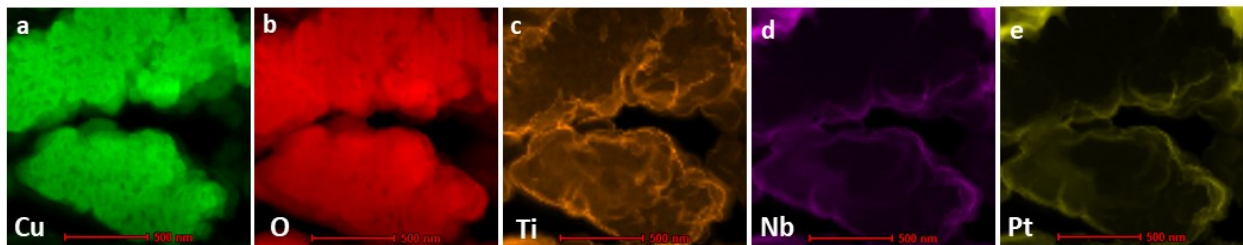


ESI Figure 4.13. XPS characterization of $\text{Li}_x\text{Cu}_{1-x}\text{O}$ photocathodes after electrochemical stability tests at the respective potentials vs. RHE for 15 minutes each in the dark (left side, a and c) and under AM1.5G illumination (right side, b and d). The upper two diagrams show the deconvolution of the $\text{Cu } 2p_{3/2}$ peaks into a Cu(I) -component at 932.4 eV and a Cu(II) -component at ca. 933.6 eV. At the lowest potential (0.0 V vs. RHE) a third feature appears at higher binding energies, which might be caused by differential charging of the samples as a result of preceding corrosion. The corresponding $\text{Cu } L_3VV$ Auger signals are displayed in the graphs (c) and (d) below with the positions of the Cu(I) and Cu(II) peaks indicated by the dashed lines.

How photocorrosion can trick you: A detailed study on low-bandgap Li doped CuO photocathodes for solar hydrogen production

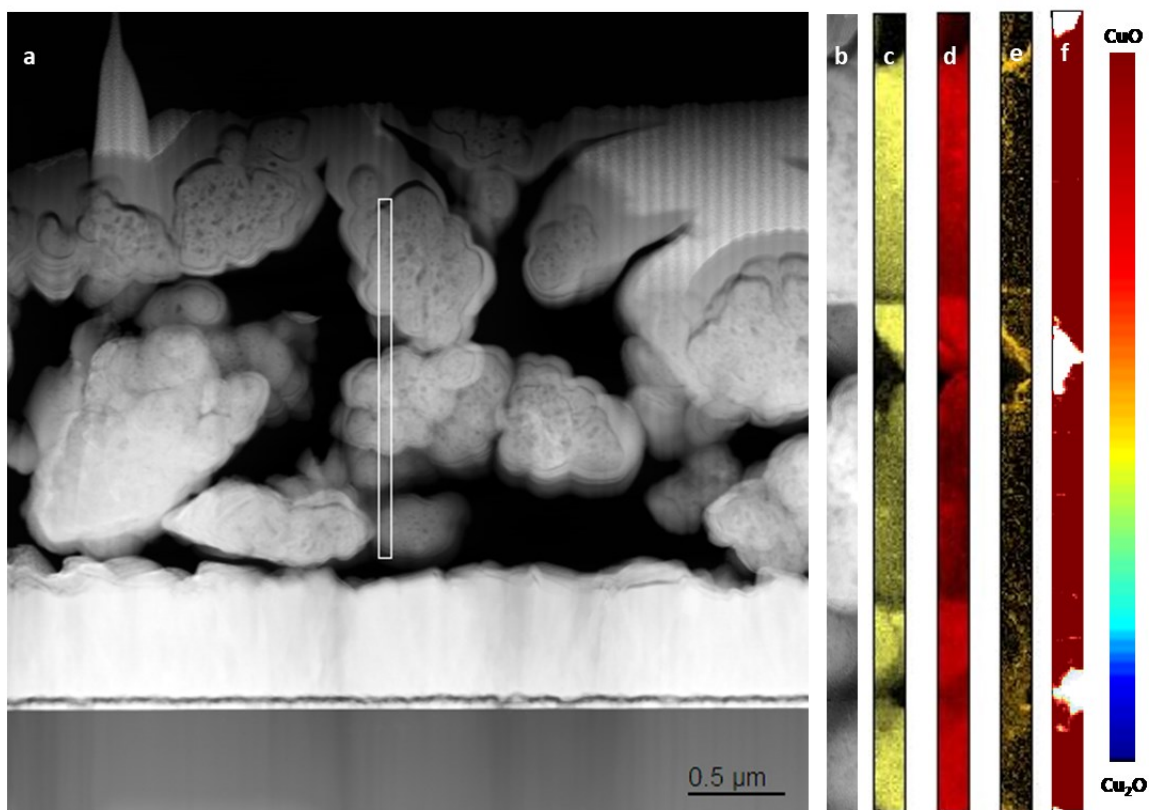


ESI Figure 4.14. Cyclic voltammograms of $\text{Li}_x\text{Cu}_{1-x}\text{O}$ photocathodes covered with $\text{Nb}:\text{TiO}_2$ (NTO) or TiO_2 (TO). A protection layer of 2.5 nm NTO showed the highest activity of all tested NTO layer thicknesses (a) and also an improvement compared to undoped TiO_2 (b).

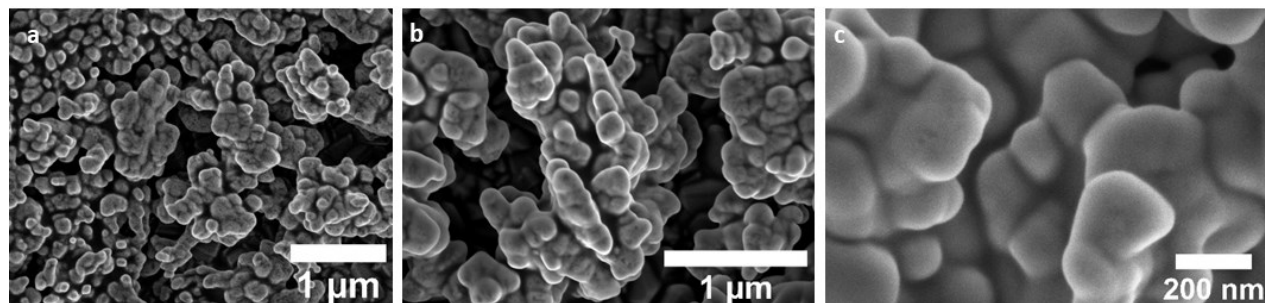


ESI Figure 4.15. Energy dispersive X-ray (EDX) mappings of a $\text{Li}_x\text{Cu}_{1-x}\text{O}/\text{NTO}/\text{Pt}$ TEM cross section. The $\text{Li}_x\text{Cu}_{1-x}\text{O}$ structure (a, b) is homogeneously covered with $\text{Nb}:\text{TiO}_2$ (NTO, c, d) and Pt (e).

Supporting Information

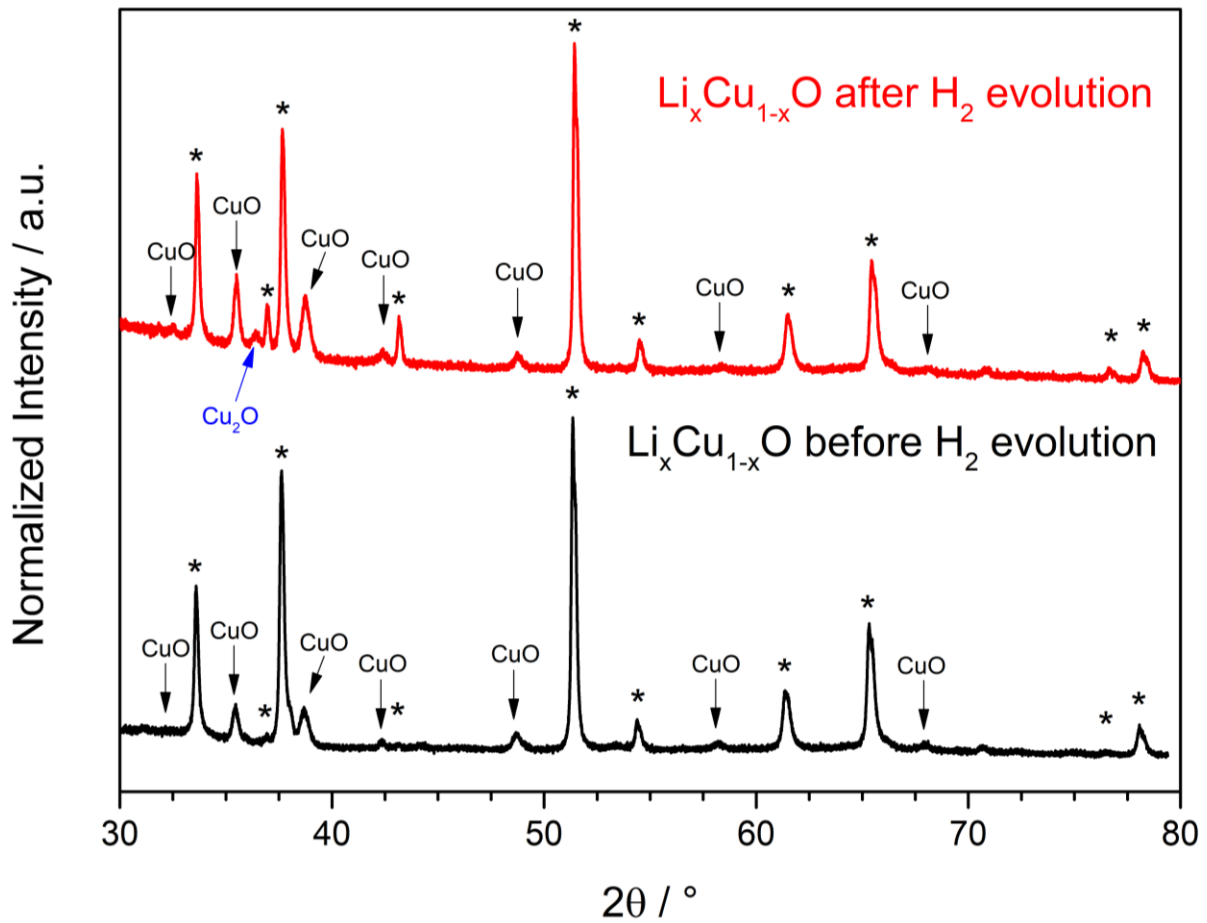


ESI Figure 4.16. a) TEM cross section of a $\text{Li}_x\text{Cu}_{1-x}\text{O}/\text{NTO}/\text{Pt}$ device held for 15 min at 0.2 V vs. RHE under AM1.5 illumination. The marked area (white, b) was used for EDX mapping of Cu (c), O (d) and Ti (e). The corresponding EELS map (f) shows no sign of photocorrosion.



ESI Figure 4.17. SEM top view images of a $\text{Li}_x\text{Cu}_{1-x}\text{O}/\text{NTO}/\text{Pt}$ photocathode after 90 minutes at 0.3 V vs. RHE and AM1.5G substrate illumination. The 20 nm sized Pt particles are not adhering on the surface anymore, which is believed to cause the observed loss in activity.

How photocorrosion can trick you: A detailed study on low-bandgap Li doped CuO photocathodes for solar hydrogen production



ESI Figure 4.18. XRD patterns of unprotected $\text{Li}_x\text{Cu}_{1-x}\text{O}$ films before (black) and after (red) the hydrogen evolution test at 0.3 V vs. RHE (Figure 4.5a). After 30 minutes of illumination and progressing photocorrosion, the cuprite phase of Cu_2O emerges (blue). Reflections of the FTO substrate are marked with (*).

References

4.5 References

- (1) *Basic research needs for solar energy utilization*; Office of Basic Energy Sciences, US Department of Energy: 2005.
- (2) Fornarini, L.; Nozik, A. J.; Parkinson, B. A., The energetics of p/n photoelectrolysis cells. *The Journal of Physical Chemistry* **1984**, *88* (15), 3238-3243.
- (3) Heller, A., Hydrogen-Evolving Solar Cells. *Science* **1984**, *223* (4641), 1141-1148.
- (4) Walter, M. G.; Warren, E. L.; McKone, J. R.; Boettcher, S. W.; Mi, Q.; Santori, E. A.; Lewis, N. S., Solar Water Splitting Cells. *Chemical Reviews* **2010**, *110* (11), 6446-6473.
- (5) van de Krol, R.; Liang, Y.; Schoonman, J., Solar hydrogen production with nanostructured metal oxides. *Journal of Materials Chemistry* **2008**, *18* (20), 2311.
- (6) Khaselev, O.; Bansal, A.; Turner, J. A., High-efficiency integrated multijunction photovoltaic/electrolysis systems for hydrogen production. *International Journal of Hydrogen Energy* **2001**, *26* (2), 127-132.
- (7) Dominey, R. N.; Lewis, N. S.; Bruce, J. A.; Bookbinder, D. C.; Wrighton, M. S., Improvement of photoelectrochemical hydrogen generation by surface modification of p-type silicon semiconductor photocathodes. *Journal of the American Chemical Society* **1982**, *104* (2), 467-482.
- (8) Sim, U.; Yang, T.-Y.; Moon, J.; An, J.; Hwang, J.; Seo, J.-H.; Lee, J.; Kim, K. Y.; Lee, J.; Han, S.; Hong, B. H.; Nam, K. T., N-doped monolayer graphene catalyst on silicon photocathode for hydrogen production. *Energy & Environmental Science* **2013**, *6* (12), 3658-3664.
- (9) Hou, Y.; Abrams, B. L.; Vesborg, P. C. K.; Björketun, M. E.; Herbst, K.; Bech, L.; Setti, A. M.; Damsgaard, C. D.; Pedersen, T.; Hansen, O.; Rossmeisl, J.; Dahl, S.; Nørskov, J. K.; Chorkendorff, I., Bioinspired molecular co-catalysts bonded to a silicon photocathode for solar hydrogen evolution. *Nature Materials* **2011**, *10*, 434.
- (10) Sick, T.; Hufnagel, A. G.; Kampmann, J.; Kondofersky, I.; Calik, M.; Rotter, J. M.; Evans, A.; Döblinger, M.; Herbert, S.; Peters, K.; Böhm, D.; Knochel, P.; Medina, D. D.; Fattakhova-Rohlfing, D.; Bein, T., Oriented Films of Conjugated 2D Covalent Organic Frameworks as Photocathodes for Water Splitting. *Journal of the American Chemical Society* **2018**, *140* (6), 2085-2092.
- (11) Haro, M.; Solis, C.; Molina, G.; Otero, L.; Bisquert, J.; Gimenez, S.; Guerrero, A., Toward Stable Solar Hydrogen Generation Using Organic Photoelectrochemical Cells. *The Journal of Physical Chemistry C* **2015**, *119* (12), 6488-6494.
- (12) Bourgeteau, T.; Tondelier, D.; Geffroy, B.; Brisse, R.; Campidelli, S.; Cornut, R.; Jusselme, B., All solution-processed organic photocathodes with increased efficiency and stability via the tuning of the hole-extracting layer. *Journal of Materials Chemistry A* **2016**, *4* (13), 4831-4839.
- (13) Sathre, R.; Scown, C. D.; Morrow, W. R.; Stevens, J. C.; Sharp, I. D.; Ager, J. W.; Walczak, K.; Houle, F. A.; Greenblatt, J. B., Life-cycle net energy assessment of large-scale hydrogen

How photocorrosion can trick you: A detailed study on low-bandgap Li doped CuO photocathodes for solar hydrogen production

production via photoelectrochemical water splitting. *Energy & Environmental Science* **2014**, 7 (10), 3264-3278.

(14) Paracchino, A.; Laporte, V.; Sivula, K.; Grätzel, M.; Thimsen, E., Highly active oxide photocathode for photoelectrochemical water reduction. *Nat Mater* **2011**, 10 (6), 456-461.

(15) Sivula, K.; Le Formal, F.; Grätzel, M., Solar Water Splitting: Progress Using Hematite (α -Fe₂O₃) Photoelectrodes. *ChemSusChem* **2011**, 4 (4), 432-449.

(16) Patil, R.; Kelkar, S.; Naphade, R.; Ogale, S., Low temperature grown CuBi₂O₄ with flower morphology and its composite with CuO nanosheets for photoelectrochemical water splitting. *Journal of Materials Chemistry A* **2014**, 2 (10), 3661-3668.

(17) Prévot, M. S.; Guijarro, N.; Sivula, K., Enhancing the Performance of a Robust Sol-Gel-Processed p-Type Delafossite CuFeO₂ Photocathode for Solar Water Reduction. *ChemSusChem* **2015**, 8 (8), 1359-1367.

(18) Joshi, U. A.; Palasyuk, A. M.; Maggard, P. A., Photoelectrochemical Investigation and Electronic Structure of a p-type CuNbO₃ Photocathode. *The Journal of Physical Chemistry C* **2011**, 115 (27), 13534-13539.

(19) Berglund, S. P.; Abdi, F. F.; Bogdanoff, P.; Chemseddine, A.; Friedrich, D.; van de Krol, R., Comprehensive Evaluation of CuBi₂O₄ as a Photocathode Material for Photoelectrochemical Water Splitting. *Chemistry of Materials* **2016**, 28 (12), 4231-4242.

(20) Kondofersky, I.; Müller, A.; Dunn, H. K.; Ivanova, A.; Štefanić, G.; Ehrensperger, M.; Scheu, C.; Parkinson, B. A.; Fattakhova-Rohlfing, D.; Bein, T., Nanostructured Ternary FeCrAl Oxide Photocathodes for Water Photoelectrolysis. *Journal of the American Chemical Society* **2016**.

(21) Sliozberg, K.; Stein, H. S.; Khare, C.; Parkinson, B. A.; Ludwig, A.; Schuhmann, W., Fe-Cr-Al Containing Oxide Semiconductors as Potential Solar Water-Splitting Materials. *ACS Applied Materials & Interfaces* **2015**, 7 (8), 4883-4889.

(22) Chiang, C.-Y.; Shin, Y.; Ehrman, S., Dopant Effects on Copper Oxide Photoelectrochemical Cell Water Splitting. *Energy Procedia* **2014**, 61, 1799-1802.

(23) Chiang, C.-Y.; Shin, Y.; Ehrman, S., Li Doped CuO Film Electrodes for Photoelectrochemical Cells. *Journal of The Electrochemical Society* **2011**, 159 (2), B227-B231.

(24) Dunn, H. K.; Feckl, J. M.; Müller, A.; Fattakhova-Rohlfing, D.; Morehead, S. G.; Roos, J.; Peter, L. M.; Scheu, C.; Bein, T., Tin doping speeds up hole transfer during light-driven water oxidation at hematite photoanodes. *Phys Chem Chem Phys* **2014**, 16 (44), 24610-20.

(25) Peter, L. M., Energetics and kinetics of light-driven oxygen evolution at semiconductor electrodes: the example of hematite. *J Solid State Electrochem* **2012**, 17 (2), 315-326.

(26) Linsebigler, A. L.; Lu, G.; Yates, J. T., Photocatalysis on TiO₂ Surfaces: Principles, Mechanisms, and Selected Results. *Chemical Reviews* **1995**, 95 (3), 735-758.

(27) Prévot, M. S.; Sivula, K., Photoelectrochemical Tandem Cells for Solar Water Splitting. *The Journal of Physical Chemistry C* **2013**, 117 (35), 17879-17893.

References

- (28) Yang, Y.; Xu, D.; Wu, Q.; Diao, P., Cu₂O/CuO Bilayered Composite as a High-Efficiency Photocathode for Photoelectrochemical Hydrogen Evolution Reaction. *Scientific Reports* **2016**, *6*, 35158.
- (29) Shaislamov, U.; Lee, H.-J., Synthesis and photoelectrochemical properties of a novel CuO/ZnO nanorod photocathode for solar hydrogen generation. *Journal of the Korean Physical Society* **2016**, *69* (7), 1242-1246.
- (30) Shaislamov, U.; Krishnamoorthy, K.; Kim, S. J.; Abidov, A.; Allabergenov, B.; Kim, S.; Choi, S.; Suresh, R.; Ahmed, W. M.; Lee, H.-J., Highly stable hierarchical p-CuO/ZnO nanorod/nanobranched photoelectrode for efficient solar energy conversion. *International Journal of Hydrogen Energy* **2016**, *41* (4), 2253-2262.
- (31) Basnet, P.; Zhao, Y., Tuning the Cu_xO nanorod composition for efficient visible light induced photocatalysis. *Catalysis Science & Technology* **2016**, *6* (7), 2228-2238.
- (32) Lim, Y.-F.; Chua, C. S.; Lee, C. J.; Chi, D., Sol-gel deposited Cu₂O and CuO thin films for photocatalytic water splitting. *Physical Chemistry Chemical Physics* **2014**, *16* (47), 25928-25934.
- (33) Chiang, C.-Y.; Shin, Y.; Aroh, K.; Ehrman, S., Copper oxide photocathodes prepared by a solution based process. *International Journal of Hydrogen Energy* **2012**, *37* (10), 8232-8239.
- (34) Barreca, D.; Fornasiero, P.; Gasparotto, A.; Gombac, V.; Maccato, C.; Montini, T.; Tondello, E., The Potential of Supported Cu₂O and CuO Nanosystems in Photocatalytic H₂ Production. *ChemSusChem* **2009**, *2* (3), 230-233.
- (35) Koffyberg, F. P.; Benko, F. A., A photoelectrochemical determination of the position of the conduction and valence band edges of p-type CuO. *Journal of Applied Physics* **1982**, *53* (2), 1173-1177.
- (36) Meyer, B. K.; Polity, A.; Reppin, D.; Becker, M.; Hering, P.; Klar, P. J.; Sander, T.; Reindl, C.; Benz, J.; Eickhoff, M.; Heiliger, C.; Heinemann, M.; Bläsing, J.; Krost, A.; Shokovets, S.; Müller, C.; Ronning, C., Binary copper oxide semiconductors: From materials towards devices. *physica status solidi (b)* **2012**, *249* (8), 1487-1509.
- (37) Heinemann, M.; Eifert, B.; Heiliger, C., Band structure and phase stability of the copper oxides Cu₂O, CuO, and Cu₄O₃. *Physical Review B* **2013**, *87* (11), 115111.
- (38) Chauhan, D.; Satsangi, V.; Dass, S.; Shrivastav, R., Preparation and characterization of nanostructured CuO thin films for photoelectrochemical splitting of water. *Bulletin of Materials Science* **2006**, *29*, 709.
- (39) Olsen, L. C.; Bohara, R. C.; Urie, M. W., Explanation for low-efficiency Cu₂O Schottky-barrier solar cells. *Applied Physics Letters* **1979**, *34* (1), 47-49.
- (40) Ba, X.; Yan, L.-L.; Huang, S.; Yu, J.; Xia, X.-J.; Yu, Y., New Way for CO₂ Reduction under Visible Light by a Combination of a Cu Electrode and Semiconductor Thin Film: Cu₂O Conduction Type and Morphology Effect. *The Journal of Physical Chemistry C* **2014**, *118* (42), 24467-24478.

How photocorrosion can trick you: A detailed study on low-bandgap Li doped CuO photocathodes for solar hydrogen production

- (41) Chand, P.; Gaur, A.; Kumar, A.; Kumar Gaur, U., Structural and optical study of Li doped CuO thin films on Si (1 0 0) substrate deposited by pulsed laser deposition. *Applied Surface Science* **2014**, *307*, 280-286.
- (42) Masudy-Panah, S.; Moakhar, R. S.; Chua, C. S.; Kushwaha, A.; Wong, T. I.; Dalapati, G. K., Rapid thermal annealing assisted stability and efficiency enhancement in a sputter deposited CuO photocathode. *RSC Advances* **2016**, *6* (35), 29383-29390.
- (43) Jang, Y. J.; Jang, J.-W.; Choi, S. H.; Kim, J. Y.; Kim, J. H.; Youn, D. H.; Kim, W. Y.; Han, S.; Sung Lee, J., Tree branch-shaped cupric oxide for highly effective photoelectrochemical water reduction. *Nanoscale* **2015**, *7* (17), 7624-7631.
- (44) Zhang, Z.; Wang, P., Highly stable copper oxide composite as an effective photocathode for water splitting via a facile electrochemical synthesis strategy. *Journal of Materials Chemistry* **2012**, *22* (6), 2456-2464.
- (45) Chiang, C.-Y.; Aroh, K.; Franson, N.; Satsangi, V. R.; Dass, S.; Ehrman, S., Copper oxide nanoparticle made by flame spray pyrolysis for photoelectrochemical water splitting – Part II. Photoelectrochemical study. *International Journal of Hydrogen Energy* **2011**, *36* (24), 15519-15526.
- (46) Wang, C.-M.; Wang, C.-Y., Photocorrosion of plasmonic enhanced Cu_xO photocatalyst. *NANOP* **2014**, *8* (1), 084095-084095.
- (47) Guo, X.; Diao, P.; Xu, D.; Huang, S.; Yang, Y.; Jin, T.; Wu, Q.; Xiang, M.; Zhang, M., CuO/Pd composite photocathodes for photoelectrochemical hydrogen evolution reaction. *International Journal of Hydrogen Energy* **2014**, *39* (15), 7686-7696.
- (48) Chen, L.; Shet, S.; Tang, H.; Wang, H.; Deutsch, T.; Yan, Y.; Turner, J.; Al-Jassim, M., Electrochemical deposition of copper oxide nanowires for photoelectrochemical applications. *Journal of Materials Chemistry* **2010**, *20* (33), 6962-6967.
- (49) Chiang, C.-Y.; Chang, M.-H.; Liu, H.-S.; Tai, C. Y.; Ehrman, S., Process Intensification in the Production of Photocatalysts for Solar Hydrogen Generation. *Industrial & Engineering Chemistry Research* **2012**, *51* (14), 5207-5215.
- (50) Emin, S.; Abdi, F. F.; Fanetti, M.; Peng, W.; Smith, W.; Sivula, K.; Dam, B.; Valant, M., A novel approach for the preparation of textured CuO thin films from electrodeposited CuCl and CuBr. *Journal of Electroanalytical Chemistry* **2014**, *717-718*, 243-249.
- (51) Choi, H.; Kang, M., Hydrogen production from methanol/water decomposition in a liquid photosystem using the anatase structure of Cu loaded TiO₂/TiO₂. *International Journal of Hydrogen Energy* **2007**, *32* (16), 3841-3848.
- (52) Paracchino, A.; Mathews, N.; Hisatomi, T.; Stefiak, M.; Tilley, S. D.; Gratzel, M., Ultrathin films on copper(i) oxide water splitting photocathodes: a study on performance and stability. *Energy & Environmental Science* **2012**, *5* (9), 8673-8681.
- (53) Xing, H.; E, L.; Guo, Z.; Zhao, D.; Li, X.; Liu, Z., Exposing the photocorrosion mechanism and control strategies of a CuO photocathode. *Inorganic Chemistry Frontiers* **2019**, *6* (9), 2488-2499.

References

- (54) Zhang, S.; Rohloff, M.; Kasian, O.; Mingers, A. M.; Mayrhofer, K. J. J.; Fischer, A.; Scheu, C.; Cherevko, S., Dissolution of BiVO₄ Photoanodes Revealed by Time-Resolved Measurements under Photoelectrochemical Conditions. *The Journal of Physical Chemistry C* **2019**, *123* (38), 23410-23418.
- (55) Toma, F. M.; Cooper, J. K.; Kunzelmann, V.; McDowell, M. T.; Yu, J.; Larson, D. M.; Borys, N. J.; Abelyan, C.; Beeman, J. W.; Yu, K. M.; Yang, J.; Chen, L.; Shaner, M. R.; Spurgeon, J.; Houle, F. A.; Persson, K. A.; Sharp, I. D., Mechanistic insights into chemical and photochemical transformations of bismuth vanadate photoanodes. *Nature Communications* **2016**, *7* (1), 12012.
- (56) Lee, D. K.; Choi, K.-S., Enhancing long-term photostability of BiVO₄ photoanodes for solar water splitting by tuning electrolyte composition. *Nature Energy* **2018**, *3* (1), 53-60.
- (57) Tunell, G.; Posnjak, E.; Ksanda, C., Geometrical and optical properties, and crystal structure of tenorite. *Zeitschrift für Kristallographie-Crystalline Materials* **1935**, *90* (1), 120-142.
- (58) Niggli, P., XII. Die Kristallstruktur einiger Oxyde I. *Zeitschrift für Kristallographie-Crystalline Materials* **1922**, *57* (1), 253-299.
- (59) Carretta, P.; Corti, M.; Rigamonti, A., Spin dynamics in CuO and Cu_{1-x}Li_xO from ⁶³Cu and ⁷Li nuclear relaxation. *Physical Review B* **1993**, *48* (5), 3433-3444.
- (60) Baeumer, C.; Funck, C.; Locatelli, A.; Menteş, T. O.; Genuzio, F.; Heisig, T.; Hensling, F.; Raab, N.; Schneider, C. M.; Menzel, S.; Waser, R.; Dittmann, R., In-Gap States and Band-Like Transport in Memristive Devices. *Nano Letters* **2019**, *19* (1), 54-60.
- (61) Roy, D.; Samu, G. F.; Hossain, M. K.; Janáky, C.; Rajeshwar, K., On the measured optical bandgap values of inorganic oxide semiconductors for solar fuels generation. *Catalysis Today* **2018**, *300*, 136-144.
- (62) Dudarev, S. L.; Botton, G. A.; Savrasov, S. Y.; Humphreys, C. J.; Sutton, A. P., Electron-energy-loss spectra and the structural stability of nickel oxide: An LSDA+U study. *Physical Review B* **1998**, *57* (3), 1505-1509.
- (63) Biesinger, M. C.; Lau, L. W. M.; Gerson, A. R.; Smart, R. S. C., Resolving surface chemical states in XPS analysis of first row transition metals, oxides and hydroxides: Sc, Ti, V, Cu and Zn. *Applied Surface Science* **2010**, *257* (3), 887-898.
- (64) Poulston, S.; Parlett, P. M.; Stone, P.; Bowker, M., Surface Oxidation and Reduction of CuO and Cu₂O Studied Using XPS and XAES. *Surface and Interface Analysis* **1996**, *24* (12), 811-820.
- (65) Laffont, L.; Wu, M. Y.; Chevallier, F.; Poizot, P.; Morcrette, M.; Tarascon, J. M., High resolution EELS of Cu-V oxides: application to batteries materials. *Micron* **2006**, *37* (5), 459-64.
- (66) Leapman, R. D.; Grunes, L. A.; Fejes, P. L., Study of the L₂₃ edges in the 3d transition metals and their oxides by electron-energy-loss spectroscopy with comparisons to theory. *Physical Review B* **1982**, *26* (2), 614-635.

How photocorrosion can trick you: A detailed study on low-bandgap Li doped CuO photocathodes for solar hydrogen production

- (67) Azevedo, J.; Tilley, S. D.; Schreier, M.; Stefik, M.; Sousa, C.; Araújo, J. P.; Mendes, A.; Grätzel, M.; Mayer, M. T., Tin oxide as stable protective layer for composite cuprous oxide water-splitting photocathodes. *Nano Energy* **2016**, *24*, 10-16.
- (68) Pore, V.; Ritala, M.; Leskelä, M.; Saukkonen, T.; Järn, M., Explosive Crystallization in Atomic Layer Deposited Mixed Titanium Oxides. *Crystal Growth & Design* **2009**, *9* (7), 2974-2978.
- (69) Hufnagel, A. G.; Häringer, S.; Beetz, M.; Böller, B.; Fattakhova-Rohlfing, D.; Bein, T., Carbon-templated conductive oxide supports for oxygen evolution catalysis. *Nanoscale* **2019**.
- (70) Ohya, S.; Kaneco, S.; Katsumata, H.; Suzuki, T.; Ohta, K., Electrochemical reduction of CO₂ in methanol with aid of CuO and Cu₂O. *Catalysis Today* **2009**, *148* (3-4), 329-334.
- (71) Rietveld, H., A profile refinement method for nuclear and magnetic structures. *Journal of Applied Crystallography* **1969**, *2* (2), 65-71.
- (72) Klahr, B. M.; Martinson, A. B.; Hamann, T. W., Photoelectrochemical investigation of ultrathin film iron oxide solar cells prepared by atomic layer deposition. *Langmuir* **2011**, *27* (1), 461-8.
- (73) Wiesenburg, D. A.; Guinasso, N. L., Equilibrium solubilities of methane, carbon monoxide, and hydrogen in water and sea water. *Journal of Chemical & Engineering Data* **1979**, *24* (4), 356-360.
- (74) Kresse, G.; Hafner, J., *Ab initio* molecular-dynamics simulation of the liquid-metal/amorphous-semiconductor transition in germanium. *Physical Review B* **1994**, *49* (20), 14251-14269.
- (75) Kresse, G.; Furthmüller, J., Efficiency of *ab-initio* total energy calculations for metals and semiconductors using a plane-wave basis set. *Computational Materials Science* **1996**, *6* (1), 15-50.
- (76) Blöchl, P. E., Projector augmented-wave method. *Physical Review B* **1994**, *50* (24), 17953-17979.
- (77) Perdew, J. P.; Burke, K.; Ernzerhof, M., Generalized Gradient Approximation Made Simple. *Physical Review Letters* **1996**, *77* (18), 3865-3868.
- (78) Heinemann, M.; Eifert, B.; Heiliger, C., Band structure and phase stability of the copper oxides Cu₂O, CuO, and Cu₄O₃. *Physical Review B* **2013**, *87* (11).
- (79) Ghijsen, J.; Tjeng, L. H.; van Elp, J.; Eskes, H.; Westerink, J.; Sawatzky, G. A.; Czyzyk, M. T., Electronic structure of Cu₂O and CuO. *Physical Review B* **1988**, *38* (16), 11322-11330.
- (80) Koffyberg, F. P.; Benko, F. A., A photoelectrochemical determination of the position of the conduction and valence band edges of p-type CuO. *J. Appl. Phys.* **1982**, *53* (2), 1173-1177.
- (81) Marabelli, F.; Parravicini, G. B.; Salghetti-Drioli, F., Optical gap of CuO. *Physical Review B* **1995**, *52* (3), 1433-1436.

References

- (82) Åsbrink, S.; Norrby, L. J., A refinement of the crystal structure of copper(II) oxide with a discussion of some exceptional e.s.d.'s. *Acta Crystallographica Section B Structural Crystallography and Crystal Chemistry* **1970**, 26 (1), 8-15.

5 Oriented Films of Conjugated 2D Covalent Organic Frameworks as Photocathodes for Water Splitting

This chapter is based on the following publication:

Torben Sick,[‡] Alexander G. Hufnagel,[‡] **Jonathan Kampmann**,[‡] Ilina Kondofersky, Mona Calik, Julian M. Rotter, Austin Evans, Markus Döblinger, Simon Herbert, Kristina Peters, Daniel Böhm, Paul Knochel, Dana D. Medina, Dina Fattakhova-Rohlfing* and Thomas Bein*, *J. Am. Chem. Soc.* **2018**, 140, 2085-2092.

[‡] These authors contributed equally to this work.

Reprinted with permission from *J. Am. Chem. Soc.* **2018**, 140, 2085-2092. Copyright 2018 American Chemical Society. Further permissions related to the material excerpted should be directed to the *American Chemical Society*.

Link to the published article: <https://pubs.acs.org/doi/10.1021/jacs.7b06081>

Supplementary cover image by Alexander G. Hufnagel.

Jonathan Kampmann performed the aqueous photoelectrochemistry and hydrogen detection experiments as well as the Platinum nanoparticle synthesis and wrote the corresponding parts of the manuscript.

Abstract

Light-driven water electrolysis at a semiconductor surface is a promising way to generate hydrogen from sustainable energy sources, but its efficiency is limited by the performance of available photoabsorbers. Here we report the first time investigation of covalent organic frameworks (COFs) as a new class of photoelectrodes. The presented 2D-COF structure is assembled from aromatic amine-functionalized tetraphenylethylene and thiophene dialdehyde building blocks to form conjugated polyimine sheets, which π -stack in the third dimension to create photoactive porous frameworks. Highly oriented COF films absorb light in the visible range to generate photo-excited electrons that diffuse to the surface and are transferred to the electrolyte resulting in proton reduction and hydrogen evolution. The observed photoelectrochemical activity of the 2D-COF films and their photocorrosion stability in water pave the way for a novel class of photoabsorber materials with versatile optical and electronic properties that are tunable through the selection of appropriate building blocks and their three-dimensional stacking.

5.1 Introduction

Photoelectrochemical (PEC) water splitting is an attractive way to generate hydrogen using renewable energy. Due to the potential of directly converting solar power into a chemical fuel or process feedstock, this process has attracted broad research interest. An ideal photoabsorber will combine efficient light harvesting with suitable band energies for water oxidation and reduction, fast interfacial charge transfer kinetics to the electrolyte, and corrosion stability under operating conditions.¹ However, the performance of known systems is modest, being primarily limited by photoabsorber material properties. On the one hand, metal oxides tend to be stable under operation (i.e. resistant against photocorrosion) but exhibit poor semiconductor properties such as short charge carrier diffusion lengths and fast recombination, which can be partially compensated by nanostructuring.²⁻⁴ On the other hand, Si and III-V semiconductors offer favorable charge transport properties and high photocurrents but are prone to photocorrosion unless protected by overlayers.⁵⁻⁶ For this reason, the discovery of new photoabsorber materials is urgent and currently the focus of combinatorial synthetic and computational research.⁷⁻¹⁰

In this work we explore covalent organic frameworks (COFs) as photoelectrodes for light-driven water splitting. COFs are an emerging class of crystalline polymers composed of organic units linked via covalent bonds to form porous networks. By using multidentate building blocks, two- or three-dimensional frameworks with a defined pore size and high specific surface area in conjunction with appreciable thermal and chemical stability can be obtained. In 2D-COFs, covalently bonded units form two-dimensional (2D) sheets, which stack due to dispersive forces (π -stacking) in the third dimension to construct extended open porous frameworks. The π -stacking mediates electronic interactions between the functional units, thereby providing another possible path for charge carrier transport in addition to transfer within the covalent sheets. The selection of appropriate building blocks, linkage motifs (from unconjugated boroxines, boronate esters and borosilicates¹¹⁻¹⁴ to conjugated imines¹⁵⁻¹⁹, imides²⁰⁻²¹ and others²²⁻²⁴), as well as their stacking mode all provide ways to tailor the optical and electronic properties of COF structures, thereby clearing the way for novel materials for optoelectronic systems. COFs have found applications in gas storage²⁵⁻²⁶, catalysis²⁷⁻²⁸, separation²⁹⁻³¹, energy storage³² and proton conduction³³. Zeolitic imidazolate frameworks (ZIFs)³⁴, carbon nitrides (CNs)³⁵⁻⁴⁰, phenyl triazine oligomers (PTOs)⁴¹, poly-(azomethine) networks (ANWs)⁴², triazine containing organic frameworks and even covalent organic frameworks (CTFs and COFs)⁴³⁻⁵⁰ were found to be active in photocatalysis and photocatalytic hydrogen evolution reactions, where photogenerated charge separation was achieved by adding noble metal co-catalysts and/or sacrificial electron donors. Fabricated as oriented COF thin films, COFs have already found use as active materials in optoelectronic devices⁵¹⁻⁵⁴. However, COF films being utilized as photoelectrodes for direct water splitting has yet to be reported. Herein, we demonstrate the first use of an imine-based COF, grown as oriented films on transparent, conducting substrates serving as a light-absorbing material. This is the first report of a COF acting as a photoelectrode to enable photoelectrochemical water splitting in aqueous electrolytes without the use of a co-catalyst or sacrificial agent. In addition, we demonstrate a four-fold increase in the obtained photocurrent by the application of a Pt nanoparticle hydrogen evolution catalyst.

5.2 Results and discussion

5.2.1 Synthesis of COF systems

For the possible use as photocathodes in photoelectrochemical water-splitting devices, we investigated a 2D-COF built from aromatic amino- and thiophene-based units. The use of nearly

Results and discussion

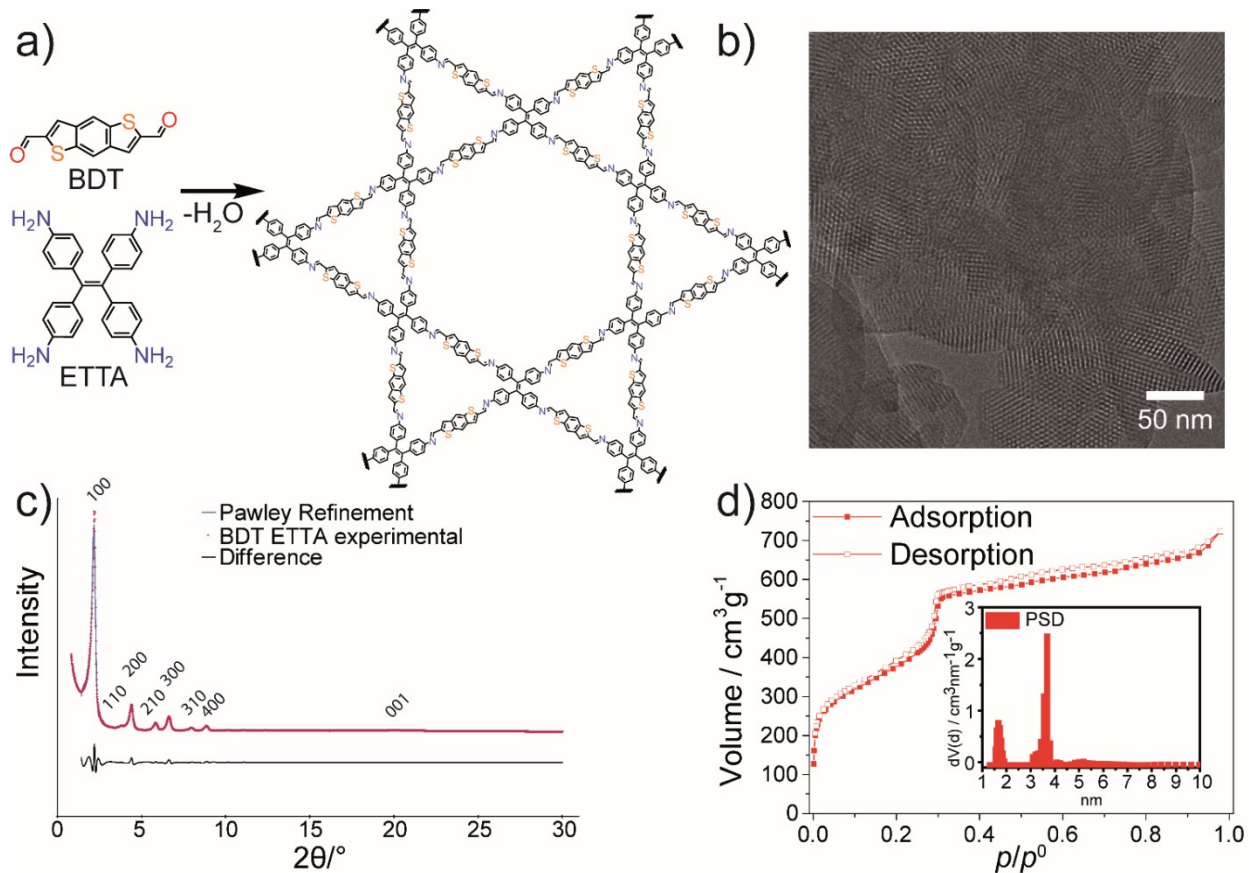


Figure 5.1. a) Synthetic approach for the formation of BDT-ETTA COF with a structural overview of the resulting 2D layers. Due to π -interactions the sheets stack in the third dimension to form the final hexagonal AA eclipsed framework b) TEM image of the resulting powder. c) PXRD of BDT-ETTA (red), comparison to a Pawley-refined pattern (blue) and difference (black line). d) Nitrogen physisorption isotherm of BDT-ETTA with a pore size distribution revealing two distinct pore sizes.

planar p-type functional building units linked via polarizable imine bonds is expected to result in conjugated p-type semiconductors, whose optoelectronic properties can be varied via the structure of the building units and the nature of their stacking in the third dimension. One building unit is a conjugated aromatic and four-fold amine-functionalized tetraphenylethylene (1,1',2,2'-tetra-*p*-aminophenylethylene, ETTA). The ETTA monomer has been investigated in 2D-imine COF powders⁵⁵, where it was shown to have a strong impact on geometry, shape, crystallinity and on the stacking distance of adjacent layers. The other component is the linear dialdehyde benzo[1,2-*b*:4,5-*b'*]dithiophene-2,6-dicarboxaldehyde (BDT), which is a donor-type dithiophene (Figure 5.1).

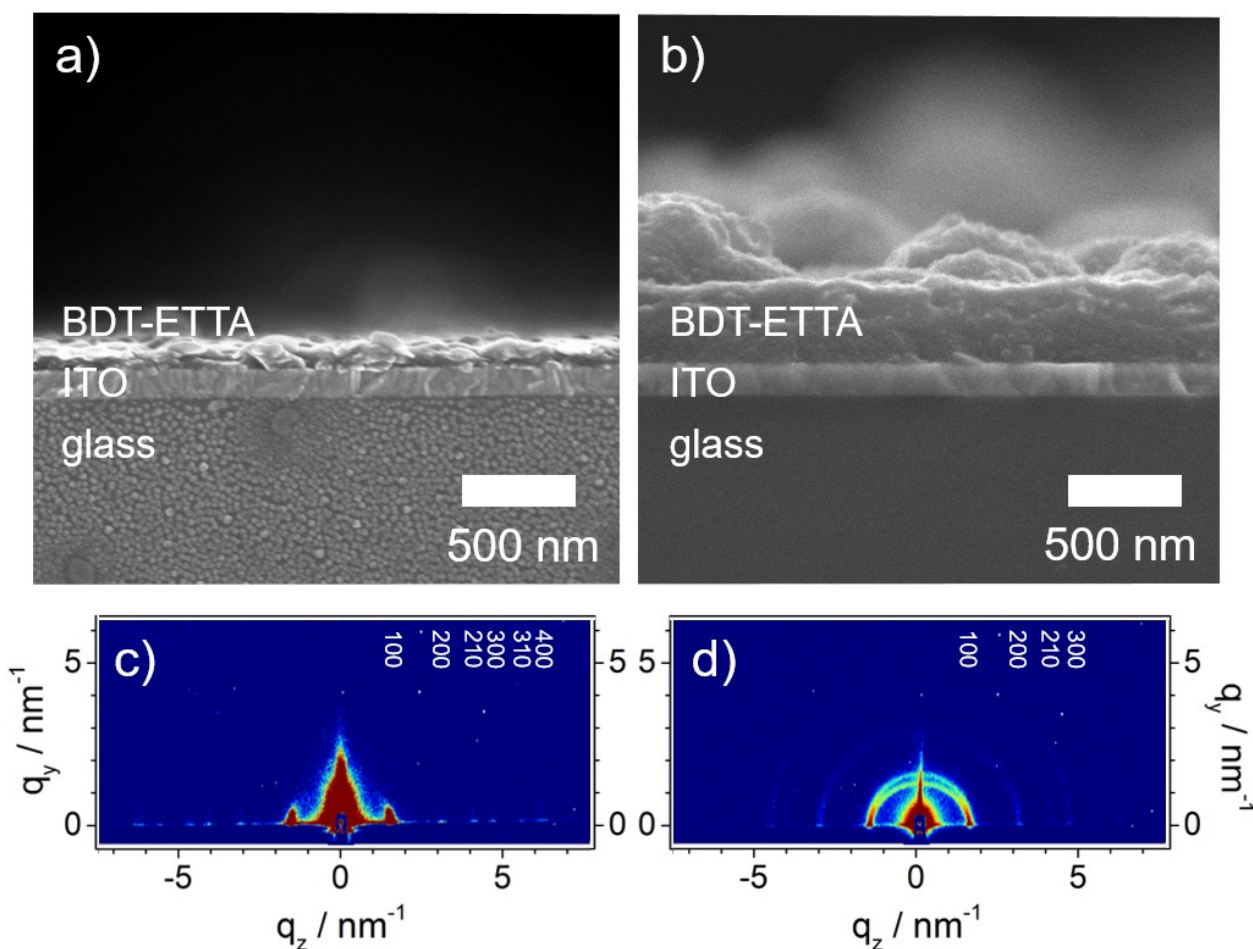


Figure 5.2. Thin (ca. 100 nm) (a, c) and thick (ca. 500 nm) (b, d) BDT-ETTA films grown on ITO substrates: SEM images (cross-section) (a, b) and grazing incidence diffraction (GID) patterns (c, d) revealing a high degree of film orientation.

For use as electrodes in photoelectrochemical cells, the COFs were grown as films on transparent conducting FTO or ITO substrates. We found that high concentrations of reactants resulted in homogeneous nucleation and growth of bulk COF powders, whereas dilute solutions promote the heterogeneous film growth on a substrate. To avoid precipitation/sedimentation of COF powders on the substrate, the substrates were placed with the ITO side downwards in a PTFE film holder in a mesitylene-dioxane (V:V = 1:1) solution in an autoclave. After adding a catalytic amount 6M acetic acid, the films were grown for 72 h at 120 °C. Intensely orange-colored BDT-ETTA COF films were obtained on FTO or ITO substrates. Cross-sectional SEM images of BDT-ETTA films (Figure 5.2) with

Results and discussion

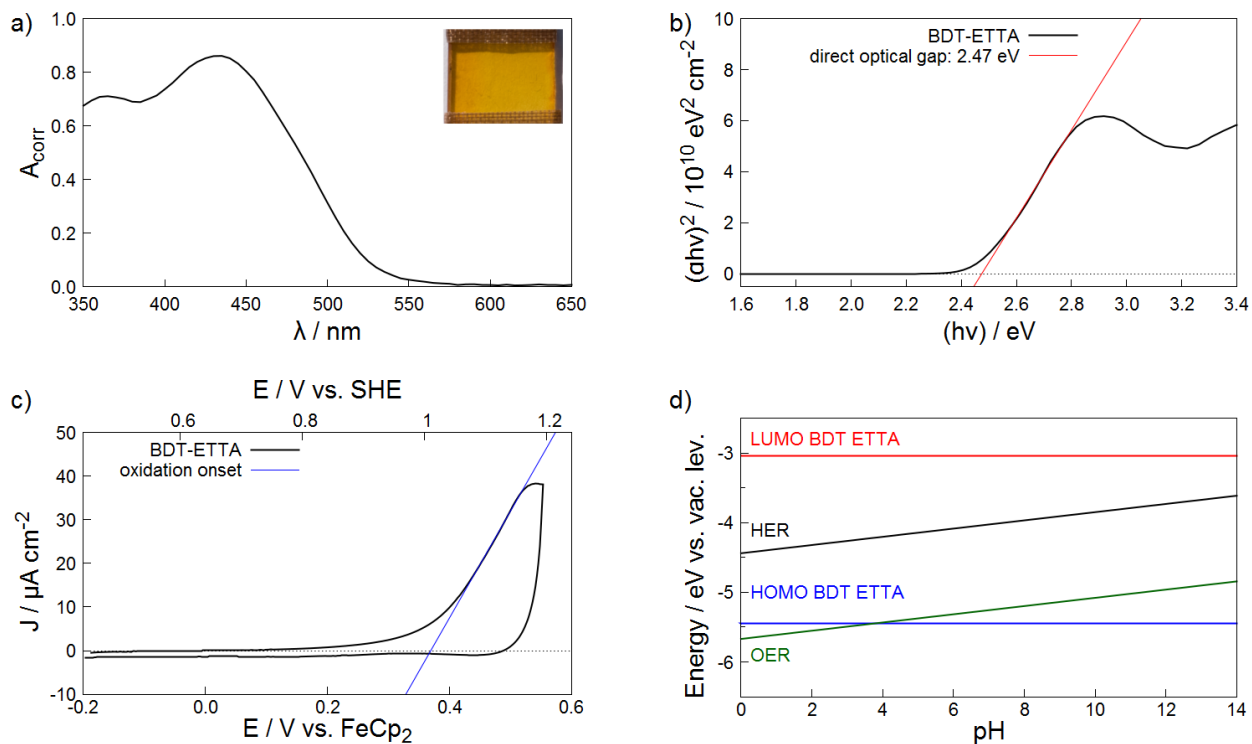


Figure 5.3. a) Absorbance spectrum of a BDT-ETTA thin film on ITO with a photograph of a representative sample masked with a PFTE adhesive tape (inset). b) Tauc plot analysis of a BDT-ETTA film on ITO showing a direct optical band gap of 2.47 eV. c) Cyclic voltammogram of a BDT-ETTA electrode in non-aqueous electrolyte. d) Calculated alignment between the HOMO and LUMO of BDT-ETTA and the water-splitting redox couples.

different thicknesses demonstrate that COF films can be grown in the thickness range between 100 to 500 nm and are well adhered to the substrate. The surface exhibits some roughness, which is notably less pronounced in the case of thinner films (compare Figure 5.2a). BDT-ETTA COF is well ordered and crystalline, as established by an intense and sharp 100 reflection and the presence of well-defined higher-order reflections in the PXRD pattern (Figure 5.1c). The reflection at around $20^\circ 2\theta$ represents the π -stacking distance, which corresponds to 0.44 nm. The experimentally obtained XRD pattern agrees well with the simulated pattern calculated for an AA eclipsed layer stacking for a hexagonal structure in P6 symmetry (see Figure 5.1c and SI Figure 5.13). The π -stacking distance is high in comparison to other COF systems, which can be explained by the strong contribution of the propeller-shaped (i.e. non-planar) ET TA motif to the final geometry compared to the planar thiophene linker.¹⁹ Notably, both the XRD measurements in reflection mode (SI Figure 5.11) as well as grazing incidence diffraction (GID) patterns (Figure 5.2c,d) provide strong evidence

for oriented growth of the COF films on the substrates. The orientation in *c*-direction is evident from the intense reflections at $q(y)=0$ originating from COF layers oriented parallel to the substrate and correspond to the reflections of the BDT-ETTA COF (compare PXRD in Figure 5.1c). A weak diffuse arc originates from randomly distributed COF particles present on top of the highly-oriented film (see SI Figure 5.9 and SI Figure 5.11). For the electrochemical investigations we used the thinner films as they constitute a well-defined system with less contributions from unordered COF material.

The nitrogen physisorption isotherms of the COF powder demonstrate that the BDT-ETTA COF forms a porous structure with clearly distinguishable micro- and mesopores (Figure 5.1d). The BET surface areas and total pore volumes for COF bulk material was calculated to be $1360 \text{ m}^2\text{g}^{-1}$ and $1.0 \text{ cm}^3\text{g}^{-1}$, respectively. The bimodal pore size distribution shows pores of 1.67 nm and 3.68 nm in diameter. The pore sizes match the predicted values for the geometry of an AA eclipsed framework.

The TEM image of BDT-ETTA (Figure 5.1b) reveals a high degree of crystallinity and order, recognizable by the large domain sizes. 2D honeycomb-type facets are visible, where the *ab* plane is oriented perpendicular to the viewing direction. In other viewing directions, channels indicate the growth orientation, highlighting the crystallinity of the COF material with domain sizes of 50-100 nm.

5.2.2 Photoelectrochemical properties of COF films

The remarkable stability of the obtained BDT-ETTA in different solvents, including water in a pH range from 3 to 14 (see SI Figure 5.12 for further details), and strong absorption of visible light led us to believe the novel BDT-ETTA COF structure would be an interesting example of photoabsorber materials for water-splitting applications. Therefore we measured the photochemical activity at pH 7.

The absorption spectrum is shown in Figure 5.3. BDT-ETTA films absorb light strongly in the visible range with an absorption threshold of around 550 nm and two absorbance maxima at 360 and 430 nm (Figure 5.3a). The Tauc plot analysis of BDT-ETTA thin films (Figure 5.3b) reveals a direct optical band gap of 2.47 eV, which is favorable for photoelectrochemical water splitting.²

To determine the absolute positions of the conduction and valence band edges of BDT-ETTA films (corresponding to their LUMO and HOMO energies, respectively), electrochemical measurements in a non-aqueous electrolyte (0.1 M NBu_4PF_6 in anhydrous acetonitrile) were performed. The cyclic voltammogram of a BDT-ETTA film electrode (Figure 5.3c) shows an anodic peak with an onset at 0.37 V vs. ferrocene/ferrocenium (FOC), which we attribute to the expected oxidation of thiophene

Results and discussion

moieties. From this, the approximate position of the HOMO can be calculated to be -5.51 eV (see SI for further details). Using the optical bandgap of 2.47 eV determined above, the LUMO position is approximately -3.34 eV. The absolute energy of the HOMO and LUMO of BDT-ETTA as well as the $\text{H}_2\text{O}/\text{H}_2$ (hydrogen evolution reaction, HER) and $\text{O}_2/\text{H}_2\text{O}$ (oxygen evolution reaction, OER) redox couples is plotted in Figure 5.3d. If we assume that the HOMO and LUMO positions do not change significantly due to protonation or deprotonation of the COF structure, the LUMO is higher in energy than the $\text{H}_2\text{O}/\text{H}_2$ redox pair in solution over the entire pH range, which means that photoexcited electrons at the COF surface should be able to spontaneously transfer to the electrolyte, resulting in proton reduction and hydrogen evolution. The driving force, i.e. the potential difference between the LUMO of the COF and the HER is significant, particularly in acidic solutions. In alkaline solutions, the HOMO energy lies below that of the OER redox couple, which would also render photoelectrochemical water oxidation and thus bias-free one-photon water-splitting thermodynamically possible. However, the potential difference is limited to approximately 0.5 V, which approaches the minimum overpotential needed to drive the OER. Therefore, in the absence of an efficient OER catalyst, this reaction is not expected to yield significant currents. The photoelectrochemical performance of 100 nm BDT-ETTA films was characterized by linear sweep voltammetry in nitrogen-purged 0.1 M Na_2SO_4 aqueous electrolyte under AM 1.5 illumination through the substrate in the potential range between 1.1 and 0.2 V vs. RHE (Figure 5.4a). The photoelectrode shows an early HER onset potential of 1.0 V vs. RHE reaching currents of up to $1.5 \mu\text{A cm}^{-2}$ at 0.2 V vs. RHE. We note that thicker (500 nm) films with a less homogeneous orientation (cf. Figure 5.2b) show a higher current density of $4.3 \mu\text{A cm}^{-2}$ at 0.3 V vs. RHE, demonstrating that the PEC performance of the COF films can be improved (SI Figure 5.2). We investigated the cause of the photoactivity using electrodes made by dropcasting the COF components BDT and ET TA individually on ITO substrates. Cyclic voltammograms of these are shown in SI Figure 5.3. ET TA shows no difference between dark and light currents below 0.4 V vs. RHE indicating that it is not photoactive by itself. The BDT electrode shows similar but lower photoactivity compared to the COF. We assume, therefore, that the photoactivity of the COF arises from the BDT component and that the formation of an oriented film in which the BDT is covalently bound amplifies its photoresponse and also improves stability. We also investigated whether the oriented porous structure of the BDT-ET TA films is required for successful water reduction. To this end, we prepared reference films using different solvents (mesitylene or anisole) for the COF growth solution, which do

Oriented Films of Conjugated 2D Covalent Organic Frameworks as Photocathodes for Water Splitting

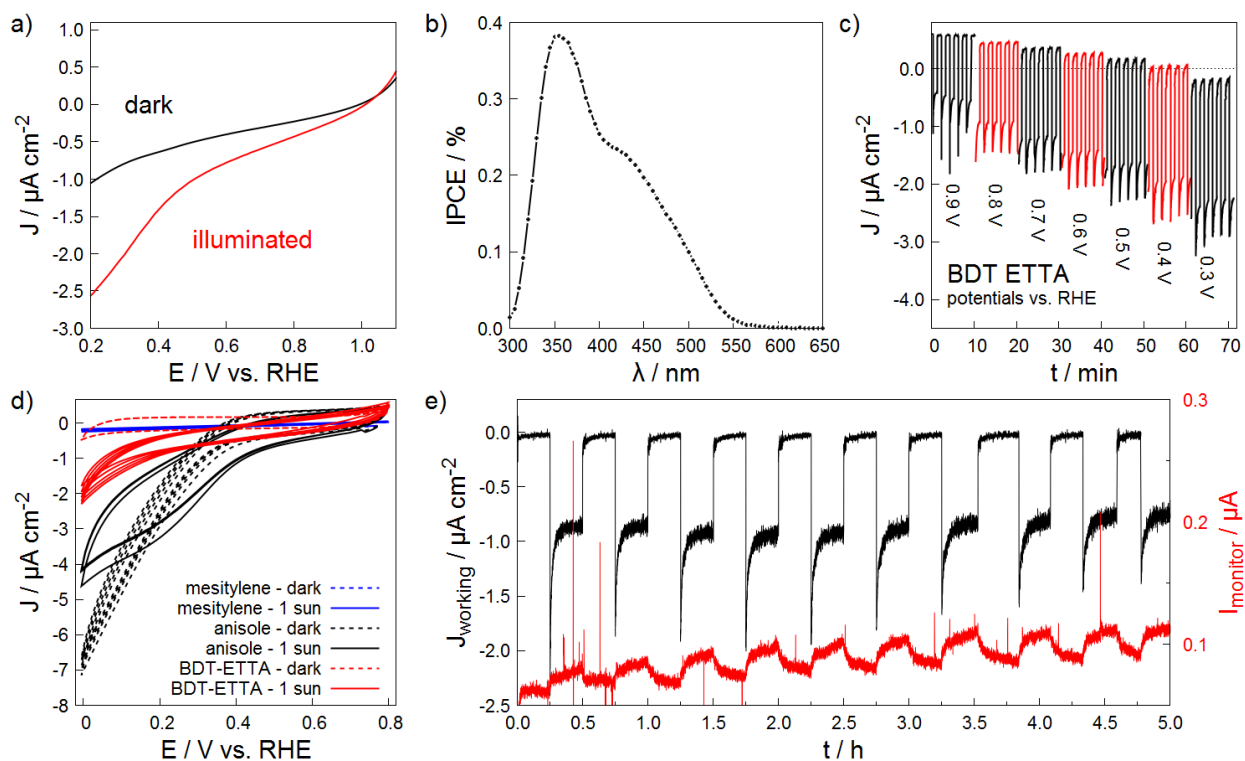


Figure 5.4. a) Linear sweep voltammograms of BDT-ETTA films on ITO performed in the dark (black) and under AM 1.5 illumination through the substrate (red). b) The corresponding IPCE spectrum quantifies the photoresponse of the COF electrodes in the visible spectral range. c) Chronoamperometric data of a BDT-ETTA film collected under chopped illumination (8.3 mHz, 455 nm, 10^{17} s $^{-1}$ cm $^{-2}$) demonstrating the photocurrent response at different potentials. d) Cyclic voltammograms of BDT-ETTA films grown from different solvents. e) Chronoamperometric data recorded on a BDT-ETTA film at 0.4 V vs. RHE (black) under chopped AM 1.5 illumination. Oxidation current recorded simultaneously on a platinum mesh indicator electrode (red) indicating the formation of hydrogen under illumination (see SI for experimental details).

not result in oriented growth. Figure 5.4d shows cyclic voltammograms of these films under dark and illuminated conditions. In the case of films grown from mesitylene, no significant currents are observed in either case. Films grown from anisole exhibit very high dark reduction currents above the HER onset potential, indicating a reaction of the film material. The subsequent CV scans under illumination yield a photocurrent lower than the original dark current over a wide potential range. This indicates that the film is neither photoactive nor stable under operating conditions. From these findings we conclude that oriented BDT-ETTA films, grown using suitable procedures such as those described in this study, are required for stable water photoreduction. Therefore, due to the well-defined geometry of the highly oriented thin (100 nm) films, we have chosen these as a system for

Results and discussion

further photoelectrochemical study. The incident-photon-to-current-efficiency (IPCE) of these thin films was determined to examine the photoelectrochemical performance of the COF electrode at different wavelengths (Figure 5.4b). The BDT-ETTA COF showed light-to-current conversion activity over a broad spectral range below 530 nm, reaching a maximum IPCE of 0.38 % at 355 nm. Stability of the photoabsorber is a main requirement for achieving energy payback via photoelectrochemical hydrogen generation.⁵⁶ To investigate this, we performed chronoamperometric measurements under chopped illumination (8.3 mHz, 455 nm, $10^{17} \text{ s}^{-1} \text{ cm}^{-2}$) at different potentials between 0.9 and 0.3 V vs. RHE for 10 min each (Figure 5.4c). BDT-ETTA films showed a stable photocurrent response over the entire potential range while the absolute values of current density followed the trend of the linear sweep voltammograms.

Further, we investigated the stability of the COF photoelectrode for an extended period of time at 0.4 V vs. RHE. At this potential, the BDT-ETTA films showed stable behavior with a negligible dark current density and good photoactivity. Chronoamperometric data was recorded at this potential for 5 hours (Figure 5.4e, black). The sample was alternately kept in the dark and illuminated by AM 1.5 simulated sunlight for 15 minutes at a time. After the initial switch-on transient a steady-state photocurrent density of $0.9 \mu\text{A cm}^{-2}$ was reached in each illumination step. To ensure that the resulting photocurrent arises from the water reduction, we have designed a four-electrode setup enabling to monitor continuously the hydrogen evolution during this stability test (see experimental details and SI Figure 5.4 for further information). A platinum indicator electrode was placed next to the photocathode and polarized at 1.1 V vs. RHE to oxidize dissolved hydrogen in the electrolyte. An oxidation current recorded at this electrode indicates hydrogen evolution in the system although quantification of the hydrogen amount via this method is challenging due to a low collection efficiency of the indicator electrode (SI Figure 5.6). Prior to measurements the indicator electrode was polarized without illumination until a stable background current of $0.06 \mu\text{A}$ was reached (SI Figure 5.5). Illumination of the COF film resulted in a photocurrent detected on the photoelectrode (Figure 5.4e, black) and a simultaneous rise in the hydrogen oxidation current at the indicator electrode (Figure 5.4e, red). Switching off the light results in a decay of photocurrent as well as the oxidation current. This behavior is stable and repeatable over the course of the measurement, indicating stability of the material under photoelectrochemical operating conditions. In order to rule out that the oxidative current observed in Figure 5.4e results from any other species than photoelectrochemically evolved hydrogen, we quantified the product with a hydrogen microsensor (*Unisense A/S H₂-NPLR*) with a

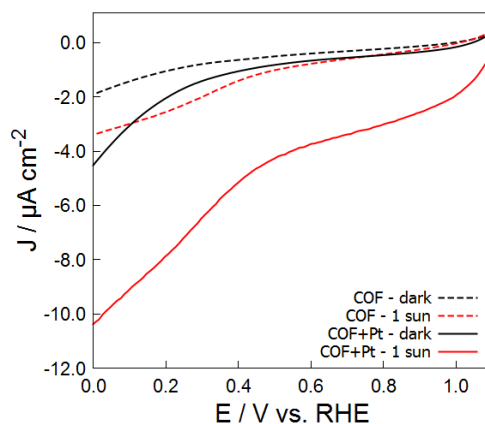


Figure 5.5. Linear sweep voltammograms of BDT-ETTA films on ITO performed in the dark (black) and under AM 1.5 illumination through the substrate (red). The combination of BDT-ETTA with platinum nanoparticles (solid lines) leads to an increased photocurrent over the whole potential range compared to bare BDT-ETTA films (dashed lines).

hydrogen-selective silicone membrane. At a static potential of the COF film of 0.4 V vs. RHE, a direct correlation between the hydrogen evolution and the illumination of the sample with AM1.5 simulated sunlight is evident (SI Figure 5.8). The long-term stability demonstrated by the COF photoelectrode shows that no components of the COF material are dissolved by photocorrosion. This demonstrates that a BDT-ETTA covalent organic framework can be used as a stable photocathode for PEC water reduction. The conversion efficiency of photoelectrodes can be enhanced by a number of methods, including the application of a co-catalyst which facilitates the charge transfer to the electrolyte. We demonstrate that this is viable for COF photocathodes by decorating the COF film with platinum nanoparticles. As shown in Figure 5.5, the BDT-ETTA/Pt films show a four-fold increase in photocurrent compared to bare BDT-ETTA photocathodes. Therefore, we see the potential to improve the efficiency of COF photoelectrodes by combining them with suitable co-catalysts.

5.3 Conclusion

Our results show that BDT-ETTA COF films are viable photocathodes for light-driven water reduction. The material meets the requirements for this application, which are efficient light harvesting, suitable band positions, and stability. The polyimine framework BDT-ETTA is the first to be investigated in this context, representing an unexplored field of applications for COFs. Given the enormous diversity

Experimental Section

of molecular building units that can be employed in the construction of COFs, both the development of new framework structures and fine-tuning the properties of existing ones is possible. We envision that future research on combinations of building blocks and stacking modes and the combination of the photoabsorber with suitable co-catalysts will allow for further optimizing charge carrier lifetimes, long term stability, and charge transfer kinetics in order to improve the conversion efficiency obtainable from COF-based photoelectrodes.

5.4 Experimental Section

All reagents and solvents were obtained from commercial suppliers and used as received. Benzo(1,2-*b*:4,5-*b'*)dithiophene (BDT, >98%, TCI), benzyl alcohol (BnOH, anhydrous, Sigma-Aldrich), mesitylene (Mes, anhydrous, Sigma-Aldrich), tetrahydrofuran (THF, extra dry, stabilized, Acros Organics), acetonitrile (Sigma-Aldrich), ITO glass substrates (Visiontek, 12 Ω /sq). FTO-coated glass substrates (Pilkington, 7 Ω /sq).

5.4.1 General procedure for BDT-ETTA COF films:

Under argon, BDT (7.88 mg, 0.032 mmol) and ETTA (76.28 mg, 0.016 mmol) were finely ground, added to a PTFE autoclave, and suspended in a mixture of benzyl alcohol and mesitylene (V/V 1:1, 2000 μ L). A glass slide holder, containing ITO or FTO slides, was introduced to the liner. Acetic acid (6 M, 200 μ L) was added, the autoclave was sealed and the mixture was kept at 120 $^{\circ}$ C for 3 days. The resulting orange film was rinsed with anhydrous THF and dried under reduced pressure. COF bulk material that precipitated beneath the film substrate holder was filtered and purified in a Soxhlet extractor for 24 h with anhydrous THF.

5.4.2 Structural characterization.

^1H NMR spectra were recorded on Bruker AV 400 and AV 400 TR spectrometers. Proton chemical shifts are expressed in parts per million (δ scale) and are calibrated using residual non deuterated solvent peaks as an internal reference (e.g. DMSO- d_6 : 2.50 ppm). Ultraviolet-vis-infrared diffuse reflectance spectra (Kubelka-Munk spectrum) of the films were recorded on a Perkin-Elmer Lambda 1050 spectrometer equipped with a 150 mm integrating sphere. Thin film absorbance spectra were measured by illuminating the sample through the substrate side and correcting it with the relating reflection.⁵⁷ Scanning electron microscopy (SEM) images were recorded with a JEOL 6500F and a FEI Helios NanoLab G3 UC scanning electron microscope equipped with a field emission gun operated at

3-5 kV. Transmission electron microscopy (TEM) was performed on an FEI Titan Themis equipped with a field emission gun operated at 300 kV. X-ray diffraction (XRD) measurements were performed using a Bruker D8 Discover with Ni-filtered Cu $K\alpha$ radiation and a LynxEye position-sensitive detector. Experimental XRD data were used for Pawley refinement to optimize the hypothetical structure. The initial structure models of the COFs were built using the Forcite module of the Accelrys Materials Studio software package. We applied the space group with the highest possible symmetry, i.e. $P6$, taking into account the propeller-like conformation of the central building blocks. Using this coarse model we determined the unit cell parameters via Pawley refinement of the PXRD data. Nitrogen sorption isotherms were recorded on a Quantachrome Autosorb 1 at 77 K within a pressure range from $p/p_0 = 0.001$ to 0.98. Prior to the measurement of the sorption isotherms the samples were heated for 24 h at 120°C under turbo-pumped vacuum. For the evaluation of the surface area the BET model was applied between 0.05 and 0.2 p/p_0 . Pore size distributions were calculated using the QSDFT equilibrium model with a carbon kernel for cylindrical pores.

5.5 Associated Content

The Supporting Information is available free of charge on the ACS Publications website at DOI: 10.1021/jacs.7b06081. Detailed information about synthetic procedures, structural and electrochemical characterization of BDT-ETTA photoelectrodes.

5.6 Author Information

Corresponding Author

*bein@lmu.de *d.fattakhova@fz-juelich.de

Author Contributions

T.S., A.G.H, J.K., D.D.M and D.F.-R. conceived and designed the project. T.S., I.K., J.M.R., A.E., M.C., S.H. and D.D.M. carried out the syntheses and characterized the materials. K.P. carried out the SEM characterization. M.D. carried out the TEM characterization. J.K., A.G.H., D.B. and I.K. carried out the electrochemical characterization. T.S., A.G.H. and J.K. wrote the manuscript with contributions of all the authors. D.F.-R. and T.B. supervised the project. All authors discussed the results and contributed to the manuscript.

Acknowledgments

Notes

The authors declare no competing financial interest.

5.7 Acknowledgments

The authors are grateful for funding from the German Science Foundation (DFG, SPP 1613), the NIM cluster (DFG) and the Free State of Bavaria (the research networks 'Solar Technologies Go Hybrid' and UMWELTnanoTECH). The research leading to these results received funding from the European Research Council under the European Union's Seventh Framework Programme (FP7/2007-2013)/ERC Grant Agreement 321339. A.G.H. gratefully acknowledges funding by the Fonds der chemischen Industrie. A.E. thanks the DAAD RISE worldwide program for the opportunity to conduct this research at the LMU.

5.8 References

- (1) Peter, L. M., *J. Solid State Electrochem.* **2012**, *17*, 315-326.
- (2) van de Krol, R.; Liang, Y.; Schoonman, J., *J. Mater. Chem.* **2008**, *18*, 2311-2320.
- (3) Sivula, K.; Le Formal, F.; Gratzel, M., *ChemSusChem* **2011**, *4*, 432-449.
- (4) Dunn, H. K.; Feckl, J. M.; Muller, A.; Fattakhova-Rohlfing, D.; Morehead, S. G.; Roos, J.; Peter, L. M.; Scheu, C.; Bein, T., *Phys. Chem. Chem. Phys.* **2014**, *16*, 24610-24620.
- (5) Hu, S.; Shaner, M. R.; Beardslee, J. A.; Lichterman, M.; Brunschwig, B. S.; Lewis, N. S., *Science* **2014**, *344*, 1005-1009.
- (6) Reece, S. Y.; Hamel, J. A.; Sung, K.; Jarvi, T. D.; Esswein, A. J.; Pijpers, J. J.; Nocera, D. G., *Science* **2011**, *334*, 645-648.
- (7) Woodhouse, M.; Parkinson, B. A., *Chem. Soc. Rev.* **2009**, *38*, 197-210.
- (8) Woodhouse, M.; Parkinson, B. A., *Chem. Mater.* **2008**, *20*, 2495-2502.
- (9) Singh, A. K.; Mathew, K.; Zhuang, H. L.; Hennig, R. G., *J. Phys. Chem. Lett.* **2015**, *6*, 1087-1098.
- (10) Castelli, I. E.; Olsen, T.; Datta, S.; Landis, D. D.; Dahl, S.; Thygesen, K. S.; Jacobsen, K. W., *Energy Environ. Sci.* **2012**, *5*, 5814-5819.
- (11) Hunt, J. R.; Doonan, C. J.; LeVangie, J. D.; Côté, A. P.; Yaghi, O. M., *J. Am. Chem. Soc.* **2008**, *130*, 11872-11873.
- (12) Côte, A. P.; Benin, A. I.; Ockwig, N. W.; O'Keeffe, M.; Matzger, A. J.; Yaghi, O. M., *Science* **2005**, *310*, 1166-1170.
- (13) Calik, M.; Sick, T.; Dogru, M.; Döblinger, M.; Datz, S.; Budde, H.; Hartschuh, A.; Auras, F.; Bein, T., *J. Am. Chem. Soc.* **2016**, *138*, 1234-1239.
- (14) Lohse, M. S.; Rotter, J. M.; Margraf, J. T.; Werner, V.; Becker, M.; Herbert, S.; Knochel, P.; Clark, T.; Bein, T.; Medina, D. D., *CrystEngComm* **2016**, *18*, 4295-4302.

- (15) Medina, D. D.; Rotter, J. M.; Hu, Y.; Dogru, M.; Werner, V.; Auras, F.; Markiewicz, J. T.; Knochel, P.; Bein, T., *J. Am. Chem. Soc.* **2015**, *137*, 1016-1019.
- (16) Uribe-Romo, F. J.; Hunt, J. R.; Furukawa, H.; Klöck, C.; O’Keeffe, M.; Yaghi, O. M., *J. Am. Chem. Soc.* **2009**, *131*, 4570-4571.
- (17) Chen, X.; Addicoat, M.; Irle, S.; Nagai, A.; Jiang, D., *J. Am. Chem. Soc.* **2013**, *135*, 546-549.
- (18) Zhang, Y.-B.; Su, J.; Furukawa, H.; Yun, Y.; Gándara, F.; Duong, A.; Zou, X.; Yaghi, O. M., *J. Am. Chem. Soc.* **2013**, *135*, 16336-16339.
- (19) Ascherl, L.; Sick, T.; Margraf, J. T.; Lapidus, S. H.; Calik, M.; Hettstedt, C.; Karaghiosoff, K.; Döblinger, M.; Clark, T.; Chapman, K. W.; Auras, F.; Bein, T., *Nat. Chem.* **2016**, *8*, 310-316.
- (20) Fang, Q.; Zhuang, Z.; Gu, S.; Kaspar, R. B.; Zheng, J.; Wang, J.; Qiu, S.; Yan, Y., *Nat. Commun.* **2014**, *5*, 4503-4510.
- (21) Fang, Q.; Wang, J.; Gu, S.; Kaspar, R. B.; Zhuang, Z.; Zheng, J.; Guo, H.; Qiu, S.; Yan, Y., *J. Am. Chem. Soc.* **2015**, *137*, 8352-8355.
- (22) Uribe-Romo, F. J.; Doonan, C. J.; Furukawa, H.; Oisaki, K.; Yaghi, O. M., *J. Am. Chem. Soc.* **2011**, *133*, 11478-11481.
- (23) Dalapati, S.; Jin, S.; Gao, J.; Xu, Y.; Nagai, A.; Jiang, D., *J. Am. Chem. Soc.* **2013**, *135*, 17310-17313.
- (24) Jackson, K. T.; Reich, T. E.; El-Kaderi, H. M., *Chem. Commun.* **2012**, *48*, 8823-8825.
- (25) Furukawa, H.; Yaghi, O. M., *J. Am. Chem. Soc.* **2009**, *131*, 8875-8883.
- (26) Doonan, C. J.; Tranchemontagne, D. J.; Glover, T. G.; Hunt, J. R.; Yaghi, O. M., *Nat. Chem.* **2010**, *2*, 235-238.
- (27) Xu, H.; Chen, X.; Gao, J.; Lin, J.; Addicoat, M.; Irle, S.; Jiang, D., *Chem. Commun.* **2014**, *50*, 1292-1294.
- (28) Ding, S.-Y.; Gao, J.; Wang, Q.; Zhang, Y.; Song, W.-G.; Su, C.-Y.; Wang, W., *J. Am. Chem. Soc.* **2011**, *133*, 19816-19822.
- (29) Oh, H.; Kalidindi, S. B.; Um, Y.; Bureekaew, S.; Schmid, R.; Fischer, R. A.; Hirscher, M., *Angew. Chem. Int. Ed.* **2013**, *52*, 13219-13222.
- (30) Ma, H.; Ren, H.; Meng, S.; Yan, Z.; Zhao, H.; Sun, F.; Zhu, G., *Chem. Commun.* **2013**, *49*, 9773-9775.
- (31) Lohse, M. S.; Stassin, T.; Naudin, G.; Wuttke, S.; Ameloot, R.; De Vos, D.; Medina, D. D.; Bein, T., *Chem. Mater.* **2016**, *28*, 626-631.
- (32) DeBlase, C. R.; Silberstein, K. E.; Truong, T.-T.; Abruña, H. D.; Dichtel, W. R., *J. Am. Chem. Soc.* **2013**, *135*, 16821-16824.
- (33) Chandra, S.; Kundu, T.; Kandambeth, S.; BabaRao, R.; Marathe, Y.; Kunjir, S. M.; Banerjee, R., *J. Am. Chem. Soc.* **2014**, *136*, 6570-6573.
- (34) Flugel, E. A.; Lau, V. W.; Schlomberg, H.; Glaum, R.; Lotsch, B. V., *Chem. Eur. J.* **2016**, *22*, 3676-3680.
- (35) Schwinghammer, K.; Tuffy, B.; Mesch, M. B.; Wirnhier, E.; Martineau, C.; Taulelle, F.; Schnick, W.; Senker, J.; Lotsch, B. V., *Angew. Chem. Int. Ed.* **2013**, *52*, 2435-2439.
- (36) Schwinghammer, K.; Mesch, M. B.; Duppel, V.; Ziegler, C.; Senker, J.; Lotsch, B. V., *J. Am. Chem. Soc.* **2014**, *136*, 1730-1733.

References

- (37) Lau, V. W.; Mesch, M. B.; Duppel, V.; Blum, V.; Senker, J.; Lotsch, B. V., *J. Am. Chem. Soc.* **2015**, *137*, 1064-1072.
- (38) Caputo, C. A.; Gross, M. A.; Lau, V. W.; Cavazza, C.; Lotsch, B. V.; Reisner, E., *Angew. Chem. Int. Ed.* **2014**, *53*, 11538-11542.
- (39) Zhang, J.; Chen, X.; Takanahe, K.; Maeda, K.; Domen, K.; Epping, J. D.; Fu, X.; Antonietti, M.; Wang, X., *Angew. Chem. Int. Ed. Engl.* **2010**, *49*, 441-444.
- (40) Wang, X.; Maeda, K.; Thomas, A.; Takanahe, K.; Xin, G.; Carlsson, J. M.; Domen, K.; Antonietti, M., *Nat. Mater.* **2009**, *8*, 76-80.
- (41) Schwinghammer, K.; Hug, S.; Mesch, M. B.; Senker, J.; Lotsch, B. V., *Energy Environ. Sci.* **2015**, *8*, 3345-3353.
- (42) Schwab, M. G.; Hamburger, M.; Feng, X.; Shu, J.; Spiess, H. W.; Wang, X.; Antonietti, M.; Mullen, K., *Chem. Commun.* **2010**, *46*, 8932-8934.
- (43) Vyas, V. S.; Haase, F.; Stegbauer, L.; Savasci, G.; Podjaski, F.; Ochsenfeld, C.; Lotsch, B. V., *Nat. Commun.* **2015**, *6*, 8508-8516.
- (44) Stegbauer, L.; Schwinghammer, K.; Lotsch, B. V., *Chem. Sci.* **2014**, *5*, 2789-2793.
- (45) Bi, J.; Fang, W.; Li, L.; Wang, J.; Liang, S.; He, Y.; Liu, M.; Wu, L., *Macromol. Rapid Commun.* **2015**, *36*, 1799-1805.
- (46) Kuecken, S.; Acharjya, A.; Zhi, L.; Schwarze, M.; Schomacker, R.; Thomas, A., *Chem Commun (Camb)* **2017**, *53*, 5854-5857.
- (47) Chen, X.; Addicoat, M.; Jin, E.; Zhai, L.; Xu, H.; Huang, N.; Guo, Z.; Liu, L.; Irle, S.; Jiang, D., *J. Am. Chem. Soc.* **2015**, *137*, 3241-3247.
- (48) Haase, F.; Banerjee, T.; Savasci, G.; Ochsenfeld, C.; Lotsch, B. V., *Faraday Discuss.* **2017**, *201*, 247-264.
- (49) He, S.; Rong, Q.; Niu, H.; Cai, Y., *Chem. Commun.* **2017**, *53*, 9636-9639.
- (50) Banerjee, T.; Haase, F.; Savasci, G.; Gottschling, K.; Ochsenfeld, C.; Lotsch, B. V., *J. Am. Chem. Soc.* **2017**.
- (51) Dogru, M.; Handloser, M.; Auras, F.; Kunz, T.; Medina, D.; Hartschuh, A.; Knochel, P.; Bein, T., *Angew. Chem. Int. Ed.* **2013**, *52*, 2920-2924.
- (52) Calik, M.; Auras, F.; Salonen, L. M.; Bader, K.; Grill, I.; Handloser, M.; Medina, D. D.; Dogru, M.; Löbermann, F.; Trauner, D.; Hartschuh, A.; Bein, T., *J. Am. Chem. Soc.* **2014**, *136*, 17802-17807.
- (53) Medina, D. D.; Werner, V.; Auras, F.; Tautz, R.; Dogru, M.; Schuster, J.; Linke, S.; Döblinger, M.; Feldmann, J.; Knochel, P.; Bein, T., *ACS Nano* **2014**, *8*, 4042-4052.
- (54) Jin, S.; Ding, X.; Feng, X.; Supur, M.; Furukawa, K.; Takahashi, S.; Addicoat, M.; El-Khouly, M. E.; Nakamura, T.; Irle, S.; Fukuzumi, S.; Nagai, A.; Jiang, D., *Angew. Chem. Int. Ed.* **2013**, *52*, 2017-2021.
- (55) Zhou, T. Y.; Xu, S. Q.; Wen, Q.; Pang, Z. F.; Zhao, X., *J. Am. Chem. Soc.* **2014**, *136*, 15885-15888.
- (56) Sathre, R.; Scown, C. D.; Morrow, W. R.; Stevens, J. C.; Sharp, I. D.; Ager, J. W.; Walczak, K.; Houle, F. A.; Greenblatt, J. B., *Energy Environ. Sci.* **2014**, *7*, 3264-3278.
- (57) Klahr, B. M.; Martinson, A. B. F.; Hamann, T. W., *Langmuir* **2011**, *27*, 461-468.

5.9 Supporting Information

5.9.1 Materials and Methods

All reagents and solvents were obtained from commercial suppliers and used as received. Benzo(1,2-*b*:4,5-*b'*)dithiophene (BDT, >98%, TCI), benzyl alcohol (BnOH, anhydrous, Sigma-Aldrich), mesitylene (Mes, anhydrous, Sigma-Aldrich), tetrahydrofuran (THF, extra dry, stabilized, Acros Organics), ITO glass substrates (Visiontek, 12 Ω /sq). FTO-coated glass substrates (Pilkington, 7 Ω /sq).

Nuclear magnetic resonance (NMR) spectra were recorded on Bruker AV 400 and AV 400 TR spectrometers. Proton chemical shifts are expressed in parts per million (δ scale) and are calibrated using residual non-deuterated solvent peaks as internal reference (e.g. DMSO-*d*₆: 2.50 ppm).

Infrared (IR) spectra were recorded on a Perkin Elmer Spectrum BX II FT-IR system and a Thermo Scientific Nicolet™ 6700 FT-IR spectrometer in transmission mode. IR data are reported in wavenumbers (cm⁻¹).

UV-Vis spectra were recorded using a Perkin-Elmer Lambda 1050 spectrometer equipped with a 150 mm integrating sphere. The reflectance-corrected absorbance A_{corr} was calculated according to Eq. 5.1, where T_{sample} , $T_{substrate}$, R_{sample} and $R_{substrate}$ denote the transmittance and reflectance of the sample (substrate with COF film) and bare substrate, respectively.¹

$$A_{corr}(\lambda) = -\log_{10} \left(\frac{\frac{T_{sample}(\lambda)}{T_{substrate}(\lambda)}}{1 - \frac{R_{sample}(\lambda) - R_{substrate}(\lambda)}{T_{substrate}(\lambda)}} \right) \quad \text{Eq. 5.1}$$

Nitrogen sorption isotherms were recorded on a Quantachrome Autosorb 1 at 77 K within a pressure range of $p/p_0 = 0.001$ to 0.98. Prior to the measurement of the sorption isotherms the samples were heated for 24 h at 120°C under turbo-pumped vacuum. For the evaluation of the surface area the BET model was applied between 0.05 and 0.2 p/p_0 . Pore size distributions were calculated using the QSDFT equilibrium model (desorption branch) with a carbon kernel for cylindrical pores.

Supporting Information

Thermogravimetric analysis (TGA) measurements were performed on a Netzsch Jupiter ST 449 C instrument equipped with a Netzsch TASC 414/4 controller. The samples were heated from room temperature to 900 °C under a synthetic air flow (25 mL min⁻¹) at a heating rate of 1 K min⁻¹.

Powder X-ray diffraction (PXRD) measurements were performed using a Bruker D8 Discover with Ni-filtered Cu-K α radiation and a LynxEye position-sensitive detector. (scan speed of 4 s per 0.01 degree 2 θ) Experimental XRD data were used for Pawley refinement to optimize the hypothetical structure.

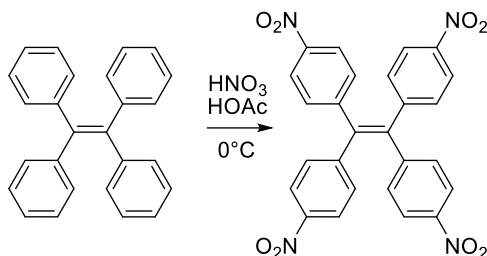
The initial **structure models of the COFs** were built using the Forcite module of the Accelrys Materials Studio software package. We applied the space group with the highest possible symmetry, i.e. *P6*, taking into account the propeller-like conformation of the central building blocks. Using this coarse model we determined the unit cell parameters via Pawley refinement of our PXRD data.

Transmission electron microscopy (TEM) was performed on an FEI Titan Themis equipped with a field emission gun operated at 300 kV.

Scanning electron microscopy (SEM) images were recorded with a JEOL 6500F and a FEI Helios NanoLab G3 UC scanning electron microscope equipped with a field emission gun operated at 3-5 kV.

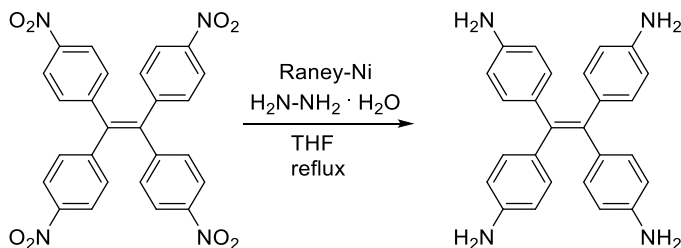
5.9.2 Synthetic procedures

5.9.2.1 1,1,2,2-Tetra(*p*-nitrophenyl)ethylene (TNPE) (adapted from Gorvin²)



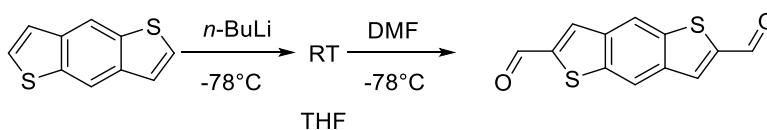
1,1,2,2-Tetraphenylethylene (3.0 g, 9.0 mmol) was slowly added with stirring at 0 °C to a mixture of 30 mL nitric acid (≥ 99%) and 30 mL glacial acetic acid. After 3 h at room temperature the solution was diluted with cold water. The resulting precipitate was filtered and dried under reduced pressure. Recrystallization from 1,4-dioxane, filtration and drying resulted in a yellow solid of TNPE with 69% yield. ¹H NMR (400 MHz, CDCl₃) δ (ppm): 8.055-8.100 (m, 8H), 7.16-7.21 (m, 8H).

5.9.2.2 1,1,2,2-Tetra(*p*-aminophenyl)ethylene (ETTA) (adapted from Lu et al.³)



TNPE (1.0 g, 1.9 mmol) was dissolved in 20 mL of anhydrous THF in a 100 mL flask under nitrogen atmosphere. Approximately 4 g of Raney-nickel catalyst slurry was added to the mixture with stirring. Hydrazine monohydrate (1.3 mL, 26 mmol) was then added dropwise to the stirred mixture. The resulting solution was heated to reflux for two hours. The solution was allowed to cool to room temperature and filtered. The filtrate was dried under reduced pressure, giving a yellow solid with 79% yield. ¹H NMR (400 MHz, DMSO-*d*₆) δ (ppm): 6.60-6.55 (m, 8H), 6.29-6.24 (m, 8H), 4.84 (s, 8H).

5.9.2.3 Benzo[1,2-*b*:4,5-*b'*]dithiophene-2,6-dicarboxaldehyde (BDT) (adapted from Kofsmehl et al.⁴)



Supporting Information

Benzo[1,2-*b*:4,5-*b'*]dithiophene (1.0 g, 5.3 mmol) was dissolved in 100 mL anhydrous, inhibitor-free THF in an outgassed 250 mL flask under nitrogen atmosphere. The stirred solution was cooled to -78°C in a dry ice/acetone cooling bath. A solution of *n*-butyl lithium (5.0 mL, 2.5 M in *n*-hexane, 12.5 mmol) was added dropwise within 10 minutes. The solution was stirred for 30 minutes at -78°C and after removal of the cooling bath for 1 h at room temperature. The solution was then cooled again to -78°C and DMF (1.0 mL, 13.0 mmol) was added dropwise. After stirring overnight, the solution was poured into ice water and filtered. The yellow precipitate was washed with water several times and further treated with small amounts of MeOH and Et₂O. The solid was dried under reduced pressure, giving a yellow solid with 46% yield. ¹H NMR (400 MHz, DMSO-*d*₆) δ (ppm): 8.53 (s, 2H), 8.89 (s, 2H), 10.20 (s, 2H); ¹³C NMR (100 MHz, DMSO-*d*₆) δ (ppm): 121.6, 135.3, 138.4, 138.9, 144.9, 186.6.

5.9.2.4 BDT-ETTA COF synthesis:

Benzo[1,2-*b*:4,5-*b'*]dithiophene-2,6-dicarboxaldehyde (BDT, 4.94 mg, 0.0201 mmol) and 1,1,2,2-tetra(*p*-aminophenyl)ethylene (ETTA, 3.94 mg, 0.0100 mmol) were finely ground and suspended in a mixture of benzyl alcohol and mesitylene (V/V 9:1, 500 μL). The resulting mixture was sonicated until complete dissolution of the educts was achieved. Acetic acid (6 M, 50 μL) was added and the mixture was kept in a culture tube at 120 °C for 3 days. The resulting orange precipitate was suction filtered, treated with anhydrous THF to remove the less volatile solvent, further purified by using a Soxhlet extraction apparatus with THF and dried under reduced pressure.

5.9.2.5 BDT-ETTA Films:

Benzo[1,2-*b*:4,5-*b'*]dithiophene-2,6-dicarboxaldehyde (BDT, 7.88 mg, 0.0320 mmol) and 1,1,2,2-tetra(*p*-aminophenyl)ethylene (ETTA, 6.28 mg, 0.0160 mmol) were finely ground, added to a PTFE autoclave, and suspended in a mixture of benzyl alcohol and mesitylene (V/V 1:1, 2000 μL). A glass slide holder, containing ITO or FTO glass slides in the horizontal position with the ITO/FTO side downwards, was transferred into the autoclave. Acetic acid (6 M, 200 μL) was added, the liner was sealed and the mixture was kept at 120 °C for 3 days. The as-synthesized COF films were rinsed with THF to remove residues of the reaction mixture. COF bulk material precipitated beneath the film substrate holder was collected by filtration and purified in a Soxhlet extractor for 24 h with anhydrous THF.

5.9.2.6 Platinum nanoparticles

PtCl₂ (4.7 mg, 17,7 μmol) was dispersed in 14 mL *tert*-butanol, transferred into a Teflon-lined steel autoclave and heated in a laboratory oven at 175°C for 24 h. The metallic grey product was separated by centrifugation (15 min, 15000 rpm) and dispersed in 6 mL ethanol. 50 μL of the resulting dispersion were dropcasted on a BDT-ETTA COF thin film and dried at room temperature before the electrode was used for photoelectrochemical characterization.

5.9.3 Electrochemical measurements

5.9.3.1 Non-aqueous photoelectrochemistry

The non-aqueous photoelectrochemical experiments were performed in a sealed borosilicate glass cell in a three-electrode configuration with the COF film as the working electrode, a Pt foil counter electrode and a silver wire as the reference. This cell was assembled in an argon-filled glove box ($c(\text{O}_2) < 0.1$ ppm, $c(\text{H}_2\text{O}) < 0.1$ ppm). The electrolyte was 0.1 M NBu₄PF₆ (Aldrich, 99.9 %) in acetonitrile (Aldrich, anhydrous); it was prepared under the same conditions and dried further using 3 Å molecular sieves. The COF films were degassed in vacuum at 120 °C for several hours prior to use. The potential of the Ag reference vs. ferrocene (Aldrich, 95 % resublimed) was established to be -200 mV in a control experiment with a blank ITO substrate. A Metrohm Autolab PGStat302N was used for the measurements. Cyclic voltammetry was performed at potentials between -0.2 and 0.5 V vs. FOC and a scan rate of 20 mV s⁻¹. The absolute energy of the HER can be calculated according to equation 2.

$$E_{RHE,abs} = -4.5 \text{ eV} + 0.059 \text{ eV} \cdot pH \quad (2)$$

The FOC redox couple in this electrolyte is at 641 mV vs. SHE⁵ with an absolute energy of the SHE of -4.5 eV⁶, this results in an absolute energy of the FOC redox couple of -5.14 eV relative to the vacuum level.

5.9.3.2 Aqueous photoelectrochemistry

Aqueous photoelectrochemistry experiments were carried out in a custom build, airtight cell with quartz glass window (Präzisions Glas & Optik GmbH, UV-Grade Fused Silica) under constant nitrogen

Supporting Information

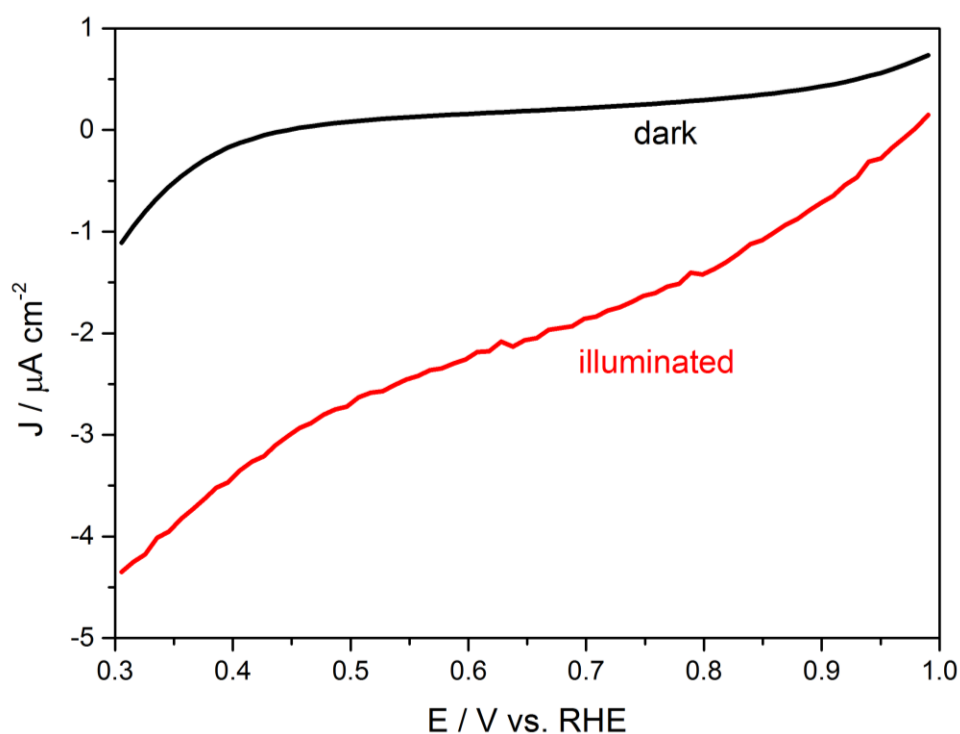
purging to remove any dissolved oxygen in the electrolyte (SI Figure 5.1). The electrolyte was 0.1 M Na₂SO₄ (Aldrich) in deionized water (Millipore Q grade, 18.2 MΩ cm) at pH 6.8. In the case of light exposure, all samples were illuminated through the substrate by an AM1.5 solar simulator (Solar Light Model 16S) at 100 mW cm⁻² or a 455 nm LED with a photon flux of 1017 s⁻¹ cm⁻² at the sample position.



SI Figure 5.1. Photograph of the custom build, airtight cell with quartz glass window and nitrogen purging used for all photoelectrochemical measurements in aqueous electrolyte.

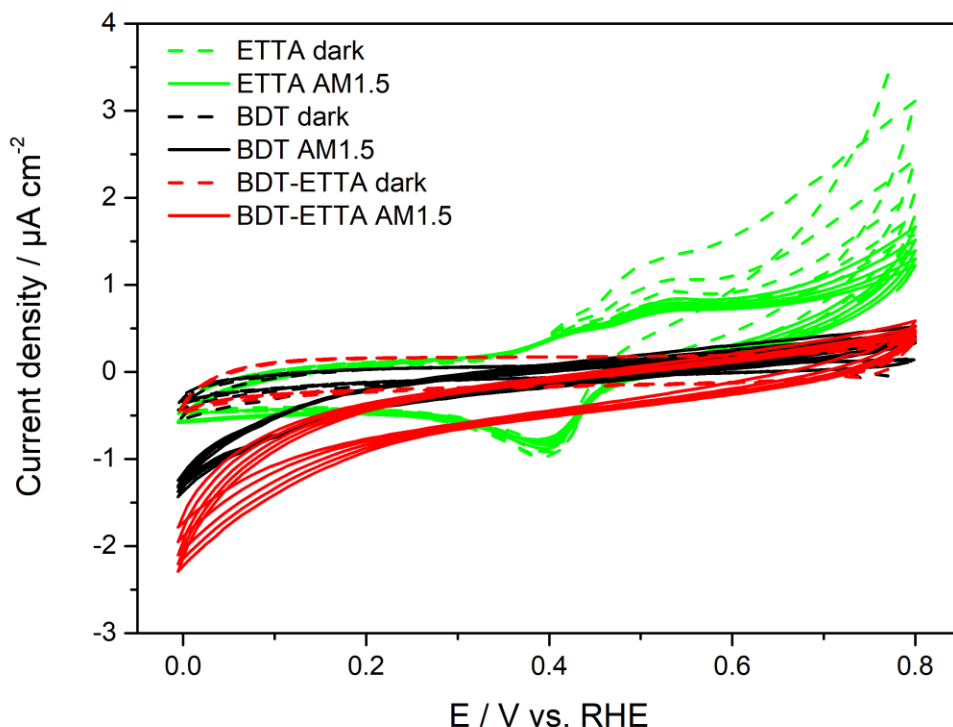
5.9.3.3 Cyclic voltammetry (CV) and chronoamperometry (CA)

CV and CA measurements were performed with a Metrohm μ -Autolab III potentiostat with FRA2 impedance analyzer with a platinum wire counter electrode and a Hg/Hg₂SO₄ reference electrode in order to apply a potential range of 0.3 – 1.0 V vs. reference hydrogen electrode (RHE). Prior to each measurement, the potential of the Hg/Hg₂SO₄ electrode was determined against RHE. The active area of the COF films was selected by masking the films with PTFE adhesive tape to expose a film area of 0.212 cm². CV measurements were performed by scanning from positive to negative potentials either in the dark or under illumination at a sweep rate of 20 mV s⁻¹.



SI Figure 5.2. Linear sweep voltammograms of a rough, 500 nm thick BDT-ETTA film on ITO performed in the dark (black) and under AM 1.5 illumination through the substrate (red).

Supporting Information



SI Figure 5.3. Cyclic voltammograms of the BDT-ETTA COF electrode (red) in the dark (dashed lines) and under AM1.5 substrate illumination (solid lines). The BDT-ETTA COF is compared with the corresponding monomers BDT (black) and ETTA (green) dropcasted on ITO substrate (2 mg monomer in 500 μL of EtOH/Acetone (v/v 1:1), respectively). We assume that the photoactivity arises from the BDT part, but the total photocurrent can be doubled for the case of a crystalline BDT-ETTA COF. In contrast, the ETTA part shows no photoactivity itself. Therefore, the formation of a COF material from photoactive building blocks like BDT allows the deposition of electrochemical stable thin film electrodes on TCO substrates.

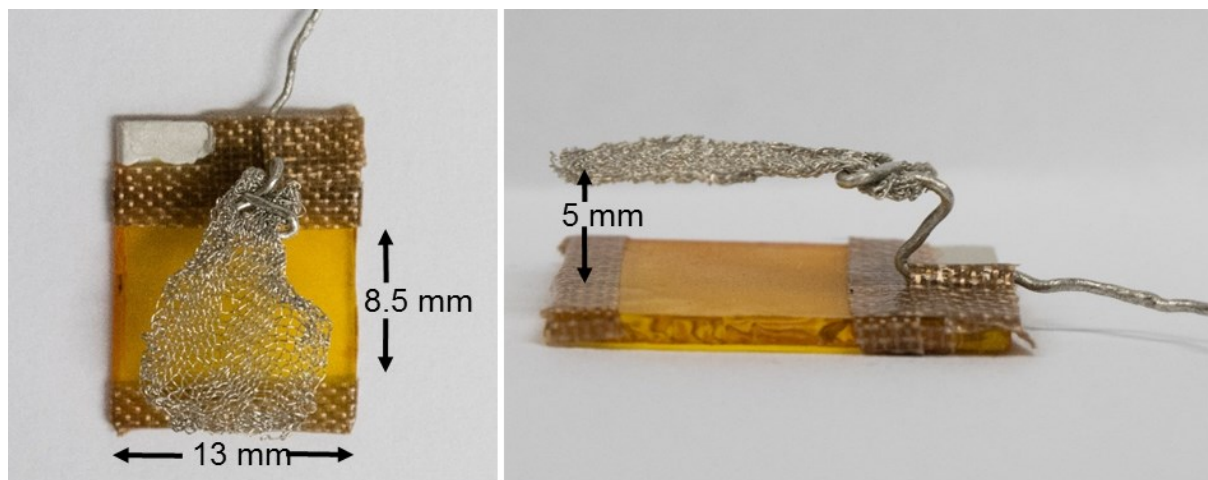
5.9.3.4 Incident Photon-to-Current conversion Efficiency (IPCE)

The IPCE measurement was performed under low-frequency chopped monochromatic light (1 Hz). A 150 W xenon lamp equipped with a monochromator and order-sorting filters was used as a light source. The sample was simultaneously illuminated by an AM1.5 solar simulator (Solar Light Model 16S) with OD3 filter (Thorlabs). The light intensity reaching the electrode was calibrated using a certified Fraunhofer ISE silicon reference cell equipped with a KG5 filter. All measurements were performed at 0.4 V vs. RHE under illumination through the substrate.

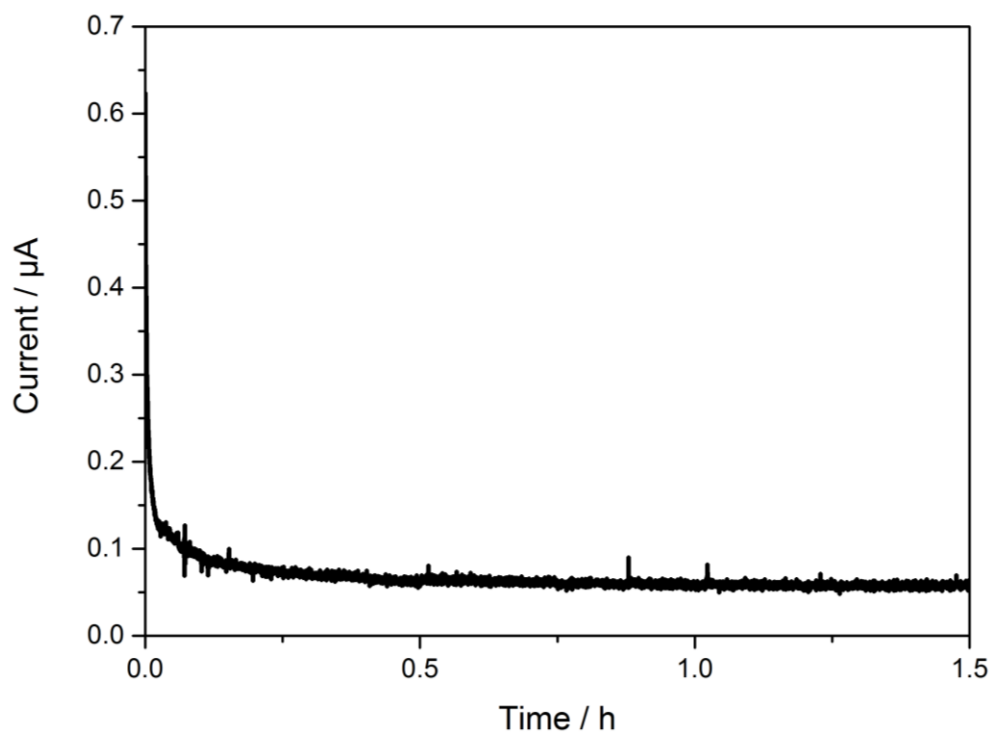
5.9.3.5 Hydrogen detection

Hydrogen detection measurements were performed in a four electrode setup with a Metrohm Autolab PGStat302N potentiostat, a platinum wire counter electrode and a Hg/Hg₂SO₄ reference electrode, whose potential was determined against a reversible hydrogen electrode within the applied measurement conditions. The exposed area of the COF thin film electrode was masked to 1.1 cm² (first working electrode) and a platinum mesh electrode was placed at a distance of 5 mm from the photoabsorber surface as second working electrode (SI Figure 5.4). In a first step prior to the hydrogen detection measurement, 1.1 V vs. RHE was applied on the platinum mesh in a three electrode mode for 1.5 hours to remove any residues which can be oxidized and therefore determine the background current (SI Figure 5.5). To drive the hydrogen evolution reaction, a potential of 0.4 V vs. RHE was applied to the COF photocathode and a potential of 1.1 V vs. RHE was set on the platinum mesh to oxidize the produced hydrogen. During the five-hour experiment, the AM1.5 illumination was manually chopped at intervals of 15 minutes. On average, the total hydrogen oxidation current increased over time (Figure 5.4e). Reference measurements with constant hydrogen evolution on blank ITO substrates with a comparable exposed area showed that it is possible to quantify only a fraction of the produced hydrogen, which was calculated from the oxidative current (SI Figure 5.6). The remaining amount is either dissolved in the electrolyte and therefore distributed over the whole volume of the measuring cell or escapes the liquid due to the moderate nitrogen purging (SI Figure 5.7). For these reasons, the absolute amount of produced hydrogen could not be determined. However, the observation that the oxidation current rises and falls with the photocurrent proves that the oxidized species is produced exclusively in the photoelectrochemical process at the COF film.

Supporting Information

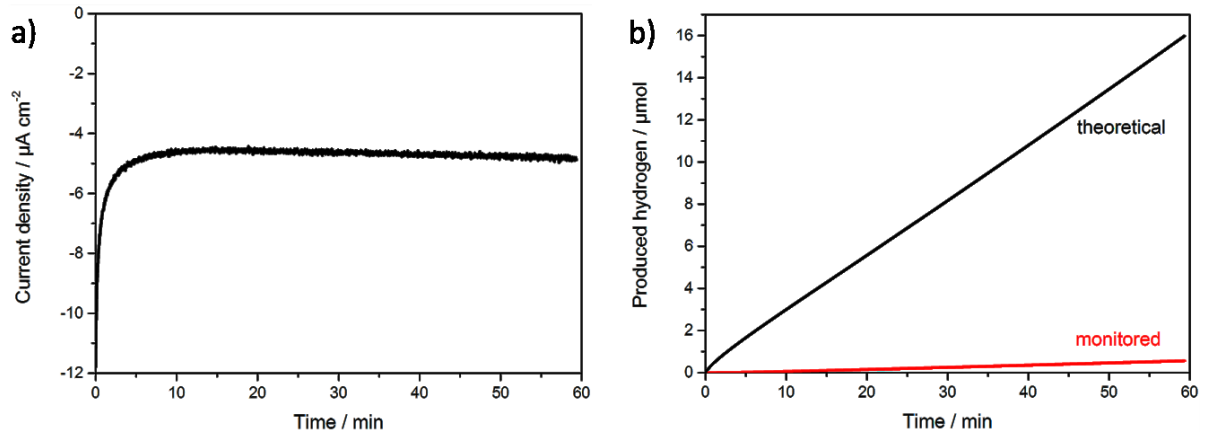


SI Figure 5.4. Photographs of a sample used for a hydrogen detection measurement: The masked COF film is contacted with silver paint (first working electrode) and a platinum mesh is placed in 5 mm distance to the film surface to oxidize the produced hydrogen.

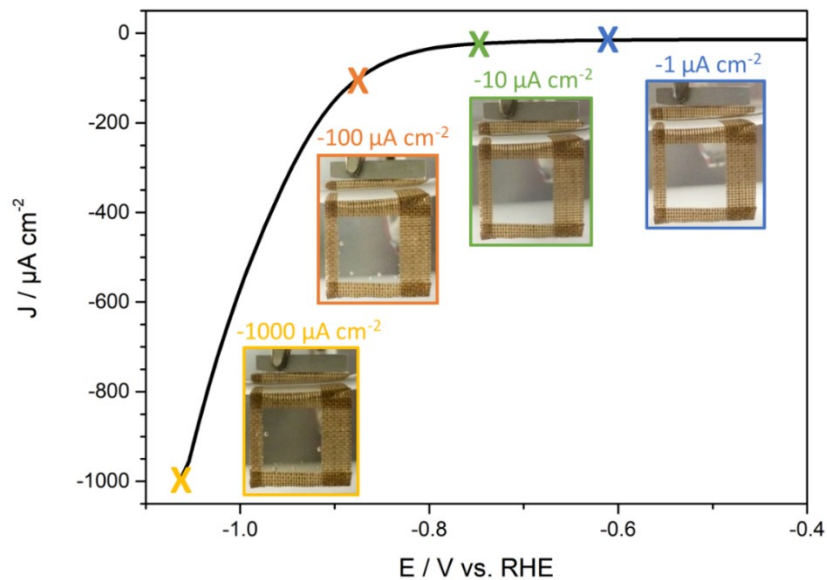


SI Figure 5.5. Any residues in the electrolyte were oxidized at 1.1 V vs. RHE on a platinum mesh prior to the hydrogen detection measurement.

Oriented Films of Conjugated 2D Covalent Organic Frameworks as Photocathodes for Water Splitting

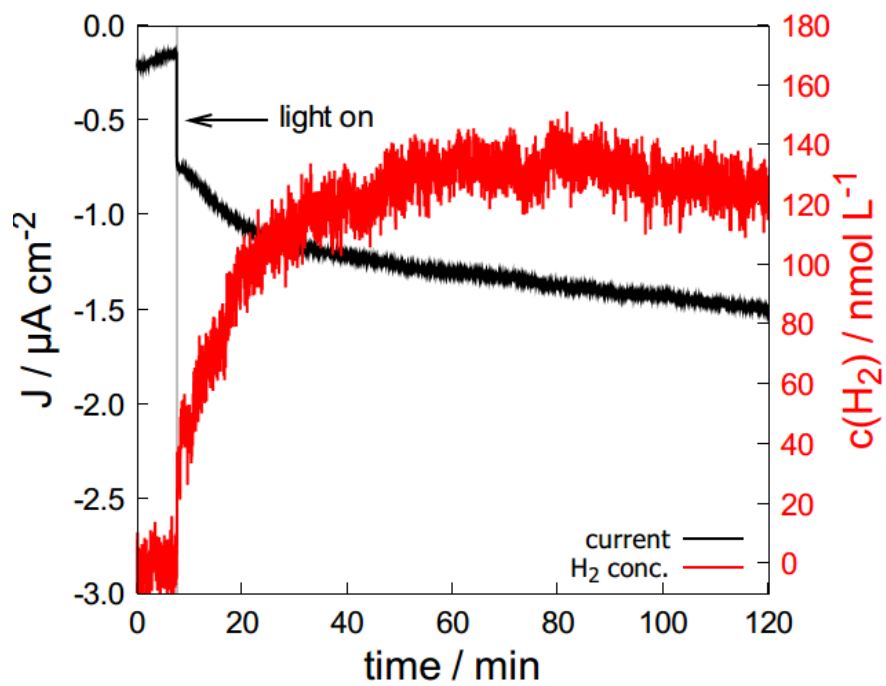


SI Figure 5.6. a) A potentiostatic measurement performed at -1.2 V vs. $\text{Hg}/\text{Hg}_2\text{SO}_4$ on a blank ITO substrate was used to evolve hydrogen with a current density of $5\ \mu\text{A cm}^{-2}$. b) The cumulative amount of hydrogen detected was calculated from the oxidative current at the platinum mesh. The mismatch between monitored and theoretical values shows that the collection efficiency of this experimental setup is about 3.5% after 60 minutes.



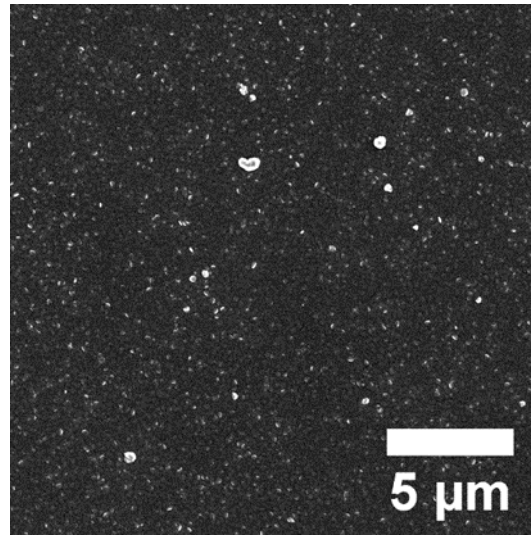
SI Figure 5.7. Cyclic voltammogram of a FTO electrode without illumination. The electrode was masked with Teflon adhesive tape to obtain an uncovered area of 1 cm^2 . Afterwards, rising current densities of $1 - 1000\ \mu\text{A cm}^{-2}$ were applied to the FTO electrode for 15 minutes each. No hydrogen formation is visible for current densities up to $10\ \mu\text{A cm}^{-2}$, as can be indicated from the pictures (insets). We assume that the produced hydrogen is directly dissolved in the electrolyte. With current densities above $100\ \mu\text{A cm}^{-2}$, the hydrogen gas is produced fast enough on the electrode surface to form bubbles.

Supporting Information



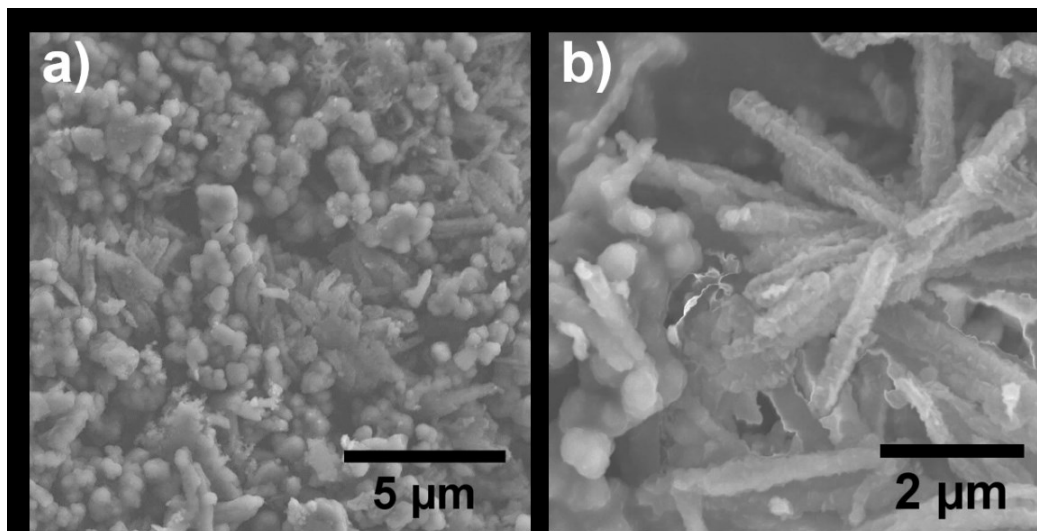
SI Figure 5.8. The hydrogen evolution on a BDT-ETTA COF electrode was quantified with a hydrogen microsensor (Unisense A/S H₂-NPLR) with selective silicone membrane at a static potential of 0.4 V vs. RHE. Illumination of the sample with AM1.5 simulated sunlight results in a photocurrent (black) and in the production of hydrogen (red).

5.9.4 SEM



SI Figure 5.9. Top-view SEM images of BDT-ETTA film on ITO.

The morphology of the COF bulk material was examined by SEM (SI Figure 5.9). SEM analysis reveals a comparable morphology of COF particles for BDT-ETTA with a spherical and intergrown rod morphology (SI Figure 5.10).

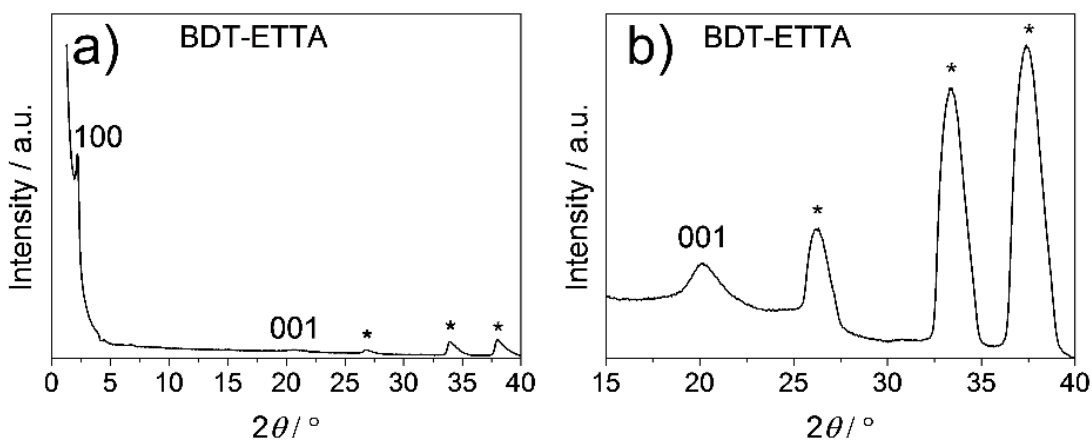


SI Figure 5.10. SEM images of BDT-ETTA bulk material (a, b). Besides a spherical morphology, BDT-ETTA COF consists of rod-shaped structures.

Supporting Information

5.9.5 X-Ray Diffraction Analysis

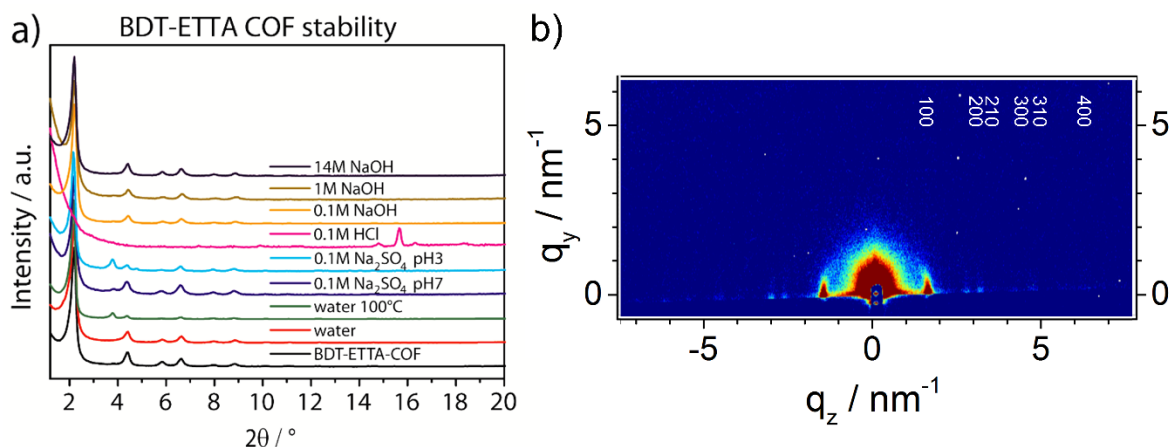
Induced by steric hindrance of close-by phenyl protons in ETTA, a propeller-like shape of the building unit is favored. In contrast to more planar building units, this results in an increased stacking distance of adjacent layers. Also, this twist leads to a lock-and-key-like molecular stacking. The conformation of the first layer leads to a predetermined conformation and alignment of the growing second layer.⁷ For COFs without this locking mechanism, AA eclipsed stacking of adjacent layers would still be most suitable. Nevertheless, a slight lateral offset of the layers can be expected and is energetically favorable for planar building blocks, especially with incorporated heteroatoms.⁸⁻⁹ This lateral offset would induce peak broadening not distinguishable from the AA eclipsed stacking by PXRD. In the case of ETTA, adjacent layers are guided by the position of ETTA in previous layers, resulting in energetically favored lateral positions and extension of oriented crystalline domains. Due to the fact that the 001 reflection of the COF films ($20.1^\circ 2\theta$ for BDT-ETTA) coincides with an ITO reflection ($21.56^\circ 2\theta$), we also grew films on FTO under the same conditions to distinguish the reflections of COF and substrate (SI Figure 5.11).



SI Figure 5.11. a) XRD of BDT-ETTA COF films on FTO in detector scan mode. 100 reflections result from less oriented COF particles on top of the film. The 001 reflection from the COF and the FTO reflections (*) are distinguishable. The 001 reflection in b) is related to π -stacking, which can be clearly distinguished from FTO reflections in the zoom-in.

5.9.5.1 Stability tests

For stability tests, the COF powder samples were soxhlet-extracted with anhydrous THF for 3 d. The COF materials were then suspended in different solvent mixtures for 24 h. After washing with anhydrous THF, the samples were vacuum-dried and their crystallinity was investigated (SI Figure 5.12).



SI Figure 5.12. a) Stability of BDT-ETTA (5 mg) powder exposed to 1 mL of different solvent mixtures for 24 h. If no temperature is noted, the experiments were performed at room temperature. In most cases, the crystallinity was maintained. An exception was the exposure to strongly acidic solutions. b) GID of a BDT-ETTA COF film after potentiostatic measurements. The still preserved crystallinity and orientation is represented by an intense first 100 reflection as well as higher order reflections visible only in the z-direction.

5.9.6 Sorption

The first steep uptake at very low p/p_0 in Figure 5.1d indicates the micropore filling, while the second one ($p/p_0 = 0.2$ to 0.3) represents the capillary condensation within the mesopores. Due to the comparably small size of the mesopores (≤ 4 nm), a type IVb physisorption isotherm without a hysteresis loop is obtained.¹⁰ The pore size distribution was calculated from QSDFT with a carbon kernel for cylindrical pore geometry.

Supporting Information

5.9.7 Structural simulations of BDT-ETTA COF

Space group: P6 with an AA-hexagonal eclipsed stacking (AA-H).

SI Table 5.1. Fractional atomic coordinates for the unit cell of AA-H calculated with the Materials Studio v7.0 modeling program.

P6 (168) – hexagonal

$a = b = 4.6413(4) \text{ nm}, c = 0.4465(5) \text{ nm}$

$\alpha = \beta = 90^\circ, \gamma = 120^\circ$

Atom	x/a	y/b	z/c
C1	0.48474	1.48621	0.48266
C2	0.51973	0.54732	0.47664
C3	0.54629	0.51248	0.47792
C4	0.57161	0.53280	0.30656
C5	0.60077	0.53204	0.29905
C6	0.60521	0.51088	0.46405
C7	0.58018	0.49066	0.63439
C8	0.55131	0.49185	0.64410
C9	0.45948	0.42899	0.65637
C10	0.45516	0.39750	0.65108
C11	0.47177	0.38927	0.46800
C12	0.49166	0.41258	0.28206
C13	0.49551	0.44380	0.28614
N14	0.53262	0.64303	0.47056
C15	0.51035	0.64986	0.40028

Oriented Films of Conjugated 2D Covalent Organic Frameworks as Photocathodes for Water Splitting

N16	0.63409	0.50822	0.45469
C17	0.66312	0.53199	0.40099
C18	0.48289	0.31631	0.40351
S19	0.44186	0.28140	0.43759
C20	0.46043	0.25631	0.4118
C21	0.49408	0.27411	0.38466
C22	0.50649	0.30898	0.3780
C23	0.51274	0.25870	0.3691
C24	0.49620	0.22457	0.37936
C25	0.46247	0.20668	0.40062
C26	0.44382	0.22213	0.4188
C27	0.45019	0.17178	0.40583
C28	0.47411	0.16473	0.39422
S29	0.51516	0.19982	0.37111
H30	0.44682	0.43498	0.80183
H31	0.43934	0.37966	0.79306
H32	0.50381	0.40660	0.13152
H33	0.51072	0.46140	0.14393
H34	0.53208	0.32700	0.35554
H35	0.53905	0.27265	0.3512
H36	0.41753	0.20819	0.43888
H37	0.42456	0.15359	0.42127
H38	0.44342	0.11098	0.37202

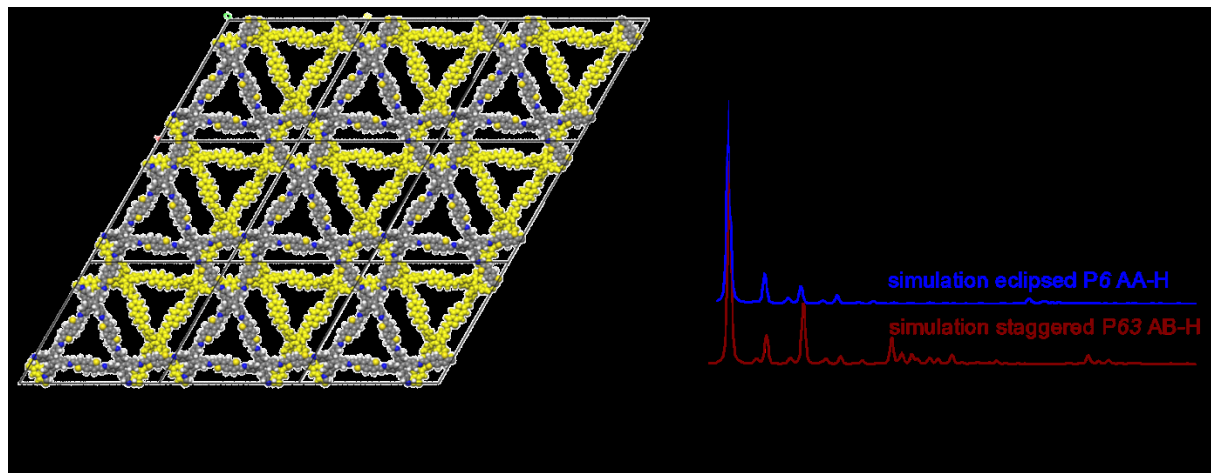
Supporting Information

H39	0.51389	0.36941	0.34694
H40	0.61941	0.54735	0.16036
H41	0.56868	0.54908	0.17619
H42	0.58314	0.47404	0.76138
H43	0.53260	0.47604	0.77652

SI Table 5.2. Space groups and cell parameters of AA-H and AB-H COFs constructed from BDT and ETTA.

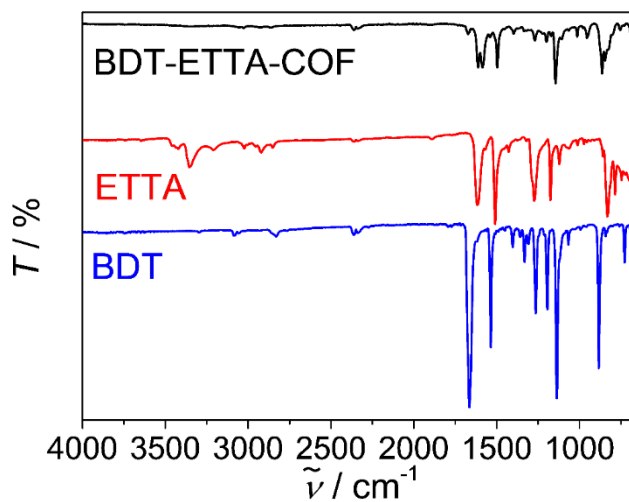
Structure	Crystal System	Space group	Cell parameters
AA-H	hexagonal	P6	a=b= 4.6413 nm, c = 0.45 nm, $\alpha=\beta=90^\circ$, $\gamma=120^\circ$
AB-H	hexagonal	P63	a=b= 4.6413 nm, c = 0.76 nm, $\alpha=\beta=90^\circ$, $\gamma=120^\circ$

For comparison, an XRD pattern of an eclipsed structure in P6 indexed as AA-hexagonal (AA-H) and a staggered structure in P63 indexed as AB-hexagonal (AB-H) were simulated (SI Figure 5.13a and b). The simulated XRD patterns coincide in several reflection positions, although the significant differences in intensities show a mismatch between the simulated structure (AB-H) and the experimental data.



SI Figure 5.13. a) Staggered structure of BDT-ETTA in P63 symmetry AB-hexagonal (AB-H). b) Resulting simulated XRD pattern of the eclipsed AA-H with P6 and the staggered AB-H with P63 symmetry. The reflection intensities in the staggered simulation differ significantly from the experimental data.

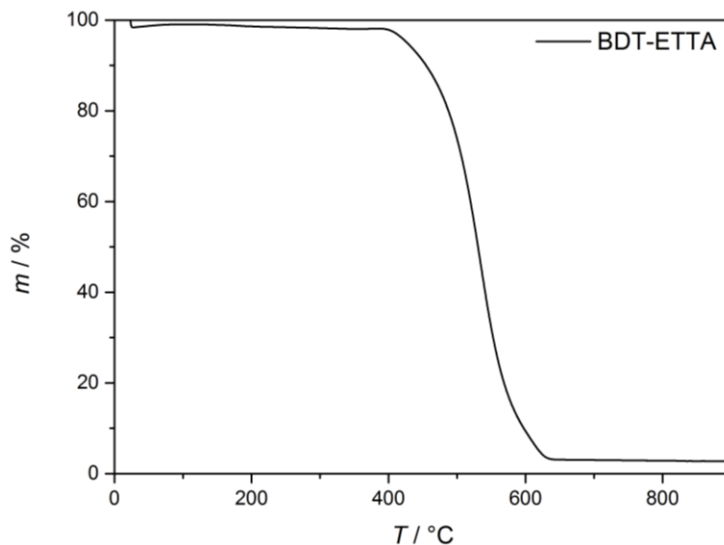
5.9.8 IR Spectroscopy



SI Figure 5.14. IR spectra of BDT-ETTA COF powder (black) and starting materials (ETTA, red and BDT, blue).

Supporting Information

5.9.9 Thermogravimetric Analysis



SI Figure 5.15. Thermogravimetric analysis of BDT-ETTA COF.

5.9.10 Elemental Analysis

SI Table 5.3. Elemental analysis of BDT-ETTA COF bulk material compared with the calculated mass percentages.

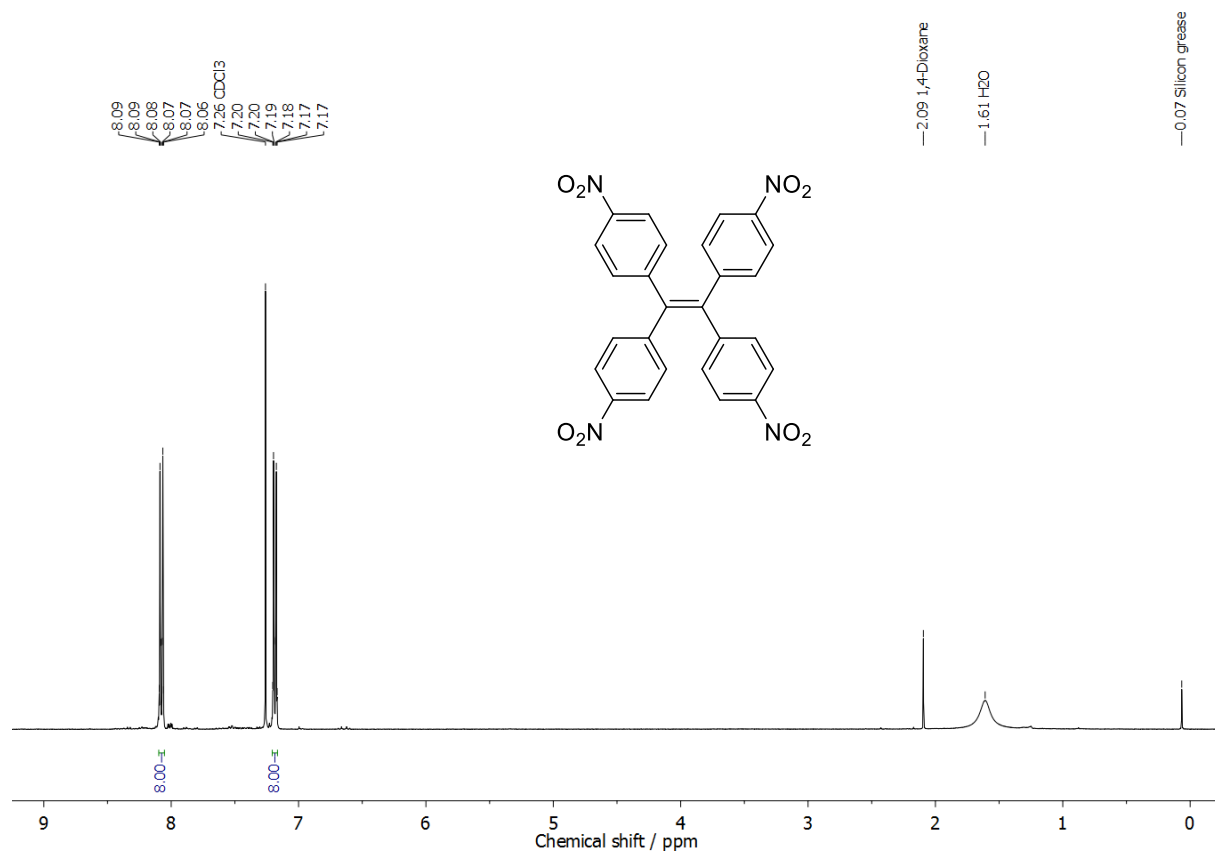
Element	BDT-ETTA	
	Theoretical percentage	Measured percentage
N	6.89	6.69
C	73.86	70.00
H	3.47	3.68
S	15.78	14.06

The deviations of theoretical and measured atomic percentages are tentatively attributed to COF structures having a certain number of defects (missing building blocks).

5.9.11 NMR Spectra

5.9.11.1 TNPE

^1H , 400 MHz, $\text{DMSO-}d_6$

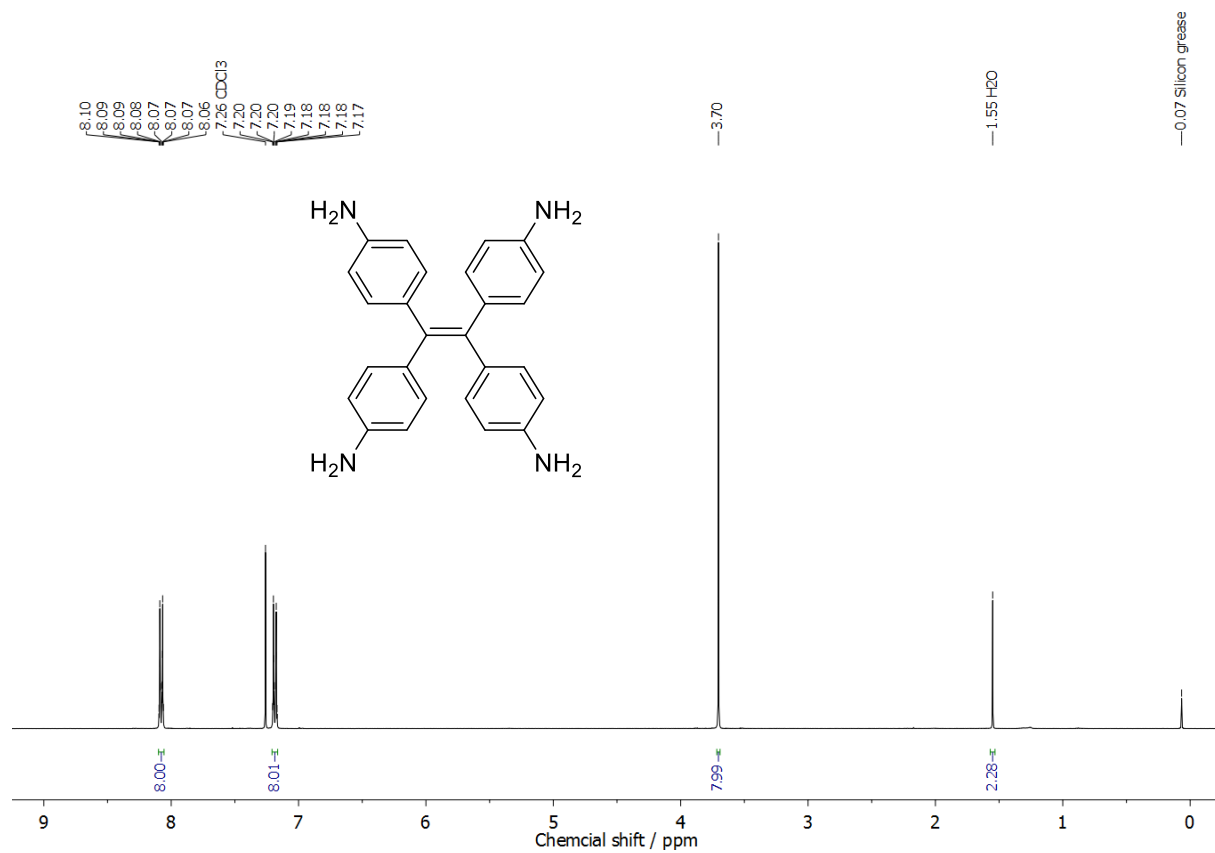


SI Figure 5.16. ^1H NMR spectrum of TNPE.

Supporting Information

5.9.11.2 ETTA

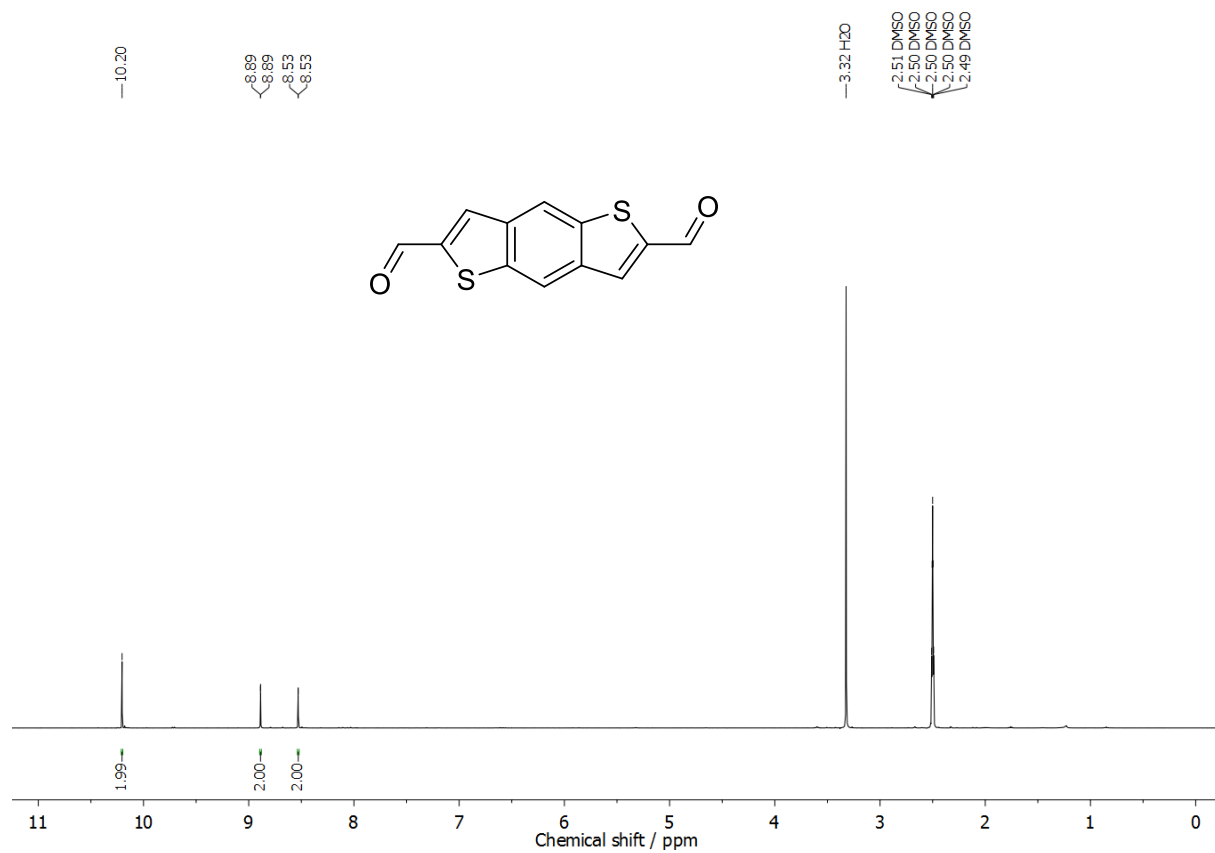
^1H , 400 MHz, $\text{DMSO-}d_6$



SI Figure 5.17. ^1H NMR spectrum of ETTA.

5.9.11.3 BDT

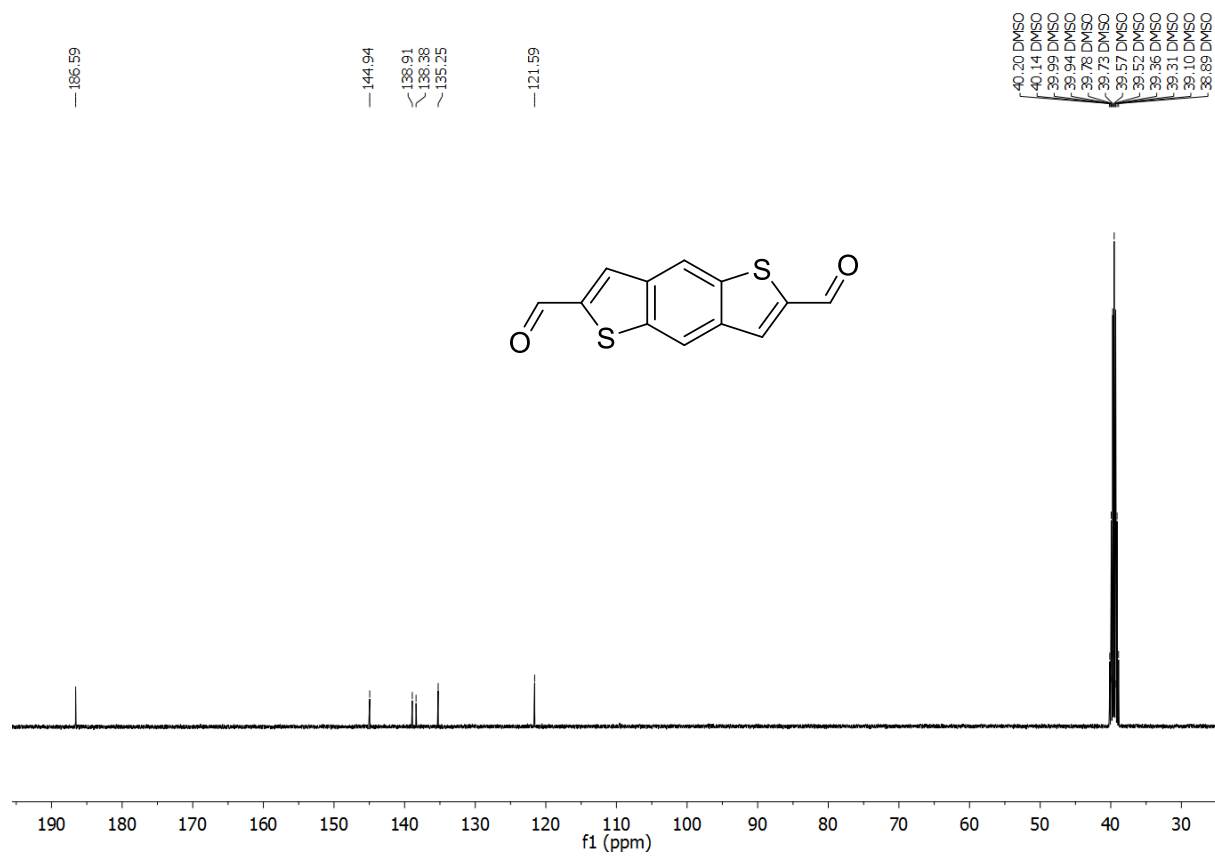
^1H , 400 MHz, $\text{DMSO-}d_6$



SI Figure 5.18. ^1H NMR spectrum of BDT.

Supporting Information

^{13}C , 100 MHz, $\text{DMSO-}d_6$



SI Figure 5.19. ^{13}C NMR spectrum of BDT.

5.9.12 References

- (1) Klahr, B. M.; Martinson, A. B.; Hamann, T. W., *Langmuir* **2011**, *27*, 461-468.
- (2) Gorvin, J. H., *J. Chem. Soc.* **1959**, 678-682.
- (3) Lu, J.; Zhang, J., *J. Mater. Chem. A* **2014**, *2*, 13831-13834.
- (4) Koßmehl, G.; Beimling, P.; Manecke, G., *Makromol. Chem.* **1983**, *184*, 627-650.
- (5) Connelly, N. G.; Geiger, W. E., *Chem. Rev.* **1996**, *96*, 877-910.
- (6) Bard, A. J.; Faulkner, L. R., *Electrochemical Methods: Fundamentals and Applications*. 2nd ed.; Wiley: New York, 2001.
- (7) Ascherl, L.; Sick, T.; Margraf, J. T.; Lapidus, S. H.; Calik, M.; Hettstedt, C.; Karaghiosoff, K.; Döblinger, M.; Clark, T.; Chapman, K. W.; Auras, F.; Bein, T., *Nat. Chem.* **2016**, *8*, 310-316.
- (8) Spitler, E. L.; Koo, B. T.; Novotney, J. L.; Colson, J. W.; Uribe-Romo, F. J.; Gutierrez, G. D.; Clancy, P.; Dichtel, W. R., *J. Am. Chem. Soc.* **2011**, *133*, 19416-19421.
- (9) Dogru, M.; Bein, T., *Chem. Commun.* **2014**, *50*, 5531-5546.
- (10) Thommes, M.; Kaneko, K.; Neimark, A. V.; Olivier, J. P.; Rodriguez-Reinoso, F.; Rouquerol, J.; Sing, K. S. W., *Pure Appl. Chem.* **2015**, *87*, 929-1069.

6 Covalent Organic Framework Films by Electrophoretic Deposition - Creating efficient Morphologies for Catalysis

This chapter is based on the following publication:

Julian M. Rotter‡, Simon Weinberger‡, Jonathan Kampmann, Torben Sick, Menny Shalom, Thomas Bein and Dana D. Medina*, *Chem. Mater.*, **2019**, 31, 24, 10008-10016.

‡ These authors contributed equally to this work.

Reprinted with permission from *Chem. Mater.*, **2019**, 31, 24, 10008-10016. Copyright 2019 American Chemical Society. Further permissions related to the material excerpted should be directed to the *American Chemical Society*.

Link to the published article: <https://doi.org/10.1021/acs.chemmater.9b02286>

Jonathan Kampmann performed the aqueous photoelectrochemistry and hydrogen detection experiments as well as the Platinum nanoparticle synthesis and wrote the corresponding parts of the manuscript.

Abstract

The ability to grow covalent organic framework (COF) films allows for studying their properties as solid layers and enables the incorporation of these materials into a variety of functional devices. Here, we report on the fabrication of COF films and coatings by electrophoretic deposition (EPD). We demonstrate that the EPD technique is suitable for depositing COFs featuring two- and three-dimensional structures linked by imine- or boronate ester-bonds, namely BDT-ETTA COF, COF-300 and COF-5. For the deposition, COF nanoparticle suspensions are prepared by dispersing the as-synthesized bulk materials in solvents with low dielectric constants. Subsequently, two electrodes are immersed into the COF particle suspensions and upon inducing electric fields ranging from 100-900 V cm⁻¹, COFs are deposited as films on the positively charged electrode. Through EPD, within two minutes, large-area films of up to 25 cm² are obtained on both smooth and corrugated surfaces. COF films prepared by EPD feature an inherent textural porosity and tunable thickness, demonstrated from 400 nm to 24 μm. By governing the deposition parameters such as duration, particle concentration and applied potential, deposits of precise thickness can be produced. Furthermore, co-depositions of several different COFs as well as COF/Pt nanoparticle suspensions are demonstrated. The film morphologies obtained by EPD are shown to be advantageous for catalysis, as demonstrated for sacrificial agent free photoelectrochemical water reduction. Here, BDT-ETTA COF photocathodes show a drastic increased photocurrent density compared to the respective dense and oriented surface-grown films. Typical BDT-ETTA COF/Pt nanoparticle hybrid films exhibit photocurrent densities of over 100 μA cm⁻². The rapid and highly scalable deposition of COF particles as films and coatings through EPD is a versatile addition to the toolbox of COF film fabrication techniques, allowing for the tailoring of COF film architectures for desired functionalities.

6.1 Introduction

Covalent organic frameworks (COFs) are a novel class of ordered, light-weight organic polymers exhibiting great structural and chemical diversity. COFs are constructed by connecting rigid molecular organic building blocks through condensation polymerization reactions under slightly reversible conditions. Depending on the geometry of the respective COF building blocks, COFs form 2D or 3D porous solids, featuring long-range order, permanent porosity and high surface areas.^{1,2} Due to their structural and chemical versatility, COFs have been examined for various applications, such as gas storage,³ separation,⁴⁻⁶ catalysis,⁷⁻¹² photovoltaics and optoelectronics¹³⁻¹⁵ or energy storage.¹⁶⁻¹⁹

Introduction

The deposition of COFs onto surfaces as homogenous coatings or as thin films is an important step towards the incorporation of this novel class of materials into a variety of functional platforms.²⁰ Commonly, COFs are synthesized under solvothermal conditions and precipitate as intergrown nanocrystalline bulk materials, which are difficult to process and to convert into high-quality COF films on surfaces.²¹ Exploring routes for processing COF powders and developing techniques which allow for the direct deposition of COFs on substrates as films is hence of great importance. To date, the growth of thin COF films onto surfaces is based mainly on “bottom-up” approaches where the substrates are exposed to a reactive precursor solution. Oriented thin COF films, featuring open channels orthogonal to the substrate surface, are accessible by this so-called *in-situ* approach, where COF powders and films are often forming simultaneously. However, this approach provides limited control over the resulting film thickness.²²⁻²⁴ In this context, a continuous flow setup was reported, which allowed for a finer tuning of film thickness.²⁵ A major draw-back of the *in-situ* approach is the overall low synthesis yield, defined by the mass ratio of the deposited COF material and the COF bulk precipitate. Facing this challenge, we developed the vapor-assisted conversion (VAC) approach for the deposition of boronate-ester COFs as films exclusively on surfaces. In contrast to the *in-situ* approach, in VAC, precursors in a thin precursor solution layer react to form a COF film on a surface. This allows for control over the film thickness and morphology, ranging from dense thin films to thick coatings consisting of intergrown particles and interstitial voids.²⁶ For applications such as catalysis, COF films featuring additional textural porosity and a large interface can be highly beneficial for rapid diffusion of reactants and products in and out of the film and thereby enhancing the catalytic performance.²⁷ However, a rapid fabrication of such film morphologies applicable to the different COF types in high yields is still lacking.

Electrophoretic deposition (EPD) is an efficient method for the deposition of particles bearing an intrinsic surface charge on an electrode by creating an external electric field.²⁸ In general, the electric field between two electrodes immersed into a particle suspension in a non-conducting solvent induces a migration of charged particles towards the electrode of opposite charge. The EPD method was adopted for various inorganic and hybrid materials, such as silica,²⁹ zeolites,³⁰ metal oxides,³¹ quantum dots,³² carbon nitrides,³³ carbon nanotubes³⁴ and conducting organic polymers, such as polythiophene or polyanilines.^{35,36} Additionally, metal-organic frameworks as well as a covalent-ionic-organic framework, containing a ligand especially tailored with cationic functional groups for the deposition, were reported.³⁷⁻⁴⁰

Here, we expand the paradigm of EPD into a highly general method for the rapid fabrication of COF films featuring a high textural porosity on conductive surfaces. For the deposition, we utilize various well-characterized bulk COF materials namely COF-5,⁴¹ BDT-ETTA COF⁴² and COF-300.⁴³ Thereby, we demonstrate the versatility of EPD as being applicable for the deposition of both 2D and 3D frameworks of different particle sizes and morphologies, linked by imine or boronate ester bonds. Prior to the deposition, stable COF particle suspensions were prepared by COF powder attrition or simply by immersion in a non-conducting solvent. Through EPD, COF films and coatings were deposited within minutes with control over the film thicknesses ranging from hundreds of nanometers to several micrometers. Furthermore, co-depositions of two different COF materials, as well as a COF/Pt nanoparticle mixture are demonstrated, yielding homogeneous hybrid films. Additionally, the catalytic performance of BDT-ETTA COF and BDT-ETTA COF/Pt films, prepared by EPD, was evaluated for the light-driven electrochemical production of hydrogen and compared to state-of-the-art dense and oriented BDT-ETTA COF films.⁴²

6.2 Experimental Section

Chemicals. All materials were purchased from Aldrich, Fluka, Acros, Activate Scientific or TCI Europe in the common purities purum, puriss or reagent grade. Materials were used as received without additional purification and handled under air unless denoted. All solvents used were anhydrous and purged with inert gas. 4,4',4'',4'''-(1,1,2,2-ethylenetetrayl)tetrakis(aniline) (ETTA) and 2,6-benzo[1,2-b:4,5-b']dithiophene dialdehyde (BDT) were synthesized as reported in literature.⁴²

BDT-ETTA COF. Under argon atmosphere BDT (benzo[1,2-b:4,5-b']dithiophene-2,6-dicarboxaldehyde, 74 mg, 0.30 mmol) and ETTA (1,1,2,2-tetra(p-aminophenyl)ethylene, 58.6 mg, 0.15 mmol) were suspended in a mixture of benzyl alcohol and mesitylene (V/V 9:1,5 mL) in a 25 mL Schott-Duran vial. Acetic acid (6 M, 500 μ L) was added to the vessel and the mixture was placed in a pre-heated oven at 120 °C for 3 days. The resulting orange precipitate was suction filtered, soxhlet-extracted with dry THF and dried at reduced pressure.

COF-300. Tetrakis(4-aminophenyl)methane (100 mg, 0.26 mmol) and terephthalaldehyde (60 mg, 0.44 mmol) were suspended in a mixture of 1,4-dioxane (5 mL) and acetic acid (6 M, 500 μ L) in a 25 mL Schott-Duran vial. The mixture was subject to a short sonication and placed in a preheated oven at 120 °C for 3 days. The yellow precipitate was suction filtered, soxhlet-extracted with dry THF and dried at reduced pressure.

Experimental Section

COF-5. Benzene-1,4-diboronic acid (18.7 mg, 0.113 mmol) and 2,3,6,7,10,11-hexahydroxytriphenylene hydrate (24.3 mg, 0.075 mmol) were placed in a 5 mL microwave vial and 4 mL of a 1,4-dioxane and mesitylene 1:1 mixture was added. The vial was sonicated for 5 min and then placed in the microwave and heated for 3 h at 100 °C. The grey precipitate was suction filtered, subsequently washed with anhydrous acetone and dried at reduced pressure.

COF-300 and COF-5 suspension preparation. COF particle suspensions were prepared by adding the amount to deposit (0.5 mg for COF-5 and, depending on the desired thickness of COF-300 films 0.05 – 0.5 mg of COF-300 (SI Figure 6.11) of the respective COF into ethyl acetate (10 mL). A brief sonication in an ultrasonic bath was then applied to homogeneously disperse the particles in the solvent. After the treatment, homogeneous COF dispersions colored yellow or grey for COF-300 or COF-5, respectively, were obtained. For COF-5, we observed a severe impact on crystallinity if sonication times exceeded 15 seconds.

BDT-ETTA COF particle attrition and suspension preparation. Prior to deposition, BDT-ETTA COF was subjected to an ultrasound-based attrition process to break up large, intergrown agglomerates. Therefore 5 mg of COF was suspended in 25 mL of deposition solvent and a sonication amplitude of 70% for 30 min was chosen. During the process, the particle suspension was cooled using an ice bath. After the treatment, the suspension was centrifuged at a relative centrifugal force of 7000 g after which the supernatant was used for deposition. Using this process, particle size could be greatly reduced and suspensions stable for more than one week were obtained. The concentration of the produced BDT-ETTA COF suspension was determined by subtracting the weight of the centrifuge COF residue from the initial COF mass. A BDT-ETTA COF concentration of 0.74 mg per 25 mL ethyl acetate, or 0.03 mg mL⁻¹, was determined.

Electrophoretic Deposition. In a typical EPD experiment, two conductive substrates were contacted by alligator clamps to the potentiostat parallel and with the conducting sides facing each other, and with a horizontal distance of 1 cm between the electrodes. Subsequently, the electrodes were dipped into the COF particle suspension (10 mL). The electrode area submerged in the suspension was 1 cm × 1 cm. Then, the desired potential was applied between the electrodes for the respective deposition time (e.g. 900 V for 2 min). After deposition, the applied potential was set to zero and the electrodes were removed from the solvent and subsequently dried under nitrogen flow. For the COF-5 deposition (films are depicted in Figure 6.1), 0.5 mg material was used. For the preparation of the large area films two FTO (fluorine-doped tin oxide) substrates (8 cm × 5 cm) were used, where the

Covalent Organic Framework Films by Electrophoretic Deposition - Creating efficient Morphologies for Catalysis

submerged area used for deposition was 5 cm × 5 cm. For the co-deposition of COF-300 and BDT-ETTA COF, 2 mL of the ultrasound attrited BDT-ETTA COF particle suspension was diluted with 8 mL of ethyl acetate. Then, 0.2 mg of COF-300 was added and the mixture was sonicated in a sonication bath for 1 min for homogenization. The subsequent deposition was carried out on an ITO (indium doped tin oxide) coated glass substrate at 900 V for 2 min. Assuming a complete suspension depletion and employing defined concentrations of both samples afford a ratio of 0.06:0.2 mg/mg for the BDT-ETTA COF and COF-300 codeposition film.

Photoelectrochemical hydrogen production. For the 3 μm thick BDT-ETTA COF films used in PEC-based hydrogen production, 15 mL (7.5 mL for the 1.5 μm thick film) of the BDT-ETTA COF suspension in ethyl acetate, fabricated as described before, were used and deposited on a 1 cm × 1 cm large area of FTO (total dimensions of FTO electrode was 1 cm × 4 cm). Pt nanoparticles were synthesized as reported in literature.⁴⁴ A zeta potential of -24.3 mV in water was recorded for the synthesized particles. Subsequently, Pt nanoparticles were isolated through lyophilization under dynamic vacuum. Hereby, Pt nanoparticles of 2–4 nm in diameter were obtained, as measured from TEM micrographs (SI Figure 6.16). Additionally, the hydrodynamic radii of the citrate capped nanoparticles were determined by dynamic light scattering (DLS) and sizes ranging from 4–9 nm were found (SI Figure 6.17). For the codeposition, 10 mL of the BDT-ETTA suspension were used, to which 0.15 mg of Pt nanoparticles were added. Then, the mixed suspension was subjected to an additional sonication step (as described in BDT-ETTA COF suspension preparation) for 10 min to homogenize the mixture. The deposition was carried out at 900 V for 2 min on an ITO coated glass substrate. During the deposition, additional Pt particles (0.10 mg in 2 mL ethyl acetate) were steadily added to the deposition suspension by a syringe.

Characterization Methods. PXRD and film XRD patterns were measured on a Bruker D8 Discover instrument equipped with a Lynx Eye detector in Bragg-Brentano geometry and Ni-filtered Cu Kα X-ray radiation. Scanning electron microscopy (SEM) images were recorded on a FEI Helios Nanolab G3 UC microscope at an acceleration voltage of 2.5 kV. Energy dispersive X-ray spectra (EDX) were recorded at 20 kV. Prior to analysis, the samples were coated with carbon. TEM micrographs were obtained from a FEI Titan Themis 60-300 TEM at an acceleration voltage of 300 kV. Electrochemical measurements were performed on a Metrohm μAutolab III/FRA2 instrument. Fourier-transformed infrared (FT-IR) spectra were recorded on a Thermo Scientific Nicolet iN10 FT-IR microscope in reflection on a steel substrate. FT-IR spectra of the films were acquired by scratching-off the

Results and Discussion

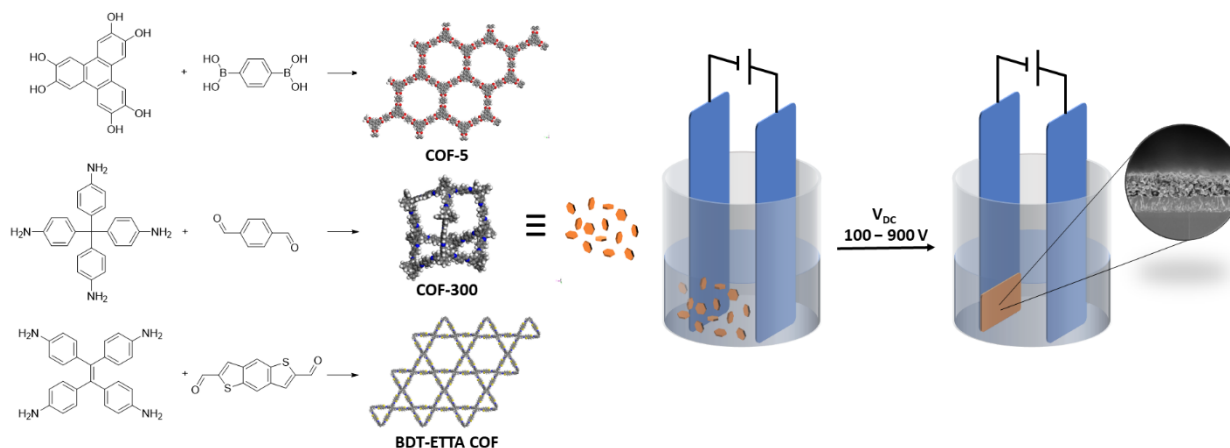
respective COF deposits. Microwave based COF synthesis was carried out using a Biotage Initiator microwave. Ultrasonic particle attrition was carried out using a Bandelin Sonopuls HD 4100 homogenizer with a TS113 13 mm tip. For electrophoretic deposition (EPD), a Heinzinger LNC 3000 potentiostat was used. Dynamic light scattering (DLS) and zeta potential measurements were recorded using a Malvern Zetasizer instrument at room temperature using 10 mm path length cuvettes. Nitrogen physisorption data was recorded using a Quantachrome Autosorb iQ system. Prior to the measurement, samples were heated at 120 °C for 6 h under high vacuum. Measurements were performed at 77.35 K. For sorption measurements, the respective materials were obtained by scratching-off the COF deposits from five films.

6.3 Results and Discussion

The central aspect addressed in this study is the development of a general COF film fabrication method, applicable for a variety of structures, providing tunable film thicknesses and textural porosity. Therefore, we established a processing protocol utilizing COF particle suspensions and subsequently EPD for obtaining the desired deposit. We chose well-characterized and -known structures to validate the developed EPD-based protocol as a structure-independent approach. For this purpose, we synthesized highly crystalline 2D and 3D COF bulk materials under solvothermal conditions, namely the imine-linked BDT-ETTA COF and the COF-300, and the boronate ester-based COF-5.⁴¹⁻⁴³ The isolated COF powders were suspended in a non-conducting and low dielectric constant solvent and subsequently deposited by EPD onto a conductive substrate serving as an electrode. For the deposition, the external electric field between two electrodes allowed for the migration of COF nanoparticles, bearing an intrinsic surface charge, to the electrode of opposite charge.

In the EPD setup, two conductive substrates (1 cm x 1 cm), such as FTO, ITO or titanium foil were submerged into a COF particle suspension (Scheme 6.1, SI Figure 6.1). Untreated COF-5 agglomerates, nanoparticles of BDT-ETTA COF as well as almost micrometer-sized COF-300 single crystallites were suspended in an adequate organic solvent and subsequently deposited using the same deposition protocol. Aprotic, organic solvents of low polarity, such as ethyl acetate, toluene or anisole (SI Figure 6.2), were found to be suitable media for the preparation of stable COF particle suspensions and for effective electrophoresis.

Covalent Organic Framework Films by Electrophoretic Deposition - Creating efficient Morphologies for Catalysis



Scheme 6.1. COF building blocks and structures of the resulting frameworks used in the EPD. Schematic presentation of the EPD set-up with a typical COF film SEM cross-section as an inset.

While COF-5 and COF-300 particles were suspended in the respective solvents without further treatment, the robust BDT-ETTA COF was subjected to an ultrasonic attrition process to disassociate intergrown and agglomerated COF crystals using a 20 kHz ultrasonic disintegrator at high amplitudes. Dynamic light scattering (DLS) measurements of the obtained suspension revealed average particle sizes of about 200 nm (SI Figure 6.3). This shows that the ultrasonic treatment provided sufficient mechanical force for separating the COF agglomerates into isolated and well-suspended nanocrystals.

The EPD COF films were produced by inducing an electric field of 900 V cm^{-1} between the electrodes for two minutes. Under these conditions, the particles of the different COFs readily migrate to the positively charged electrode, indicating that the COF particles, regardless of their linkage-type, bear an intrinsic negative surface charge. Within seconds, a colored deposit formed on the surface of the submerged electrode and within two minutes a complete discoloration of the suspension was observed, indicating a quantitative deposition of the suspended material. After the deposition, the obtained COF films were dried under an air stream, revealing a continuous, colored deposit on the substrate (Figure 6.1).

Top view scanning electron microscopy (SEM) micrographs of all the examined EPD COF films revealed uniform deposits on the immersed conducting electrode surfaces (Figure 6.1). The deposits

Results and Discussion

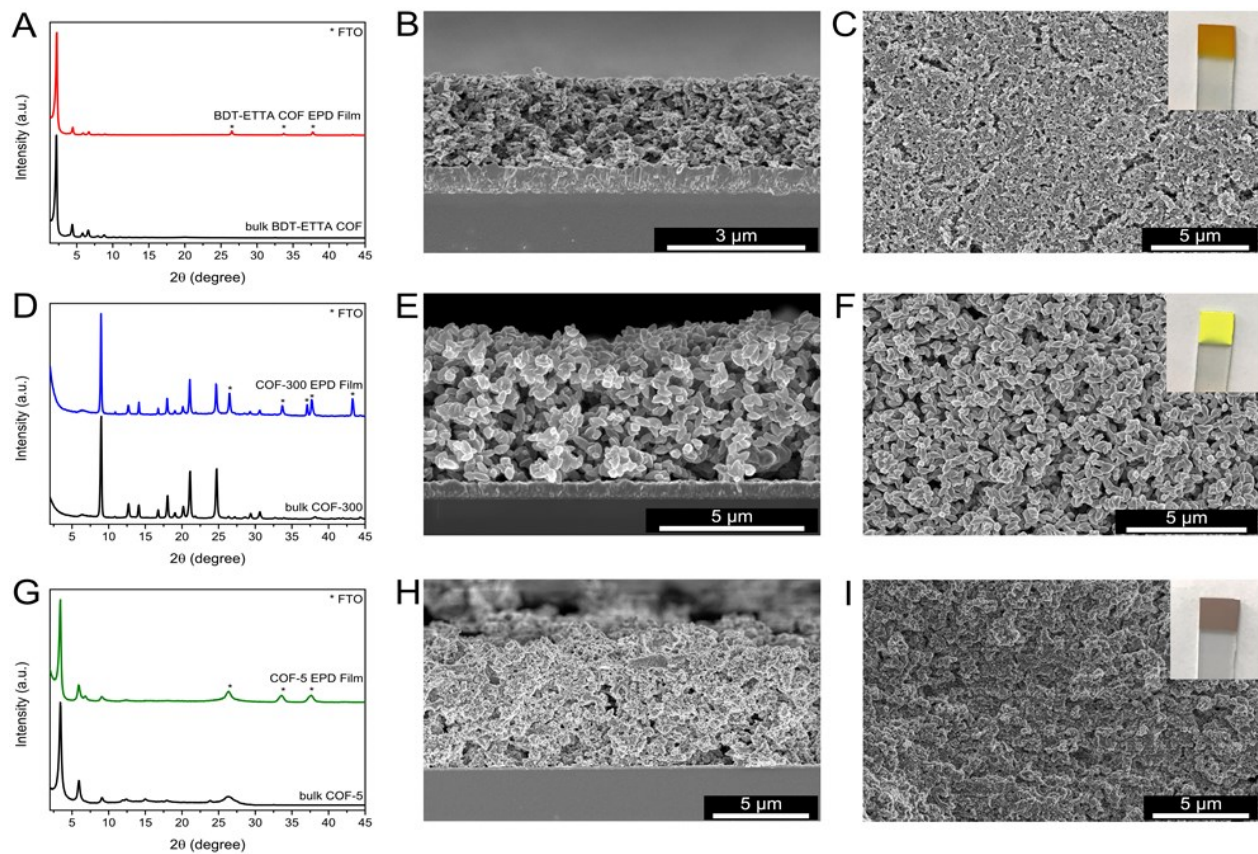


Figure 6.1. (A) XRD of BDT-ETTA COF as EPD film and as bulk material. (B) SEM cross-section and (C) top-view of BDT-ETTA COF film and a photograph of the film as an inset. (D) XRD of COF-300 as EPD film and as bulk material. (E) SEM cross-section and (F) top-view of COF-300 film and a photograph of the film as an inset. (G) XRD of COF-5 as EPD film and as bulk material. (H) SEM cross-section and (I) top-view of COF-5 and a photograph of the film as an inset.

consist of closely packed particles of similar size creating interstitial voids. Cross-section SEM micrographs revealed continuous COF deposits on the substrates featuring an even thickness throughout the respective films. Using the deposition conditions of 900 V cm^{-1} and 2 minutes deposition time, a film thickness of $2 \mu\text{m}$ was obtained for the BDT-ETTA COF suspension. In the cases of the untreated COF-5 and COF-300 suspensions, thicknesses of $14 \mu\text{m}$ and $6 \mu\text{m}$ were determined, respectively. Notably, interstitial voids between the particles are apparent throughout the films and therefore, textural porosity is characteristic for all the examined samples. X-ray diffraction (XRD) measurements confirmed that all the deposited films consist of crystalline COF particles, and the obtained diffraction patterns are in excellent agreement with the respective bulk materials (Figure 6.1). Transmission electron microscopy (TEM) analysis of a BDT-ETTA COF film powder removed

Covalent Organic Framework Films by Electrophoretic Deposition - Creating efficient Morphologies for Catalysis

from the substrate revealed crystalline domains of about 100 nm without traces of an amorphous phase (SI Figure 6.4). This observation confirms that the milling process applied to the BDT-ETTA COF suspension is vigorous enough to dissociate the COF aggregates into individual particles without causing structural degradation.

In contrast, the non-treated COF-300 powder consists of relatively uniform individual crystallites of about 500 nm in size. Here, the COF powder was suspended in ethyl acetate without the need for particle attrition to form a stable suspension. Therefore, films deposited from such COF suspensions consist of single COF crystallites and feature structural characteristics of the bulk material (SI Figure 6.5). These observations indicate that with the COF-300 particles no significant agglomeration occurred in the course of the film deposition. In the case of EPD COF-5 films, intergrown crystallite agglomerates exceeding 100 nm are visible, nevertheless forming a continuous deposit (SI Figure 6.6). Importantly, the XRD and TEM analyses of the films illustrate the compatibility of the different COF materials with the electrophoretic process, as no electrochemical reaction or degradation of the framework is observed. Nitrogen physisorption experiments of scratched-off COF film material showed the respective isotherm shapes and confirmed the retention of porosity for all deposited frameworks (SI Figure 6.7). Additionally, Fourier-transform infrared (FT-IR) spectra of the deposited materials match those of the bulk COF powders. This further indicates that no chemical alteration of the framework occurred during the deposition and emphasizes the compatibility of COFs with the EPD process (SI Figure 6.8).

The migration of the COF particles to the respective electrode is driven by their intrinsic surface potential. Interestingly, independent of their structure and chemical composition, COFs readily migrate to the positive electrode, indicating negative surface potential. Zeta-potential measurements performed for COF-300 suspensions in ethyl acetate confirmed this observation and revealed a negative particle surface potential of -21 mV. To invert the surface potential through protonation of the terminal amine groups, glacial acetic acid was added to suspensions of COF-300 particles in ethyl acetate. Zeta-potential measurements of the protonated COF-300 particle suspensions revealed a change in the surface potential to 11.9 mV. Notably, acetic acid treated COF-300 particles readily migrated to the opposite, negatively charged electrode during electrophoretic depositions, illustrating the significant role of the terminal functional groups in the EPD process.

To further study the parameters governing the EPD of COF films, we focused our following investigations on COF-300 as the first representative for 3D COF films on conducting substrates and

Results and Discussion

on the photoactive BDT-ETTA COF, serving as a representative for 2D COFs.^{42,43} Achieving control of the COF film thickness is essential for applications such as sieving, sensing or optimizing photocatalytic performance.⁴⁵ Furthermore, film deposition techniques providing COF film thicknesses of more than several hundred nanometers are rare.^{20,24,45} In EPD, the amount of the deposited material is directly proportional to deposition time and the mass of the suspended material.⁴⁶ Accordingly, the film thickness can be easily predetermined and systematically adjusted by varying parameters such as deposition time and particle concentrations, thus, enabling a fine control over film thickness. For the deposition of BDT-ETTA COF, we found that adjusting the deposition time allows for controlling and predetermining the film thickness.

To determine the film deposition rate, we fabricated a series of BDT-ETTA COF films using different EPD deposition times, ranging from 5 s to 120 s. The XRD patterns of the film series showed a linear increase in the COF (100) reflection intensity, relative to a constant FTO reflection intensity (observed at $25.9^\circ 2\theta$) serving as an internal reference. We attribute this steady intensity increase to a linear increase in film thickness (Figure 6.2A). SEM cross-section analysis revealed a film thickness of about 2 μm corresponding to a deposition time of two minutes. Remarkably, we observed a complete surface coverage and a film thickness of about 400 nm already within 10 s (Figure 6.2B). To calculate the deposition rate, the BDT-ETTA COF film thicknesses, obtained from the SEM analysis, were plotted against the deposition times (SI Figure 6.9). After an initial time of about 10 seconds during which steady-state conditions are established, we observed a linear dependence of the film thickness on the deposition time with a calculated deposition rate of 16 nm s^{-1} .

Additionally, we investigated the effect of the applied voltage on the growth rate and film homogeneity. For this purpose, BDT-ETTA COF particles were deposited using potentials of 100, 200, 300, 600 and 900 V while keeping the deposition time constant at 2 min. Using these deposition parameters, a steady increase in the COF (100) reflection intensity in the XRD pattern relative to the FTO reflection intensity was observed. This is attributed to the applied higher deposition voltages, indicating a higher mass transfer rate from the suspension to the electrode (SI Figure 6.10). SEM top-view micrographs of the films deposited at 100, 200 and 300 V cm^{-1} reveal randomly scattered COF particles only partially covering the electrode surface. At 600 V cm^{-1} a nearly continuous film was observed, but in contrast to the film fabricated under the optimal conditions of 900 V cm^{-1} , large cracks protruding the film were still visible (SI Figure 6.10).

Covalent Organic Framework Films by Electrophoretic Deposition - Creating efficient Morphologies for Catalysis

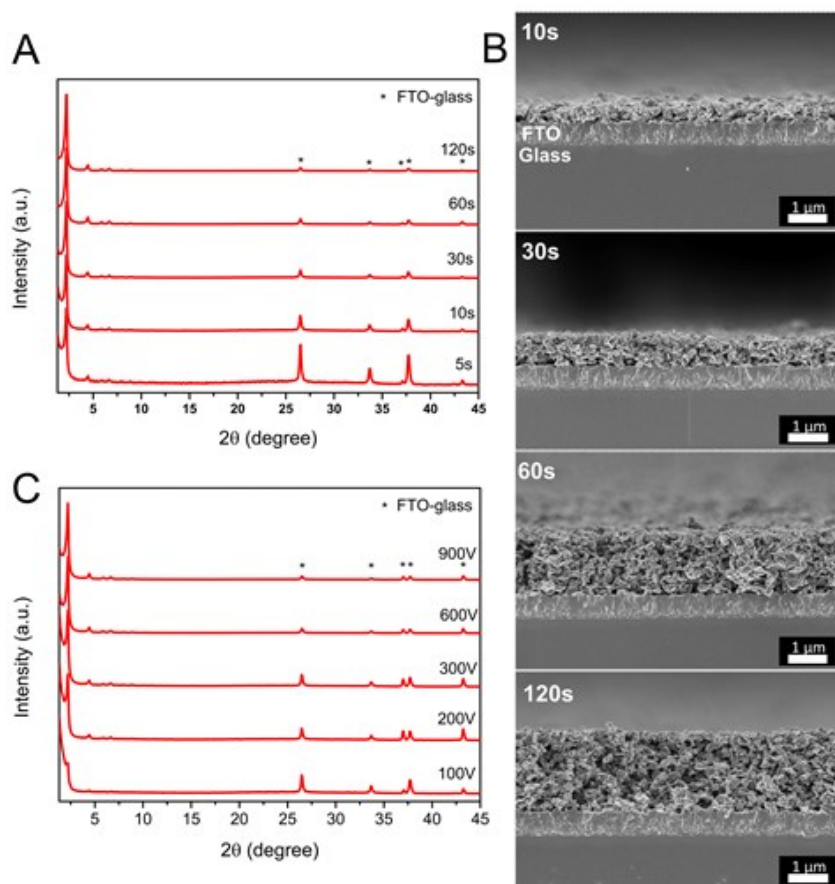


Figure 6.2. (A) XRD film patterns of BDT-ETTA COF films resulting from different deposition times (deposition voltage 900 V). (B) Corresponding SEM cross-sections of BDT-ETTA COF films (deposition voltage 900 V). (C) XRD patterns of BDT-ETTA COF films deposited at different electrode potentials.

Recently, advanced synthesis approaches for growing single crystals of COFs, in some cases even exhibiting sizes suitable for single crystal XRD analysis, were reported.⁴⁷ For boronate ester COFs, such as COF-5, in the form of larger single crystals, size-dependent effects such as prolonged lifetimes of excitons were observed by transient absorption spectroscopy.⁴⁸ So far, COF film synthesis methods have not been successfully used for the preparation of films comprising single crystal domains. Here, we found that the as-synthesized near micrometer-sized COF-300 particles are directly dispersible as individual crystallites in the deposition solvent and therefore, a quantitative deposition of COF-300 crystals from the suspension is feasible. For a quantitative deposition, we found that up to 1 mg of COF-300 powder in 10 mL of ethyl acetate yields a stable suspension. The suspended crystallites can directly be deposited on 1 cm² of electrode area within 2 minutes at 900 V cm⁻¹, resulting in a film

Results and Discussion

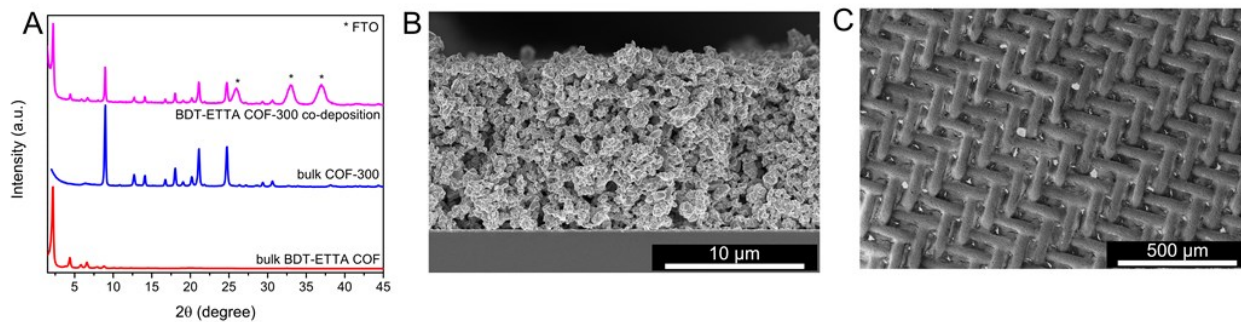


Figure 6.3. (A) XRD pattern of co-deposited COF-300 and BDT-ETTA COF materials compared with the respective bulk PXRD patterns of the individual COFs, and (B) the corresponding SEM cross-section. (C) Deposition of COF-300 on a stainless-steel mesh.

thickness of 24 μm. Assuming a complete depletion of the particles in the suspension, we can establish a film deposition formula suitable for predetermining film thickness, e.g. 24 μm film thickness per mg COF powder and cm² electrode area (24 μm mg⁻¹ cm⁻²) for COF-300 (SI Figure 6.11).

The scalability of the EPD process is a central advantage for obtaining coatings on conductive surfaces. To the best of our knowledge, a process that allows for the direct preparation of COF films on surfaces larger than a few cm² has yet to be reported. To probe the scalability of EPD for COF films, we fabricated a BDT-ETTA COF film on a 5 cm × 5 cm large FTO substrate by increasing the COF and solvent quantities used for the deposition on a 1 cm² substrate by 25 times, while keeping the deposition time and potential constant at 2 min and 900 V cm⁻¹, respectively. The obtained film features a macroscopic homogeneous deposit similar to deposits on smaller substrates. This confirms that the established COF EPD protocol is indeed highly scalable and applicable to the rapid deposition of COF crystals on large surface (SI Figure 6.12). In the context of COF film preparation, this versatile deposition technique constitutes a significant improvement over other state-of-the-art methods in terms of deposition yield, growth time, scalability and thickness control. We conclude that COFs are especially suitable for EPD due to faster growth rates and homogeneous film coverages, compared to related materials.^{40,49}

The EPD of COF materials opens new perspectives regarding the facile production of films and coatings for applications such as sensing, catalysis or molecular sieving. Here, we demonstrate the feasibility of using EPD for the preparation of COF-based membranes supported by a porous grid. For this purpose, a stainless-steel grid featuring a mesh size of 270 (53 μm pore size) was used as the

Covalent Organic Framework Films by Electrophoretic Deposition - Creating efficient Morphologies for Catalysis

deposition electrode for COF-300 (Figure 6.3C). Adjusting the mass of the suspended COF and applying EPD for 2 minutes at 900 V cm^{-1} resulted in the formation of a homogeneous coating covering the grid and its cavities, the permeable areas. The deposition on such a mesh demonstrates that EPD can be used for the fabrication of COF coatings not only on flat surfaces but also on corrugated 3D surfaces (Figure 6.3 and SI Figure 6.13). Harnessing the ability to prepare COF suspensions from synthesized COF powders and developing a deposition formula for high yields, we explored the simultaneous deposition of two structurally distinct COF particles featuring different pore shapes and sizes from a mixed COF crystallite suspension. To this end, we produced a suspension consisting of BDT-ETTA COF and COF-300 particles in ethyl acetate and deposited this COF particle mixture onto FTO at 900 V cm^{-1} and 2 minutes deposition time (for more details see the Supporting Information). The XRD pattern of the obtained film shows the characteristic (100) and the (111) reflections for BDT-ETTA COF and COF-300 at 2.26° and $8.89^\circ 2\theta$, respectively. Furthermore, higher-order reflections of both COFs with relative intensities similar to the bulk powder are visible, indicating that the COF long-range order remained intact. This demonstrates the deposition of a mixed 2D/3D COF film consisting of crystallites featuring three pore types (micropores and mesopores in BDT-ETTA COF and micropores in COF-300), exhibiting different chemical environments and dimensions (Figure 6.3A). The homogeneous mixing of the two COFs was confirmed by SEM cross-section micrographs, where both COF morphologies, namely large, oval COF-300 particles and BDT-ETTA COF nanocrystallites, are evenly distributed throughout the film (Figure 6.3B).

Photocatalytic water reduction has become a major interest for potential COF applications. Typically, COF powder is used in combination with a sacrificial agent to facilitate or enable the solar driven hydrogen evolution.⁴⁵ Recently, we demonstrated the use of highly oriented thin films of BDT-ETTA COF as photocathodes for the sacrificial agent free photoelectrochemical hydrogen production and provided a detailed characterization of the catalytic properties of the material as a dense and oriented film.⁴² This allows for studying the impact of morphology on the performance of EPD BDT-ETTA COF films on the photoelectrochemical (PEC) catalysis performance, already shown for this type of COF. Therefore, we measured light-induced photocurrent generation for these films in a water-splitting setup. A three-electrode setup was used with a BDT-ETTA COF film supported by FTO as the photocathode working electrode, a platinum mesh counter-electrode and a reverse hydrogen electrode (RHE) as a reference electrode.

Results and Discussion

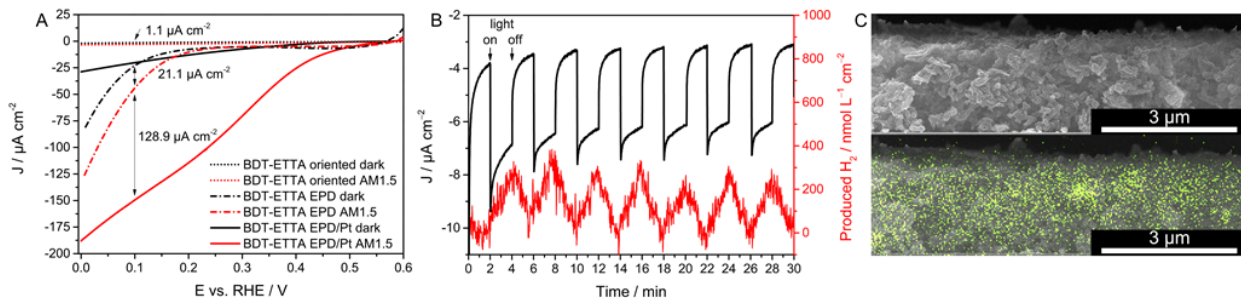


Figure 6.4. (A) PEC linear sweep voltammograms of electrodes coated with BDT-ETTA COF as a dense and oriented film, a 3 μm thick film prepared by EPD, and a COF/Pt nanoparticle hybrid film prepared via EPD. Illumination at AM1.5G. (B) Dynamic hydrogen evolution measurement under chopped AM1.5G illumination of a BDT-ETTA COF electrode at 0.2 V vs. RHE. (C) SEM cross-section of BDT-ETTA COF and the corresponding EDX elemental mapping of Pt recorded at an electron acceleration voltage of 20 kV.

A BDT-ETTA COF film of 3 μm thickness, in a 0.1 M Na_2SO_4 aqueous, nitro-gen-purged electrolyte, was measured by linear sweep voltammetry either in the dark or under illumination through the substrate by simulated sunlight (AM1.5G, 100 mW cm^{-2}). The measurements were carried out at potentials ranging from 0.6 V to 0 V vs. RHE. Prior to measuring PEC current generation, a linear potential sweep was carried out in the dark to quantify non-PEC related electrochemical reactions and film capacitance. PEC measurements of the pristine BDT-ETTA COF film under illumination showed a photocurrent onset at 0.25 V vs. RHE and a high photocurrent density of $21.1 \mu\text{A cm}^{-2}$ at 0.1 V vs. RHE (Figure 6.4A). The recorded photocurrent density is 19-times higher compared to the value previously reported on dense and oriented thin BDT-ETTA COF films at the same potential.⁴² Furthermore, we performed a dynamic hydrogen evolution experiment under chopped illumination with an interval time of two minutes. Here, the dissolved hydrogen gas was quantified using a microsensor, equipped with a hydrogen selective silicone membrane. The measurement was carried out at 0.2 V vs. RHE, close to the photocurrent onset potential, to prove that the observed photocurrent is indeed generated by proton reduction. Upon illumination, an instant current response was observed followed by a typical photocurrent transient. This photocurrent is directly correlated with an increase in the simultaneously recorded hydrogen concentration. In the dark, the recorded current density regresses rapidly and the hydrogen concentration simultaneously declines. This light-on and -off sequence was repeated several times and showed stable current and hydrogen concentration responses over the recorded course of 30 minutes (Figure 6.4B). Subsequently, XRD analysis of this film proved the retention of crystallinity of the active material (SI Figure 6.15). To

Covalent Organic Framework Films by Electrophoretic Deposition - Creating efficient Morphologies for Catalysis

investigate whether charge carrier transport efficiently occurs throughout the whole EPD COF film thickness, a film of half the thickness, about 1.5 μm , was used in the same experimental setup. Here, a reduced photocurrent density of 16.7 $\mu\text{A cm}^{-2}$ at 0.1 V vs. RHE was observed (SI Figure 6.14). This reduction in photocurrent correlates with the reduction of the film thickness, indicating that PEC activity is indeed thickness-dependent, and charge carriers are sufficiently transported throughout the porous film morphology. Furthermore, it illustrates that a tight contact and continuous interface between the active COF material and the electrode are not necessarily prerequisites for effective electrocatalysis. We attribute the overall enhanced performance of the BDT-ETTA COF film prepared by EPD to the greatly enlarged interface between the photoabsorber and medium provided by the textural porosity. This compensates for the decreased areal interaction of the COF with the electrode, obtained by using a dense film. Besides the textural porosity, the inherent porosity of the COF can contribute to its catalytic performance. A stabilized current density output under constant illumination was recorded for the 1.5 μm thick film by chronoamperometric measurements at 0.1 V vs. RHE, which showed a constant photocurrent density of 14.3 $\mu\text{A cm}^{-2}$ over the course of 10 minutes (SI Figure 6.14). Next, we focused on the co-deposition of BDT-ETTA COF and an inorganic co-catalyst to facilitate electron charge transfer from the COF photoabsorber towards the aqueous electrolyte, whereby a further improvement of the PEC performance is expected.⁵⁰ Platinum nanoparticles sized 2–4 nm were included into the BDT-ETTA COF particle suspension prior to the EPD (SI Figure 6.16 and SI Figure 6.17). To prevent a premature depletion of the Pt nanoparticles during deposition, due to their higher mobility under electrophoretic conditions, additional Pt nanoparticle suspension was continuously added to the COF/Pt deposition medium in the course of the deposition process. Hereby, a homogeneous distribution of Pt in the COF film was achieved, confirmed by elemental mapping analysis using energy-dispersive X-ray spectroscopy on a film cross-section in the SEM (Figure 6.4C). Subsequently, the exact same linear potential sweeps measurements were repeated for this COF/Pt hybrid film. Strikingly, a PEC photocurrent density of 128.9 $\mu\text{A cm}^{-2}$ was recorded at 0.1 V vs. RHE for the COF/Pt films, which is an additional 6.1-fold increase with respect to the pristine COF EPD film and 29-times higher than the current density previously reported for dense and oriented thin BDT-ETTA COF film decorated with Pt nanoparticles on the surface.⁴² An additional valuable effect of the incorporation of the platinum co-catalyst is an earlier photocurrent onset, which is shifted from 0.25 V to 0.45 V vs. RHE. Moreover, the dark current was strongly reduced. These results show that the COF film morphology plays a pivotal role in determining device performance. We postulate that the nanostructured film exhibiting a large interfacial area allows for an efficient charge separation

Conclusion

and transport paths attributed to a direct transfer of electrons from the COF/Pt catalytic center to the surrounding water while holes can travel through the aggregated COF particle pathways towards the transparent conductive oxide (TCO) substrate.^{42,51} These separated charge carrier transport pathways enable the use of even thicker COF films. In the case of a dense film, electrons and holes are generated in the bulk film and travel throughout the whole film thickness to reach a catalytic center or the TCO support. Therefore, charge carriers may be more likely to recombine, thus providing an overall limited effective film thickness and photocurrent density. According to these results, we conclude that film morphologies must be carefully chosen and tailored towards the respective application.

6.4 Conclusion

In conclusion, we demonstrate the preparation of COF films and coatings by depositing COF particles on conducting substrates in an electric field through EPD. Hereby, 2D and 3D imine and boronate-ester linked COFs of different particle sizes and morphologies were deposited on metal, transparent conducting metal oxides or steel meshes. By adjusting the EPD parameters, such as deposition times, particle concentrations, and electrode potentials, film thicknesses could be tuned and predetermined. The obtained films feature an inherent textural porosity with interstitial voids between the deposited particles, thereby allowing for an increased contact to active media for applications such as catalysis. In addition, we showed that through EPD, film composites consisting of mixed COFs can be straightforwardly prepared, enabling encoded functionalities such as multi-pore COF films. Finally, a BDT-ETTA COF film as well as a COF/Pt nanoparticle hybrid film were examined regarding their PEC performance, where a 19- and 117-fold catalytical improvement, respectively, was found over our previously reported dense and oriented BDT-ETTA COF films. To put these results in perspective, it shows that film morphology plays a crucial role for different applications and should be considered in combination with the inherent properties of the COFs. This, as well as the simplicity and generality of the approach, underlines the importance of EPD as an addition to the field of COF film preparation methods. Therefore, we believe that this work will assist in designing high-performance devices for specific applications.

6.5 Associated Content

Supporting Information. Experimental details, additional XRD, SEM, TEM and electrochemical characterizations are supplied as Supporting Information. This material is available free of charge via the Internet at <https://pubs.acs.org/doi/10.1021/acs.chemmater.9b02286>.

6.6 Author Information

Corresponding Author

*(D.D.M.) E-mail: dana.medina@cup.uni-muenchen.de

Author Contributions

† J. R. and S. M. contributed equally. The manuscript was written through contributions of all authors.

Notes

The authors declare no competing financial interest.

6.7 Acknowledgment

The authors are grateful for funding from the German Science Foundation (DFG; Research Cluster NIM) and the Free State of Bavaria (Research Network SolTech). The research leading to these results has received funding from the European Research Council under the European Union's Seventh Framework Programme (FP7/2007-2013)/ERC Grant Agreement No. 321339). The authors thank Dr. Markus Döblinger and Michael Beetz for the transmission electron microscopy.

6.8 Abbreviations

COF, covalent organic framework; VAC, vapor-assisted conversion; EPD, electrophoretic deposition; FTO, fluorine doped tin oxide; ITO, indium doped tin oxide; SEM, scanning electron microscopy; XRD, X-ray diffraction; TEM, transmission electron microscopy; FT-IR, Fourier transformed infrared spectroscopy; PEC, photoelectrochemical; RHE, reversible hydrogen electrode; TCO, transparent conductive oxide.

References

6.9 References

- (1) Diercks, C. S.; Yaghi, O. M. The atom, the molecule, and the covalent organic framework. *Science* **2017**, *355*.
- (2) Jin, Y.; Hu, Y.; Zhang, W. Tessellated multiporous two-dimensional covalent organic frameworks. *Nat. Rev. Chem.* **2017**, *1*, 56.
- (3) Furukawa, H.; Yaghi, O. M. Storage of hydrogen, methane, and carbon dioxide in highly porous covalent organic frameworks for clean energy applications. *J. Am. Chem. Soc.* **2009**, *131*, 8875–8883.
- (4) Sharma, A.; Malani, A.; Medhekar, N. V.; Babarao, R. CO₂ adsorption and separation in covalent organic frameworks with interlayer slipping. *CrystEngComm* **2017**, *19*, 6950–6963.
- (5) Fan, H.; Mundstock, A.; Feldhoff, A.; Knebel, A.; Gu, J.; Meng, H.; Caro, J. Covalent Organic Framework-Covalent Organic Framework Bilayer Membranes for Highly Selective Gas Separation. *J. Am. Chem. Soc.* **2018**, *140*, 10094–10098.
- (6) Zhang, S.; Zheng, Y.; An, H.; Aguila, B.; Yang, C.-X.; Dong, Y.; Xie, W.; Cheng, P.; Zhang, Z.; Chen, Y. *et al.* Covalent Organic Frameworks with Chirality Enriched by Biomolecules for Efficient Chiral Separation. *Angew. Chem. Int. Ed.* **2018**, *57*, 16754–16759.
- (7) Ding, S.-Y.; Gao, J.; Wang, Q.; Zhang, Y.; Song, W.-G.; Su, C.-Y.; Wang, W. Construction of covalent organic framework for catalysis: Pd/COF-LZU1 in Suzuki-Miyaura coupling reaction. *J. Am. Chem. Soc.* **2011**, *133*, 19816–19822.
- (8) Sun, Q.; Aguila, B.; Ma, S. A bifunctional covalent organic framework as an efficient platform for cascade catalysis. *Mater. Chem. Front.* **2017**, *1*, 1310–1316.
- (9) Lin, S.; Diercks, C. S.; Zhang, Y.-B.; Kornienko, N.; Nichols, E. M.; Zhao, Y.; Paris, A. R.; Kim, D.; Yang, P.; Yaghi, O. M. *et al.* Covalent organic frameworks comprising cobalt porphyrins for catalytic CO₂ reduction in water. *Science* **2015**, *349*, 1208–1213.
- (10) Aiyappa, H. B.; Thote, J.; Shinde, D. B.; Banerjee, R.; Kurungot, S. Cobalt-Modified Covalent Organic Framework as a Robust Water Oxidation Electrocatalyst. *Chem. Mater.* **2016**, *28*, 4375–4379.
- (11) Thote, J.; Aiyappa, H. B.; Deshpande, A.; Díaz Díaz, D.; Kurungot, S.; Banerjee, R. A covalent organic framework-cadmium sulfide hybrid as a prototype photocatalyst for visible-light-driven hydrogen production. *Chemistry* **2014**, *20*, 15961–15965.
- (12) Wang, X.; Chen, L.; Chong, S. Y.; Little, M. A.; Wu, Y.; Zhu, W.-H.; Clowes, R.; Yan, Y.; Zwiijnenburg, M. A.; Sprick, R. S. *et al.* Sulfone-containing covalent organic frameworks for photocatalytic hydrogen evolution from water. *Nat. Chem.* **2018**, *10*, 1180–1189.
- (13) Dogru, M.; Handloser, M.; Auras, F.; Kunz, T.; Medina, D.; Hartschuh, A.; Knochel, P.; Bein, T. A photoconductive thienothiophene-based covalent organic framework showing charge transfer towards included fullerene. *Angew. Chem. Int. Ed.* **2013**, *52*, 2920–2924.
- (14) Bessinger, D.; Ascherl, L.; Auras, F.; Bein, T. Spectrally Switchable Photodetection with Near-Infrared-Absorbing Covalent Organic Frameworks. *J. Am. Chem. Soc.* **2017**, *139*, 12035–12042.
- (15) Guo, J.; Xu, Y.; Jin, S.; Chen, L.; Kaji, T.; Honsho, Y.; Addicoat, M. A.; Kim, J.; Saeki, A.; Ihee, H. *et al.* Conjugated organic framework with three-dimensionally ordered stable structure and delocalized π clouds. *Nat. Commun.*, *4*, 2736.

**Covalent Organic Framework Films by
Electrophoretic Deposition - Creating efficient Morphologies for Catalysis**

- (16) DeBlase, C. R.; Silberstein, K. E.; Truong, T.-T.; Abruña, H. D.; Dichtel, W. R. β -Ketoenamine-linked covalent organic frameworks capable of pseudocapacitive energy storage. *J. Am. Chem. Soc.* **2013**, *135*, 16821–16824.
- (17) Chandra, S.; Roy Chowdhury, D.; Addicoat, M.; Heine, T.; Paul, A.; Banerjee, R. Molecular Level Control of the Capacitance of Two-Dimensional Covalent Organic Frameworks: Role of Hydrogen Bonding in Energy Storage Materials. *Chem. Mater.* **2017**, *29*, 2074–2080.
- (18) Halder, A.; Ghosh, M.; Khayum M, A.; Bera, S.; Addicoat, M.; Sasmal, H. S.; Karak, S.; Kurungot, S.; Banerjee, R. Interlayer Hydrogen-Bonded Covalent Organic Frameworks as High-Performance Supercapacitors. *J. Am. Chem. Soc.* **2018**, *140*, 10941–10945.
- (19) Wang, D.-G.; Li, N.; Hu, Y.; Wan, S.; Song, M.; Yu, G.; Jin, Y.; Wei, W.; Han, K.; Kuang, G.-C. *et al.* Highly Fluoro-Substituted Covalent Organic Framework and Its Application in Lithium-Sulfur Batteries. *ACS Appl. Mater. Interfaces* **2018**.
- (20) Wuttke, S.; Medina, D. D.; Rotter, J. M.; Begum, S.; Stassin, T.; Ameloot, R.; Oschatz, M.; Tsotsalas, M. Bringing Porous Organic and Carbon-Based Materials toward Thin-Film Applications. *Adv. Funct. Mater.* **2018**, *28*, 1801545.
- (21) Beuerle, F.; Gole, B. Covalent Organic Frameworks and Cage Compounds: Design and Applications of Polymeric and Discrete Organic Scaffolds. *Angew. Chem. Int. Ed.* **2018**, *57*, 4850–4878.
- (22) Colson, J. W.; Woll, A. R.; Mukherjee, A.; Levendorf, M. P.; Spitler, E. L.; Shields, V. B.; Spencer, M. G.; Park, J.; Dichtel, W. R. Oriented 2D covalent organic framework thin films on single-layer graphene. *Science* **2011**, *332*, 228–231.
- (23) Medina, D. D.; Werner, V.; Auras, F.; Tautz, R.; Dogru, M.; Schuster, J.; Linke, S.; Döblinger, M.; Feldmann, J.; Knochel, P. *et al.* Oriented thin films of a benzodithiophene covalent organic framework. *ACS Nano* **2014**, *8*, 4042–4052.
- (24) Wang, H.; He, B.; Liu, F.; Stevens, C.; Brady, M. A.; Cai, S.; Wang, C.; Russell, T. P.; Tan, T.-W.; Liu, Y. Orientation transitions during the growth of imine covalent organic framework thin films. *J. Mater. Chem. C* **2017**, *5*, 5090–5095.
- (25) Bisbey, R. P.; DeBlase, C. R.; Smith, B. J.; Dichtel, W. R. Two-dimensional Covalent Organic Framework Thin Films Grown in Flow. *J. Am. Chem. Soc.* **2016**, *138*, 11433–11436.
- (26) Medina, D. D.; Rotter, J. M.; Hu, Y.; Dogru, M.; Werner, V.; Auras, F.; Markiewicz, J. T.; Knochel, P.; Bein, T. Room temperature synthesis of covalent-organic framework films through vapor-assisted conversion. *J. Am. Chem. Soc.* **2015**, *137*, 1016–1019.
- (27) Zhao, X.; Pachfule, P.; Li, S.; Langenhahn, T.; Ye, M.; Schlesiger, C.; Praetz, S.; Schmidt, J.; Thomas, A. Macro/Microporous Covalent Organic Frameworks for Efficient Electrocatalysis. *J. Am. Chem. Soc.* **2019**, *141*, 6623–6630.
- (28) BESRA, L.; LIU, M. A review on fundamentals and applications of electrophoretic deposition (EPD). *Prog. Mater. Sci.* **2007**, *52*, 1–61.
- (29) Castro, Y.; Ferrari, B.; Moreno, R.; Durán, A. Coatings produced by electrophoretic deposition from nano-particulate silica sol-gel suspensions. *Surf. Coat. Technol.* **2004**, *182*, 199–203.
- (30) Seike, T.; Matsuda, M.; Miyake, M. Preparation of FAU type zeolite membranes by electrophoretic deposition and their separation properties. *J. Mater. Chem.* **2002**, *12*, 366–368.

References

- (31) Limmer, S. J.; Seraji, S.; Wu, Y.; Chou, T. P.; Nguyen, C.; Cao, G. Z. Template-Based Growth of Various Oxide Nanorods by Sol–Gel Electrophoresis. *Adv. Funct. Mater.* **2002**, *12*, 59.
- (32) Salant, A.; Shalom, M.; Hod, I.; Faust, A.; Zaban, A.; Banin, U. Quantum dot sensitized solar cells with improved efficiency prepared using electrophoretic deposition. *ACS Nano* **2010**, *4*, 5962–5968.
- (33) Xu, J.; Shalom, M. Electrophoretic Deposition of Carbon Nitride Layers for Photoelectrochemical Applications. *ACS Appl. Mater. Interfaces* **2016**, *8*, 13058–13063.
- (34) Casagrande, T.; Imin, P.; Cheng, F.; Botton, G. A.; Zhitomirsky, I.; Adronov, A. Synthesis and Electrophoretic Deposition of Single-Walled Carbon Nanotube Complexes with a Conjugated Polyelectrolyte. *Chem. Mater.* **2010**, *22*, 2741–2749.
- (35) Garate, J.-A.; English, N. J.; Singh, A.; Ryan, K. M.; Mooney, D. A.; MacElroy, J. M. D. Electrophoretic deposition of poly(3-decylthiophene) onto gold-mounted cadmium selenide nanorods. *Langmuir* **2011**, *27*, 13506–13513.
- (36) Li, G.; Martinez, C.; Semancik, S. Controlled electrophoretic patterning of polyaniline from a colloidal suspension. *J. Am. Chem. Soc.* **2005**, *127*, 4903–4909.
- (37) Han, H.; Yuan, X.; Zhang, Z.; Zhang, J. Preparation of a ZIF-67 Derived Thin Film Electrode via Electrophoretic Deposition for Efficient Electrocatalytic Oxidation of Vanillin. *Inorg. Chem.* **2019**, *58*, 3196–3202.
- (38) Feng, J.-F.; Yang, X.; Gao, S.-Y.; Shi, J.; Cao, R. Facile and Rapid Growth of Nanostructured Ln-BTC Metal-Organic Framework Films by Electrophoretic Deposition for Explosives sensing in Gas and Cr³⁺ Detection in Solution. *Langmuir* **2017**, *33*, 14238–14243.
- (39) Wang, L.; Zeng, C.; Xu, H.; Yin, P.; Chen, D.; Deng, J.; Li, M.; Zheng, N.; Gu, C.; Ma, Y. A highly soluble, crystalline covalent organic framework compatible with device implementation. *Chem. Sci.* **2019**, *10*, 1023–1028.
- (40) Hod, I.; Bury, W.; Karlin, D. M.; Deria, P.; Kung, C.-W.; Katz, M. J.; So, M.; Klahr, B.; Jin, D.; Chung, Y.-W. *et al.* Directed growth of electroactive metal-organic framework thin films using electrophoretic deposition. *Adv. Mater.* **2014**, *26*, 6295–6300.
- (41) Côté, A. P.; Benin, A. I.; Ockwig, N. W.; O’Keeffe, M.; Matzger, A. J.; Yaghi, O. M. Porous, crystalline, covalent organic frameworks. *Science* **2005**, *310*, 1166–1170.
- (42) Sick, T.; Hufnagel, A. G.; Kampmann, J.; Kondofersky, I.; Calik, M.; Rotter, J. M.; Evans, A.; Döblinger, M.; Herbert, S.; Peters, K. *et al.* Oriented Films of Conjugated 2D Covalent Organic Frameworks as Photocathodes for Water Splitting. *J. Am. Chem. Soc.* **2018**, *140*, 2085–2092.
- (43) Uribe-Romo, F. J.; Hunt, J. R.; Furukawa, H.; Klöck, C.; O’Keeffe, M.; Yaghi, O. M. A crystalline imine-linked 3-D porous covalent organic framework. *J. Am. Chem. Soc.* **2009**, *131*, 4570–4571.
- (44) Wu, G.-W.; He, S.-B.; Peng, H.-P.; Deng, H.-H.; Liu, A.-L.; Lin, X.-H.; Xia, X.-H.; Chen, W. Citrate-capped platinum nanoparticle as a smart probe for ultrasensitive mercury sensing. *Anal. Chem.* **2014**, *86*, 10955–10960.
- (45) Wang, H.; Zeng, Z.; Xu, P.; Li, L.; Zeng, G.; Xiao, R.; Tang, Z.; Huang, D.; Tang, L.; Lai, C. *et al.* Recent progress in covalent organic framework thin films: fabrications, applications and perspectives. *Chem. Soc. Rev.* **2019**, *48*, 488–516.
- (46) Hamaker, H. C. Formation of a deposit by electrophoresis. *Trans. Faraday Soc.* **1940**, *35*, 279.

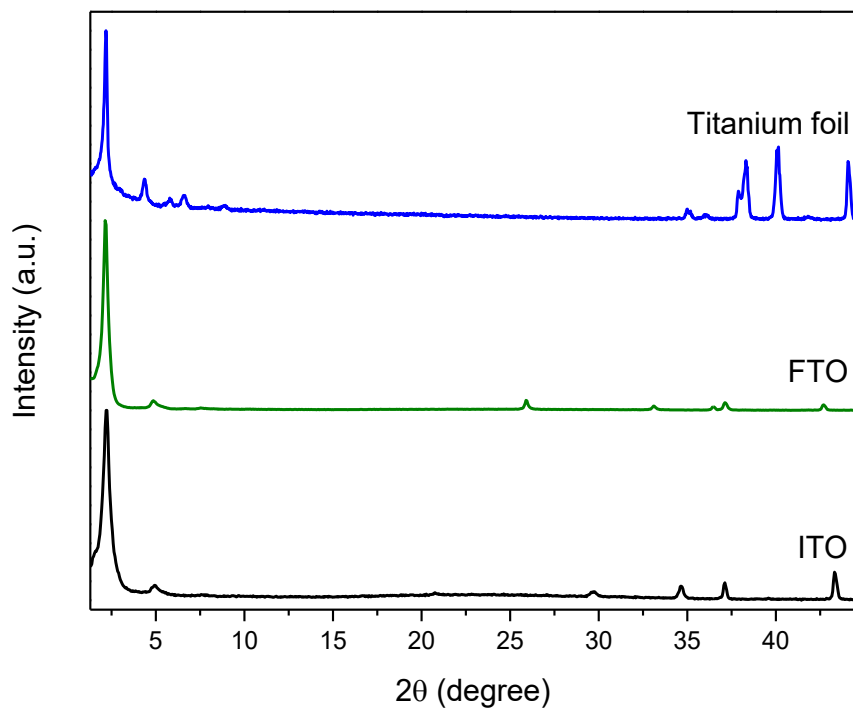
**Covalent Organic Framework Films by
Electrophoretic Deposition - Creating efficient Morphologies for Catalysis**

- (47) Ma, T.; Kapustin, E. A.; Yin, S. X.; Liang, L.; Zhou, Z.; Niu, J.; Li, L.-H.; Wang, Y.; Su, J.; Li, J. *et al.* Single-crystal x-ray diffraction structures of covalent organic frameworks. *Science* **2018**, *361*, 48–52.
- (48) Evans, A. M.; Parent, L. R.; Flanders, N. C.; Bisbey, R. P.; Vitaku, E.; Kirschner, M. S.; Schaller, R. D.; Chen, L. X.; Gianneschi, N. C.; Dichtel, W. R. Seeded growth of single-crystal two-dimensional covalent organic frameworks. *Science* **2018**, *361*, 52–57.
- (49) Safaei, J.; Mohamed, N. A.; Mohamad Noh, M. F.; Soh, M. F.; Ludin, N. A.; Ibrahim, M. A.; Roslam Wan Isahak, W. N.; Mat Teridi, M. A. Graphitic carbon nitride (g-C₃N₄) electrodes for energy conversion and storage: a review on photoelectrochemical water splitting, solar cells and supercapacitors. *J. Mater. Chem. A* **2018**, *6*, 22346–22380.
- (50) Kemppainen, E.; Bodin, A.; Sebok, B.; Pedersen, T.; Seger, B.; Mei, B.; Bae, D.; Vesborg, P. C. K.; Halme, J.; Hansen, O. *et al.* Scalability and feasibility of photoelectrochemical H₂ evolution: the ultimate limit of Pt nanoparticle as an HER catalyst. *Energy Environ. Sci.* **2015**, *8*, 2991–2999.
- (51) Medina, D. D.; Petrus, M. L.; Jumabekov, A. N.; Margraf, J. T.; Weinberger, S.; Rotter, J. M.; Clark, T.; Bein, T. Directional Charge-Carrier Transport in Oriented Benzodithiophene Covalent Organic Framework Thin Films. *ACS Nano* **2017**, *11*, 2706–2713.

Supporting Information

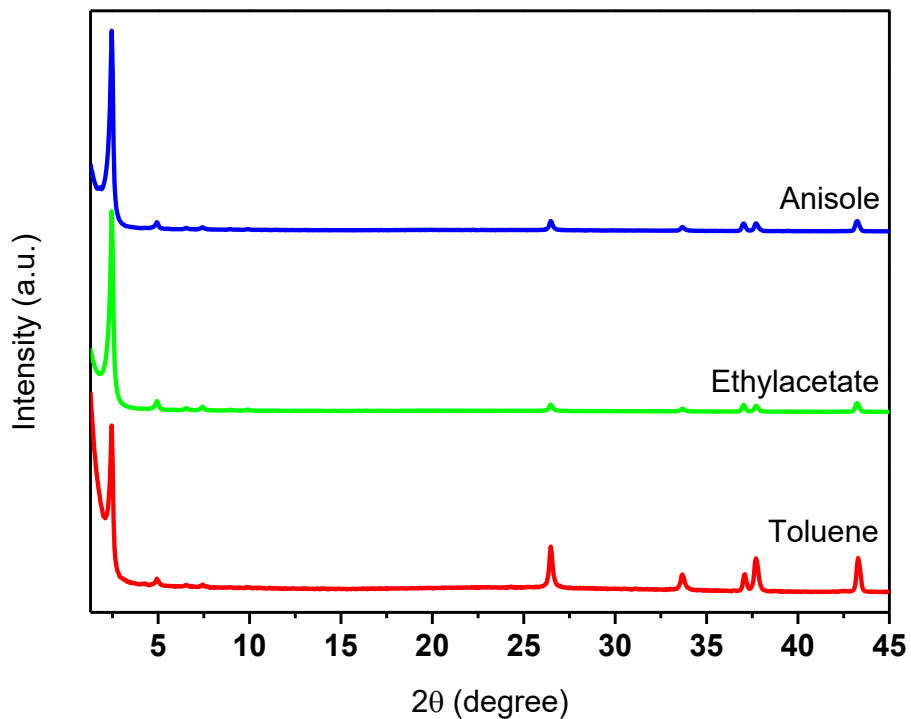
6.10 Supporting Information

6.10.1 Deposition of BDT-ETTA on FTO, ITO and titanium foil



SI Figure 6.1. Deposition of BDT-ETTA COF on different conducting surfaces, namely titanium foil, glass coated with FTO and glass coated with ITO. All depositions were carried out using 10 mL of BDT-ETTA COF suspension in ethyl acetate at 900 V for 2 min.

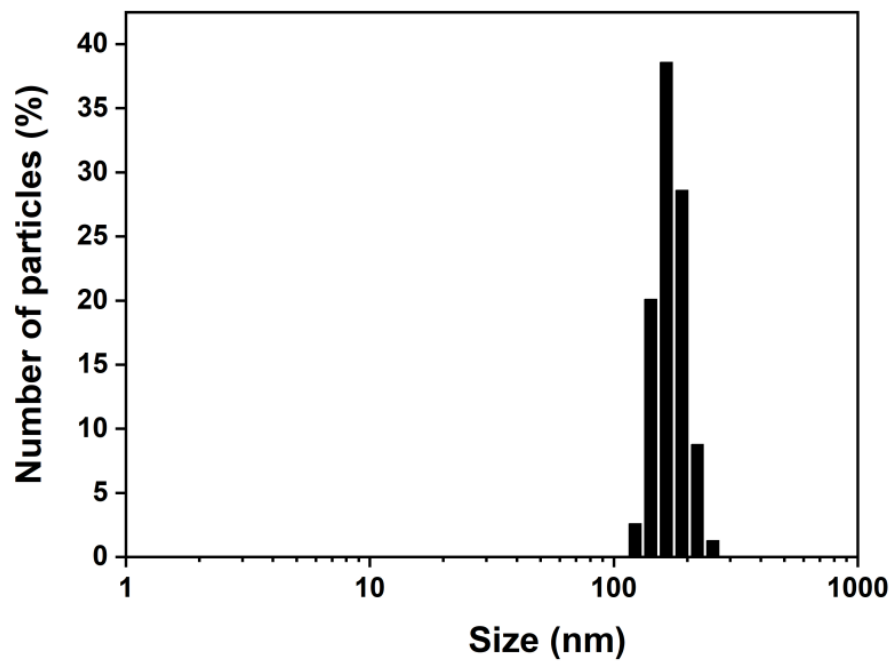
6.10.2 Deposition of BDT-ETTA in anisole, ethyl acetate and toluene



SI Figure 6.2. Deposition of BDT-ETTA COF from different solvents, namely anisole, ethyl acetate and toluene. All depositions were carried out using 10 mL of the respective BDT-ETTA COF suspension at 900 V for 2 min.

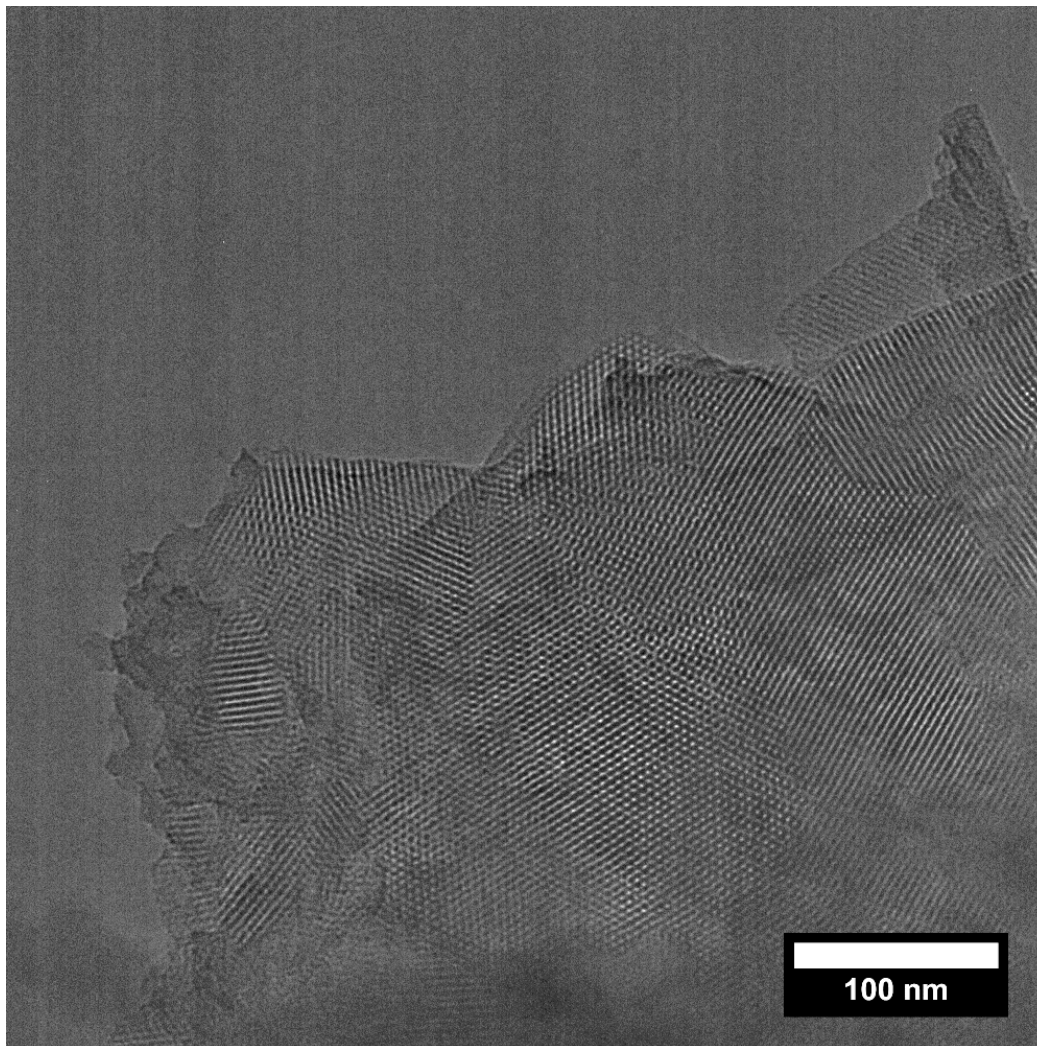
Supporting Information

6.10.3 DLS Data for ultrasound treated BDT-ETTA COF



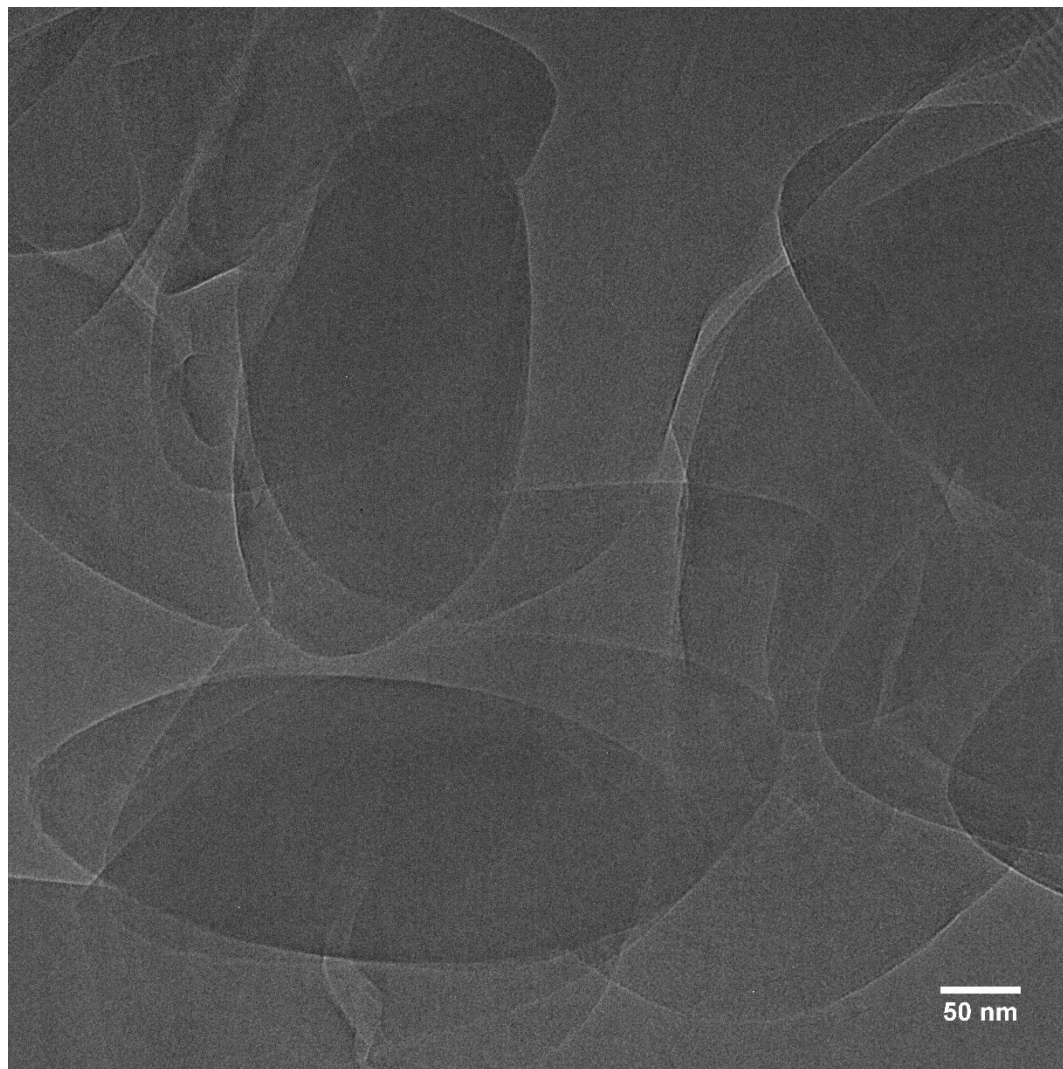
SI Figure 6.3. Particle size distribution of BDT-ETTA COF after the ultrasonic milling process.

6.10.4 Transmission electron micrographs



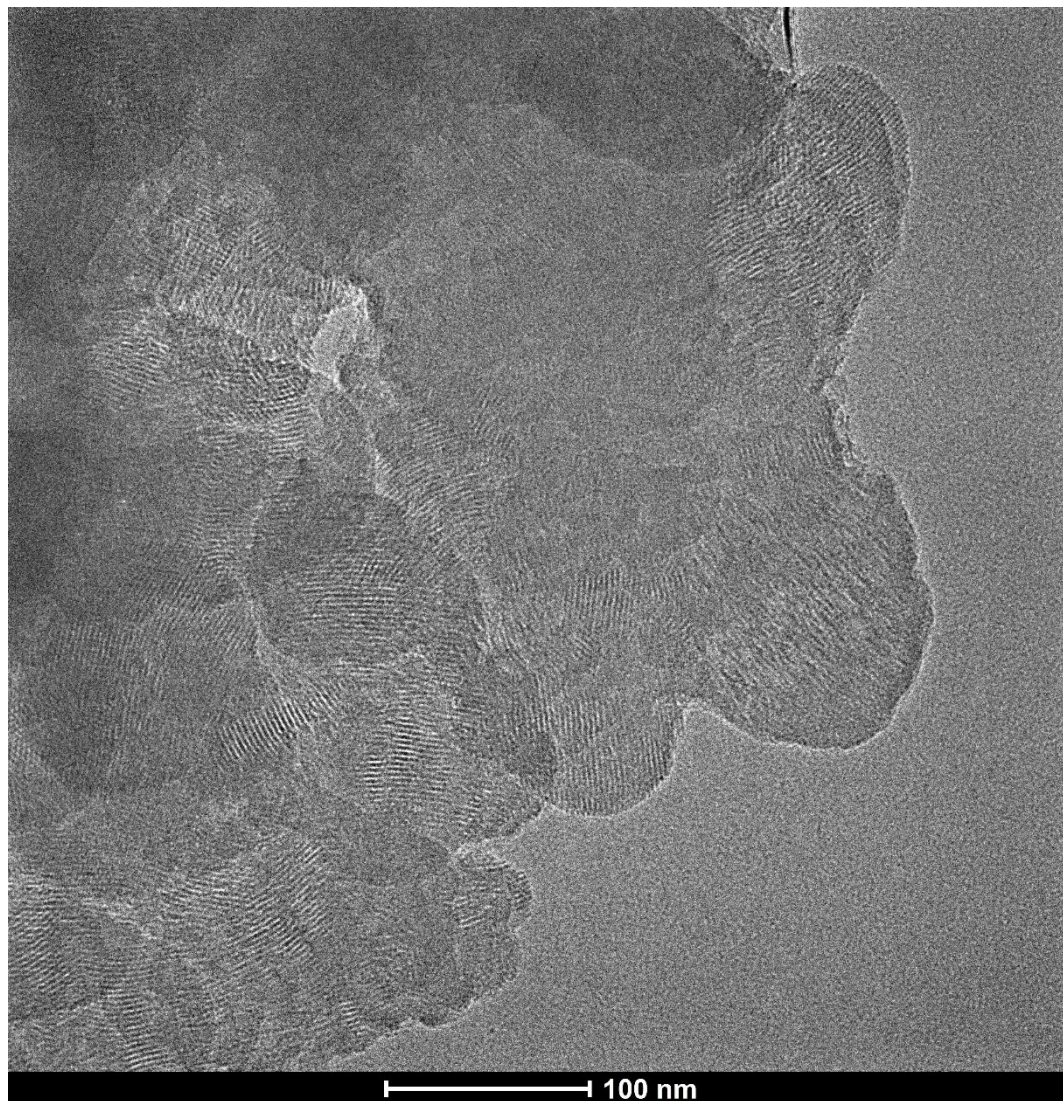
SI Figure 6.4. TEM image of deposited BDT-ETTA COF particles after the ultrasonic milling process.

Supporting Information



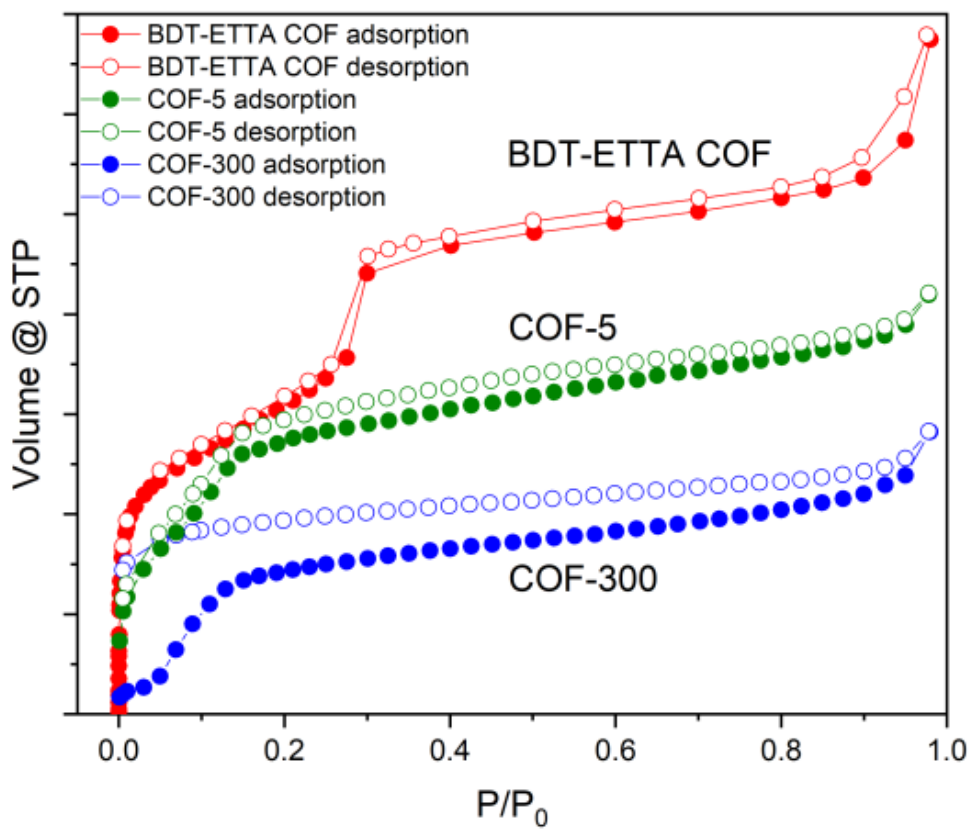
SI Figure 6.5. TEM image of deposited COF-300 particles.

**Covalent Organic Framework Films by
Electrophoretic Deposition - Creating efficient Morphologies for Catalysis**



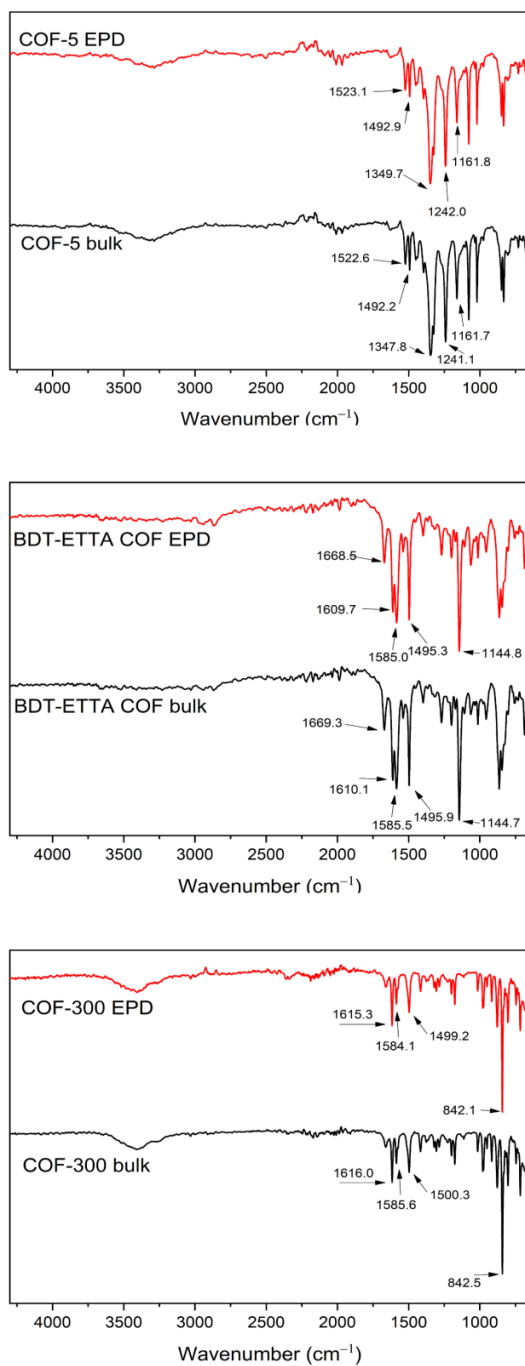
SI Figure 6.6. TEM image of deposited COF-5.

6.10.5 COF EPD film physisorption



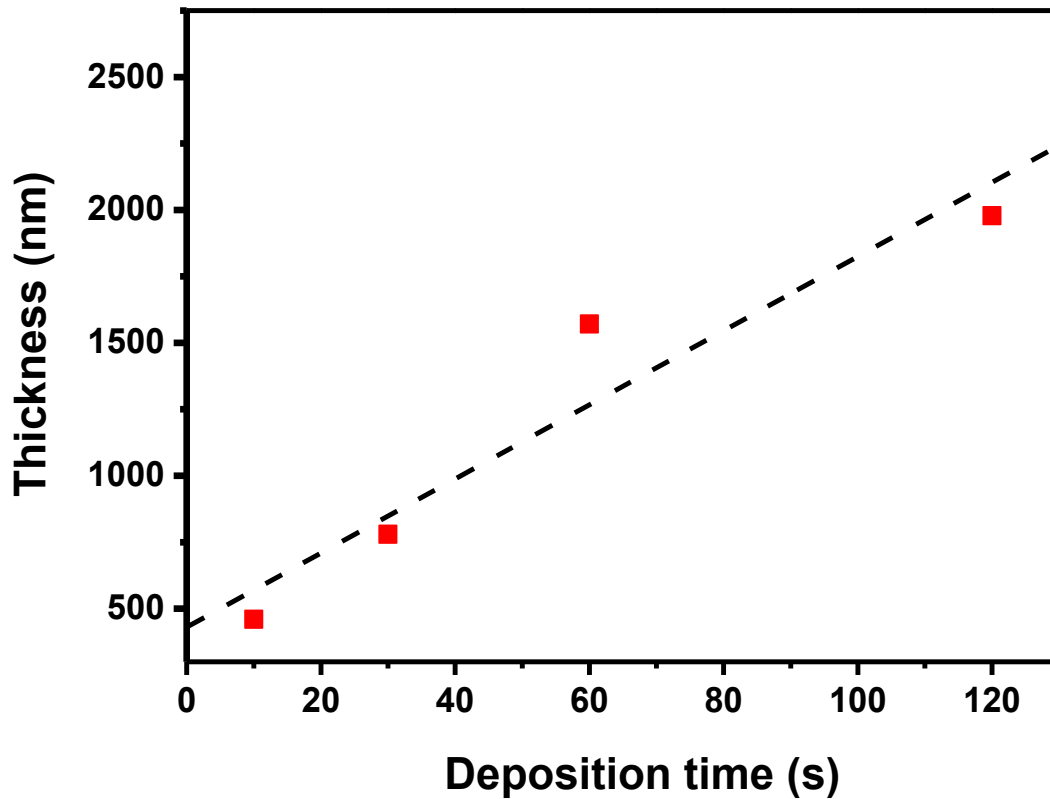
SI Figure 6.7. Nitrogen physisorption isotherms of scratched-off powder from the respective COF EPD films. Due to the low mass of the scratched-off powders, quantitative nitrogen uptake could not be accurately determined.

6.10.6 Fourier-transformed infrared spectroscopy



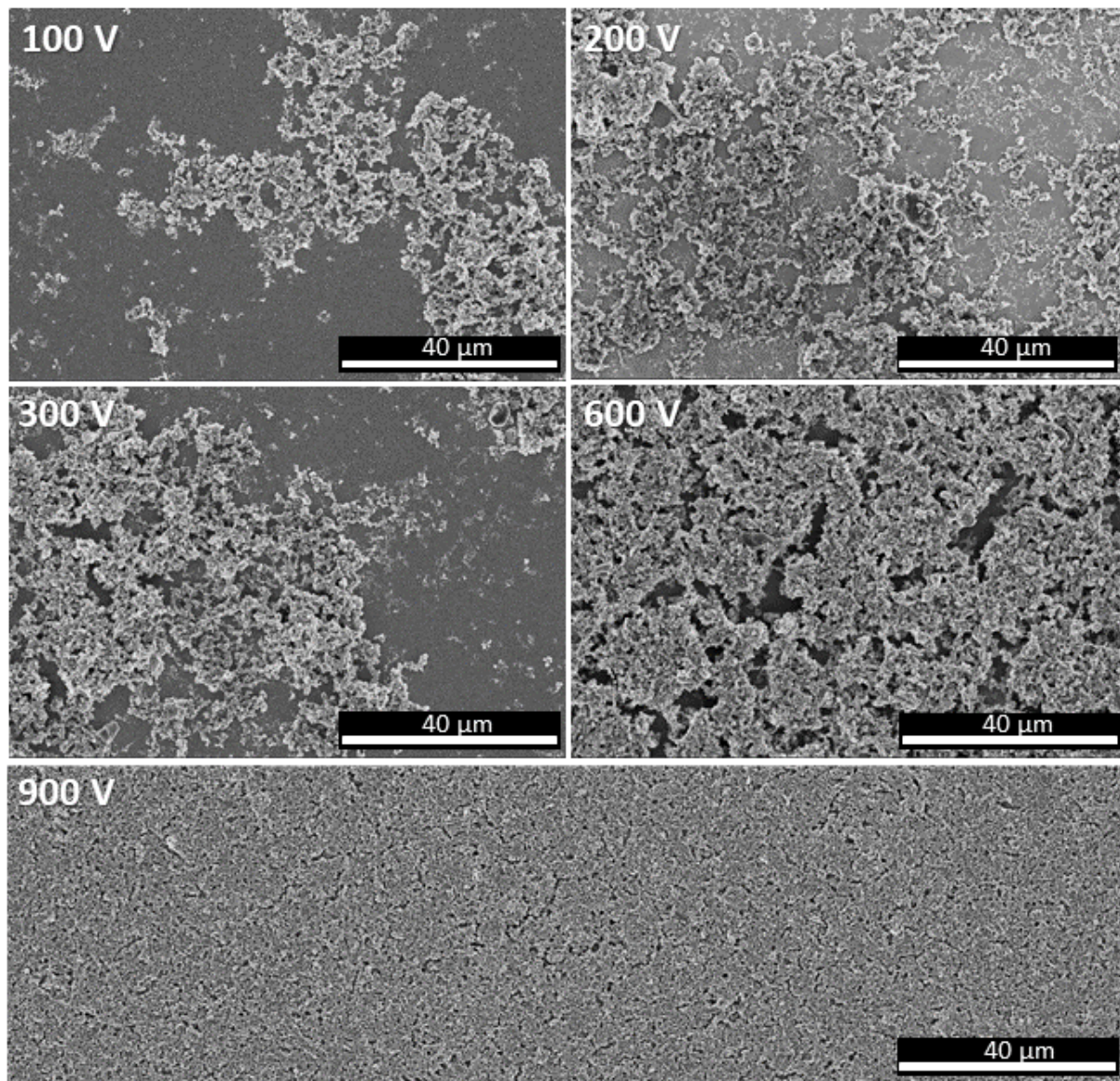
SI Figure 6.8. FT-IR spectra of the as-synthesized bulk material and as scratched-off EPD film materials. In all three cases IR vibrations are preserved. This indicates that no chemical degradation occurred during the EPD process.

6.10.7 BDT-ETTA COF time-dependent thickness plot



SI Figure 6.9. Time-dependent thickness plot of BDT-ETTA COF deposited from ethyl acetate at 900 V. Thicknesses obtained from SEM cross-sections.

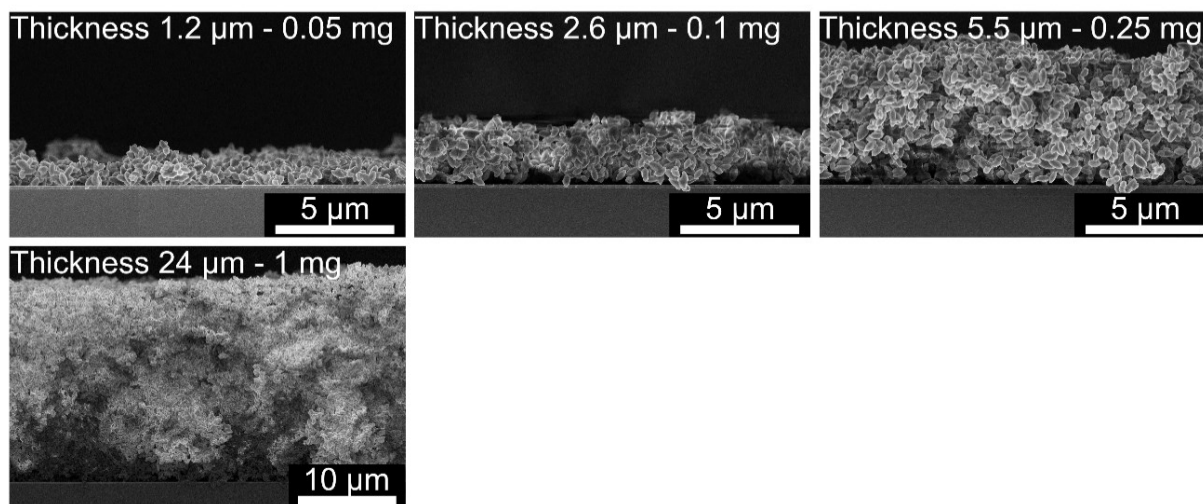
6.10.8 Voltage dependent deposition of BDT-ETTA



SI Figure 6.10. SEM top-view images of BDT-ETTA COF deposited at different voltages for 2 min from ethyl acetate.

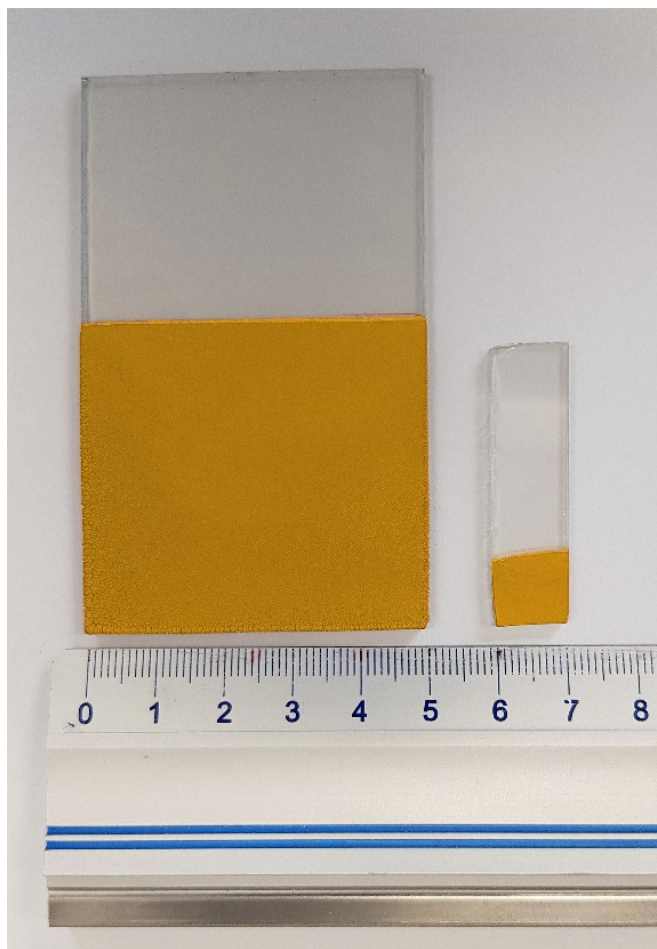
Supporting Information

6.10.9 Mass-dependent deposition of COF-300



SI Figure 6.11. SEM cross-section images of depositions of COF-300 using different masses and the resulting film thicknesses. Depositions were carried out at 900 V for 2 min from ethyl acetate.

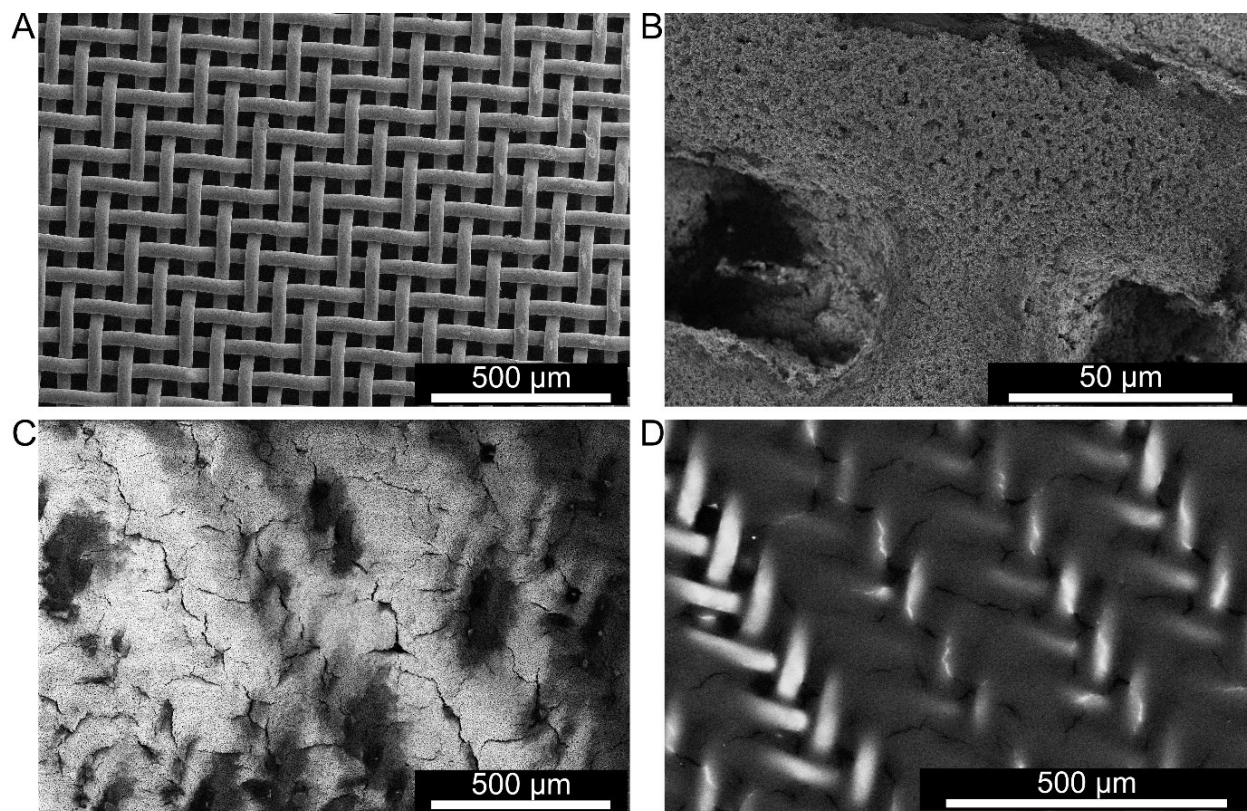
6.10.10 Large area deposition of BDT-ETTA COF



SI Figure 6.12. Photograph of an EPD of BDT-ETTA COF on 5 cm × 5 cm electrode area as well a 1 cm × 1 cm film. Both depositions were carried out on FTO at 900 V for 2 min.

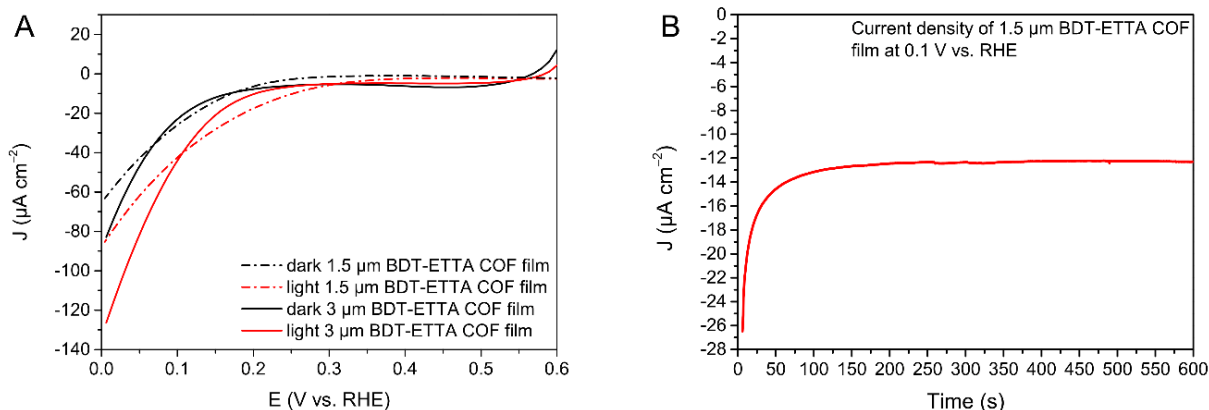
Supporting Information

6.10.11 SEM Micrographs of BDT-ETTA COF deposited on a porous mesh



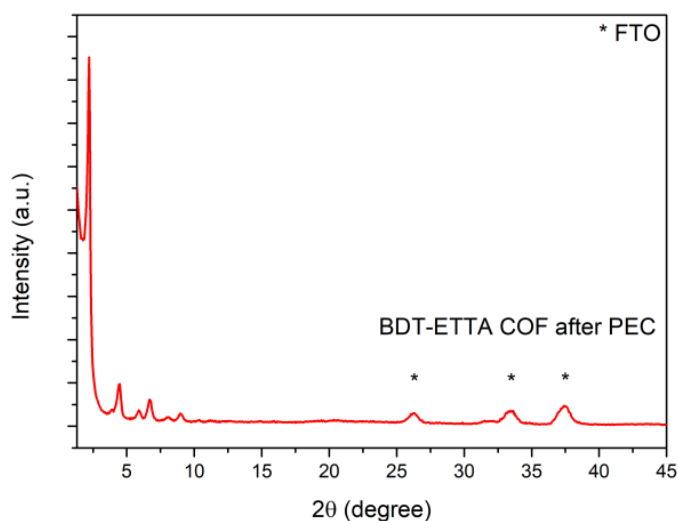
SI Figure 6.13. SEM top view micrographs of BDT-ETTA COF depositions on a porous steel mesh (mesh size 270). (A) Image of the bare mesh prior to deposition. (B) High magnification of BDT-ETTA COF particles deposited on the mesh. (C) Deposition of BDT-ETTA COF in high concentration on a steel mesh, revealing the complete coverage of the pores. (D) Corresponding back-scattered electron micrograph at 30 kV acceleration voltage, revealing the underlying mesh structure.

6.10.12 Thickness dependent PEC Current measurements and Chronoamperometry



SI Figure 6.14. (A) Thickness dependent PEC linear sweep voltammograms of electrodes coated with BDT-ETTA COF. Illumination at AM1.5G. (B) Chronoamperometric current density measurement of BDT-ETTA COF under illumination.

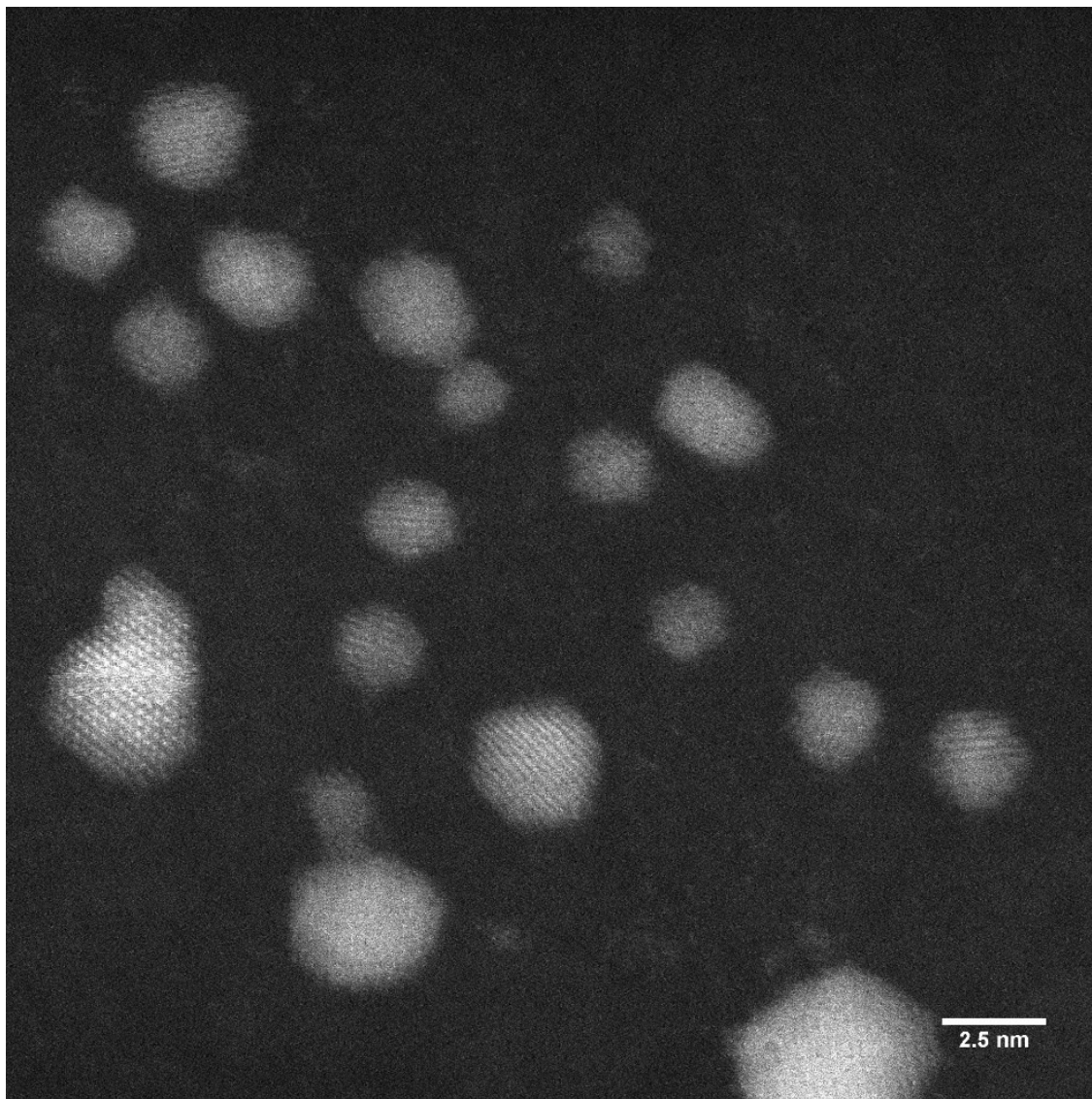
6.10.13 Stability of BDT-ETTA COF after PEC catalysis



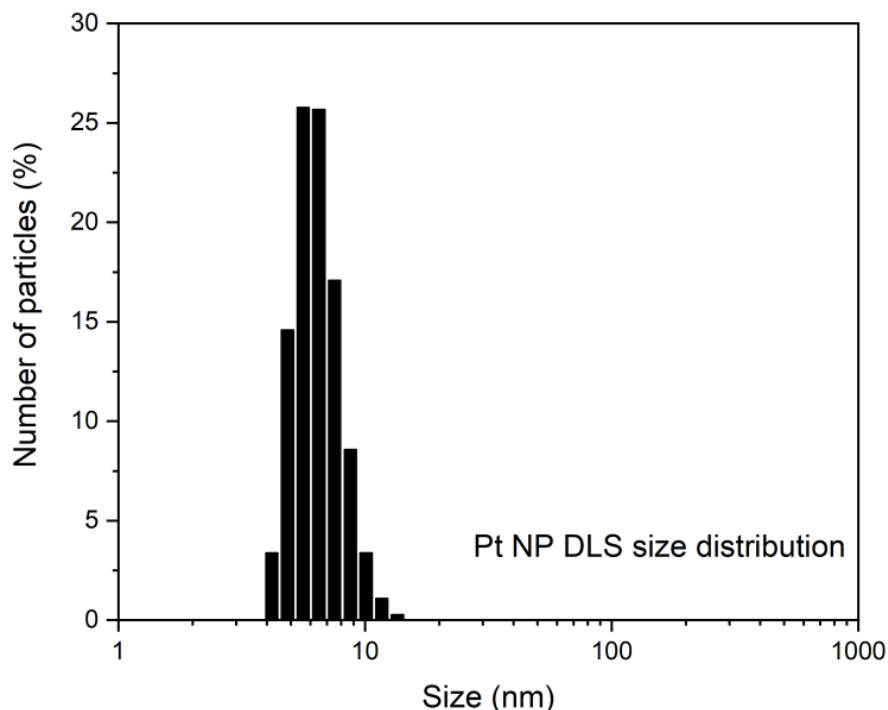
SI Figure 6.15. Stability of BDT-ETTA COF after 30 minutes of chopped illumination at 0.1 V vs. RHE.

Supporting Information

6.10.14 TEM of Pt nanoparticles



SI Figure 6.16. TEM micrograph of Pt nanoparticles after lyophilization.



SI Figure 6.17. DLS profile of Pt nanoparticles after lyophilization.

6.10.15 References

- (1) Sick, T.; Hufnagel, A. G.; Kampmann, J.; Kondofersky, I.; Calik, M.; Rotter, J. M.; Evans, A.; Döblinger, M.; Herbert, S.; Peters, K. et al. Oriented Films of Conjugated 2D Covalent Organic Frameworks as Photocathodes for Water Splitting. *JACS* **2018**, 140, 2085–2092, DOI: 10.1021/jacs.7b06081.
- (2) Uribe-Romo, F. J.; Hunt, J. R.; Furukawa, H.; Klöck, C.; O'Keeffe, M.; Yaghi, O. M. A crystalline imine-linked 3-D porous covalent organic framework. *JACS* **2009**, 131, 4570–4571, DOI: 10.1021/ja8096256.
- (3) Calik, M.; Sick, T.; Dogru, M.; Döblinger, M.; Datz, S.; Budde, H.; Hartschuh, A.; Auras, F.; Bein, T. From Highly Crystalline to Outer Surface-Functionalized Covalent Organic Frameworks--A Modulation Approach. *JACS* **2016**, 138, 1234–1239, DOI: 10.1021/jacs.5b10708.
- (4) Wu, G.-W.; He, S.-B.; Peng, H.-P.; Deng, H.-H.; Liu, A.-L.; Lin, X.-H.; Xia, X.-H.; Chen, W. Citrate-capped platinum nanoparticle as a smart probe for ultrasensitive mercury sensing. *Analytical chemistry* **2014**, 86, 10955–10960, DOI: 10.1021/ac503544w.

Supporting Information

7 Conclusions and Outlook

Artificial photosynthesis by photoelectrochemical water splitting was presented as a promising technology for sustainable hydrogen production. However, the field is still dominated by a quest for finding efficient light absorbing semiconductors as well as suitable cocatalysts for a prospective industrial application of this technology. Both the solar-to-hydrogen efficiency and the stability of the *state-of-the-art* materials are not yet sufficient to become a viable technology and to compete with already established processes. Nevertheless, basic research on photoelectrochemistry teaches a lot about semiconductor and catalyst design, which was the guiding principle of this work.

The first half of this thesis dealt with metal oxides serving as both photoanode and -cathode materials for the evolution of oxygen and hydrogen, respectively. Photoelectrochemical water splitting had been invented based on this materials class and, consequently, it is a well-studied field. However, the described materials are either not efficient enough (e.g., TiO_2 , WO_3 or $\alpha\text{-Fe}_2\text{O}_3$) or are facing fundamental stability issues, including the best-performing materials like Cu_2O and BiVO_4 . Future studies on these materials should therefore explore them as model systems. This would give further insights into the effect of doping on band structure, charge transport and charge transfer properties. Especially the intrinsic instable material candidates can be used to develop robust and affordable protection strategies and study their impact on the semiconductor - electrolyte interface. Due to their intrinsic robustness, hematite photoanodes were studied in this thesis to explore doping effects on crystallization behavior, band gap position and charge carrier properties. While the photoelectrochemical performance of tin doped hematite peaks at a tin doping concentration of 6 mol%, exceptionally high homogeneous tin doping concentrations up to 33 mol% could be realized by the use of atomic layer deposition. With rising tin content, the number of grain boundaries formed is increased and the band structure of hematite becomes more and more metallic, which was further confirmed by density functional theory calculations. While both observed effects are observed to be counterproductive in terms of photoelectrochemical studies, these devices may find applications making use of the lattice expansion and other solid solution effects. Continued research in this area

would likely benefit from a focus on stability, investigating light or potential induced corrosion and dissolution of already established materials, as it was shown with the example of lithium doped copper oxide as part of this work. Commonly used characterization methods were found to be repeatedly misinterpreted by various researchers in terms of performance and stability. The shown work gives a full picture of the photocorrosion of Li doped CuO, which is reduced to Cu₂O all over the CuO - electrolyte interface and forms even distinct cuboid Cu₂O nanocrystals on the electrode surface. Furthermore, a possible protection strategy is described using a thin and amorphous Nb doped TiO₂ layer prepared by atomic layer deposition combined with a Pt cocatalyst. This stabilized the photoabsorber for 30 minutes against decomposition and produced a stable hydrogen evolution. Besides this, the catalytic properties of various metal oxides should be evaluated to substitute currently used noble metal catalysts and therefore bring electrochemical hydrogen evolution from water and renewable energy a significant step further down the road towards a broadly utilized technology.

The second half of the discussed projects introduced covalent organic frameworks as a class of conductive polymers applicable as photocathode materials for hydrogen evolution. With almost endless possible combinations of organic building blocks, which can be individually optimized towards their targeted application, COFs may become a promising materials class within this field of research. Focusing on the example of the *BDT-ETTA* COF, this thesis revealed the intrinsic catalytic properties of the organic framework to be the bottleneck for achieving efficiencies comparable to metal oxides. In future work, this challenging aspect could be targeted by implementing catalytically active functional groups directly into the structure of the COF. Furthermore, photoelectrochemical water splitting is known to be a process that is strongly controlled by the nature of the relevant interfaces. As part of this thesis, electrophoretic deposition was described as a viable and scalable technique for the deposition of comparably large COF films exhibiting high textural porosity. Through combination of the described approaches, a robust and efficient class of materials can be envisioned that would solely be composed of light and easily available elements like hydrogen, carbon, nitrogen, oxygen and sulfur.

Finally, based on these newly attained insights in materials science and photoelectrochemistry, the combination of dark electrolysis and solar cells or wind power plants is, according to the current state of technology, capable of producing larger quantities of hydrogen compared to photoelectrochemical water splitting and will probably dominate the hydrogen production from renewable energy in the

Conclusions and Outlook

next ten to twenty years. Nevertheless, with continued research on semiconductors and catalysts, photoelectrochemical water splitting will have the chance to become widely applicable, standing side by side with other technologies with the purpose of harvesting and storing renewable energy.

8 Publications and Conference Contributions

8.1 Publications

Oriented Films of Conjugated 2D Covalent Organic Frameworks as Photocathodes for Water Splitting, Torben Sick, Alexander G. Hufnagel, J. Kampmann, Ilina Kondofersky, Mona Calik, Julian M. Rotter, Austin M. Evans, Markus Döblinger, Simon Herbert, Kristina Peters, Daniel Boehm, Paul Knochel, Dana D. Medina, Dina Fattakhova-Rohlfing and Thomas Bein, *J. Am. Chem. Soc.*, **2018**, 140, 6, 2085-2092.

Covalent Organic Framework Films through Electrophoretic Deposition - Creating Efficient Morphologies for Catalysis, Julian M. Rotter, Simon Weinberger, Jonathan Kampmann, Torben Sick, Menny Shalom, Thomas Bein and Dana D. Medina, *Chem. Mater.*, **2019**, 31, 24, 10008-10016.

Sn-Doped Hematite for Photoelectrochemical Water Splitting: The Effect of Sn Concentration, Siyuan Zhang, Hamidreza Hajiyani, Alexander G. Hufnagel, Jonathan Kampmann, Benjamin Breitbach, Thomas Bein, Dina Fattakhova-Rohlfing, Rossitza Pentcheva and Christina Scheu, *Zeitschrift für Physikalische Chemie*, **2019**.

How photocorrosion can trick you: A detailed study on low-bandgap Li doped CuO photocathodes for solar hydrogen production, Jonathan Kampmann, Sophia Betzler, Hamidreza Hajiyani, Sebastian Häringer, Michael Beetz, Tristan Harzer, Jürgen Kraus, Bettina V. Lotsch, Christina Scheu, Rossitza Pentcheva, Dina Fattakhova-Rohlfing and Thomas Bein, *submitted*.

8.2 Contribution to Conferences

8.2.1 Oral Presentations

1. "Oriented Films of Conjugated 2D Covalent Organic Frameworks as Photocathodes for Water Splitting"

Jonathan Kampmann, Torben Sick, Alexander G. Hufnagel, Ilina Kondofersky, Markus Döblinger, Kristina Peters, Daniel Böhm, Dina Fattakhova-Rohlfing and Thomas Bein.

DFG SPP 1613 Workshop on New Absorbers, Gießen, Germany, March 2018.

2. "How photocorrosion can trick you: A detailed study on low-bandgap Li doped CuO photocathodes for solar hydrogen production"

Jonathan Kampmann, Sophia Betzler, Hamidreza Hajiyani, Sebastian Häringer, Michael Beetz, Tristan Harzer, Jürgen Kraus, Bettina V. Lotsch, Rossitza Pentcheva, Dina Fattakhova-Rohlfing and Thomas Bein.

Bunsen-Discussion-Meeting on Fundamentals and Applications of (Photo) Electrolysis for Efficient Energy Storage, Taormina, Italy, April 2019.

8.2.2 Poster Presentations

1. "Mixed Metal Oxide Nanostructures for Photoelectrochemical Water Splitting"

Alexander G. Hufnagel, Ilina Kondofersky, Jonathan Kampmann and Thomas Bein.

DFG SPP 1613, Summer School/Project Meeting, Berlin, Germany, September 2016

2. "Oriented films of conjugated 2D Covalent Organic Frameworks as Photocathodes for Water Splitting"

Jonathan Kampmann, Torben Sick, Alexander G. Hufnagel, Ilina Kondofersky, Markus Döblinger, Kristina Peters, Daniel Böhm, Dina Fattakhova-Rohlfing and Thomas Bein.

NIM Conference Nanostructured functional Materials for sustainable Energy Provision, Munich, Germany, July 2017.

Publications and Conference Contributions

3. "Oriented films of conjugated 2D Covalent Organic Frameworks as Photocathodes for Water Splitting"

Jonathan Kampmann, Torben Sick, Alexander G. Hufnagel, Ilina Kondofersky, Markus Döblinger, Kristna Peters, Daniel Böhm, Dina Fattakhova-Rohlfng and Thomas Bein.

6th SolTech Conference, Munich, Germany, October 2017.

4. "Metal oxide nanostructures and 2D Covalent Organic Frameworks for electrochemical and photoelectrochemical water splitting"

Jonathan Kampmann, Daniel Böhm, Torben Sick, Alexander G. Hufnagel, Michael Beetz, Ilina Kondofersky, Markus Döblinger, Kristina Peters, Maximilian Schuster, Dina Fattakhova-Rohlfng and Thomas Bein.

DFG SPP 1613 Project Meeting, Hofgeismar, Germany, October 2017.

5. "Conjugated 2D Covalent Organic Framework Thin Films as novel Absorber Material for Photoelectrochemical Hydrogen Evolution"

Jonathan Kampmann, Torben Sick, Alexander G. Hufnagel, Ilina Kondofersky, Markus Döblinger, Kristna Peters, Daniel Böhm, Dina Fattakhova-Rohlfng and Thomas Bein.

7th SolTech Conference, Würzburg, Germany, October 2018.

6. "Conjugated 2D Covalent Organic Framework Thin Films as novel Absorber Material for Photoelectrochemical Hydrogen Evolution"

Jonathan Kampmann, Torben Sick, Alexander G. Hufnagel, Ilina Kondofersky, Markus Döblinger, Kristna Peters, Daniel Böhm, Dina Fattakhova-Rohlfng and Thomas Bein.

nanoGe Fall Meeting 2018, Malaga, Spain, October 2018.

7. "A 2D-COF for photoelectrochemical hydrogen evolution - Morphology and cocatalyst effects"

Jonathan Kampmann, Julian Rotter, Torben Sick, Alexander G. Hufnagel, Simon Weinberger, Menny Shalom, Markus Döblinger, Daniel Böhm, Dana D. Medina, Dina Fattakhova-Rohlfng and Thomas Bein.

EuroMOF, Paris, France, October 2019.